UNIVERSITY OF OKLAHOMA

GRADUATE COLLEGE

UNDERSTANDING ULTIMATE SHEAR BEHAVIOR OF PRESTRESSED CONCRETE GIRDER BRIDGES AS A SYSTEM THROUGH EXPERIMENTAL TESTING AND ANALYTICAL METHODS

A DISSERTATION

SUBMITTED TO THE GRADUATE FACULTY

in partial fulfillment of the requirements for the

Degree of

DOCTOR OF PHILOSOPHY

By

CAMERON DAVID MURRAY
Norman, Oklahoma
2017

UNDERSTANDING ULTIMATE SHEAR BEHAVIOR OF PRESTRESSED CONCRETE GIRDER BRIDGES AS A SYSTEM THROUGH EXPERIMENTAL TESTING AND ANALYTICAL METHODS

A DISSERTATION APPROVED FOR THE
SCHOOL OF CIVIL ENGINEERING AND ENVIRONMENTAL SCIENCE

BY

_____
Dr. Royce W. Floyd, Chair

_____
Dr. Christopher C. E. Ramseyer

_____
Dr. Jeffery S. Volz

_____
Dr. P. Scott Harvey, Jr.

_____
Dr. Lisa Holliday

To my incredible and inspiring teachers over the years.

Acknowledgements

An unfortunate truth about research is that failure sometimes seems to come more often than success. These three years at the University of Oklahoma have fortunately been filled with many successes and few failures. As I look back it seems I owe many of the successes to those whom I have been lucky enough to call colleagues. Through the ups and downs I am also fortunate to have wonderful friends and family who have brought me so much joy. I am humbled by the help, friendship, mentorship, and love that the people listed here have provided through the course of this Ph.D.

Before I begin, I want to thank the Oklahoma Department of Transportation (ODOT) for the funding that made this project possible. This dissertation reports my views, and not necessarily those of ODOT. Thanks to Walt Peters of ODOT for his guidance and input in helping us form some of our goals. I also wish to thank the Dwight David Eisenhower Transportation Fellowship Program for their funding and for sending me to the Transportation Research Board Annual Meeting to share this work with my peers.

I would like to thank my adviser, Dr. Royce Floyd. His devotion to teaching and scholarship has long been an inspiration to me. I also must thank the rest of the committee, Dr. Chris Ramseyer, Dr. Jeff Volz, Dr. Scott Harvey, and Dr. Lisa Holliday. Dr. Jin-song Pei has also provided much help and guidance during this Ph.D. as a co-PI on the project. They have all set a wonderful example of mentorship.

The laboratory work presented in this dissertation was supported by an exceptional group of undergraduate and master's students: Alex Stumps, Connor Casey, Chandler Funderburg, Ashwin Kesiraju, Stephen Tanksley, Darion Mayhorn, Brittany

Cranor, Troy Bowser, Soroush Mohammadzadeh, Peng Tang, and Kyle Roeschley. I want to also thank Troy Bowser, Jonathan Drury, and Sam Sherry; they have been a source of academic support and encouragement and I am thankful to count them as friends. Mr. Mike Schmitz was also instrumental to much of the lab work in this dissertation and I have been extremely fortunate to learn from him.

I want to thank Katelyn Burks for listening to my “interesting” bridge facts on road trips and for her love and support. Finally, I want to thank my parents, David and Kathryn Murray for all that they have done for me. They have always been an inspiration to me, and I owe more to them than can be put into words.

Table of Contents

List of Tables

List of Figures

Abstract

A prestressed concrete bridge is a complex system. The interconnectivity of several girders, a deck, and secondary elements such as diaphragms makes their behavior difficult to represent. Additionally, the shear behavior of in service prestressed concrete girders can be difficult to predict, particularly when older codes were used in design and where damage is present in the girders. This work contains laboratory testing to investigate the residual shear performance of two older American Association of State Highway and Transportation Officials (AASHTO) Type-II prestressed concrete girders, as well as the behavior of a scale prestressed concrete bridge loaded in shear to failure. The full-scale girders were found to be capable of carrying their full capacity even when corrosion affected the failure mechanism. Based on these tests, the modified compression field theory (MCFT) methods were recommended for estimating the capacities of older girders. The scale bridge provided information about load distribution at ultimate capacity, and the influence of secondary elements (diaphragms) on load transfer after girder failures. The bridge test also documented the ultimate behavior of a prestressed concrete bridge, findings that are not common in the literature. The bridge failure was controlled by punching shear, and the diaphragms were seen to provide a significant means of load transfer after a girder failed. Finally, simple computer models were built that are capable of reducing the conservativism of the codified distribution factor (DF) methodology, increasing the usable capacity of bridges. These models simplify the girders and slab into a “grillage” of beam elements with appropriate stiffnesses. A parametric study suggests that for AASHTO Type-II girder bridges, load ratings tend to be conservative for smaller girder spacing and

shorter span lengths. Code DFs were generally found to be conservative for all configurations of typical Type-II girder bridges.

Chapter 1: Introduction

Prestressed concrete bridges form an important part of American highway infrastructure. As of 2016, there were 155,701 prestressed concrete bridges (both simple span and continuous) in service out of 614,386 total bridges in the United States (U.S.) (Federal Highway Administration, 2016). As an example, the state of Oklahoma had 4,582 prestressed concrete bridges in service in 2016, many of which were built in the early days of the interstate highway system and are now over 40 years old. These older bridges are reaching the end of their design lives and their replacement can be expensive, time consuming, and disruptive to the overall transportation system. There are several concerns about bridges of this age, environmental deterioration, structural deficiency, and functional obsolescence. A common form of deterioration comes in the form of corrosion damage at the ends of the girders. Even as these older bridges are replaced, concerns about corrosion damage to end regions of concrete girders are likely to be revisited in the future as the newer infrastructure ages. Other parts of the bridge can sustain environmental damage, but end region damage to the girders is of significant consequence as these are the main elements of strength in the bridge.

One concern for the residual capacity of these bridges is the shear performance. Corrosion in the end regions could lead to issues with prestressing strand bond, potentially reducing shear capacity. Additionally, the way the bridge design code has handled shear has changed considerably over the years. The shear capacity equations have become more complex and rational, and the shear demands have changed since the 1960s. The only way to truly understand the effects of these changes in concert with the

deterioration of similar girders is to test real examples in a laboratory setting and compare the results to the code predictions.

Another area of interest in relation to prestressed concrete bridges is the question of ultimate shear capacity of the entire bridge. Bridges are designed on the basis of the strength of their components. Put simply, bridge girders are designed on the basis of their individual ultimate strength, despite the interconnectivity of the bridge system. The system level behavior is accounted for using *distribution factors* (DFs) which determine the individual demands on girders based primarily on the geometric parameters of the bridge system. These factors are derived from elastic behavior however, and the ultimate behavior of a bridge system may be different. Few examples of ultimate load tests of bridges exist, and these investigations are necessary to better understand system level behavior at extreme loads.

Finally, load distribution in bridges has been a source of debate, and the methods to determine DFs have changed over the years. When it comes to load rating older bridges, overly conservative DFs can reduce the life of bridges that are still capable of serving their owners. If the loads on a girder are not estimated accurately the girder may be replaced prematurely. While several DF methods have been proposed since the 1990s, a methodology developed in the late 1980s is still used by the current American Association of State Highway and Transportation Officials (AASHTO) Load and Resistance Factor Design (LRFD) bridge code. One promising improvement on current methods is the use of grillage models, simple representations of bridges composed of beam elements in a finite element or structural analysis program. Because of the ubiquity of computers, the use of these simple models could improve DF

calculations and reduce an unnecessary level of conservativism in bridge design and rating of older bridges.

1.1 Research Scope

This dissertation describes several studies carried out to address the concerns outlined above. To address the issue of corroded girders and look at the capacity of girders that have been in service for years, two full-scale AASHTO Type-II bridge girders were recovered from a bridge at the end of its life for laboratory testing. The results of that testing are reported here with particular focus on the effects of end region corrosion, behavior from the quarter span point of the girders to the ends, effects of diaphragms, and overall shear performance. The results of the first girder test were reported in a previous student's work (Cranor, 2015); in this dissertation special focus was paid to the corrosion in the girder and to drawing broader conclusions including the second girder test. To better understand system level shear performance of a prestressed concrete bridge, a scale bridge was constructed in the lab and tested both elastically and to its ultimate capacity. The purpose of this test was to observe load distribution at ultimate capacity, observe post-cracking behavior, investigate the effects of the diaphragms, especially at ultimate loads, and compare total bridge behavior to individual girder behavior. Finally, a grillage model of the scale bridge was made to compare to experimental load distribution. Upon validation of this technique using the scale bridge a parametric study of load distribution for Type-II girder bridges was carried out and compared to three real-world Oklahoma bridges including the bridge spans from which the full-scale girders were taken. These real-world bridges provide

some context for the results of the grillage models, and also allow comparison of load ratings to actual laboratory testing.

1.2 Research Importance

Individually, this dissertation contains three separate studies that are valuable additions to the literature. First, there are very few examples of full-scale girders tested to ultimate capacity in a lab after years in service, especially to investigate residual shear performance. The corrosion to the prestressing strands of the girders tested in this study also make it unique. The only way to be sure about the actual capacity of older bridges is to test older girders, so this part of the work will provide bridge owners with much needed information about similar bridges. Investigating the capacity of corroded bridge girders from the late 1960s in shear will be an important part of this work.

Secondly, tests of full composite bridge sections to their ultimate capacity are exceedingly rare. Many studies have tested bridges at service level demands, but studies which investigate the post cracking behavior of prestressed concrete bridges are quite uncommon. As computer modeling becomes more popular, real bridges must be tested so that actual failure mechanisms can be documented and model behavior verified. End and intermediate diaphragms are commonly detailed for prestressed bridges, but their contribution to the ultimate capacity of bridges is unclear. This study investigated the effects of these diaphragms on failure. Because there are so few examples of ultimate load level bridge tests (especially recently), this work provides new and important information about how bridges behave after girder failures.

Finally, grillage modeling seems to be the future of load DFs for highway bridges (Dymond, French, & Shield, 2016). Grillages have been used to verify load

distribution models in the past, but their potential to replace the existing DF framework is significant. In this study, a grillage modeling paradigm was verified based on the behavior of the scale bridge. Next, 48 parametric models of Type-II girder bridges were built to look at what factors most influence load distribution, and to see what configurations lead to the most conservative factors from the AASHTO LRFD code. There have been many DF studies since the 1990s, and grillage models are often used, but this study focuses on a specific bridge type, and the findings can be applied across the country to inform load ratings and hopefully encourage implementation of grillage modeling. Grillages were built for some real-world bridges and their results were used to load rate the bridges, showing how conservative load ratings can be for some bridges. This could allow bridge owners to extend the life of these common bridge types by reducing the live load demands.

Individually, there are three valuable studies incorporated here. Taken as a whole they present a holistic view of the behavior of Type-II girder bridges, from the component level (full-scale tests), to ultimate behavior of the system (scale bridge test), to broader conclusions about load distribution and load ratings (model parametric study and synthesis of information). This dissertation combines experimental and analytical research to present broad conclusions useful for decision making for older bridges which can be valuable to researchers and bridge owners around the country.

1.3 Document Overview

This dissertation consists of five chapters. Chapter 1 is the introduction, describing the problem to be addressed. Chapter 2 contains the literature review, which covers prestressed concrete, shear capacity and demand, load distribution, grillage

modeling, load rating, and similar studies. Chapter 3 contains information related to the full-scale girder tests. Chapter 4 pertains to the scale girder and bridge tests. Chapter 5 contains all the information about grillage modeling. Chapters 3-5 each contain separate methods, results, and discussions related to the portion of the research discussed in that chapter. The Appendices include raw data, material properties, parameters for the grillage models, and other information.

The work of two other authors is incorporated here. Brittany Cranor (Cranor, 2015) was responsible for testing the first of the two full-scale sections reported here. The author of this dissertation was present for this testing and collaborated on much of it, but some information here related to testing procedures and testing results is also reported in that master's thesis. Darion Mayhorn was responsible for designing the scale girder sections used in this project (Mayhorn, 2016). In both cases the current work uses the information discovered by these fellow graduate students in ways not considered previously. Finally, some of the results reported in this dissertation are also incorporated in a report submitted to the Oklahoma Department of Transportation (Floyd, Pei, Murray, Cranor, & Tang, 2016).

Chapter 2: Literature Review

2.1 Prestressed Concrete

Prestressed concrete is a composite material consisting of concrete and high strength steel wire or strand. Since concrete is relatively weak in tension, a prestressing wire or strand can be placed wherever tensile stresses in the concrete member are expected and tensioned, putting the concrete around it into compression. By using multiple strands, it is possible to design a concrete member which theoretically never goes into tension under service stresses. The benefits of this marriage of materials include: longer spans for beams and girders, improved durability from reduced cracking, larger load carrying capacity, and reduced deflections (Wight & MacGregor, 2012).

Prestressed concrete was invented by a French bridge engineer, Eugène Freyssinet, in 1928. Its development was halted in 1939, due to the outbreak of World War II. The war devastated European infrastructure, and steel shortages created a need for a material to rebuild Europe's bridges. Prestressed concrete soon became the material of choice for this kind of construction in post-war Europe. The technology was brought to the U.S. in the 1940s and 50s, culminating in the design of the Walnut Lane Memorial Bridge in Philadelphia, PA. The successful implementation of this new technology led to the birth of the prestressed concrete industry in America. Around the same time, seven-wire stress relieved strand was invented, and became the standard for prestressed concrete. In the late 1950s, construction began on the U.S. interstate highway system; this provided both a demand for prestressed concrete bridge girders, and a means for transporting the girders to jobsites. Since these early developments, the

precast-prestressed concrete bridge girder has become a staple of US infrastructure (Nasser, Tadros, Sevenker, & Nasser, 2015).

2.2 Prestressing Strand Bond

An important design consideration for prestressed concrete is the concept of transfer and development length. The transfer of the force in the strands to the concrete affects the shear and moment capacity of the member. In pretensioned, prestressed concrete (referred to simply as prestressed concrete in this dissertation), strands are tensioned and then concrete is cast around them. Once the concrete reaches an acceptable strength, the ends of the strands are released, which imparts a compressive force into the hardened concrete through bond stresses between the steel and concrete. Alternately, in post-tensioned, prestressed concrete (generally referred to simply as post-tensioned concrete), ducts are placed in the concrete in which strands can be tensioned after the concrete is hardened and the force is transferred through anchorages embedded in the concrete.

In pretensioned concrete, after the tensioned strand is released, the stress imparted to the concrete varies from zero at the ends of the member, to the maximum prestress at some distance into the member. This distance is known as the transfer length, or the bond length needed to transfer full prestress into the concrete (ACI Committee 318, 2014). As a member is loaded in flexure, the stress in the strand increases up to the point when the moment capacity of the member is reached. The additional bonded length needed to develop this force is known as the flexural bond length (ACI Committee 318, 2014). The sum of the transfer length and flexural bond length is the development length, or the embedment length needed to develop the

moment capacity of the member (ACI Committee 318, 2014). This concept is shown graphically in Figure 1. Note that these stress variations are assumed to be linear, whereas in reality their distribution will vary. The development length equation given in the American Concrete Institute (ACI) code is shown in Equation 1. The first term in this equation is the transfer length, and the second is the flexural bond length.

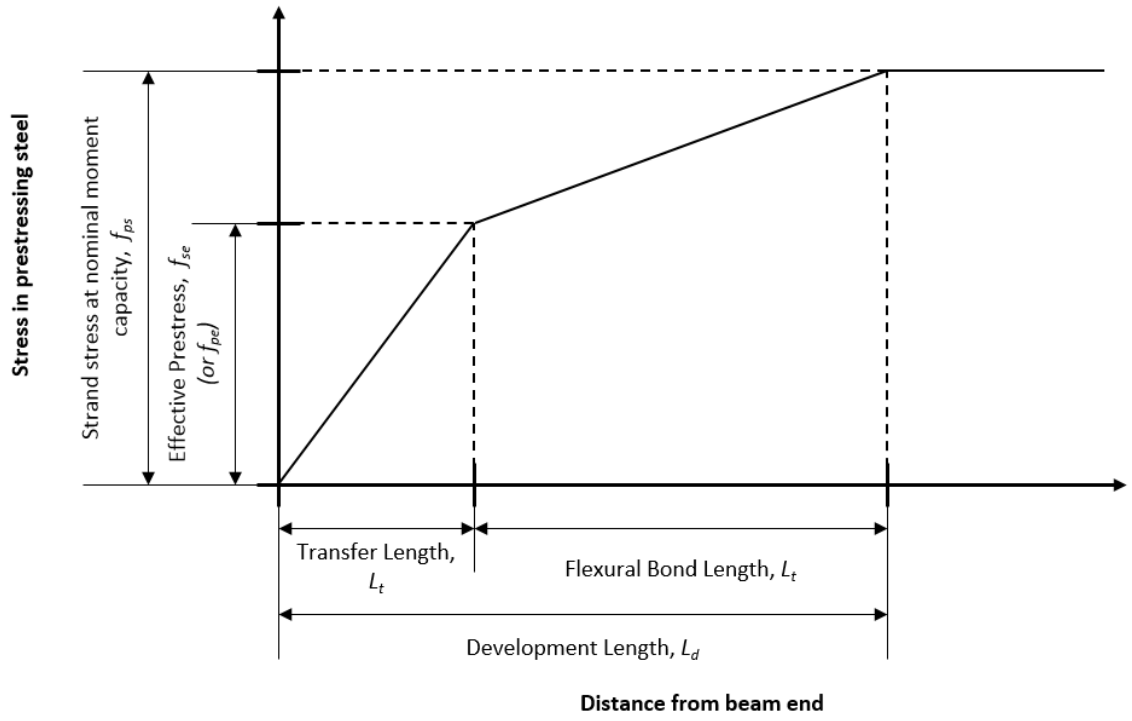

Figure 1: Concept of transfer length and development length

$$l_d = \left(\frac{f_{se}}{3000}\right) d_b + \left(\frac{f_{ps} - f_{se}}{1000}\right) d_b \quad (1)$$

Where:

l_d = Development length (in.)
f_{se} = Effective prestress after losses (psi)
d_b = Strand diameter (in.)
f_{ps} = Stress in strand at nominal flexural strength (psi)

In the AASHTO LRFD code, the development length equation also appears in AASHTO LRFD Section 5.11.4.2 (AASHTO, 2015), albeit slightly reorganized. This is given in Equation 2. Note that the equation is the same as the ACI equation except with some reorganization. The stress units are in ksi instead of psi, and there is an inequality sign to indicate that this is the minimum expected development length. An additional transfer length relationship is given by both ACI and AASHTO LRFD. ACI allows 50 strand diameters and AASHTO allows 60 strand diameters to be taken as the transfer length. In ACI this distance is given for the purpose of reducing the prestress force used when calculating shear capacity (Section 22.5.9 in 2014 ACI code).

$$l_d \geq \kappa \left(f_{ps} - \frac{2}{3} f_{pe} \right) d_b \tag{2}$$

Where:

κ = 1.0 for depth less than or equal to 24.0 in., 1.6 for greater than 24.0 in.
f_{ps} = Average stress in prestressing steel (ksi)
f_{pe} = Effective stress in prestressing steel after losses (ksi)

The seminal experimental work in the area of strand bond was performed in the 1950s, in the early years of prestressed concrete use in the U.S. (Janney, 1954). Guyon (1953) also presented mathematical relationships for strand bond and force transfer. Since then, researchers have focused on improving the formulas used to estimate transfer and development length. Several examples like this exist in the literature (Hanson & Kaar, 1959; Zia & Mostafa, 1977; Russell & Burns, 1996). Another important area of research however is the effect of shear forces in the transfer zone. In concrete beams, shear forces and moments interact near the beam ends, causing inclined stress planes (Figure 2). This results in diagonal tension cracks towards the end of the

beam (Wight & MacGregor, 2012). Prestressing adds to the shear resistance of concrete by altering the stress trajectories, confining the concrete, and increasing the cracking moment; however, if a crack forms within the transfer length, loss of bond can occur, resulting in decreased capacity (Nordby & Venuti, 1957; Kaufman & Ramirez, 1988). Because shear forces can affect the bond of prestressing strands and even cause bond failure, end region detailing of a prestressed beam is of particular importance to its performance.

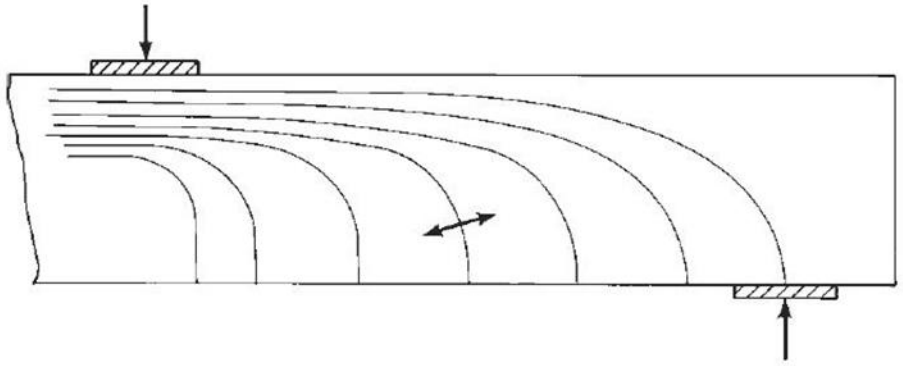

Figure 2: Compression stress trajectories in an un-cracked nonprestressed concrete beam (from Wight & MacGregor 2012)

2.3 Shear in Prestressed Concrete Members

Shear in prestressed concrete members differs from shear in reinforced concrete. The presence of an internal axial force (fully effective beyond the transfer length) alters the stress trajectories in the member. The horizontal compression from the prestress has the effect of flattening the angle of the diagonal tension forces (and resulting cracks), which can mobilize a greater number of shear stirrups and thus increase ductility. The structural designer's goal is typically to create a member that has sufficient ductility so that there are noticeable deflections and visible cracking before a sudden, catastrophic failure. This is typically done by designing the member such that

flexural capacity is the controlling factor. Shear in concrete members can be a sudden and an unpredictable failure mode. As such there has been extensive research in shear over the years. Shear cracking is usually split into two categories: web-shear and flexure-shear cracking. Web-shear cracks initiate in the web of a member and flexure shear cracks begin as flexural cracks (vertical) before re-orienting themselves to the load point and becoming diagonal.

Aside from the typical web-shear and flexure-shear type failures, often a shear failure is associated with loss of bond in the prestressing strands. Recent work has sought to present a uniform system of characterizing failures where strand slip occurs (Naji, Ross, & Floyd, 2017). This work uses the shear span to depth ratio (*a/d*) to describe the testing location. This nomenclature is common in shear tests. Bond-shear failures are associated with cracking near the supports and strand slip or bond loss. A bond-shear failure is defined as a failure with cracking near the supports, strand slip, and no flange crushing. When flange crushing occurs, and the *a/d* is less than 2.5, the failure can be characterized as bond-shear/flexure. If the *a/d* is greater than 2.5 and less than 4.5, and when the nominal moment is exceeded, the failure can be characterized as flexure-bond. When the nominal moment is not reached, the terminology is bond-flexure. This effort was useful in providing guidance for evaluating a failure where slip occurs.

Some important early work regarding shear in prestressed concrete girders was performed at the University of Illinois in the mid-1960s (MacGregor, Sozen, & Siess, 1965). These researchers tested 104 prestressed concrete beams in shear, varying the locations and amounts of transverse reinforcement and concrete strength, among other

variables. The researchers found that transverse reinforcement helped to restrain cracking and improved ductility after web cracks occurred and used this finding to create an empirical equation for shear capacity of girders with transverse steel. Following this work, MacGregor published another paper with code recommendations which were eventually adopted by the ACI 318 Building Code Requirements for Structural Concrete (ACI Committee 318, 2014) and are still used today (MacGregor & Hanson, 1969). The ACI equations are largely empirical and the methodology has not changed much since the 1970s. The code that bridge designers use is the AASHTO LRFD bridge code (AASHTO, 2015). Compared to the ACI shear methodology, the AASHTO code methodology has changed considerably over time.

2.3.1 ACI Code Equations for Shear

The ACI treatment of shear in prestressed concrete is given in Chapters 9 and 22 of the 2014 code (ACI Committee 318, 2014) and involves a separate calculation of the contribution of the steel (V_s) and the concrete (V_c) to the shear resistance. The nominal shear capacity (V_n) of a section is given by Equation 3:

$$V_n = V_c + V_s \tag{3}$$

The method of separating the shear capacity of the concrete and steel is common in the design codes. For prestressed concrete members, the ACI code offers two methods to calculate shear capacity of the concrete: a simplified method and a more complex method that takes into account different cracking behavior and failure mechanisms. Both methods account for the tensile strength of the concrete based on the square root of the compressive strength. The complex method provides an equation for web-shear cracking and flexure-shear cracking to find the controlling type of cracking

at a given section (and the capacity related to these two types). The simplified method is given in Equation 4.

$$V_c = \left(0.6\lambda\sqrt{f'_c} + 700\frac{V_u d_p}{M_u}\right) b_w d \tag{4}$$

Where:

λ = Modification factor for lightweight aggregate; 1.0 for normal weight
f'_c = Specified compressive strength of concrete (psi)
V_u = Factored applied shear at section (lb)
d_p = Depth to centroid of prestress force from extreme compression fiber (in.)
M_u = Factored moment at section (in.-lb)
b_w = Width of web (in.)
d = Distance from extreme compression fiber to centroid of tensile reinforcement (in.)

For this equation, the concrete strength contribution is also limited by the relationship given in Equation 5:

$$2\lambda\sqrt{f'_c}b_w d \leq V_c \leq 5\,\lambda\sqrt{f'_c}b_w d \tag{5}$$

Generally speaking, the square root of concrete compressive strength provides an empirical relationship to the tensile strength in the shear equations. For the more complex method in ACI, the concrete contribution related to flexure-shear capacity is given by Equations 6, 7, 8, and 9.

$$V_{ci} = 0.6\lambda\sqrt{f'_c}b_w d_p + V_d + \frac{V_i M_{cre}}{M_{max}} \tag{6}$$

Where:

$$d_p \geq 0.8h \tag{7}$$

$$M_{cre} = \left(\frac{I}{y_t}\right)\left(6\lambda\sqrt{f'_c} + f_{pe} - f_d\right) \tag{8}$$

$$V_{ci} \geq 1.7\lambda\sqrt{f'_c}b_w d \tag{9}$$

and:

V_{ci} = Nominal shear strength provided by concrete when diagonal cracking results from combined shear and moment (lb)

V_d = Shear force at section due to un-factored dead load (lb)

V_i = Factored shear force at section due to externally applied loads associated with M_{max} (lb)

M_{cre} = Moment causing flexural cracking at section due to external loads (in.-lb)

M_{max} = Maximum factored moment due to external loads (in.-lb)

y_t = Distance from centroid of gross section to tension face (in.)

I = Moment of inertia of cross-section (in^4)

f_{pe} = Stress in concrete due to effective prestress force at tension face (psi)

f_d = Stress due to unfactored dead load at tension face (psi)

h = Height of section (in.)

Note: other variables are previously defined

The nominal shear force required to cause web-shear cracking is given by Equations 10 and 11.

$$V_{cw} = \left(3.5\lambda\sqrt{f'_c} + 0.3f_{pc}\right)b_w d_p + V_p \tag{10}$$

where:

$$d_p \geq 0.8h \tag{11}$$

and:

V_{cw} = Nominal shear strength provided by concrete when diagonal cracking results from high principal tensile stress in web (lb)

f_{pc} = Compressive stress in concrete after losses at centroid of the section resisting external loads or at the junction of the web and the flange when the centroid is within the flange (psi)

V_p = Vertical component of effective prestress force at section (psi)

The shear strength supplied by the transverse reinforcement is given by Equation 12. For vertical shear stirrups, the ACI code assumes a crack angle of 45 degrees. This approach likely overestimates the angle of shear cracking for prestressed beams but will give a conservative value for the steel contribution to shear strength. A minimum shear steel requirement is given if the nominal resistance of the concrete is less than 50% of the ultimate shear demand.

$$V_s = \frac{A_v f_{yt} d}{s} \tag{12}$$

Where:

A_v = Area of shear reinforcement within spacing, s (in^2)
f_{yt} = Yield strength of transverse reinforcement (psi)
s = Spacing of shear reinforcement at section (in.)

The ACI methodology has changed little since the 1970s. ACI also allows the use of a strut-and-tie model (STM) for analysis and design in discontinuity regions of concrete beams. Discontinuity regions, or D-regions, are locations in beams near points of sudden change in load or geometry. For bridge girders, locations near the supports are D-regions, and in these locations the assumptions of Bernoulli beam theory become less accurate. This explains the need for different mathematical models for shear capacity near the ends, as well as why accurate equations for shear capacity have proven difficult to derive over the years.

2.3.2 AASHTO Standard Specifications Shear Equations

In the older AASHTO Standard Bridge Specifications (hereafter referred to as AASHTO-STD) (AASHTO, 1973), the shear capacity of a member is handled in a similar fashion to the ACI 318 code. This code was selected here because it was in use at the time the full-scale girders tested in this study were cast. As for ACI 318, these

equations were largely empirical. The AASHTO-STD used a load factor design (LFD) philosophy for concrete, whereas the current code uses the LRFD philosophy. The sum the contributions of the steel and the concrete to shear resistance is given in Equation 13.

$$V_n = V_c + V_s = 0.06f'_c b'jd + \frac{2A_v f_{sy} jd}{s} \quad (13)$$

Where:

b' = Width of web (in.)

j = Ratio of distance between centroid of compression force and centroid of tension force and total depth

f_{sy} = Tensile capacity of shear reinforcement (psi)

This procedure is quite similar to the ACI method, although it is less complicated with regards to the contribution of concrete to shear strength. As for the steel contribution to shear strength, the "2" in the numerator of the second term in Equation 13 corresponds to a crack angle of 26.6 degrees, as opposed to 45 degrees in the ACI code. A smaller crack angle makes sense because prestress forces are known to flatten stress trajectories in girders, but if the actual crack angle is greater than 26.6 degrees the steel capacity will be overestimated. A minimum shear steel requirement is given by AASHTO-STD provided in Equation 14.

$$A_v \geq \frac{100b's}{f_{sy}} \quad (14)$$

There is no upper limit on shear reinforcement in AASHTO-STD. However, the concrete contribution to shear strength is constrained by an upper limit on compressive strength of 3000 psi. A conservative result of this requirement is that most girders designed using this code required a larger amount of shear steel. This conservativism

with regards to concrete strength could improve the ductility of girders from this time period loaded in shear.

2.3.3 AASHTO Load and Resistance Factor Design Shear Procedures

The AASHTO Bridge Design Specification has also changed considerably overall since the 1970s. The current code now uses a probabilistic LRFD design philosophy. For the rest of this dissertation, the current code (2015 version) will be referred to as the AASHTO LRFD code. In 2004, the code switched to a "sectional design model" using Modified Compression Field Theory (MCFT). The so-called sectional model refers to the division of a member into design spans (typically at tenth points along the span), each of which would have a different demand and capacity.

MCFT was developed in the late 1980s to provide a general method for determining stresses in reinforced concrete members without the use of a computer (Vecchio & Collins, 1986). MCFT assumes that, when shear cracks form, an array of diagonal compression struts are formed in the web. These struts also carry some tension, the sum of which is the concrete contribution to shear strength. When using MCFT in the context of AASHTO LRFD, the designer may determine the factors theta (θ) and beta (β) using tables provided in the code. The factor θ is the crack angle (or angle of diagonal compressive stress) and β describes the ability of the concrete to transmit tension and shear. This meant MCFT was an iterative process that designers disliked because of its complexity and the challenge of performing the calculations by hand (Hawkins, Kuchma, Mast, & Reineck, 2005). Due to the complications associated with MCFT, revisions were published in 2008 allowing the use of MCFT without iteration, simplifying the design process by providing beta-theta equations. The revision

also allowed designers to use a method similar to the ACI code (simplified method), and this revision is reflected in the current standard (AASHTO, 2015). However, the current code allows the designer to use the simplified method, or MCFT by beta-theta equations or tables.

For all of the current AASHTO methods, the nominal shear resistance (V_n) is represented by the sum of the concrete and steel contributions to shear strength (V_c, V_s) and an additional component, V_p, representing additional resistance to shear from the prestressing force. The overall shear strength formulation is given in AASHTO LRFD Section 5.8.3.3.

AASHTO Simplified Method

The AASHTO LRFD code simplified method is similar to the ACI method in that the concrete contribution to shear strength is determined based on flexure-shear and web-shear cracking (Hawkins, Kuchma, Mast, & Reineck, 2005). The simplified procedures are given in AASHTO LRFD Section 5.8.3.4.3. Shear resistance is taken as the sum of the concrete shear strength, steel contribution to shear strength, and a term to account for the influence of prestress force on shear strength. Concrete contribution to shear strength is taken as the lesser of the resistance when cracking is caused by combined shear and moment or the resistance when cracking occurs in the web due to shear only (Equations 15, 16, and 17).

$$V_c = lesser\ of\ V_{ci}, V_{cw} \tag{15}$$

$$V_{ci} = 0.02\sqrt{f'_c}\,b_v d_v + V_d + \frac{V_i M_{cre}}{M_{max}} \geq 0.06\sqrt{f'_c}\,b_v d_v \tag{16}$$

$$V_{cw} = \left(0.06\sqrt{f'_c} + 0.30 f_{pc}\right) b_v d_v + V_p \tag{17}$$

Where:

b_v = Effective web width taken as the minimum web width within d_v (in.)

d_v = Effective shear depth taken as the distance between the resultant tensile and compressive forces due to flexure (in.)

Note: All force units in kips; some variables same as in previous equations

The steel contribution in the AASHTO LRFD code is generally a function of the crack angle, rebar spacing, effective section depth, stirrup angle, reinforcement area, and yield strength of the reinforcement. When vertical shear reinforcement is used, the steel contribution to shear strength is given by Equation 18. As in MCFT, the crack angle is represented by the greek letter theta (θ).

$$V_s = \frac{A_v f_y d_v}{s} cot\theta \tag{18}$$

For the simplified method, the term *cot* θ simplifies to 1.0 if $V_{ci} < V_{cw}$, otherwise it can be found using Equation 19.

$$cot\theta = 1.0 + 3\left(\frac{f_{pc}}{\sqrt{f'_c}}\right) \leq 1.8 \tag{19}$$

The simplified method provides an alternative to MCFT that is more familiar and comfortable for designers used to the ACI and AASHTO-STD methods.

AASHTO MCFT Method

Some drawbacks of MCFT were listed previously, but the benefits of MCFT are important. While the typical moment capacity methods are rationally derived, and work across various section types (columns, beams, slabs), shear methods have typically been empirically derived for many types of structures. The benefit of MCFT is that it is a rational method for reinforced and prestressed shear design for all types of members. In order to find shear resistance by MCFT, the factors β and θ must be determined. In

LRFD, the MCFT can be used two ways: the first is with beta-theta equations and the second is through the use of beta-theta tables given in Appendix B5 of AASHTO. An example of one of the AASHTO tables is reproduced in Table 1. The values of β and θ depend on the amount of transverse reinforcement provided. ε_x refers to the longitudinal strain in the web of the member. An expression for ε_x is also given in Appendix B5.

Table 1: Table to find beta adapted from Appendix B5 of AASHTO 2015

β	ε_x *1000								
v_u/f'_c	≤ -0.2	≤ -0.1	≤ -0.05	≤ 0	≤ 0.125	≤ 0.25	≤ 0.5	≤ 0.75	≤ 1
≤ 0.075	6.32	4.75	4.1	3.75	3.24	2.94	2.59	2.38	2.23
≤ 0.1	3.79	3.38	3.24	3.14	2.91	2.75	2.5	2.32	2.18
≤ 0.125	3.18	2.99	2.94	2.87	2.74	2.62	2.42	2.26	2.13
≤ 0.15	2.88	2.79	2.78	2.72	2.6	2.52	2.36	2.21	2.08
≤ 0.175	2.73	2.66	2.65	2.6	2.52	2.44	2.28	2.14	1.96
≤ 0.2	2.63	2.59	2.52	2.51	2.43	2.37	2.14	1.94	1.79
≤ 0.225	2.53	2.45	2.42	2.4	2.34	2.14	1.86	1.73	1.64
≤ 0.25	2.39	2.39	2.33	2.33	2.12	1.93	1.7	1.58	1.5

Note: v_u is the average factored shear stress on the concrete in ksi

Because of the perceived complexity of MCFT (specifically regarding use of tables), a new procedure based on equations instead of tables was developed by Bentz, Vecchio, & Collins (2006) to simplify the MCFT procedure. If the minimum amount of shear steel is not provided, the equation for β assumes no transverse reinforcement. These simplified calculations should be more conservative for almost all combinations of β and θ as compared to the original tabular method. The equation for β is shown in Equations 20 and 21 (found in AASHTO LRFD Section 5.8.3.4.2). A minimum transverse steel requirement is given in AASHTO LRFD Section 5.8.2.5.

If $A_v \geq$ Minimum A_v,

$$\beta = \frac{4.8}{(1 + 750\varepsilon_s)} \tag{20}$$

Else,

$$\beta = \frac{4.8}{(1 + 750\varepsilon_s)} \frac{51}{(39 + s_{xe})} \tag{21}$$

Where:

ε_s = Net longitudinal tensile strain at the centroid of the tension reinforcement

s_{xe} = A spacing factor given in the AASHTO LRFD code

The crack angle, θ, can be found by the relationship in Equation 22.

$$\theta = 29 + 3500\varepsilon_s \tag{22}$$

Once the value of β and θ are found, the concrete and steel contributions to shear strength can be calculated, as in the tabular method. The concrete contribution is a function of β and is given in Equation 23.

$$V_c = 0.0316\beta\sqrt{f'_c}b_v d_v \tag{23}$$

Finally, the steel contribution in AASHTO LRFD is generally a function of the crack angle, rebar spacing, depth, stirrup angle, area, and yield strength of the reinforcement. This relationship is given in Equation 24. Note, the simplified method uses a simpler version of this equation (see Equation 18).

$$V_s = \frac{A_v f_y d_v (cot\theta + cot\alpha) sin\alpha}{s} \tag{24}$$

Where:

α = Angle of inclination of transverse reinforcement

2.3.4 Changes in AASHTO Demands

Of particular interest in relation to girders which have been in service for many years is whether the codes in use at the time those bridges were constructed are

adequate for today's loads and compatible with the current code requirements. Generally, codes tend to become less conservative over time as more information is available to the designer and the probability of failure can be reduced; however, there are cases where older equations are less conservative. For this project, one concern is on the demand side of the equation. In the 1970s, the critical section for shear was permitted to be taken at the "quarter-point" of the girder (known as the quarter-point rule). In other words, the maximum shear force used in design could be taken at a quarter of the length into the girder (AASHTO, 1973). Today, maximum shears are calculated at a location much closer to the support, possibly resulting in increased shear stresses (AASHTO, 2015). It is difficult to say what general effect this has on older designs because the geometry, detailing, and demand on individual bridges varies greatly.

2.4 Previous Testing of Older Bridge Girders

There are several types of experimental studies of shear in prestressed concrete beams that encompass most published research. Traditionally, researchers will build scale sections, typically no more than 24 in. tall and 20 ft long (e.g. Hanson & Hulsbos, 1964; Peterman, Ramirez, & Olek, 2000; Zwoyer & Siess, 1954; Elzanaty, Nilson, & Slate, 1986). Occasionally full-scale replicas will be constructed for lab testing, although relatively few labs around the country have the capability to test sections this large (>24 in. depth) (Shahawy & Batchelor, 1996; Morcous, Hanna, & Tadros, 2011). The most uncommon research in this area is testing of full-scale, aged girders, taken from bridges that have been in service for many years. Many of these full-scale tests look at flexural capacity, and not shear capacity. Tests of these girders are important

because they can provide insight into the residual performance of older bridges, they allow researchers to evaluate the effects of time (e.g., corrosion and prestress losses), and they can provide a benchmark to judge other similar bridges still in service. Many bridges in the U.S. were designed and built more than 30 years ago with a design life of only 50 years, so understanding the behavior of these bridges is useful for rating and prioritizing bridges for repair and replacement. This section will review some of the past testing of girders taken out of service throughout the U.S.

In Connecticut in 1987, the Walnut Street Bridge was taken out of service and researchers at the University of Connecticut were able to retrieve two girders from the bridge for testing. The girders were 27 in. deep box girders, one of which was in good condition and the other showed minor signs of cracking and spalling. The girders were tested at 1/3 points causing a constant maximum moment in the middle 1/3 of the girder. The researchers found that beam behavior was still ductile, the ultimate strength was higher than predicted, and strain compatibility accurately estimated behavior. The researchers observed little shear cracking (Shenoy & Frantz, 1991). Design details of the girders were not available.

In the 1950s, the Ohio Department of Transportation constructed some bridges with prestressed inverted T beams. At the time they were constructed, some were tested in the laboratory. Over 40 years later some of these bridges were taken out of service and two specimens were tested at the University of Cincinnati to compare to the original results. The samples were tested using a single point load at mid-span. The researchers found that the beams remained strong and ductile even after 40 years in service. Prestress losses were around 20-26% based on the observed cracking moment and the

beam performance was very similar to the new beams tested in the 1950s. There was no shear cracking observed during the tests (Halsey & Miller, 1996). As these bridges were designed in the 1950s, it is likely they were designed using the American Association of State Highway Officials (AASHO) code which used the Allowable Stress Design (ASD) philosophy as opposed to the Load Factor Design (LFD) adopted in the 1970s.

In Pennsylvania in 1996, two girders were tested to determine the residual prestress by finding the decompression load after 28 years in service. The girders tested were found to be in excellent condition with no cracking occurring during service. Prestress losses of 18% were found, roughly 60% of the predicted losses. These girders were not tested to failure and no shear testing was performed (Pessiki, Kaczinski, & Wescott, 1996).

A study performed in Minnesota looked at the shear capacity at both ends of a girder taken from a bridge in the state. The goal of these tests was to consider whether previous codes (pre-1980) led to girders under designed for shear. Despite a smaller amount of shear steel than would be required today, the girder carried a greater applied shear than the factored demands in the newer LRFD code (Runzell, Shield, & French, 2007).

The Florida Department of Transportation recovered four Type-III AASHTO girders while reconstructing some bridges on I-75. The girders were 30 years old at the time and were tested with a single point load and an *a/d* ratio of 1.2 to 5.4. The girders were cut from the bridge such that a 28 in. wide section of deck was left atop the girders. The researchers found that the girders did not exhibit reduced capacity compared to code estimates for shear and moment strength despite their age. For *a/d*

ratios of 3 or less, bond-shear failures were observed. When *a/d* was 4, shear compression failure was observed. For *a/d* of 5, a flexural failure was observed. Analysis found that MCFT and the ACI provisions provided conservative failure values for situations with *a/d* less than 3 despite the bond-shear failure, which is not explicitly accounted for by these methods (Ross, Ansley, & Hamilton III, 2011; Hamilton III, Llanos, & Ross, 2009).

Seven girders from a 42-year-old bridge in Utah were obtained to determine effective prestress force and ultimate shear capacity. The shear tests were performed at *a/d* = 1.5 using a single point load. The authors found that the code equations were conservative for the failure loads observed in testing. The research showed that STM was more accurate for loads near a discontinuity and a finite element model showed that concrete compressive strength had a larger effect on shear capacity than stirrup spacing (Osborn, Barr, Petty, Halling, & Brackus, 2010).

Prior work at the University of Oklahoma has also focused on shear capacity of aged prestressed concrete girders. In 2008, a 40-year-old bridge girder was tested in order to compare experimental values with code values from the 1973 AASHTO-STD and 2004 AASHTO LRFD Specifications. The research also compared the AASHTO-STD, AASHTO LRFD and ACI specifications for shear. The results showed that all codes were conservative with regards to shear failure at *a/d* = 1 (Martin, Kang, & Pei, 2011). This past research is the basis of the continued research performed today for the Oklahoma Department of Transportation (ODOT). The current project examined behavior at additional *a/d* ratios, included a girder with a concrete deck, and the girders

used in the current study exhibited less physical damage prior to testing. The current work also extends to full bridge behavior.

2.5 Previous Studies on Ultimate Bridge Capacity

There is a dearth of information on the ultimate behavior of bridges, particularly prestressed concrete bridges. Obviously, opportunities to bring full-scale bridge sections to their ultimate capacity are limited, and constructing a bridge in a laboratory setting can be cost and space prohibitive. However, there have been several studies that examined the ultimate behavior of bridges. Studies of the behavior of full bridge sections are important because their behavior is fundamentally different from that of individual bridge girders. Bridge decks represent a complex system that shares force effects by distribution through the deck and the girders. Elastic analysis of these sections is complex; ultimate behavior is even more vexing. Ultimate bridge tests can provide insight into how bridges behave after the elastic limit of their components is reached.

Jorgenson and Larson (1972) tested a three-span reinforced concrete slab bridge to failure. The bridge was 10 years old when tested and was being taken out of service when the highway was realigned. A four-wheel patch loading and line loading pattern was placed on the bridge. The section was analyzed as a channel loaded about its weak axis, as the cross-section of the bridge was a flat slab with curbs on each side. Based on the maximum moment applied via line load at failure, the bridge could theoretically support eight HS-20 trucks before permanent deformation occurred and 20 HS-20 trucks before collapse, indicating a very high strength given that the span was only about 25 ft (Jorgenson & Lawson, 1972).

Burdette and Goodpasture (1973) performed what they described as "the first failure tests of full-size bridges performed in this country (USA)." Four bridges were tested, including superstructures consisting of AASHTO Type-III girders, reinforced concrete T-beams, and rolled steel sections. The Type-III girder bridge had a 70-degree skew, making it a particularly unusual case and difficult to use for making generalizations. All bridges were described as structurally sound at the time of testing (they were soon to be inundated by the construction of a reservoir). Rolling load and vibration tests were performed before the ultimate load test. Load was arranged in such a way as to simulate the HS-20 truck and apply maximum moment to the bridges. The load was applied through small holes in the bridge deck anchored to the bedrock below the bridge. The researchers noted diaphragm cracking in the concrete bridges at early stages of loading, but this cracking seemed to have little effect on load-deflection behavior. In the Type-III girder bridge, failure initiated with cracking along the web-deck interface and diagonal shear cracks appeared near the supports. The slab was observed to "dish," or deflect more noticeably at the interior girders compared to the exterior girders. The girder separated from the deck near the load, and at this point the behavior changed and more load was carried by the adjacent girders. The final failure occurred when diagonal cracks propagated in the interior girders (Burdette & Goodpasture, 1973).

In 1994, researchers at the University of Cincinnati performed a destructive test on a 38-year-old two lane "concrete slab bridge". The bridge had a 30-degree skew and exhibited significant deterioration due to freeze/thaw and alkali-silica reaction. One lane of the bridge was loaded in a way as to simulate the HS-20 truck. Despite the bridge

being decommissioned for structural reasons, the deck held a large ultimate load (22 HS-20 trucks). The researchers observed that previous damage to the deck affected the final failure mechanism (punching shear). Although punching shear occurred at a lower than estimated load, the overall performance of the bridge exceeded design capacities (Miller, Aktan, & Shahrooz, 1994).

A 2011 study at the University of Delaware involved the destructive testing of a scale steel bridge (Bechtel, McConnell, & Chajes, 2011). The authors here noted that in the few examples of destructive bridge tests since the 1970s (some listed above), a common finding was a large reserve of strength relative to the design code predictions and rating techniques. The bridge tests listed in this study were all for steel or reinforced concrete superstructures, not prestressed concrete. The increase in bridge strength relative to design strength is attributed to redistribution of force not accounted for in the code. The scale test performed in the study showed that the ability of the bridge to carry load efficiently hinged on the condition of the deck; i.e., the deck was unable to distribute load effectively when significant damage occurred. The researchers concluded that efforts to test bridge sections to failure must be made due to the uniqueness of individual bridge designs (Bechtel et al., 2011). The authors emphasized that analytical models must always be verified against the results of destructive tests to ensure their accuracy.

A recent Minnesota Department of Transportation study involved testing of older girders in shear and the full-scale testing of a bridge constructed in the laboratory to investigate load distribution, ultimate bridge behavior, and the effects of secondary elements (diaphragms and parapet walls) (Dymond et al., 2016). The bridge test showed

a reserve of strength in the bridge system relative to the component level capacities, this was attributed to the use of elastic load DFs. The study also examined DFs using a variety of computer models. 2D grillage models were found to be accurate as a means of finding elastic DFs. A major result of the study was a screening tool to help determine which bridges are in need of load rating and which methods to use to determine the demands for these bridges (Dymond et al., 2016). Grillages were recommended to find DFs in some cases, and ignoring diaphragms and parapet walls were seen as reasonable simplifications.

2.6 Live Load Distribution

The concept of live load distribution was developed in the 1930s and 40s and has been in use by AASHTO ever since (Westergaard, 1930; Newmark, Siess, & Peckham, 1946). The method is a simplification of bridge behavior to avoid more complex analyses, especially for typical bridge types. Live load DFs are an approximate method of analyzing shears, moments, and deflections in the beams that support a highway bridge deck. According to Taly (2014), there are three main steps to analyzing a bridge structure using DFs:

1. Bending moments and shears are calculated based on the notional truck and lane loads in the code. These loads are placed on a beam (whether continuous or simple) in a manner such as to cause maximum force effects. The beam is analyzed based on principles of structural mechanics. At this step, the actual details of the bridge (spacing, superstructure type, etc.) are unimportant.
2. The live load effects on a single girder are determined by multiplying the moments and shears from step 1 by DFs. These factors are calculated for both

shear and moment, and for interior and exterior girders (four total factors). These factors are based on the spacing, superstructure type, and other geometric details.

3. If the bridge is built with a skew, i.e. not perpendicular to supports, a skew factor must also be applied.

These DFs are applied to the load effects (moments and shears) after accounting for other factors that affect the load. These other factors include the impact factor (IM), load factors, and skew correction factors.

2.6.1 AASHTO LRFD Distribution Factor Procedures

This dissertation focuses on 4-girder or more beam-slab type bridges consisting of a series of parallel girders with a slab connecting them. The DFs for these types of bridges are given in AASHTO LRFD Section 4.6.2.2 (AASHTO, 2015). Table 2 contains the code equations for DFs for beam-slab bridges with one design lane loaded. The "lever rule" referenced in this table is an analogy used in the code to determine DFs in some specific cases. For an exterior girder, it involves placing a wheel load 2 ft from the curb on a bridge and treating the slab as simply supported across the first two girders. Using statics, the reaction at the exterior girder can be found as a ratio of the dimensions of the section, this ratio is used as the DF for the exterior girder. In effect, it is a simple and relatively accurate tool for assessing load distribution in exterior girders or for bridges with only three girders. In order to use the following equations, the deck must have a constant width and the beams must be parallel.

Table 2: Distribution factor equations for 1 design lane loaded

Force effect	Distribution Factor	Range of Applicability

Moment in Interior Beams	$0.06 + \left(\frac{S}{14}\right)^{0.4} \left(\frac{S}{L}\right)^{0.3} \left(\frac{K_g}{12.0Lt_s^3}\right)^{0.1}$	$3.5 \le S \le 16.0$ $4.5 \le t_s \le 12.0$ $20 \le L \le 240$ $N_b \ge 4$ $10{,}000 \le K_g \le 7{,}000{,}000$
Moment in Exterior Beams	Lever Rule	$-1.0 \le d_e \le 5.5$
Shear in Interior Beams	$0.36 + \frac{S}{25}$	$3.5 \le S \le 16.0$ $35 \le L \le 240$ $4.5 \le t_s \le 12.0$ $N_b \ge 4$
Shear in Exterior Beams	Lever Rule	$-1.0 \le d_e \le 5.5$

Where: S = Girder spacing, L = Span length, t_s = slab thickness, N_b = Number of beams, K_g = see eqn. 25, d_e = distance from center of exterior girder to curb

Equations 25 and 26 show some of the parameters for DF calculations.

$$K_g = n\left(I + Ae_g^2\right) \tag{25}$$

$$n = \frac{E_b}{E_D} \tag{26}$$

Where:

n = modular ratio
E_b = Modulus of beams (ksi)
E_D = Modulus of deck (ksi)
A = Gross area of beam (in^2)
e_g = distance between c.g. of deck and beam (in.)

The code also contains equations for load distribution with two design lanes loaded. At the design stage, it is assumed that the number of design lanes (N_L) is equal to the integer part of the ratio of clear roadway width to 12.0 ft (one design lane). In cases where a bridge must support multiple design lanes, there are separate DF cases to check for two or more design lanes loaded in addition to a single lane loaded (as in Table 2). The DF equations for two or more design lanes are given in Table 3.

Table 3: Distribution factor equations for 2+ design lanes loaded

Force effect	Distribution Factor	Range of Applicability
Moment in Interior Beams	$0.075 + \left(\frac{S}{9.5}\right)^{0.6}\left(\frac{S}{L}\right)^{0.2}\left(\frac{K_g}{12.0Lt_s^3}\right)^{0.1}$	$3.5 \le S \le 16.0$ $4.5 \le t_s \le 12.0$ $20 \le L \le 240$ $N_b \ge 4$ $10{,}000 \le K_g \le 7{,}000{,}000$
Moment in Exterior Beams	$e \times DF_{interior}$ $e = \frac{d_e}{9.1}$	$-1.0 \le d_e \le 5.5$
Shear in Interior Beams	$0.2 + \frac{S}{12} - \left(\frac{S}{35}\right)^{2.0}$	$3.5 \le S \le 16.0$ $35 \le L \le 240$ $4.5 \le t_s \le 12.0$ $N_b \ge 4$
Shear in Exterior Beams	$e \times DF_{interior}$ $e = 0.6 + \frac{d_e}{10}$	$-1.0 \le d_e \le 5.5$

One important takeaway from these equations is that girder spacing is the most important parameter for load distribution. This makes sense; all other things equal a longer span will result in a more flexible beam, and load transfer occurs through the slab acting as a beam. Some other factors that can affect load distribution but are less influential in these equations include span length, slab thickness, stiffness of beams, stiffness of slabs, and presence/dimensions of diaphragms. The superstructure of a bridge acts as a stiffened plate (Taly, 2014) with many complex variables from these various components of the structure. DFs serve as a simplification of this complex system, but more detailed analyses could result in a more accurate picture of load distribution in a given bridge.

In addition to the procedures listed previously, the AASHTO LRFD code provides an additional procedure for finding DFs for exterior girders when end

diaphragms are present. This is often referred to as "special analysis" and it is given in AASHTO LRFD Section 4.6.2.2.2d (AASHTO, 2015). Using this special analysis, the DF is taken as the greater of the DFs based on the equations above, or the DF obtained assuming that the bridge deflects and rotates as a rigid cross-section. This process is given by Equation 27.

$$R = \frac{N_L}{N_b} + \frac{X_{ext} \sum^{N_L} e}{\sum^{N_b} x^2} \tag{27}$$

Where:

R = Reaction on exterior girder in terms of lanes
e = Eccentricity of a design truck or design lane load from the center of gravity of all girders (ft)
x = Horizontal distance from the center of gravity of the pattern of girders to each girder (ft)
X_{ext} = Horizontal distance from the center of gravity of all girders to the exterior girder (ft)

This so called special analysis requires placement of design trucks in adjacent lanes in such a way as to create the maximum resultant on the exterior girder. There are additional factors to account for skew of bridges, but this study focuses on straight bridges only.

Finally, there is another factor included in the DF equation in the tables above known as the "multiple presence factor." This factor must be applied to the lever rule and the "special analysis" since it is not already accounted for in these methods. The multiple presence factor is based on an evaluation of multiple load cases and is meant to represent the worst-case loading scenario. For this study, the multiple presence factor was removed for comparison to computer model results. These factors are merely an increase in loading to account for the possibility of truck loads larger than the HL-93 for

the case of one design lane loaded (Cross, et al., 2009). The multiple presence factors from LRFD are given in Table 4.

Table 4: Multiple presence factors from AASHTO LRFD

Number of loaded lanes, N_L	Multiple presence, m
1	1.20
2	1.00
3	0.85
3+	0.65

2.6.2 Previous Studies on Load Distribution

There has been a large amount of research on load distribution in bridges and the subject is a source of considerable debate in the research community. Many load distribution paradigms have been proposed, and the current methods have been derided both as too simple and not simple enough. This section highlights several of the more comprehensive studies on live load distribution in bridges.

DFs have been used for bridge design in the U.S. since the 1930s as a simplification of the complex behavior of bridge decks. Likely the first load distribution relationships for bridges were proposed by Westergaard (Westergaard, 1930). Further development of the concept continued in 1946 (Newmark et al., 1946). At this time load distribution was based on the theory that the bridge deck deforms as an elastic plate. In truth, the deck is a plate stiffened by supporting beams (Taly, 2014). The initial work by Newmark et al. (1946) was included in the AASHTO Standard Specifications up to 2002 (AASHTO, 2002). The Standard Specifications used so-called *S/D* (spacing divided by a constant in the denominator), or "S-over" equations which were found to be less accurate for some bridge types (Zokaie, 2000). The LRFD DFs were developed based on a series of studies performed in the late 80s and early 90s (Nutt, Schamber, &

Zokaie, 1988; Zokaie, Osterkamp, & Imbsen, 1991a; Zokaie, Imbsen, & Okstercamp, 1991b). These studies were intended to increase the applicability of the DF equations to more bridge types.

More recently, efforts have been made to further improve DFs. The most comprehensive push to change the equations was explained in the National Cooperative Highway Research Program (NCHRP) Report 592 (Mertz, 2006). The goal of this NCHRP project was to simplify the DF equations. The study looked at the effects of skew, diaphragms, vehicle position, and a variety of bridge types and dimensions. As a simplification, the report recommended the use of simple equilibrium formulae (i.e., lever rule), or a kinematic assumption (uniform distribution of load). After these methods are used, the results are scaled up or down by calibration factors based on the specific bridge parameters. Despite a greater degree of accuracy, the new methods proposed in this research did not gain much traction. According to Dymond et al. (2016), the methods were criticized as not enough of a simplification to warrant a change. Additionally, the use of grillage analyses was seen as the future of load distribution analysis (Dymond et al., 2016).

Since 2000, there have been several studies to investigate load distribution using either computer models or field testing. Barr, Eberhardt, and Stanton (2001) evaluated code equations for load distribution in prestressed concrete girder bridges using finite-element models and load tests on a real bridge. This study paid particular attention to the diaphragms, continuity, skew, and load type. AASHTO LRFD distribution equations were found to be conservative to a degree that varied among the different configurations tested. End diaphragms were found to reduce DFs and intermediate

diaphragms were observed to have little effect on load distribution. DFs found using the lane loading were lower than those for the truck loading, indicating that a truck is the conservative case for DF estimation. The researchers also found that the specific bridge examined in their work could have been designed for a 39% higher load based on their finite-element modeling (Barr, Eberhard, & Stanton, 2001).

Altay, Arabbo, Corwin, Dexter, & French (2003) instrumented three prestressed concrete bridges to investigate the effects of larger truck loads on bridges in Minnesota. The researchers found that shear cracking tended to occur for wide bridges with a high ratio of live load stress to dead load stress. Additionally, it was noted that increases in permit truck weights could lead to shear cracking, which could "significantly effect service life". DFs were found to be conservative and interior diaphragms were found to influence load distribution and stresses in the girders (Altay et al., 2003).

Sotelino, Liu, Chung, & Phuvoravan (2004) suggested a simplified load DF procedure and also compared load DFs based on a number of finite-element models of both steel and concrete bridges. The study also considered the effects of diaphragms on load distribution. For prestressed concrete bridges the AASHTO LRFD DFs were found to be conservative by 30%. Secondary elements (end and interior diaphragms) were found to increase transverse distribution of moment; load DFs were 39% less when these elements were considered (Sotelino et al., 2004).

Patrick, Huo, Puckett, Jablin, & Mertz (2006) observed the effects of live load placement on load distribution using grillage models. The study investigated truck placement in design lanes for the purpose of speeding up computation time in computer analysis of bridges. The analysis was performed for both steel and prestressed concrete

girder bridges. The researchers concluded that vehicle spacing has little effect on DFs (Patrick et al., 2006).

Despite efforts to improve DFs, the current equations are still being used in AASHTO LRFD. The research community has also observed the benefits of simple computer models to come up with DFs. Absent in the literature are specific studies of individual types of bridges to discern trends. For example: in Oklahoma, AASHTO Type-II girders are commonly used in spans between 30 and 70 ft and at spacings between 6 and 12 ft. It is valuable to have references in the literature that look at common arrangements like these to highlight the combinations of variables that warrant further attention at the design or load rating stage. In particular, bridges that were designed under older codes and are now being load rated can be earmarked for special attention when they are used in a certain configuration that is deemed to be of particular concern.

2.7 Grillage Modeling

A simple and safe method of computer analysis of a bridge system is the use of a "grillage model." Grillage models are so called because they consist of a grillage of beam elements used to represent the girders and slab of a simple bridge. The benefits of this style of analysis include: ease of comprehension and use, inexpensive cost, accuracy, and applicability to a wide range of bridge types (Hambly, 1991). According to Hambly (1991), it is not simple to make a set of general rules for creating a grillage model, but this text is often cited as a guide for building grillage models. Some modeling suggestions given in this text include: placing grillage beams at locations of designed strength (main girders, diaphragms), transverse spacing of beams should be

less than 1/4 of the effective span, longitudinal spacing and transverse spacing should be relatively similar, and point loads should be used to represent distributed loads. Figure 3 shows a simple example of a grillage analogy for a bridge.

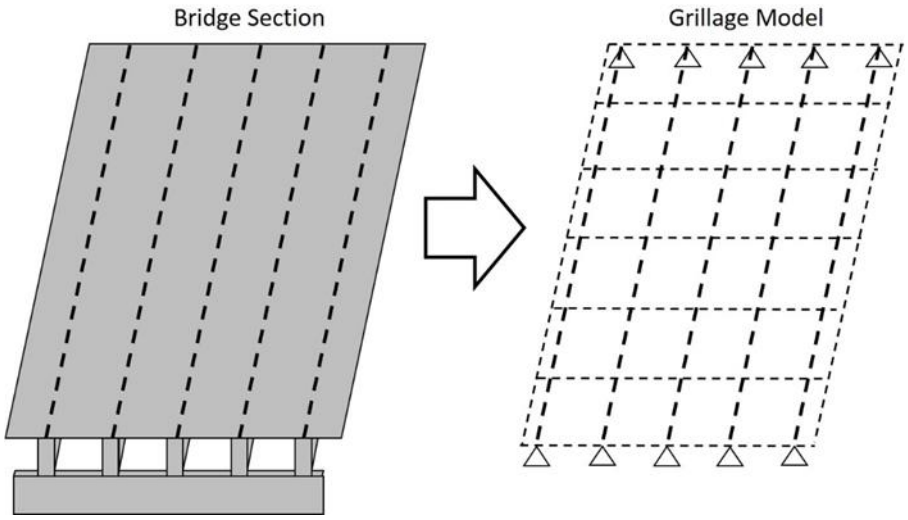

Figure 3: Grillage example

For bridges like those consisting of simply supported prestressed girders, Hambly suggests using longitudinal grillage members coincident with the girders and using transverse beams at 1/4 to 1/8 of the effective span. Diaphragms at the supports are to be modeled with grillage beams, and there are special rules for diaphragms at the center of the span. Hambly states that for many concrete and steel I-girders, the torsion constant, *C*, can be ignored since these sections often have a torsion stiffness much smaller than their bending stiffness.

More guidance for grillage modeling of beam and slab bridges is given by O'Brien and Keogh (1999). In this text, beam and slab bridges are described as bridge systems where a large portion of the stiffness is concentrated at discrete locations (beams), and the slab provides load distribution between these beams. The authors note

the importance of modeling the slab properly, as the stiffness of the slab directly determines the ability of the slab to transfer load between beams. Diaphragms are described as providing additional load transfer, and if they are wide enough they are likely to contribute to shear strength at the support. Spacing of transverse members is recommended at one to three times the spacing of longitudinal members (O'Brien and Keogh, 1999).

O'Brien and Keogh (1999) recommend using an approximation for torsional stiffness that sums the stiffness of rectangles that approximate the section. This approximation is reasonably accurate for beam-slab type bridges. The approximation for torsional stiffness given in this text was reported by Ghali and Neville (1997), and it consists of representing a complex shape, such as an I-shaped prestressed concrete beam, as a series of rectangles. More complex methods of estimating the torsion constant exist, but the accuracy of simplified methods is adequate according to Ghali and Neville (1997). An example of this rectangular approximation of more complex shapes is given in Figure 4. The equation for the torsion constant of a rectangular section is given by Equation 28 (Ghali & Neville, 1997). This can be summed to approximate a non-rectangular shape with rectangles.

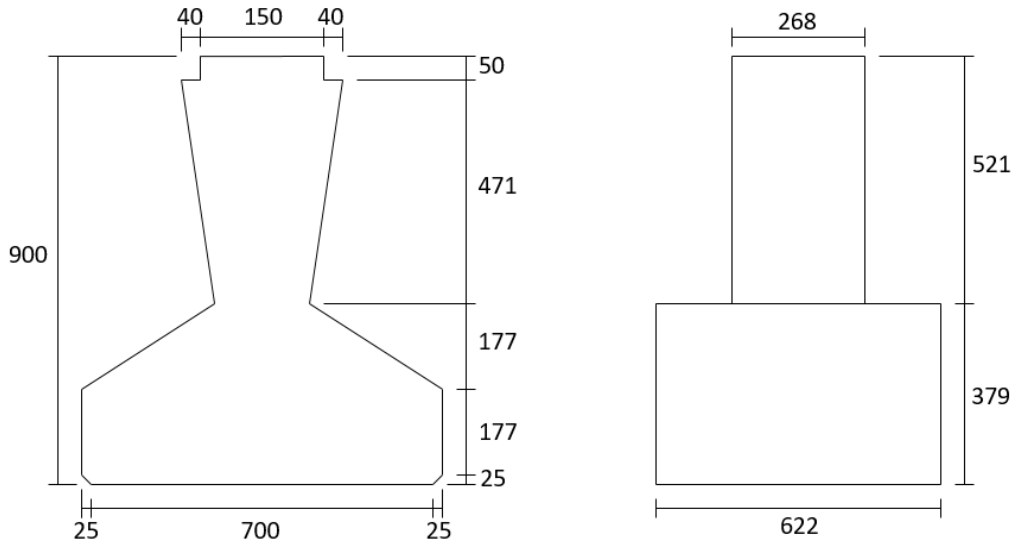

Figure 4: Equivalent shape to find torsion constant (from O'Brien and Keogh 1997) (dimensions in mm)

$$J = ba^3\left[\frac{1}{3} - 0.21\frac{a}{b}\left(1 - \frac{a^4}{12b^4}\right)\right] \tag{28}$$

Grillage modeling techniques were pioneered for computer use by Lightfoot and Sawko in the late 1950s (Lightfoot & Sawko, 1959). Because these models have proven useful in accurately representing bending stresses (Hambly, 1991), they have been used in bridge research somewhat regularly. A National Cooperative Highway Research Program (NCHRP) study used grillage modeling to look at shear DFs in 2006 (Mertz, 2006). The researchers found that grillage models compare well with more rigorous finite element models, especially for load distribution. As such, grillage models were used as the basis for the findings of the report. The effectiveness of grillages was also corroborated by Dymond, French, and Shield (2016) and Peterson-Gauthier (2013).

2.8 Load Rating of Bridges

Evaluating old bridges is an important step in maintaining infrastructure, especially as heavier vehicles travel over bridges that may not have been designed for that level of load. These evaluations are important from two standpoints; first, they ensure that older bridges are still safe to traverse, and second, they save money by extending the usable life of older bridges.

The AASHTO specification for evaluating in-service bridges is known as the AASHTO Manual for Bridge Evaluation (AASHTO, 2011). This document will be referred to here as the AASHTO Manual. This document provides standard guidance to bridge owners to help maintain safe bridges. This guidance applies to every bridge on public roads with a span of 20 ft or longer. The FHWA collects all bridge condition information in a database called the National Bridge Inventory (NBI) for the purpose of being consistent across all bridge owners. The NBI provides a rating for the substructure, superstructure, and deck of a bridge. These ratings are assigned based on visual inspection on a scale of 0-9, as given in Table 5.

Table 5: Bridge condition ratings

Code	NBI Rating Definition
N	Not applicable
9	Excellent
8	Very good
7	Good
6	Satisfactory
5	Fair
4	Poor
3	Serious
2	Critical
1	Imminent failure
0	Failed

The AASHTO Manual suggests quality control standards including education standards and training for bridge inspection personnel, but needless to say there is some subjectivity involved in rating bridges visually on a numerical scale. In bridge visits by the author, it was noted that rating variability between bridges and owners was not uncommon. These structure evaluations are used for load rating and load posting of bridges, so their accuracy is important.

The AASHTO Manual uses a process known as load and resistance factor rating (LRFR) similar to the LRFD probabilistic concept used in the bridge design code. The general load rating equation for any live load effect from this document is given in Equation 29.

$$RF = \frac{\phi_c \phi_s \phi R_n - \gamma_{DC} DC - \gamma_{DW} DW \pm \gamma_P P}{\gamma_L LL(1 + IM)} \quad (29)$$

Where:

RF = Rating factor
R_n = Nominal member resistance
DW = Dead-load effect due to wearing surface and utilities
DC = Dead load effect due to structural components and attachments
P = Permanent loads other than dead loads
LL = Live load effect
IM = Dynamic load factor
γ = LRFD load factor
ϕ = LRFD resistance factor
ϕ_c = Condition factor
ϕ_s = System factor

This fraction represents the additional capacity available for live load after the dead loads are applied (RF). The condition factor (ϕ_c) is based on the result of the bridge inspection as referenced in the previous section. There are only three possible values of the condition factor (1.00, 0.95, and 0.85) even though the condition of the bridge is rated on a scale of 1-9. A summary of how the condition factor is selected is

given in Table 6. Note that bridges below a "poor" rating of 4 cannot be load rated. The system factor (ϕ_s) is based on the spacing of girders, e.g. for a typical 4 girder prestressed concrete bridge the factor is 1.00. The LRFD load factors for all possible limit states used in this equation are given in the AASHTO Manual Table 6A.4.2.2-1.

Table 6: Bridge condition factor

Structural Condition of Member	ϕ_c	NBI Rating Code
Good or satisfactory	1.00	6 to 9
Fair	0.95	5
Poor	0.85	4

When a rating factor is determined, the rating factor can be directly multiplied by the load case being considered. For example, if the HL-93 load case is being considered, the allowable load of a bridge is the rating factor times the HL-93 load. A RF greater than 1.0 indicates a greater capacity than the loads considered, and a number less than one indicates that the allowable load must be proportionally reduced and posted. The rating is done on a component basis, so the weakest component of a bridge system controls for rating the entire structure (Fu, 2013).

The process for rating an existing bridge includes determining the live load demands on the bridge the same way as for a new bridge, using DFs. Additionally, shear resistance is calculated using the LRFD equations. There are two levels of load rating: an inventory rating and an operating rating. The inventory rating refers to the bridge's ability to carry current design loads for an indefinite period of time. The operating rating has to do with the maximum permissible live load; this level is not intended to be reached with regularity, or the life of the bridge will be diminished (Sanayei, Reiff, Brenner, & Imbaro, 2015). The difference between the two is a

question of structural reliability; the load factor applied for the inventory rating is higher than the operating rating, indicating a greater uncertainty and duration of the load. If a bridge passes the inventory rating (RF>1) for the HL-93 loading, the structure will have adequate capacity for all AASHTO legal loads. Bridges that pass at the operating level but not the inventory rating must be checked for loads greater than the AASHTO trucks.

For the case of shear, the AASHTO manual states, “In-service concrete bridges that show no visible signs of shear distress need not be checked for shear when rating for the design load or legal loads.” In other words, where shear cracking is not apparent bridge owners must only check the RF for permit loads. In light of the fact that demands may be higher than they were taken when the girders were designed (quarter-point rule), and the changes in the shear capacity calculations over the years, this requirement is unusual. Permitting owners to ignore shear load ratings unless cracking is visible is problematic if the actual capacity of a bridge is low compared to current methods, or if the current demands exceed the demands at the time the bridge was designed.

2.9 Literature Review Summary

The literature review revealed a dearth of experimental research on shear behavior of older AASHTO Type-II prestressed concrete girders and of the ultimate behavior of bridge systems loaded in shear. The work detailed in this dissertation adds valuable information in both of these areas. Additionally, previous research has reported the conservativism of the AASHTO DFs and the limitations of the code equations. Grillage modeling represents a modernization of the DF formulation that can be applied to a wide variety of bridges. This dissertation investigated the variations in shear DFs in

relation to several bridge variables using a grillage modeling approach. Additionally, the parametric study provides information about a very common type of bridge in Oklahoma, which can be used by ODOT to help make decisions about older bridges. For bridges that do not show signs of shear cracking, grillage models combined with the shear capacity analyses recommended here can provide an accurate rating of prestressed concrete bridges.

Chapter 3: Full-Scale Girder Testing

This chapter contains information about the full-scale girder tests described in this dissertation. A discussion of analysis methods used is included first. Some of this information is already discussed in the literature review, but this section contains additional details about how the methods were applied specifically for this work. Other information in this chapter includes background about the girders, their transportation, and the procedures related to the actual testing. Finally, the results are described, followed by a further discussion of their implications. In this chapter, any discussion of the conservativism of the code methods is only in relation to these girder tests. The shear capacity methods described here are based on years of research. A goal of this study was to merely describe their accuracy in predicting the capacities of the particular girders tested in this project.

3.1 Girder Analysis

The literature review chapter discussed the code based shear capacity calculation methods available to analyze the girders in this study. In general, analyses of the sections tested in this study were performed using an Excel spreadsheet programmed with the various methods and designed during the course of this project. The inputs for the spreadsheet include the physical dimensions of the section, the concrete properties, the location of steel (prestressed or otherwise), and the age of the girders (to find prestress losses). The sheet calculates the section properties, and given the loading configuration computes the shear and moment capacities using several methods. Details about the creation of this spreadsheet are given by Cranor (2015).

Another program used to calculate capacities and demands for the girders tested in this project was LEAP Bridge Concrete (Bentley Systems, Inc., 2016). This program is a commercially available concrete bridge design and analysis software. In the program, a bridge can be built and the AASHTO LRFD code is applied to the bridge to evaluate demands and capacities. This program was used to verify results from the aforementioned analysis spreadsheet and to find demands on the bridge sections based on the AASHTO loadings. The program can calculate moment capacity based on strain compatibility or the AASHTO equations as well as shear capacity using the beta-theta equations or tables, or the simplified method. The program utilizes the sixth edition of the AASHTO bridge code (AASHTO, 2012).

The same methods were used to analyze the scale girders as used to calculate the capacities of the full-scale sections. Materials properties determined from cylinder tests were used for all analyses.

3.2 Data Acquisition

All programs built for data acquisition in this research were programmed using National Instruments (NI) LabVIEW software (National Instruments, 2016). This software was chosen because it would interface easily with the hardware available at the Donald G. Fears Structural Engineering Lab (Fears Lab). Originally, a data acquisition program was built for the tests of the first girder test (later referred to as girder A) by an electrical engineering undergraduate student contracted for this purpose (Cranor, 2015). Future tests were performed using programs developed by the author. LabVIEW is a graphical programming language, in which functions (addition, subtraction, signal

processing) are connected together by wires which carry input data to the proper locations. A typical LabVIEW VI (virtual instrument) is shown in Figure 5.

On the hardware side, all data was collected using a NI data acquisition system consisting of a CompactDAQ (cDAQ-9178) chassis with 8 slots for various analog input modules tailored to different sensors. This system allows collection of a number of input channels for multiple sensor types outputting voltage. The analog input modules attached to this system were the NI-9205, the NI-9219, and the NI-9236 (x2). The NI-9205 primarily reads direct voltage output, the NI-9219 has improved signal conditioning for multiple sensor types, and the NI-9236 is intended for collecting information from strain gauges.

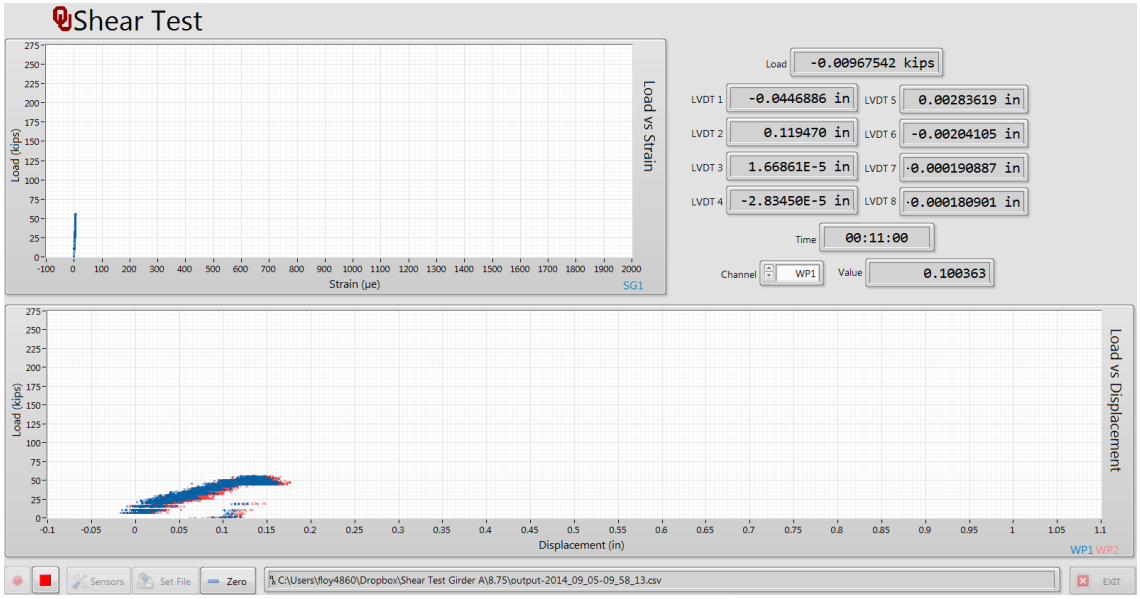

Figure 5: Typical LabVIEW front panel during test

For displacement measurement, two types of sensors were used: wire potentiometers (wire pots) and linear variable differential transformers (LVDTs). Wire pots were used for expected displacements greater than 1 in., and LVDTs were used for

smaller displacements (<1 in.). The magnitude of the applied loads were measured using load cells. Load cells used in this study were the 1200 series load cells from Interface, Inc (400 kip and 100 kip capacity). The 1200 series are general purpose load cells with moment compensating capabilities. For strain measurement, primarily Bridge Diagnostics, Inc. (BDI) strain transducers were used. These gauges can be attached to the surface of the concrete using rapid setting epoxy applied to the steel tabs of the gauges. The gauge length for the BDI gauges is 3 in. Foil type strain gauges were also used in this study, in particular Micromeasurements foil gauges, manufactured by Vishay Precision Group (1.25 in. and 2.5 in. size). A larger gauge size was preferred, but it was difficult to obtain the 2.5 in. size, leading to the use of the 1.25 in. gauges.

Before any test was performed, all the sensors would be attached to the data acquisition system and tested in the configuration to be used in the test. If the sensors gave the proper output signal, they would all be calibrated one by one. Strain gauges have a gauge factor that is given by the manufacturer. LVDTs were calibrated using a micrometer and wire pots were calibrated using a ruler. The linear voltage responses were scaled to the measurements given by the micrometer and ruler yielding a calibration factor. The load cells were either calibrated in a Baldwin universal testing machine or a Forney compression machine.

Because of the size of most files collected during tests, Matlab was often used for data analysis. In the case of the scale individual girder tests, Microsoft Excel was used. Appendix A includes an example of Matlab code used to create graphs from the raw data collected during the full-scale girder tests.

3.3 Full-Scale Shear Tests

This section contains procedural information about the full-scale girder tests explained in this dissertation. The first of the two girders was tested as part of a Master's thesis reported by Cranor (2015), and more information about this girder and can be found in that thesis. Since this testing is used to draw conclusions about the behavior of older girders, the methods used to test this girder are listed in this section. The author of this dissertation participated in the testing of the first girder, so needless to say there is some overlap in the two documents regarding the testing of the first girder. The information presented here is intended to go deeper into the failure mechanisms and compare with the second girder test. Table 7 summarizes the locations and dimensions of the shear tests described in this dissertation.

Table 7: Summary of full-scale girder test locations

Test	Shear Span to Depth Ratio, *a/d*	Shear Span, *a* (ft)	Total span, *L* (ft)
A1	2.5	7.5	18.75
A2	2.0	6	19.0
C1	3.0	9	25
C2	3.83	11.5	28

3.3.1 Girder Background

Two girders taken from the I-244 bridge over the Arkansas river in Tulsa, Oklahoma, were tested as part of a project sponsored by the Oklahoma Department of Transportation (ODOT) between 2014 and 2016. The bridge from which the girders were taken was constructed in the late 1960s and was designed using the AASHTO Standard Specifications. The two girders were selected from the I-244 Eastbound bridge over the Arkansas River in Tulsa during a visit to the site in the spring of 2013 before

demolition began on the bridge. These two specific girders were chosen as representative of two of the four reinforcement configurations used for the AASHTO Type-II girders in different spans of the bridge. This visit was performed by the principal investigators on the project before this author arrived at OU (all activity performed before summer 2014 was performed without the author present, but this information is included for completeness). The girders were named alphabetically based on the various girder designs in the original plans (girders with the cross-section designs "A" and "C" were obtained for this study). The first, girder "A," was a 32-ft-long AASHTO Type-II girder prestressed with six straight ½ in. strands and four harped strands. This girder had been cut from the full bridge in a way that left a section of the 8.5 in. thick deck with a width roughly equal to that of the top flange intact. The second girder, labeled girder "C" in this study, was taken from a different span of the same bridge. Girder C was a 46-ft-long AASHTO Type-II girder prestressed with ten straight strands and six harped strands. It was delivered with a roughly 36 in. wide portion of deck. The deck was not cut symmetrically about the center of the girder however, so an additional 10 in. of deck was cast on the short side to regain section symmetry using a concrete mixture designed to match the strength of cores taken from the deck of Girder A (more information about this process is given in Section 3.3.3). Girder C also had partial diaphragms remaining at the center and the ends, both spans of the I-244 bridge had end and middle diaphragms in service. Both girders were reinforced for shear with double No. 4 Z-bars spaced at 4 in. for the first 12 in. of the girder from each end, 8 in. until 30% of the girder length from each end, and 12 in. for the interior 40% of the girder. Figures Figure 6 and Figure 7 show the cross-sections of the girders and the

sections including the deck, respectively. The deck of both girders included a 2 in. concrete wearing overlay.

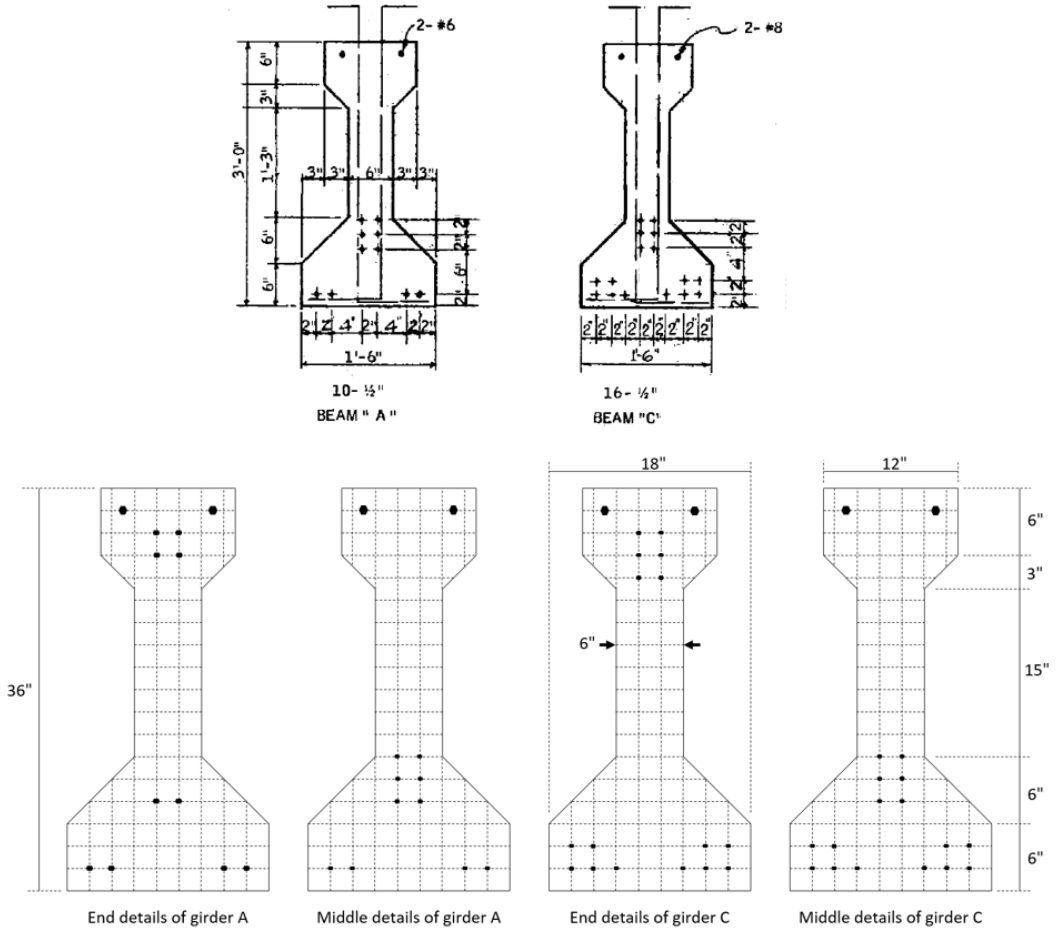

Figure 6: Details of girders A and C. Top image scanned from original plans provided by ODOT, bottom image made by the author to show dimensions more clearly

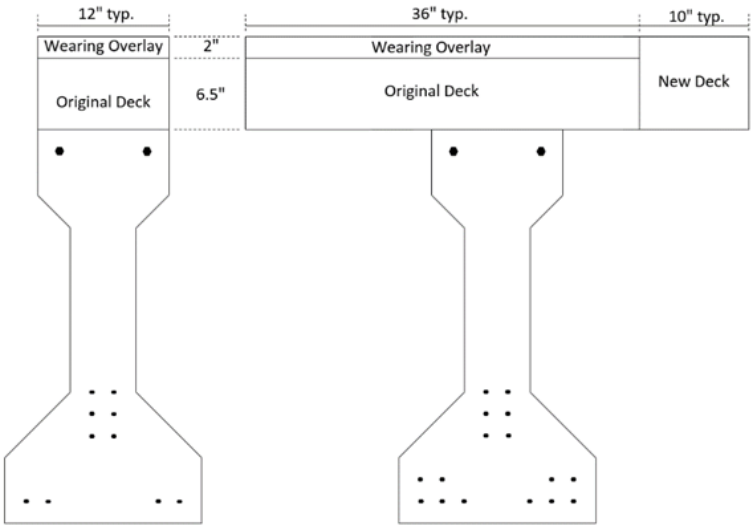

Figure 7: Deck details as tested for girder A (left) and girder C (right)

The *a/d* ratio is a common way to identify shear test locations, because it represents the distance from a discontinuity as a ratio of the depth of the section. Girder A was tested once on each end, at *a/d* ratios of 2.5 and 2.0. Girder C was tested at *a/d* ratios of 3.0 and 3.83 (the "quarter-point"). These locations were selected to test the girders in locations on the edge of a D-region (*a/d* = 2.0) and in B regions. The girders were supported at one end and at a location that left the opposite end overhanging such that it would not be damaged by or influence the test of the opposite end. Neoprene bearing pads with dimensions matching those shown on the plans provided by ODOT were used since the typical prestressed concrete girder in Oklahoma bears on neoprene pads. A single point load was applied through a steel plate using a hydraulic actuator. The load configuration was selected for simplicity's sake, as well as to apply the largest shear possible near the end of the girder.

3.3.2 Transporting girders to Fears Structural Engineering Lab

The locations of the chosen girders within the bridge are shown in Figure 8, and the typical bridge cross-section at these locations is shown in Figure 9. As stated previously, girder A was cut from the bridge with the deck intact out to the edges of the top flange, girder C was cut from the deck such that a 3 ft width of the deck and diaphragms transverse to the girder were removed with the girder. It was intended that this deck would be symmetric about the girder axis, but the actual cut was not. The removal of girder C from the bridge is shown in Figure 10.

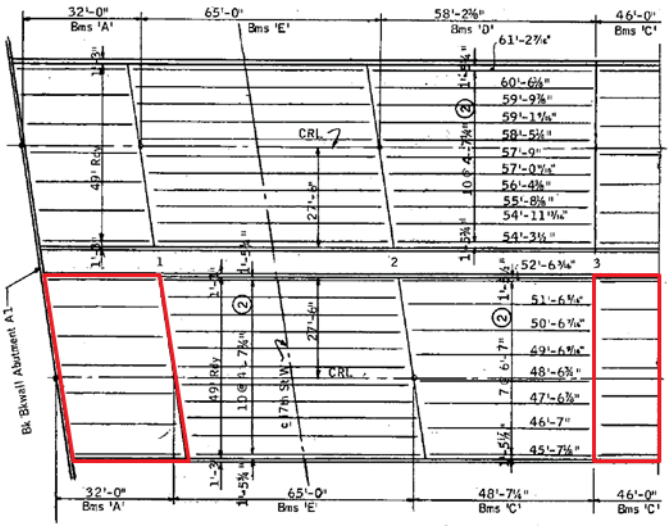

Figure 8: Locations of girders A and C in original plans of the I-244 bridge

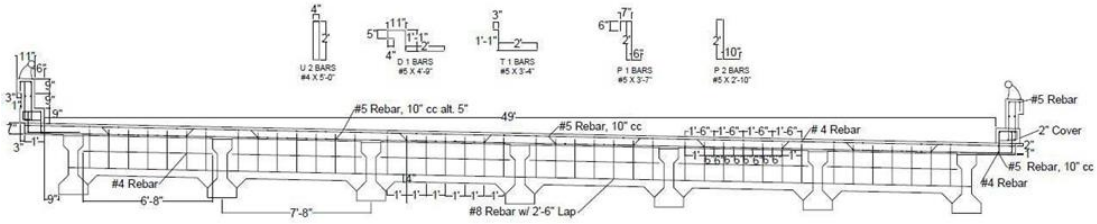

Figure 9: Cross-section of typical span of I-244 bridge

Figure 10: Removal of girder C from the I-244 bridge over the Arkansas river in Tulsa, OK on September 4, 2013 (photo courtesy of Gary Quinonez with Manhattan Road & Bridge)

The two girders were delivered to Fears Structural Engineering Laboratory on October 18, 2013 on flatbed trailers, as shown in Figure 11, and were unloaded using two 20 ton cranes rented from Allied Steel Construction, as shown in Figure 12 and Figure 13. The girders were placed on wooden supports in the storage yard of Fears Lab and were stabilized with timber bracing. Several views of each girder are shown in Figure 14 and Figure 15.

Figure 11: Arrival of girders at Fears Lab on flatbed trailers on October 8, 2013

Figure 12: Unloading of girder A using 20 ton rental cranes on October 8, 2013

Figure 13: Unloading of girder C using 20 ton rental cranes on October 8, 2013

Figure 14: Two views of girder A showing details of condition on October 8, 2013

Figure 15: Two views of girder C showing details of condition on October 8, 2013

The two girders were stored in the yard until space related to other projects was cleared inside Fears Lab. The girders were moved into Fears Lab on July 29, 2014 using 15 ton and 10 ton capacity forklifts rented from Allied Steel Construction. The transportation of the girders into Fears Lab can be seen in Figure 16 and Figure 17.

Figure 16: Transportation of girder A into Fears Lab on July 29, 2014

Figure 17: Placement of girder A into the load frame at Fears Lab (left), and girder C into its storage position within the lab (right)

3.3.3 Preparing Girders for Shear Tests

A variety of non-destructive tests were performed on girder A before destructive shear testing was performed. This testing was outside of the purview of this dissertation, and more can be read about this testing in a previous thesis (Cranor, 2015). *a/d* ratios of 2.0 and 2.5 were selected for girder A in order to create maximum shear stresses within a section of the girder where beam behavior controls, or outside of D-regions. This is defined as a region located more than a distance equal to the section depth away from a load or geometric discontinuity. Testing locations for girder C at *a/d* ratios of 3.0 and 3.83 (quarter-point) were selected in order to encapsulate the behavior from the quarter-point to the end. Support conditions were chosen based on several discussions including ODOT engineers as mentioned previously (elastomeric bearings). Instrumentation was chosen such as to collect the data required to accurately describe the behavior of the girder under load.

The remaining end diaphragms were removed from the ends of girder A using a sledge hammer and a variety of chisels while stored in Fears Lab. Immediately after the girders were brought into Fears Lab, girder A was painted white and a 3 in. reference grid was drawn along the length of the member. The calculated girder centerline was used as the datum (zero) for the reference grid. Numbered vertical grid lines were placed every 1 ft along the length of the girder to create a unified numbering system. The grid continued to approximately 15 ft in each direction from the base point. A similar system would be used for girder C. The ends of girder A were skewed during construction to align with the skew of the girder span. Mr. Matt Romero of ODOT brought a team from the Materials Division to Fears Lab and used a Hilti PS 1000 ground penetrating radar system to locate the transverse reinforcement and harping points for the prestressing strands. These locations were marked on the girder surface in green as part of the grid system. The steel location and finished grid system are shown in Figure 18. Each proposed load point was prepared for load application by placing Hydro-Stone gypsum cement to remove any surface irregularities and create a smooth surface for load application.

Figure 18: Mr. Matt Romero using ground penetrating radar to locate reinforcing bars in girder A (left), and finished reference grid showing steel locations for girder A (right)

Preparation for testing girder C was very similar to that for testing girder A. These preparations included analysis of the girder section, preparation of a detailed instrumentation and testing plan, configuration and testing of all instruments and data acquisition equipment, and preparation of the girder and test setup.

The experience obtained during testing of girder A was used to develop the shear testing setup and instrumentation plan for girder C. The estimated material and sectional properties were used in calculations for strength of the girder in the proposed testing configurations. Values of 3.0 and 3.83 were selected for the *a/d* ratios in order to create maximum shear stresses within a B-region of the girder and to increase the number of data points beyond those obtained for girder A. Support conditions were the same as used for girder A. Instrumentation was chosen such as to collect the data required to accurately describe the behavior of the girder under load and is described in the section on data acquisition (Section 3.2) and in the shear test procedures (Section 3.3.4).

Additional strain gauge channels were added to the data acquisition system from what was used for girder A in the form of the two NI 9236 strain gauge modules. These modules were needed to accommodate foil gauges to be installed on the deck and web of girder C. All instruments were calibrated in the same way as for girder A.

Girder C was first painted white during the summer of 2015 to facilitate observation of cracks during testing and a vertical reference grid was drawn at 1 ft intervals for use in identifying crack locations (see Figure 19). The grid was numbered using the same procedure as for girder A described earlier in this section. This grid was later detailed to every 6 in. vertically and horizontally in the areas near the load points. The girder was moved into position in Fears Lab using Hilman™ rollers placed under each end and hand winches attached the Fears Lab strong floor as shown in Figure 19. Lifting seats were constructed to ensure stability of the non-symmetric section.

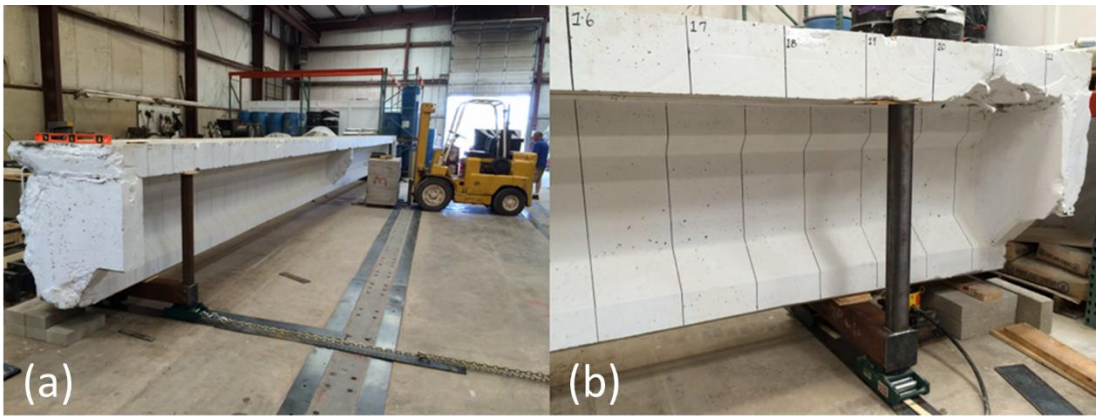

Figure 19: Moving of girder C (a) and the gridlines on girder C (b)

As explained earlier in this chapter, girder C was removed from the bridge with the intention of obtaining a 36 in. wide section of the bridge deck symmetric about the girder web. The deck section as-received was not symmetric and 10 in. of concrete was added to the deck to create a symmetric section after the girder was in place in the

testing frame. Reinforcing bars matching the original reinforcement configuration and sufficient to transfer the expected compression forces across the joint were doweled into the existing deck using a structural epoxy specifically intended for anchoring reinforcing bars in concrete. Interface forces were calculated using AASHTO LRFD Section 5.8.4 (AASHTO, 2012). Preparation for casting the deck extension is shown in Figure 20. A concrete mixture designed to match the strength of deck cores taken from girder A was used to cast the extension. No. 4 reinforcing bars were used at the interface. The concrete surface was roughened with a rotary hammer to improve the bond between the old and new deck concrete and meet the roughened surface requirements described in AASHTO LRFD Section 5.8.4.3 (AASHTO, 2012).

Figure 20: Construction of deck extension of girder C in progress

3.3.4 Shear Test Procedures

3.3.4.1 Girder A Procedures

A total of three shear tests were conducted on girder A, designated A1, A2, and A3. A3 is not included in this dissertation. More can be found on test A3 in the thesis by Cranor (2013). For all tests, the girder was supported on 8 in. x 18 in. x 1 in. thick

neoprene bridge bearings resting on reinforced concrete blocks. The bearing pads were placed flush with the end of the girder at the end being tested and at an interior point in the girder decided upon based on the span length tested. The span lengths for the shear tests of girder A were 18.75 ft and 19 ft for tests A1 and A2, respectively. In these tests, the untested girder end was cantilevered allowing the tested span to support the load, leaving the cantilevered section relatively untouched. A third test was performed with a short span at the center of the girder, but this test was unrelated to this dissertation and can be read about in the master's thesis mentioned previously (Cranor, 2015). Test A1 was performed at an *a*/*d* ratio of 2.5 (point load at 7.5 ft from the girder end). Test A2 was tested at an *a/d* ratio of 2.0 (6 ft from the girder end). Figure 21 shows the testing configuration for shear tests A1 and A2.

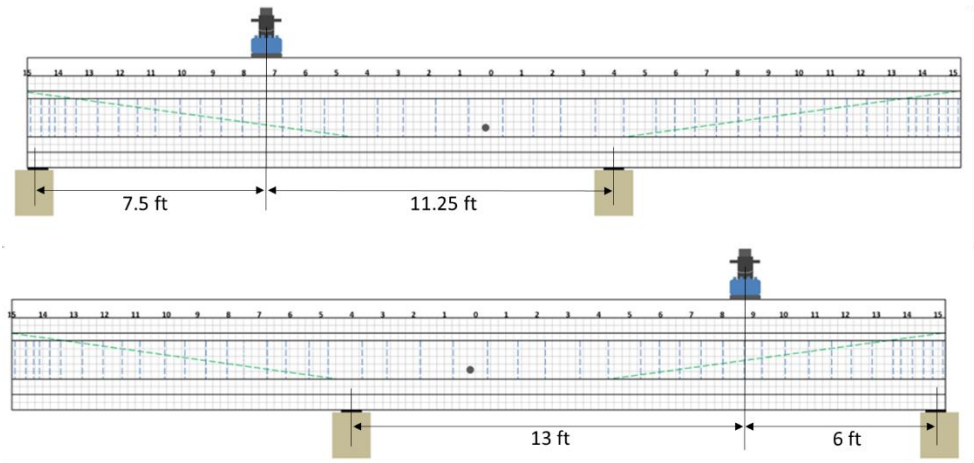

Figure 21: Loading configuration for girder A tests A1 (top) and A2 (bottom)

Load, deflection at the load point, displacement of the bearing pads, strain at discrete points, and strand end slip at the tested end were monitored during the test as described in the section on data acquisition (Section 3.2). Figure 22 shows the arrangement of the individual instruments. Applied load was monitored using a 400 kip

capacity Interface model 1252 load cell. Deflection was monitored with two wire potentiometers at the load point, placed an equal distance from each edge of the bottom flange, to account for any torsion during the tests. For test A1, one wire potentiometer was also located between the load point and each support. Tests A2 included only the two wire potentiometers at the load point, and deflection was monitored manually for these two tests using a laser level and a scale attached to the girder web as shown in Figure 23. This manual measurement was included after issues with electronic deflection measurements occurred during test A1. Deflection caused by deformation of the bearing pads was measured using two LVDTs at each support attached to the bottom girder flange using brackets as shown in Figure 22.

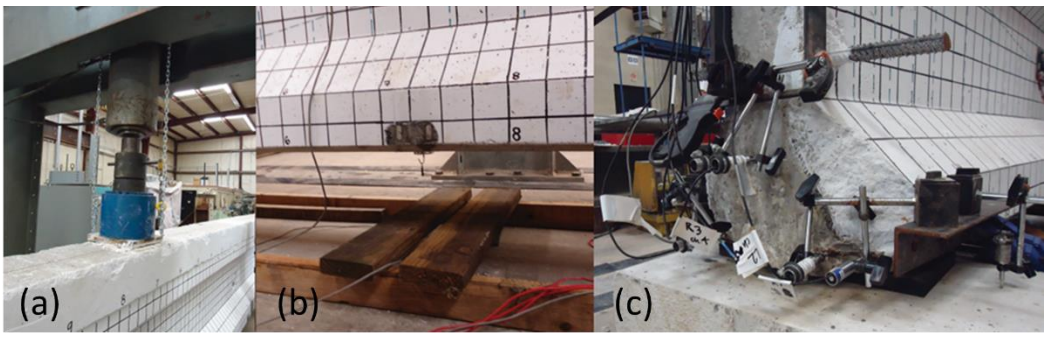

Figure 22: Load application using hydraulic actuator and 400 kip load cell (a), deflection monitoring under load using wire potentiometers (b), and strand slip monitoring with LVDTs (c)

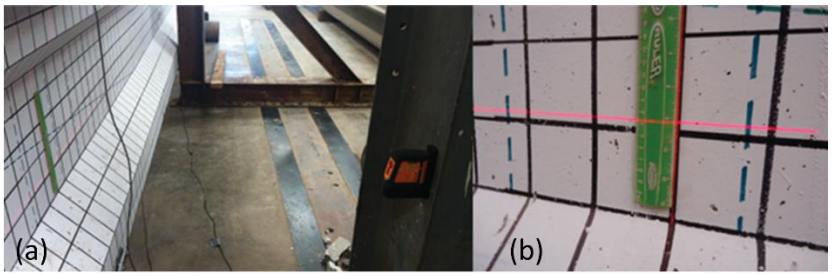

Figure 23: Cross-line self-leveling laser level (a) and ruler attached to girder (b) for manual deflection measurements

End slip was monitored for 8 strands (all straight strands and two draped strands) during shear tests A1 and A2. The LVDTs were placed on brackets with the tip of the LVDT touching the exposed strand such that any slip of the strand was recorded by a corresponding extension of the LVDT. Placement of the LVDTs is shown in Figure 22 and the arrangement of LVDTs for both tests is shown in Figure 24.

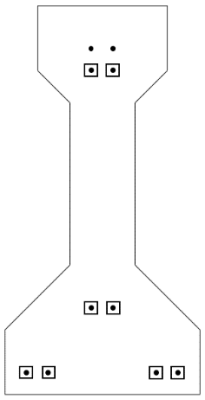

Figure 24: Girder A LVDT placement indicated by boxes

Strain was monitored at points of interest using Bridge Diagnostics, Inc. (BDI) ST-350 dynamic strain transducers, shown in Figure 25. The surface was first prepared using a grinder to create a uniform surface for bonding the gauges and the gauges were attached at the desired locations using steel tabs and epoxy. The locations of the strain gauges were chosen such as to provide strain at the tension fiber and attempt to provide strain information for determining shear stress in the web. During test A1, strain rosettes on the web were used. For A2 strain in the tension fiber was monitored as well.

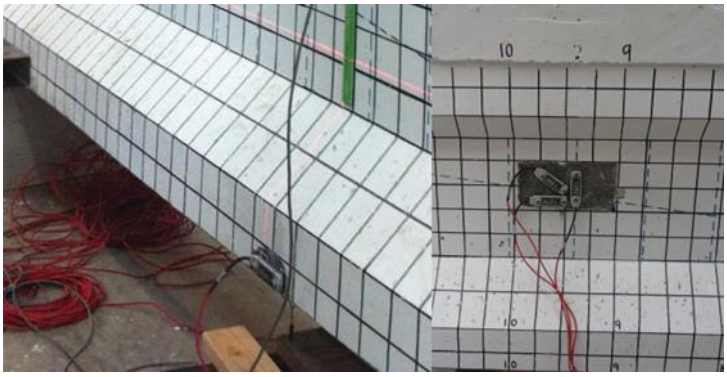

Figure 25: BDI strain gauges for girder A tests

Load was applied for each test in 5 kip increments with a pause between increments to inspect the test setup and look for visible cracking. Once the first crack was observed, it was traced with red permanent marker and the load at which it was observed was marked, as shown in Figure 26. Once the girder reached the estimated failure load, or showed signs of eminent failure, cracks were no longer marked after each increment for safety reasons. Videos and pictures were taken to document significant moments during all shear tests, the records of which were used for detailed analysis of failure mechanism in conjunction with automatically recorded time histories of all data measurement.

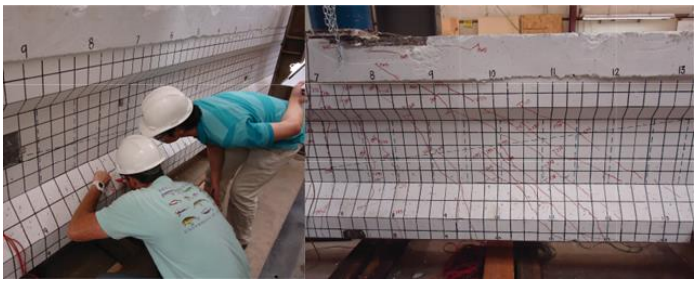

Figure 26: Students marking cracks (left) and cracking pattern from test A1 with cracks marked in red ink (right)

3.3.4.2 Girder C test procedures

Girder C was tested at both ends using similar procedures to the tests of girder A. After girder A was tested at *a*/*d* ratios of 2.0 and 2.5, girder C was tested further from the end at *a/d* ratios of 3.0 (9 ft from end) and 3.83 (11.5 ft from end). These *a/d* ratios were selected to examine shear behavior in a B-region. An overview of the testing configurations for girder C is shown in Figure 27. Girder C was instrumented more heavily than girder A in an attempt to gather more information about the shear behavior. LVDTs were used to measure strand slip in eight of the ten straight strands in the girder (Figure 28). As in previous testing, wire potentiometers were used to measure deflection at the load point and four LVDTs were used to account for deflection of the bearing pads. Five BDI strain gauges were attached to the top and bottom flanges of the girder at the load point to monitor strain distribution in the section. Additionally, 15 foil type strain gauges were attached to the concrete at strategic locations. Four of these gauges were placed on top of the deck to observe the distribution of compression strain along the width of the deck. Six were arranged on the web of the girder at an angle perpendicular to expected shear cracks in order to catch shear cracks as they formed and to observe the strain in the web before the formation of these cracks (Figure 29). The rest were arranged in a similar fashion to the BDI gauges. Unfortunately, several of these gauges were damaged during installation. The foil gauges are very delicate, and it is not unusual for there to be some attrition during installation.

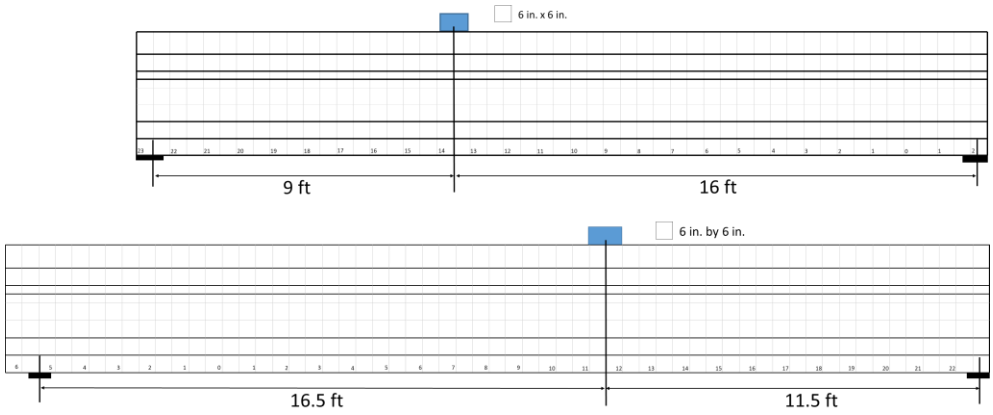

Figure 27: Girder C loading configurations (test C1 top, test C2 bottom)

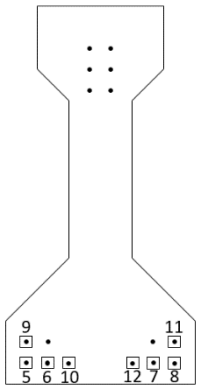

Figure 28: Girder C LVDT placement indicated by boxes

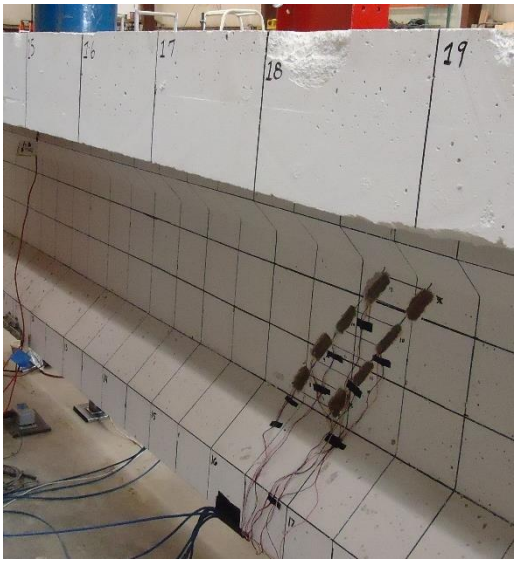

Figure 29: Foil gauge placement on girder C web

Since previous testing at OU (Martin, Kang, & Pei, 2011) was performed closer to the support, the second shear test of girder C (C2) was performed at the quarter-point as the upper limit to data points throughout the end regions. At the time these girders were designed, the critical section for shear was taken at one quarter of the length of the girder. For this girder, the quarter-point corresponds to 11.5 ft into the girder from the end (grid location 11.5 ft) for an a/d ratio of 3.83. The span for this test was 28 ft (3 feet longer than for shear test one) in order to increase the shear demand on the tested end. At this location, the shear and moment capacities were expected to be very similar and a flexural failure was anticipated. The location was still deemed a useful location for testing since it would provide information about the capacity as received at the quarter-point and the shorter span than used in service would cause greater shear demand at the design moment capacity. A summary of the test parameters for the full-scale shear tests iss given in Table 7.

3.4 Results from Full-Scale Tests

The following sections detail the results of shear tests on girders A and C. The testing of girder A has been reported in a previous thesis in more detail (Cranor, 2015), but an overview is presented here. More discussion of the results of the tests follows in a later section, including comparison to design codes.

3.4.1 Full-Scale Girder Material Properties

Material properties for girder A were reported previously by Cranor (2015) but are repeated here for completeness. Cores were taken from both girders for material testing and modulus of elasticity testing after the full-scale tests were completed using

the procedures outlined in ASTM C42 (ASTM, 2016). Core correction factors were found using ACI 214.4 (2003) assuming the “Air dried” moisture condition.

Twelve 3 in. by 6 in. cores were taken from the web of girder A. Core locations were selected to provide a distribution of cores along the length and height of the member. A photo of some of the core locations is shown in Figure 30. Two approximately 2 in. diameter cores were taken from the deck 3.5 and 0.5 ft from the center of the girder. Seven 4.25 in. cores were taken from the portion of the girder A outside of the heavily damaged sections for elastic modulus tests. Six 3.75 in. diameter cores were taken from the web of girder C for compressive strength and modulus of elasticity testing, and three 3.75 in. cores were taken from the deck of girder C for compression testing. Two samples each of prestressing strand and mild steel were taken from girder A for tensile strength and modulus of elasticity testing. It was assumed that the steel properties were very similar for girders A and C and no additional tests were conducted specifically for girder C.

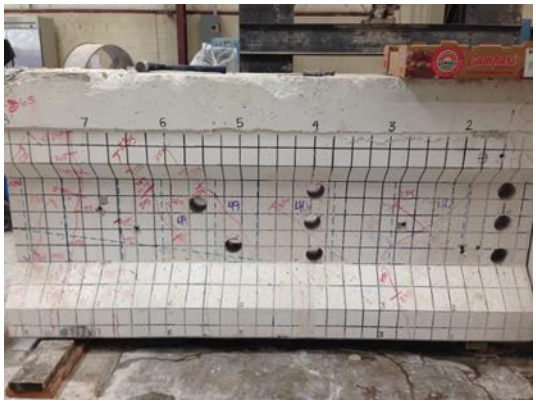

Figure 30: Locations of some of the cores taken from girder A

Girder A Concrete Properties

Six 3 in. diameter cores taken at different locations along girder A were tested for compressive strength. The specimen IDs are descriptive of the location of the core. The first letter (N or S) indicates whether the core was taken from north or south of the center of the girder. The number is the distance in feet from the center line. If multiple cores were obtained from the same location, the final letter (T, M or B) stands for top, middle, and bottom of the web of the girder.

The results of the compressive strength tests for the cores taken from the web of girder A are presented in Table 8. The average compressive strength for the cores was 6,270 psi. Using the ACI 214.4 (2003) specification factor of 1.05, the equivalent compressive strength of the girder is 6,570 psi. This factor corrects for the length to diameter ratio, the core diameter, the core moisture condition, and the damage caused by drilling. The measured compressive strength is close to the specified compressive strength of 6,000 psi. There was not a significant difference in compressive strength along the length of the girder for the cores tested.

Table 8: Compressive strengths of 3 in. cores taken from girder A web

Specimen ID	Load (lb)	Compressive Strength (psi)
N4.00T	45,680	6,460
N4.00M	46,920	6,630
N1.25T	40,700	5,760
N1.25M	47,130	6,660
S9.75T	42,605	6,020
S10.25B	43,235	6,110
Average	*44,380*	*6,270*

Two cores approximately 2 in. in diameter were taken from the deck in the center section of the girder at locations 3.5 and 0.5 ft from the center of the girder. Each

core was cut into three equal cylinders and tested for compressive strength. Table 9 documents the compressive strength from the cores.

Table 9: Compressive strength of 2 in. diameter cores taken from girder A deck

Specimen ID	Load (lb)	Compressive Strength (psi)
S3.5a	31,160	7,830
S3.5b	27,455	6,900
S3.5c	30,390	7,640
S0.5a	27,900	7,010
S0.5b	27,805	6,990
S0.5c	27,325	6,870
Average	*28,670*	*7,210*

The average compressive strength of the deck concrete cores at 3.5 ft from the center was 7,730 psi. Specimen b was disregarded due to mild steel in the sample causing an inaccurate measurement of the concrete compressive strength. The average compressive strength of the concrete cores at 0.5 ft from center was 6,960 psi. The average compressive strength of all 5 cores (excluding Specimen S3.5b) was 7,270 psi. The modification by ACI 214.4 (2003) factor of 1.08 gives a compressive strength for the deck of 7,840 psi. The estimated modulus of elasticity was 5,050 ksi based on the correlation in ACI 19.2.2.1b ($E_c = 57{,}000 f'^{0.5}_c$) based on compressive strength. Using the correlation in AASHTO C5.4.2.4 ($E_c = 1{,}820 f'^{0.5}_c$) the modulus was 5,105 ksi.

Modulus of elasticity of the girder concrete was determined using the seven approximately 4.25 in. diameter cores taken from the girder web using the methods of ASTM C469. The modulus of elasticity for each core based on the second and third loading cycles is provided in Table 10. The average modulus of elasticity of the girder concrete was 4,750 ksi. The estimated modulus of elasticity using the ACI relationship was 4,620 ksi based on the adjusted compressive strength. The measured modulus of

elasticity is greater than the predicted modulus of elasticity (by 7.5%) which makes the code estimate a conservative one. Based on the AASHTO correlation the modulus of elasticity was 4,665 ksi, also a conservative estimate. The modulus of elasticity did not show a significant difference along the length of the girder for the cores tested.

Table 10: Modulus of elasticity of 4.25 in. cores taken from the web of girder A

Specimen ID	Modulus of Elasticity-Test 2 (ksi)	Modulus of Elasticity-Test 3 (ksi)	Modulus of Elasticity (ksi)
N0.50	4,947	5,042	4,995
S0.50	4,966	5,109	5,038
S3.00	4,525	4,542	4,534
S3.75T	4,420	4,431	4,426
S3.75B	4,831	4,916	4,874
S4.50T	4,696	4,795	4,746
S4.50B	4,615	4,623	4,619
Average	*4,710*	*4,780*	*4,750*

Girder C Concrete Properties

When taking cores from girder C, care was taken to avoid reinforcement and existing cracks. For this reason, cores were taken closer to the center of the girder to avoid damage from the shear tests and to be in the region with the largest stirrup spacing. The diameter of the cores was roughly 3.75 in. and the length was typically around 6 in., corresponding to the thickness of the web. The cores were grinded on the ends to provide a plane surface perpendicular to the length. One compressive strength cylinder (W3) included a longitudinal crack, potentially affecting the strength (Figure 31), but the compressive strength of this cylinder was still greater than the specified 28-day strength (as explained further below).

Figure 31: Crack on web core W3

The compressive strength of the cores taken from the web and deck of girder C are presented in Table 11. The average compressive strength of the cores taken from the girder web (after applying ACI 214.4 correction) was 7,180 psi (7,130 psi before correction) and the average compressive strength for the cores taken from the deck was 6,060 psi (6,050 psi before correction). One deck core appeared to have low compressive strength relative to the other breaks; if this break is removed the corrected compressive strength of the deck is 6,690 psi. The compressive strengths listed in the table are prior to application of correction factors. The complete calculations are given in Appendix B.

Table 11: Compressive strength of 3.75 in. cores from girder C

Girder Section	Specimen ID	Load (lb)	Compressive Strength (psi)
Web	W1	85,850	7,830
	W2	73,195	6,920
	W3	72,780	6,430
	Average	*77,275*	*7,060*
Deck	D1	71,925	6,340
	D2	74,760	6,550
	D3	52,850	4,640
	Average	*66,510*	*5,840*

Girder C was needed for future testing of concrete repair materials, limiting the number of cylinders that could be retrieved. All usable cylinders from the web were used for compressive strength, and the deck cores were not tall enough to test for modulus of elasticity. Based on the ACI modulus of elasticity correlation, the web modulus was 4,830 ksi and the deck modulus was 4,440 ksi. Using the AASHTO equation the expected moduli were 4,875 psi and 4,480 psi for the web and deck, respectively. Based on the accuracy of the girder A correlations and the similarity of the concrete, it is likely that these modulus estimates are reasonably accurate and slightly conservative.

Steel Properties from Girder A

Two prestressing strand samples taken from the section of girder A between 0.75 and 2.25 ft from center were tested for tensile strength and modulus of elasticity conforming to ASTM A1061 (ASTM, 2016). Table 12 provides the modulus of elasticity and ultimate strength of each strand. The average modulus of elasticity of the strands was 26,350 ksi. The average tensile strength of the strands was 283 ksi, confirming that the strands were Grade 270, as specified in the plans provided by

ODOT. As stated previously, it was assumed these properties were consistent with girder C since the girders were likely manufactured around the same time and in the same location.

Table 12: Properties of prestressing strand from girder A

Specimen ID	Modulus of Elasticity (ksi)	Ultimate Strength (ksi)
0.75-2.25 West	26,600	282.8
0.75-2.25 East	26,100	284.3

Two samples of mild steel used for the shear stirrups in girder A and from the steel in the diaphragm (removed prior to testing) were tested for yield stress, ultimate strength, and modulus of elasticity. Tests were performed in the Baldwin Universal Testing machine at Fears Lab. The results are shown in Table 13. The average yielding strength, modulus of elasticity, and ultimate strength for the shear steel were 54.8 ksi, 32,750 ksi, and 87.9 ksi, respectively. For the diaphragm steel these values were 51.1 ksi, 27,500 ksi, and 84.2 ksi. These properties confirm that the steel was most likely Grade 40 which was assumed during the preliminary analysis based on the original plans.

Table 13: Mild steel properties from girder A

Property	Stirrup 1	Stirrup 2	Diaphragm 1	Diaphragm 2
Yield Stress (ksi)	54.4	55.2	51.6	50.5
Modulus of Elasticity (ksi)	29,300	36,200	26,800	28,200
Ultimate Strength (ksi)	87.4	88.4	85.5	82.8

3.4.2 Girder A Results

The first shear test of girder A (A1) was performed at an *a/d* of 2.5 with a span length of 18.75 ft. Initial cracking, due to flexure, occurred at a load of 170 kips directly

under the load point (775 kip-ft applied moment, 107 kips shear). The first shear crack was a web shear crack 4.5 ft away from the load point towards the near support and occurred at a load of 225 kips (138 kips shear). As the load was increased, several shear cracks began to enter the bottom flange. At a load of 255 kips, the bottom four strands slipped, leading to a loss of load carrying capacity. Slip was measured for six of the strands before failure, possibly influenced by corrosion (Figure 32) present at the girder end. According to discussions with ODOT engineers and site visits by the author and collaborators, similar corrosion is frequently observed at the ends of prestressed girders in Oklahoma bridges. Load was increased to 260 kips, at which point the deck overlay delaminated. The maximum load resulted in an applied moment of approximately 1162 k-ft and applied shear of approximately 155 kips, including dead load. The cracking pattern for this test is shown in Figure 33. Initial flexure cracking occurred in the immediate vicinity of the load point. Flexure-shear and web shear cracks occurred between the load point and near support as shown in Figure 33. The failure mode for test A1 can be characterized as “bond-shear” because strand slip reduced the capacity of the section and ultimately led to a shear failure. The strand slip reduced the available prestress force and contributed to the shear cracking and shear failure mechanism. A picture of the failure is given in Figure 34. The deflection measurements for test A1 were lost due to a malfunction of the wire potentiometers, so load versus deflection data were not available for this test.

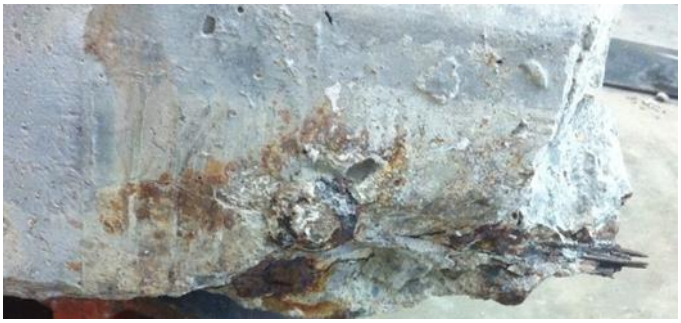

Figure 32: Corrosion at end of girder during test A1

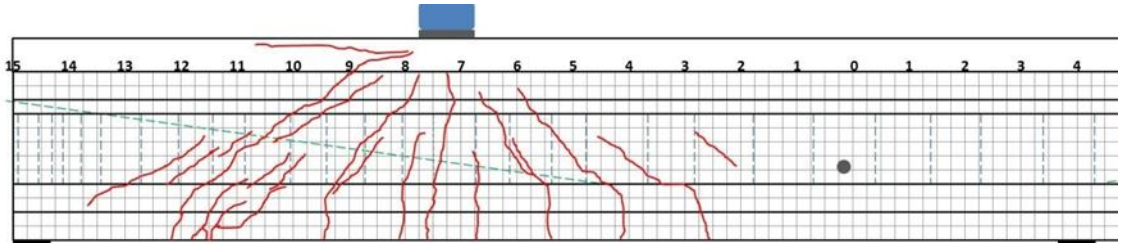

Figure 33: Shear test A1 cracking pattern (3 in. grid shown) (from Cranor 2015)

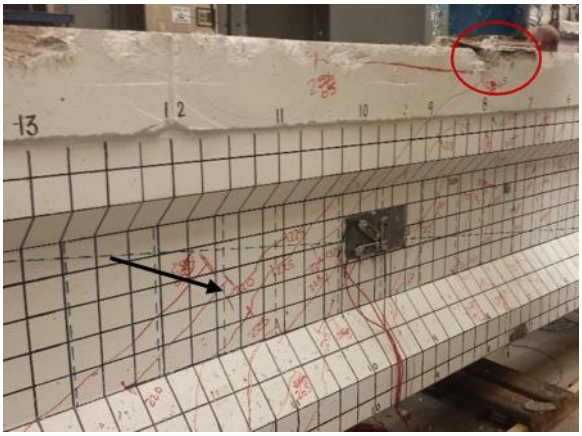

Figure 34: Cracking and failure pattern from test A1; shear cracking marked by black arrow, crushing in deck marked by red circle

The second shear test of girder A (A2) was performed at an *a/d* of 2.0 with a span length of 19 ft. Initial cracking, due to flexure, occurred directly under the load point at a load of 190 kips, corresponding to an applied moment of approximately 761 k-ft, and applied shear of approximately 133 kips. The first shear crack was observed in

the web and the bottom flange roughly 1 ft away from the support at a load of 225 kips (158 kips shear). Load was increased to 289.5 kips, corresponding to an applied moment of 1197 k-ft and applied shear of 193 kips, at which point there was a sudden failure corresponding to delamination of the deck overlay and rupture of multiple prestressing strands. The strands ruptured approximately 1 ft away from the load point in the direction of the longer side of the span. The cracking pattern is shown in Figure 35 and failure photos are given in Figure 36 and Figure 37.

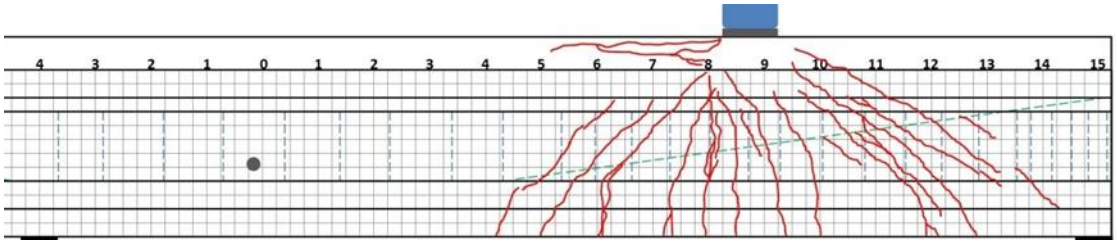

Figure 35: Shear test A2 cracking pattern (strand ruptured at 8 ft mark), 3 in. grid shown (from Cranor 2015)

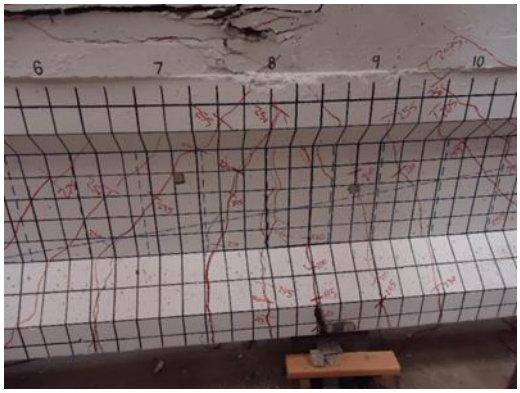

Figure 36: Test A2 failure showing deck crushing at the top of the figure and large open flexural crack at the bottom (where strand rupture occurred)

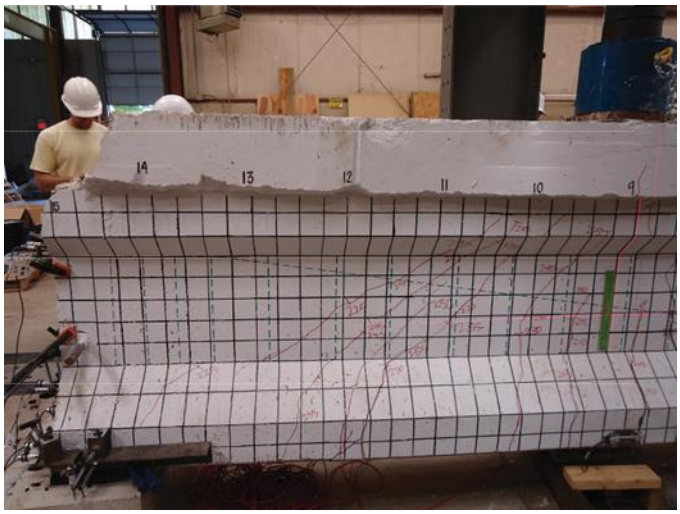

Figure 37: Cracking from test A2 showing shear span

The load deflection plot for test A2 is shown in Figure 38. This plot indicates a period of constant load and yielding at the maximum load which is indicative of the ductility associated with a flexural failure. This failure type was confirmed by crushing of the extreme compression fiber and fracture of at least two of the bottom layer prestressing strands. Figure 38 includes markers for when initial flexural cracking and shear cracking was observed, as well as the ultimate load. The circle in this plot indicates when an unseen flexural crack occurred, based on the change in slope of the load-deflection curve.

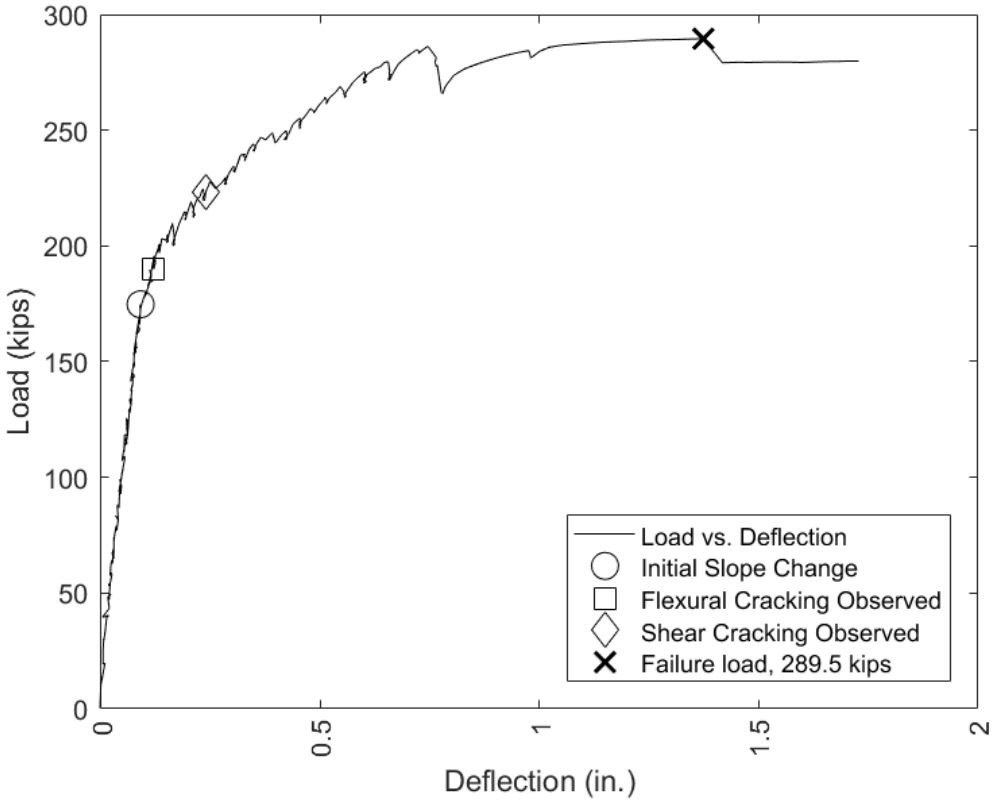

Figure 38: Load versus deflection for test A2

3.4.3 Girder C Results

The first shear test of girder C (C1) was performed at an *a/d* of 3.0 with a span length of 25 ft. Once the data acquisition software was initialized, load was applied in 10 kip increments and the researchers present for the test monitored the girder for any signs of cracking. At an applied load of 90 kips, spalling was observed at the end nearest the load point, directly above the support bearing. Corrosion of the prestressing strands was present at that end similar to that described for girder A, and the corrosion had initiated several cracks, particularly on the outer strands. The level of corrosion on this end is typical based on site visits to girders from this time period (Mayhorn, 2016). The bearing force caused the pre-existing cracks at this end to open and for pieces of

concrete to spall off of the bottom flange (Figure 39). At this point the test had to be stopped so the LVDTs on the strands at that end could be repositioned. The LVDTs monitoring strand slip and bearing deflection were mounted to the sides of the bottom flange on this end of the girder, so spalling caused these instruments to move and no longer provide accurate readings. The spalling behavior ceased at a load of 110 kips, so it appears there were no bearing issues outside of the initial spalling due to the weakened concrete surrounding the corroded strands.

Figure 39: Spalling and cracking at girder end initiated by corrosion cracks

When the test was resumed, the load continued to be increased at 10 kip increments until web-shear cracks were observed at a load of 160 kips (904 kip-ft moment, 103 kips shear) at the web-top flange interface (Figure 40). At this point, load increments were decreased to 5 kips. From 160 kips of load on, web shear cracking was observed at every load increment, and either these cracks grew or new ones appeared at every step (Figure 41). The initial web shear cracks extended the full height of the web at a roughly 26-degree angle, beginning 2 ft away from the support. The location of

these cracks and the fact that they were recognized before any cracks under the load point formed indicate that shear was the controlling load case at this point.

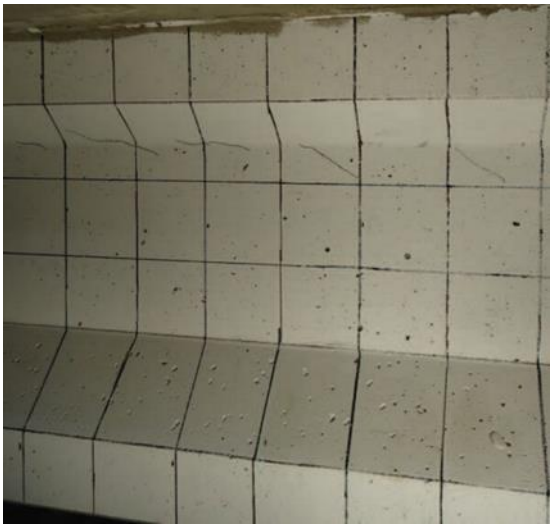

Figure 40: Initial shear cracking for test C1

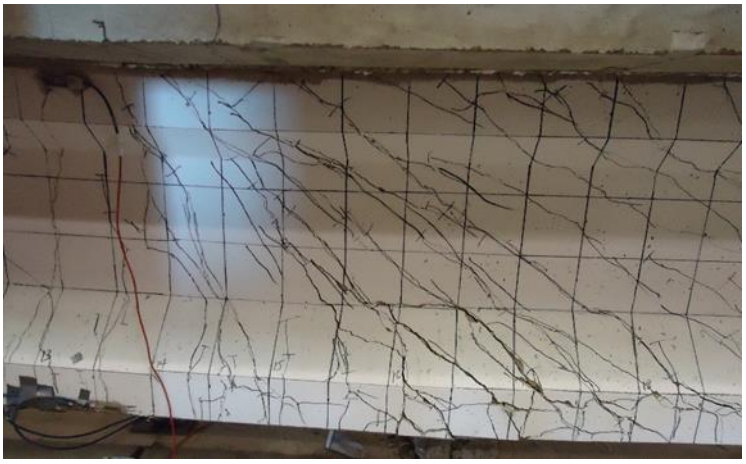

Figure 41: Test C1 failure, note large shear cracks and horizontal cracks in bottom flange

Flexural cracking under the load was observed at 185 kips (1,045 kip-ft moment, 119 kips shear), and at a load of 195 kips (1,102 kip-ft moment,125 kips shear) some shear cracks began to enter the bottom flange of the girder. A data acquisition error caused this test to be halted at 195 kips before continuing the load to failure. The load

was removed, and the error fixed, at which point loading was continued. This also provided an opportunity to re-position the LVDT's that had been shifted by the spalling concrete. After fixing the data acquisition error, load was returned to 195 kips at the same increments as before. Between load steps the girder was observed in order to verify that no new cracks formed; no new cracks were seen by the researchers. As load increased beyond 195 kips, several shear cracks began to align themselves with the strands in the bottom flange, indicative of a possible bond-shear issue (Figure 42).

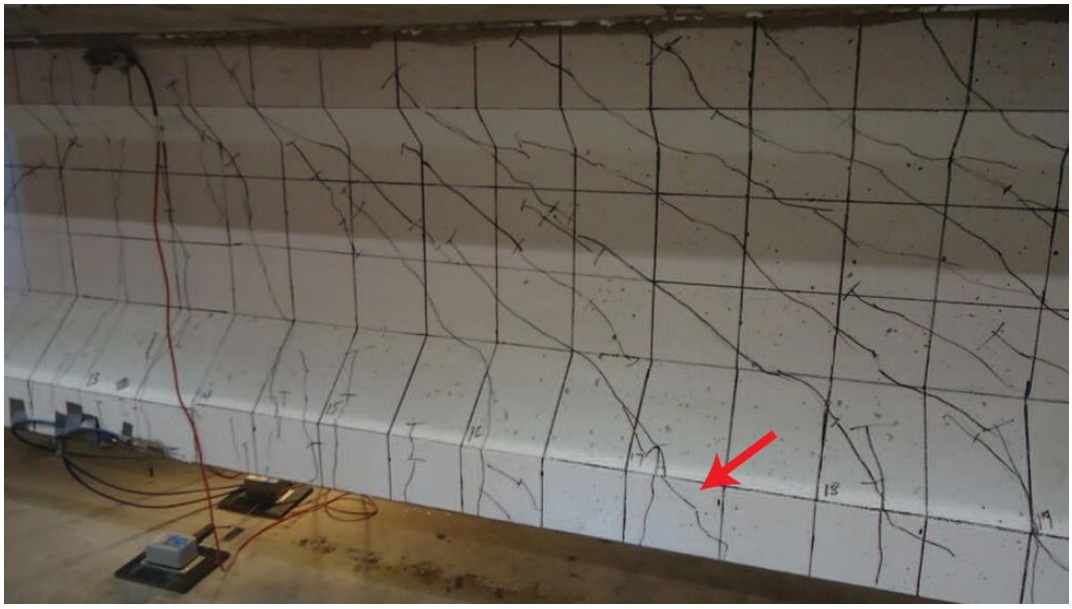

Figure 42: Shear cracking at 250 kips, red arrow indicates bond-shear cracking

Once the load was returned to 195 kips, the shear cracks reached the bottom flanges and made it into the bottom of the girder. Flexural cracks also continued to extend up towards the deck. As loading continued, shear cracks formed at an even spacing and on either side of the load point (Figure 43). At a load of 265 kips, some of the shear cracks in the bottom flange extended horizontally, along the same height as the prestressing strands. This sort of cracking could indicate bond-shear issues. Once

the load surpassed 300 kips, the observed behavior became more plastic and the girder became unable to sustain additional load. At this point the hydraulic ram ran out of travel, and the test was delayed to insert an additional spacer before the maximum load was applied.

After an additional spacer was added, the load was applied without interruption from 0 kips to the maximum load of 318 kips. The final stages of loading were characterized by increased deflection compared to load (loss of stiffness) and by growth of the shear cracks at the level of the prestressing strands. Ultimately, failure occurred when these shear cracks caused strand slip leading to delamination of the wearing surface. As observed in the shear tests of girder A, the weak link in the deck concrete was this overlay at the top of the deck. In each case, horizontal shear forces likely caused delamination of the wearing surface, causing failure (Figure 44). The overall cracking pattern for test C1 is shown in Figure 43 and photos of the failure are given in Figure 44.

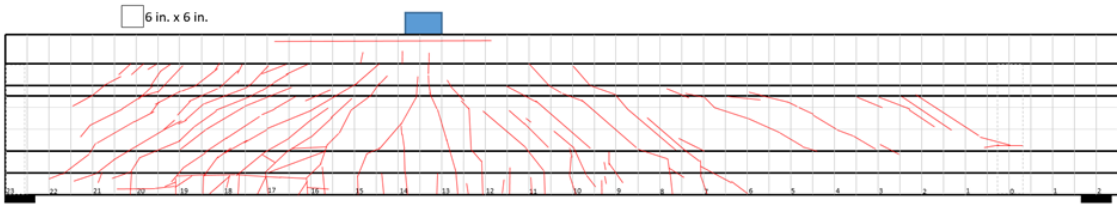

Figure 43: Test C1 cracking pattern, 6 in. grid shown

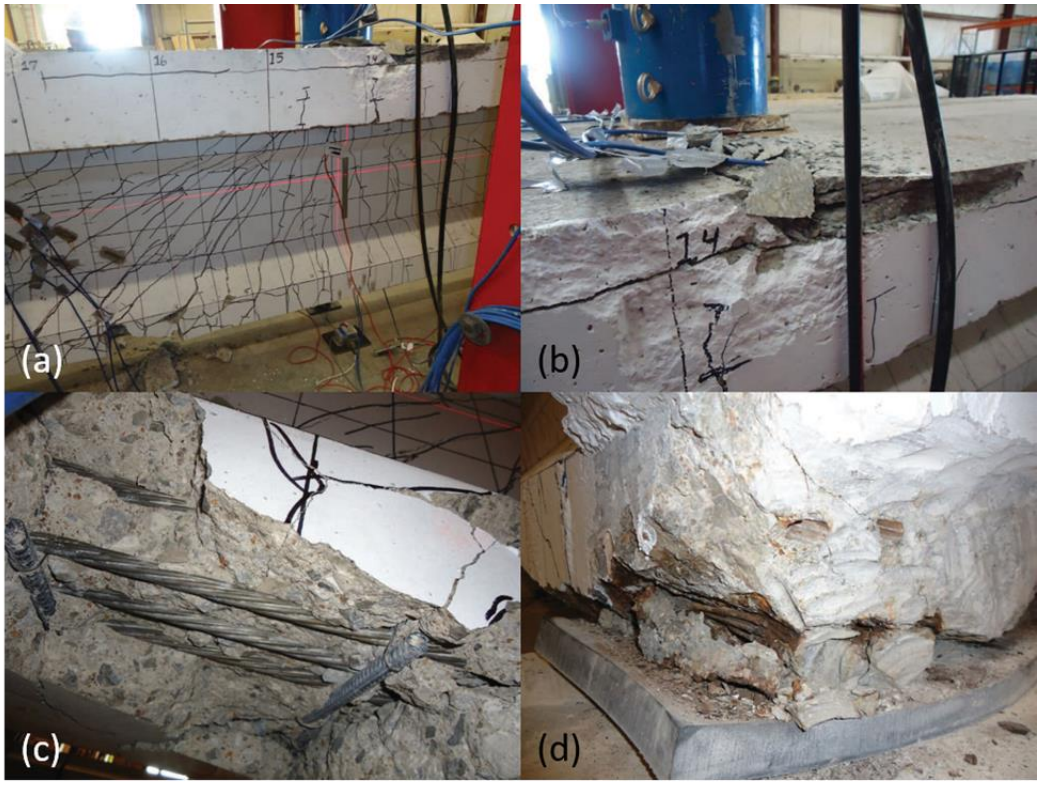

Figure 44: Final condition of girder after test C1: (a) shows overall condition at load point, (b) shows crushing at deck, (c) shows exposed strands due to bond-shear cracking, and (d) shows strand slip of roughly one inch as well as strand corrosion

Figure 45 shows a load-displacement curve for the girder from the second and third round of test C1. This figure shows the behavior of the girder from 0 kips up to the point when no additional load could be applied. There are two points highlighted on the curve: the point of initial cracking and a point when the girder showed plastic deformation. These shifts would be related to initial crack growth and moment-shear cracking from the final stages of the test, respectively. This figure shows the last two sets of data; the first, when the support deflections were disturbed by spalling concrete, is not included. Obviously, the stiffness in test B would be slightly less than in the test

A, since the initial cracking occurred after 195 kips of load, when the first test was halted.

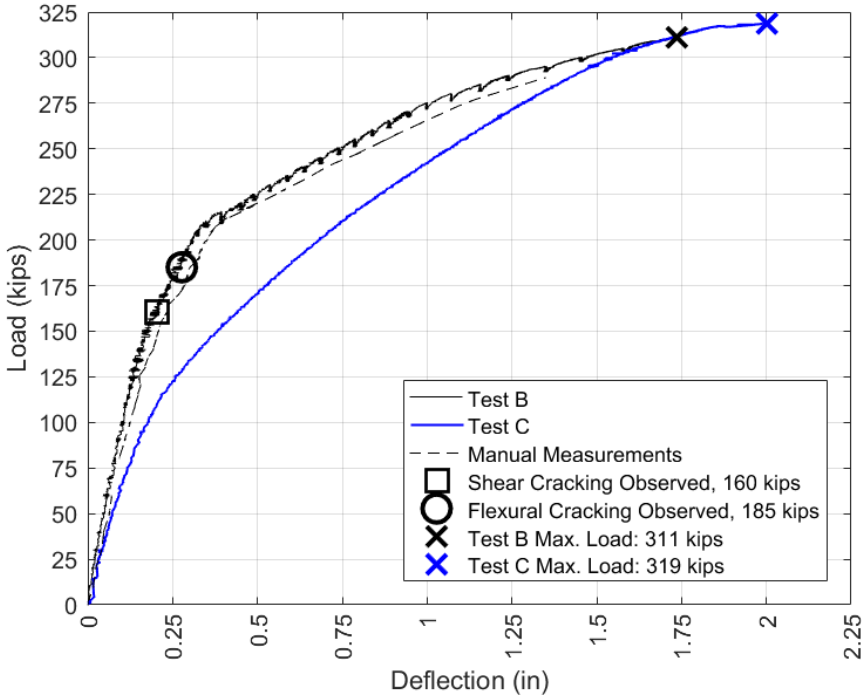

Figure 45: Test C1 load vs. deflection

Figure 46 presents the results from strain gauges atop the deck alongside the load during the third iteration of the test (test C). Strain gauge 2 was approximately 12 in. away from the center of the girder and 3 and 4 were located 20 in. from the center on either side. The purpose of these gauges was to measure the distribution of compression strain in the slab to provide an indication of compression stresses. As expected, the strain was larger close to the load and smaller toward the edge of the slab. It is clear from Figure 46 that load was distributed into the slab extension and that the deck concrete received a large portion of compression strain even towards the edges. The maximum strain is nearly 0.0025 at a location 12 in. away from the load point. The

maximum expected compression strain at failure according to the ACI code is 0.003 (ACI Committee 318, 2014). Because of shear lag, the compression strain is lower as the distance from the load point increases. Strain gauge 4 was located on the deck extension, so there is less strain measured there at failure. Visual observation of the deck failure indicated that it was related to the weak interface between the wearing overlay and original concrete, rather than crushing of the deck. This is corroborated by the measured strains in the deck which were lower than 0.003 strains.

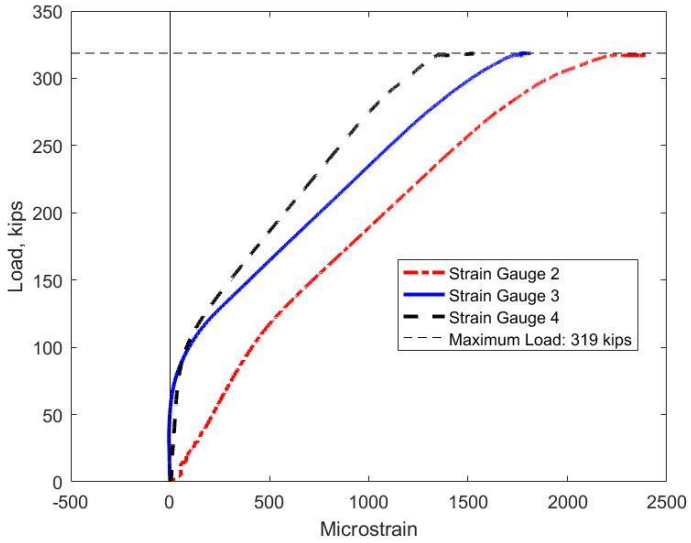

Figure 46: Strains in deck for test C1

Finally, Figure 47 shows the loss of bond, in the form of strand slip, for multiple strands on the bottom row beginning at a load of approximately 250 kips. Measurements for the LVDTs on strands 5, 7, and 10 (as described in Figure 28), which had the largest bond loss, are shown in Figure 47. LVDTs on strands 6 and 8 measured smaller slip values and strand 12 exhibited approximately zero measured slip. Shear cracks extended into the transfer length of these strands and when these cracks were wide enough the strands lost anchorage completely, leading to the failure.

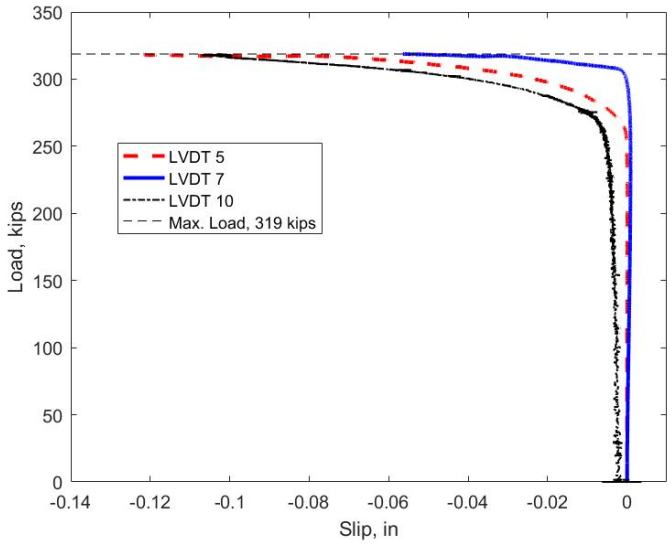

Figure 47: Strand slip in test C1

Test C2 was performed at an *a/d* of 3.83, corresponding to a quarter of the original span length, and the critical section for shear in the 1973 AASHTO-STD. However, this far into the span flexure was expected to control the failure. The test span was therefore increased to 28 ft to increase the shear demand on the short side of the span relative to the longer side.

The first observed cracks were web-shear cracks approximately 2 ft from the supports (Figure 48) at a load of 150 kips (moment of 1030 kip-ft and shear of 88 kips) followed by flexural cracking at 160 kips (moment of 1097 kip-ft and shear of 94 kips). The first cracks were several web shear cracks near the support and near the web-top flange interface. At this point load increments were decreased to 5 kips for the remainder of the test. The shear and flexural cracks increased in size and number until the end of the test. Flexural cracks reached the deck at an applied load of approximately 190 kips. At a load of 195 kips, web shear cracks began to grow into the bottom flange becoming flexure-shear cracks. As load was increased, some of these cracks oriented

themselves more horizontally, along the level of the strands (indicating some potential bond issues). An overview of the cracking from test C2 is shown in Figure 49. Load was increased up to 301 kips at which point a leak in the hydraulic actuator used to apply load caused the test to be halted. Load was removed from the girder until the hydraulic system could be topped up with fluid. After the hydraulics were corrected, load was applied continuously until ultimate failure occurred at a load of 297 kips. As in previous tests, the girder failed when the forces in the deck overlay were too large, causing the overlay to delaminate and crush. The compressive forces during this test were so large that the top flange crushed and compression steel in the top flange and the deck buckled (Figure 51 and Figure 52). This failure type could be described as compression-shear or a flexural failure. Compression-shear is caused by shear cracks entering the compression flange followed by a compression failure (Ross et al., 2011).

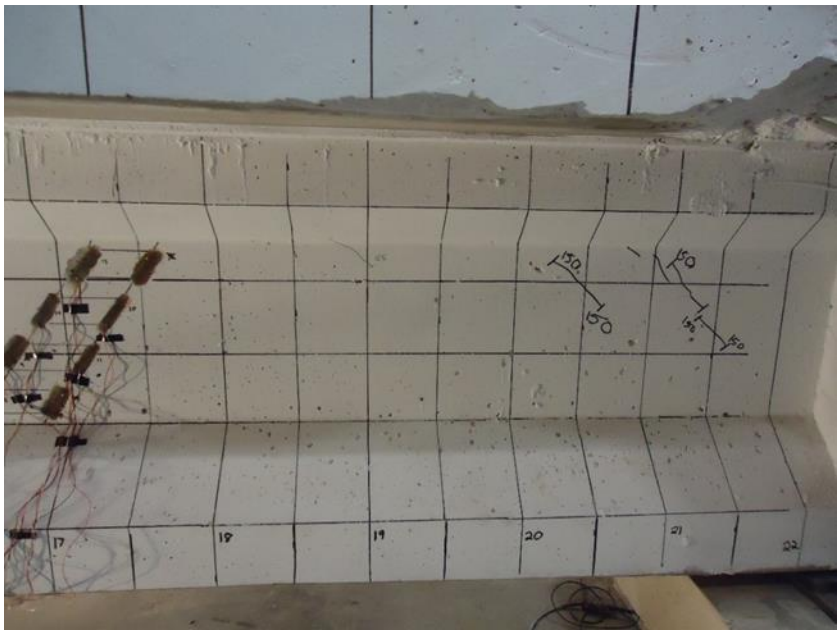

Figure 48: Initial cracking in test C2

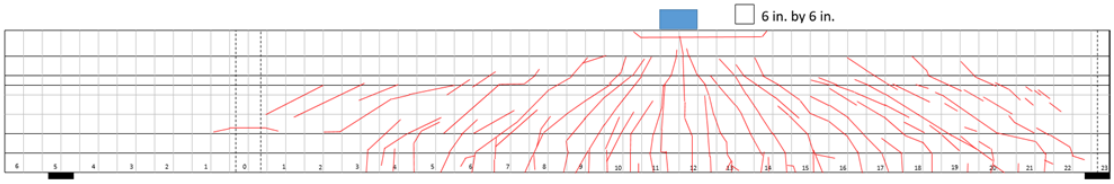

Figure 49: Overall cracking pattern for test C2

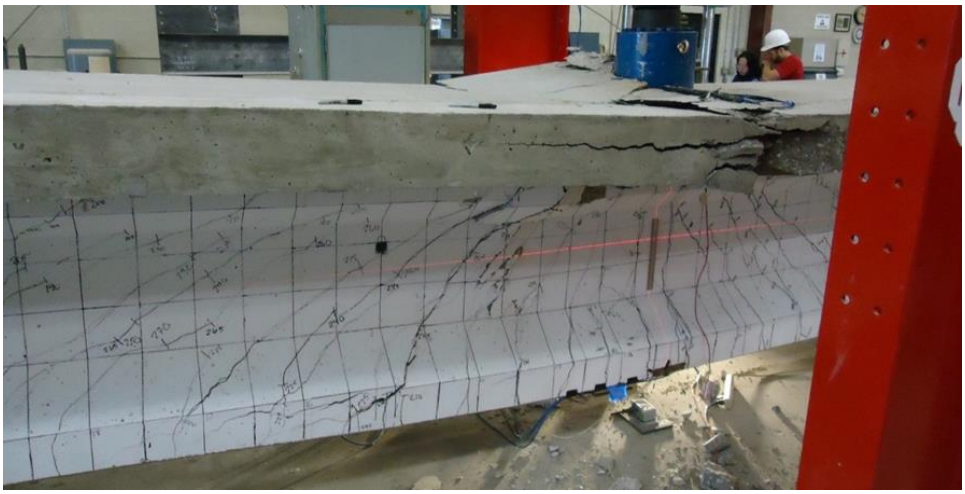

Figure 50: Test C2 failure, showing a large shear crack in the center of the image that entered the top flange where a compression failure occurred

Figure 51: Crushing in girder deck and buckling of reinforcing steel

Figure 52: Buckling of compression steel in girder flange and failed deck concrete

The load deflection curves for both iterations of test C2 (A and B) are shown in Figure 53. The wire potentiometers began to yield unreliable data at a load of approximately 230 kips, so manual measurements are shown in lieu of the potentiometer data past this point. There was good agreement between the potentiometers and the manual deflection measurements up to this point. In Figure 53 there is a clear change in the slope of the curve that occurred after the initial cracking, corresponding to a decrease in stiffness due to the cracks. After initial cracking, there was an increase in deflection of 3.75 in. and an abundance of additional cracks. This type of behavior can be characterized as ductile.

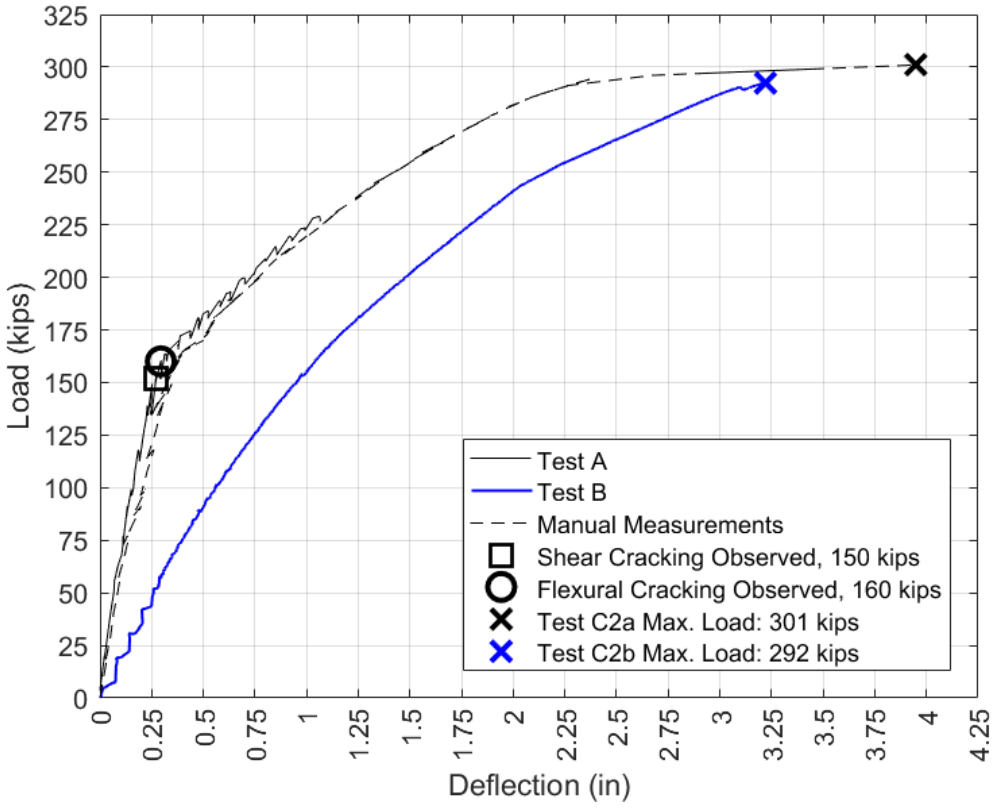

Figure 53: Load vs. deflection for test C2

Figure 54 shows the strand slip data from four of the bottom six strands of the girder. Unfortunately, the apparatus that was used to hold the strands in position shifted, causing the LVDT's to extend. Because of this, it is hard to quantitatively describe the slip in the strands during the test. It is, however, possible to determine which strands slipped and when. LVDT 10 appears to show slip at the time of initial cracking. This LVDT corresponds to the center-left strand (see Figure 28). All of the other strands on the bottom row appear to slip at some point after a load of 200 kips. Again, the magnitude of slip is difficult to determine, but it is at least 0.03 inches, which is larger than typically considered for a loss of bond between strand and concrete. It is unlikely

this slip significantly affected the moment capacity of the section given that the compression steel buckled.

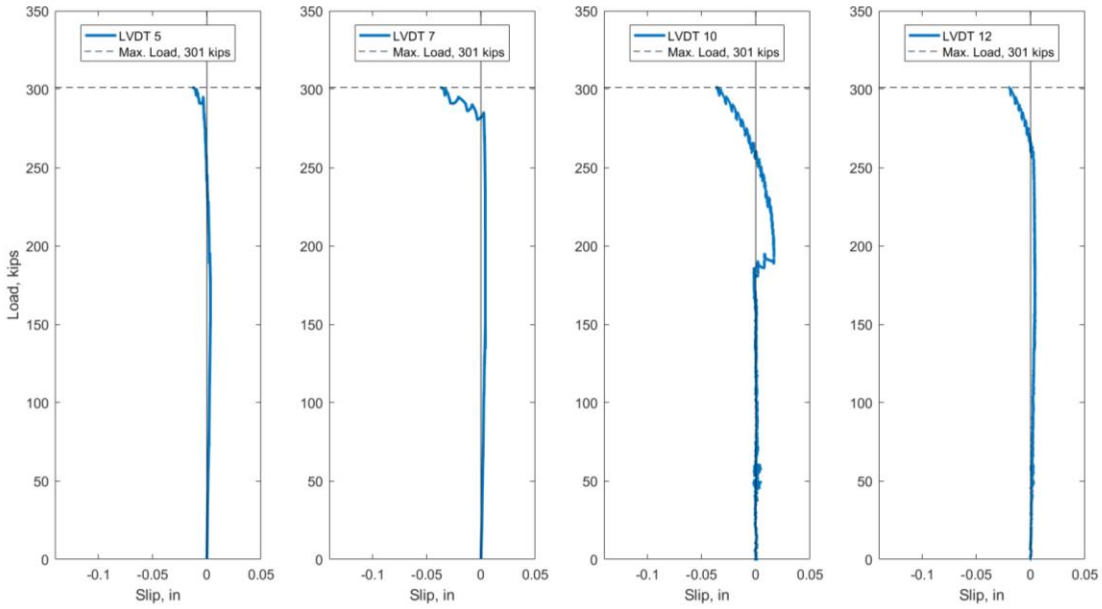

Figure 54: Strand slip for test C2

Originally, this test was described as compression-shear, but it could also be described as flexural-shear. Either way, the large shear cracks influenced the failure, and the final capacity was reached when the compression capacity of the deck was reached.

3.4.4 Summary of Full-Scale Tests

Table 14 contains a summary of the results of the full-scale shear tests. These results will be discussed again when compared with the calculated capacities for each test and when evaluating the performance of the girders in relation to their age in the next section.

Table 14: Summary of full-scale shear test results

Property/Result	A1	A2	C1	C2
a/d	2.5	2	3	3.83
Span (ft)	18.75	19	25	28
$P_{cracking}$ (kips)	170	190	160	150
$V_{cracking}$ (kips)	107	133	103	88
$M_{cracking}$ (kip-ft)	775	761	904	1,030
P_{slip} (kips)	255	N/A	250	N/A
V_{slip} (kips)	156	N/A	161	N/A
M_{slip} (kip-ft)	1,129	N/A	1,413	N/A
P_{max} (kips)	260	290	318	301
V_{max} (kips)	155	193	204	179
M_{max} (kip-ft)	1,162	1,197	1,832	2,040
Failure Mode	Bond-Shear	Flexural (strand rupture)	Bond-Shear	Compression-Shear

3.4.5 Comparison of Full-Scale Results to Code

Results from the four girder tests were compared to the ACI method (ACI Committee 318, 2014), the AASHTO LRFD simplified procedure (AASHTO-SIMP), the AASHTO LRFD MCFT procedure using beta-theta equations (MCFT-EQN), the AASHTO LRFD MCFT using the beta-theta tables (MCFT-TAB) (AASHTO, 2015), and the 1973 AASHTO Standard Specifications (1973-STD) (AASHTO, 1973). For this work, M_{max} in the equations was determined based on the expected flexural capacity of the section using strain compatibility. The value of M_{cre} was determined using estimated effective prestress forces and including the dead load from the remaining deck. The code versus experimental capacities for all tests are shown in Figure 55 with each bar indicating capacity broken into portions representing the concrete contribution and steel contribution. All expected capacities are nominal; no strength reduction factors are included. The equations compared here do not take into account D-region behavior, which may affect their accuracy especially for tests A1 and A2.

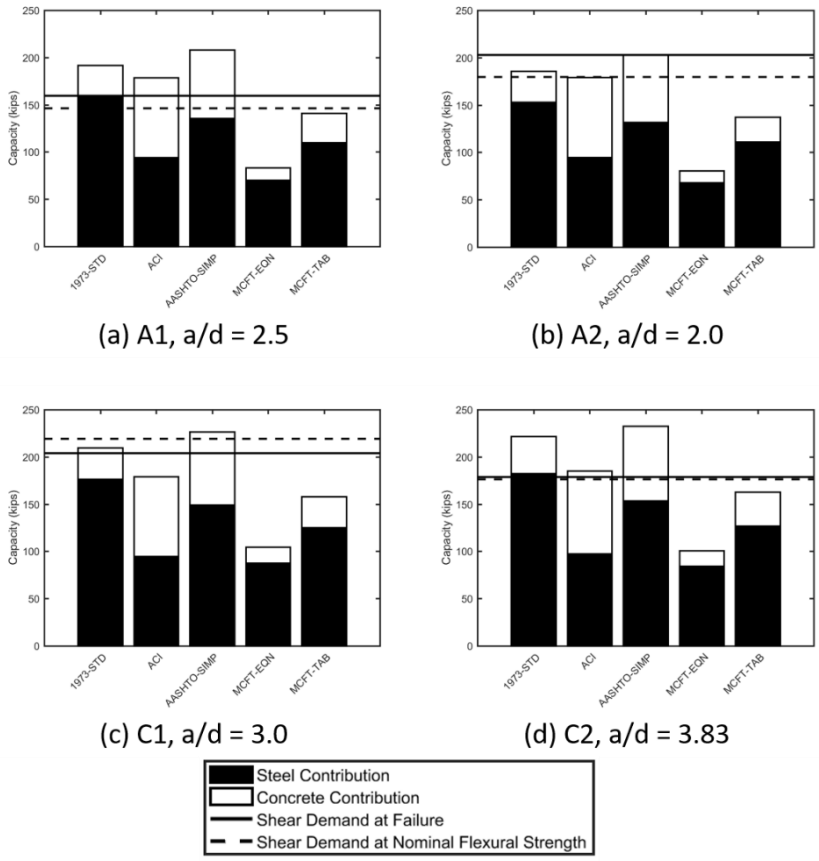

Figure 55: Code vs. experimental capacity comparisons

In Figure 55 there is a general trend that the MCFT-EQN and MCFT-TAB methods give estimates of strength less than experimental values for each location tested. In the case of the MCFT-EQN method, the estimate was conservative by a factor (experimental ultimate shear/predicted ultimate shear) of 1.8 to 2.5. The MCFT-TAB methodology was slightly less conservative, with factors between 1.10 and 1.47. The MCFT-EQN was developed as a simplification of the MCFT-TAB method, and was reported by its developers to be more conservative (Bentz et al., 2006). Both of these methods also predict a low concrete contribution to shear strength. The concrete contribution to shear strength is influenced by the factor β, which differs between the MCFT-TAB and MCFT-EQN methods. In all cases, the MCFT-EQN method provided

a low capacity and predicted a large shear crack angle (~50 degrees), limiting the capacity contribution from the stirrups. The equation for the shear crack angle is based on the strain at the level of the tension reinforcement; in the cases considered, the applied moment increased the strain, resulting in a reduced capacity. The moment was relatively high because the girder had to be supported near the center to facilitate testing both ends, increasing the applied moment for a given shear demand. The MCFT-TAB method produced a more reasonable prediction of shear crack angles than the MCFT-EQN.

The other shear equations were occasionally un-conservative. For test A1, the 1973-STD, ACI, and AASHTO-SIMP were all un-conservative, over predicting capacity by factors of 1.20, 1.12, and 1.31 respectively. During test A1, there was a loss of bond due to shear cracking and possibly due to corrosion. This test can be characterized as a bond-shear failure. Based on strain compatibility, the flexural capacity of the section should have been reached at an applied load of 239 kips, less than the 260 kips applied load at failure. In this case, the capacity of the section was estimated conservatively by strain compatibility, even when bond was lost due to shear cracking. One could argue that the estimated force to fail the section was conservative based on moment capacity determined by strain compatibility, but the shear equations failed to predict a loss of bond due to shear cracking, which is potentially un-conservative. Some of the inaccuracies of the shear capacity methods may be due to D-region behavior not accounted for in these methods.

During test A2, prestressing strands near the load point ruptured, indicating a flexural failure. The flexural capacity of the section based on strain compatibility was

exceeded during the test. The extent of shear cracking indicates that the girder maintained adequate ductility and load carrying ability during the test. At the failure load, all shear capacity calculations were conservative.

Test C1 resulted in a bond-shear failure with shear cracks entering the zone of prestress transfer and reducing the capacity of the section. The code methods were conservative with the exception of the AASHTO-SIMP, which indicated a capacity 11% higher than the experimental value. The flexural capacity was not reached in this case, so the unconservative value of the AASHTO-SIMP would be governing for this case. On the other hand, if MCFT was used to estimate the shear capacity, the section would be adequate.

Test C2 was performed at the quarter-point, the critical location for shear per the 1973 AASHTO LRFD code. In this case, the applied load exceeded the flexural capacity as calculated by strain compatibility. The code equations were conservative with the exception of the 1973-STD and 2012-SIMP which produced predictions 24% and 30% higher than the experimental values, respectively.

Calculated shear capacities were normalized by the actual measured shear capacity to compare the accuracy of the different methods. Not considering test A2, which can be characterized as a flexural failure, the normalized capacities were averaged to determine how accurate each method was in general. The results of this analysis are shown in Table 15, where a number greater than 1.0 indicates that the code method over-predicted capacity and a number less than 1.0 indicates a conservative prediction. Coefficients of variation (COV) are given to indicate the variability of the methods. It is understood that this is a limited sample size (3 tests) to indicate a COV,

and it is not included here to represent the general variability of the methods. The COV was included as an indication of how varied these methods were compared to the experimental capacities for the sections tested here. The MCFT-EQN method is by far the most conservative, followed by the MCFT-TAB method. The ACI and MCFT-TAB methods provided the most accurate results in this study. The 1973-STD and AASHTO-SIMP methods were generally un-conservative for these cases. It is important to note that although this dissertation primarily compares observed capacities to predicted shear capacities, these failures may not be entirely due to shear, with flexure or bond-loss contributing to the failure.

Table 15: Normalized capacities for various code methods

Method	Average Normalized Capacity	Coefficient of Variation
1973-STD	1.16	9.83%
ACI	1.01	12.1%
AASHTO-SIMP	1.24	8.93%
MCFT-EQN	0.533	5.01%
MCFT-TAB	0.857	8.44%

Finally, the experimental capacities were compared to the demands from the current AASHTO LRFD specifications. These comparisons are shown in Figure 56 and Figure 57. The lines in the figures represent the demands on an interior and exterior girder of the given bridge (I-244A or I-244C). These are the live load shear demands including the impact factor (1.33 times design truck shear) and load factor (strength I factor of 1.75 times LL shear demand). The experimental capacities are not modified by any strength reductions, but these capacities are much higher than the corresponding demands for every case tested. The dead load demands from the deck of the bridge are not included here. On average, the factored LL demands were 53% of the measured

capacity for interior girders, and 62% of the capacity for exterior girders. The tabulated demands for both bridges are given in Appendix D.

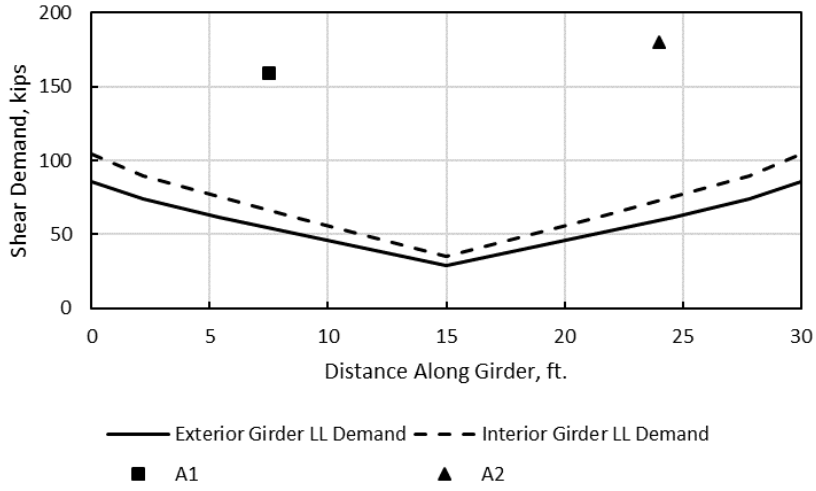

Figure 56: Shear demand versus experimental capacity, girder A

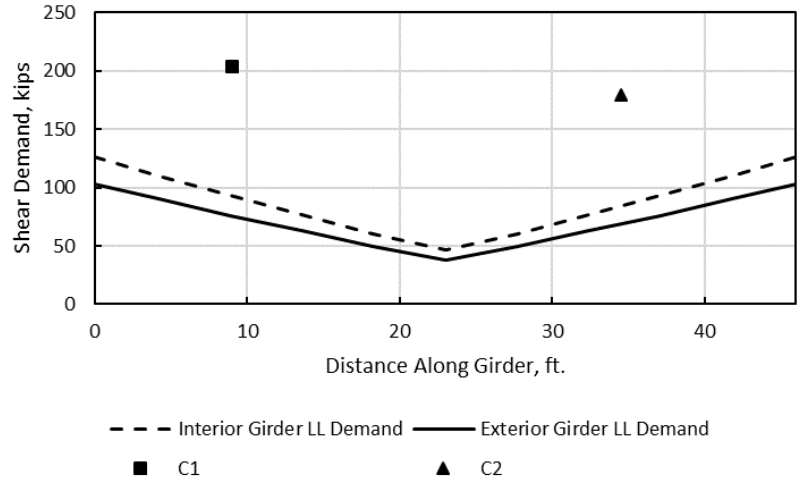

Figure 57: Shear demand versus experimental capacity, girder C

Tests A1 and A2 were performed at an *a/d* ratio of 2.5 and 2.0, respectively. In particular, A2 was performed at the border of the D-region of the girder (test A2 resulted in a flexural failure). Because of this, the code shear methods (developed for B-

regions) may not be as applicable to these tests. Strut and tie models and other methods designed for D-region behavior for these tests can be found in Cranor (2015).

3.5 Discussion of Full-Scale Tests

The goal of the full-scale testing was to evaluate the residual performance of the girders, paying specific attention to the effects of corrosion at the ends, shear capacity and behavior, and the effects of the composite deck and diaphragms. Because there are few examples of full-scale tests of older bridge girders in shear, this discussion can add to the limited literature on girders constructed during the same time period.

3.5.1 Effects of Corrosion on Shear Capacity

When the girders were received, they had visible corrosion of the prestressing strands at the ends that appeared to be at a similar level to what is commonly seen in bridges constructed in the 1960s and 70s (Mayhorn, 2016). Because these girders came from an urban area, they were occasionally exposed to deicing chemicals. One goal for the full-scale tests was to evaluate the effects of this end region corrosion on shear and bond behavior in these girders. As noted in Section 3.4, strand slip was measured in two of the full-scale tests, A1 and C1. These tests were categorized as bond-shear type failures. In the other tests (A2 and C2), the transfer and development length behavior of the strands was not an issue; therefore, it appears the corrosion had no effect on the flexural or shear strengths. In tests A1 and C1 it is possible that cracking caused by corrosion at the ends affected the anchorage behavior of the strands. During both tests A1 and C1, flexure shear cracking entered the development length and led to strand slip and horizontal cracking in the bottom flange that is indicative of loss of bond. Once bond is lost, the shear capacity of the section is either reduced or load must be carried in

a different way. Shear steel likely began carrying more of the shear force as the strands slipped.

Load versus deflection data was not available for test A1 due to a data acquisition error, but from visual observation during the test, there appeared to be sufficient ductility even after the strands slipped. A large amount of shear cracking occurred throughout the test. Comparing the experimental capacity to the code estimated capacities gives conflicting results. The 1973 Standard specifications overestimate the shear capacity, as do the ACI and AASHTO simplified procedures. On the other hand, the section reached its full flexural capacity, and the MCFT methods are conservative with regards to shear strength. MCFT appeared to be the most accurate method surveyed for test A1, and it has been shown to be accurate for a wide variety of concrete sections (Vecchio & Collins, 1986). Because of the section's adequacy based on MCFT and strain compatibility for flexure, the capacity of the section appears to be relatively unaffected by the corrosion at the end, even if it affected the failure mechanism.

Test C1 was the other load test where strand slip was measured. Cracking due to corrosion was somewhat severe at this end, and at early load steps pre-existing cracks affected the bearing of the girder. At a load of 90 kips, a significant increase in cracking and spalling had occurred due to these initial cracks. It is possible that real-world traffic could apply a similar level of shear at the end of the span (girder demand discussed further in this section). Bearing issues therefore may be of concern where visible cracking due to corrosion is observed in older girders. Despite these bearing issues, the girder continued to carry load, up to an ultimate capacity of 318 kips. Ductile load-

deflection behavior was observed, as shown in Figure 45, although there is not a region of plastic deformation typical of a flexural failure. Still, plenty of warning of the ultimate capacity was present including large amounts of cracking and deflection of 2 in. When comparing the measured capacity to the estimated capacities, the shear capacity methods are generally more conservative as compared to test A1. The 1973 Standard and AASHTO simplified shear methods overestimated capacity. Unlike test A1, the section did not reach its full flexural capacity as calculated by strain compatibility. In this case, the AASHTO simplified method was not a conservative method for calculating the residual capacity of older girders, particularly where corrosion is apparent. Similar to test A1, the MCFT methods are both conservative for test C1. It is recommended that engineers making capacity estimations for older girders use either of the more conservative MCFT methods. In general, all the tests showed good shear resistance, despite their age. MCFT was found to be the best method for calculating shear strength for these sections, as summarized in Section 3.4.5.

3.5.2 Behavior of Deck During Shear Tests

Another question approached during this work was the behavior of the composite deck during the tests. Test C2 seems to show that the composite deck, if designed correctly, is capable of carrying a large amount of compression force as evidenced by buckling of the steel during this test. Strain gauges confirmed that the strain carried by the deck decreases further from the load point due to shear lag in the deck, as expected. A common finding in all tests was the failure of the wearing surface. In older decks where the driving surface has been replaced with an overlay, the ultimate capacity of the compression zone will be limited by this overlay. Failures observed

during this research all included delamination of this surface. If possible, it would be better to design decks such that overlays are not needed. If more sacrificial deck concrete were included to be ground down as needed, overlays would not be necessary. Having said this, the overlay was always the last component to fail, and so this capacity is only needed at ultimate loads. As a conservative assumption, it is reasonable to ignore any additional capacity provided by overlays.

3.5.3 Effects of Diaphragms on Shear Performance of Girders

The presence of partial diaphragms did not appear to affect the behavior of girder C compared to girder A. There was one web shear crack that appeared to pass through the hole that the diaphragm rod passes through at the middle diaphragm. This crack was located at the center diaphragm, close to the support carrying the smallest shear force, so it did not affect the ultimate behavior. It does however appear in an orientation opposite the direction of expected tensile stresses. It is possible that the diaphragm rod near the bottom of the center diaphragm caused an upward force at this location due to differential deformation between the diaphragm and the girder. This could cause the cracking pattern visible in Figure 58. Again, this behavior did not appear to affect the capacity of the section. Typically, the center diaphragm would be subject to higher moment and lower shear, so this behavior may apply more to bridges with multiple intermediate diaphragms.

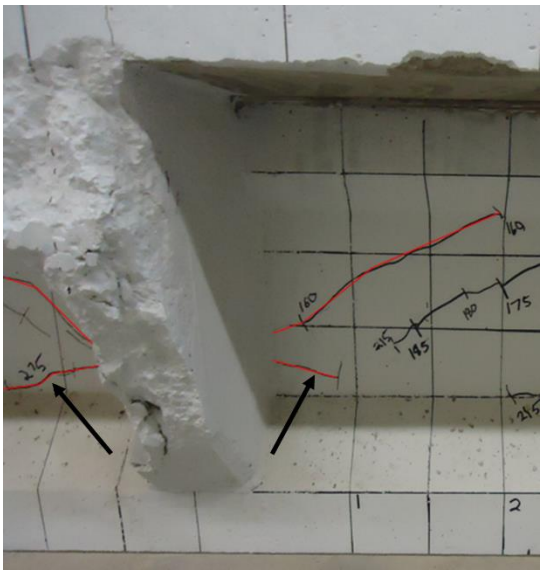

Figure 58: Cracking at center diaphragm of girder C (arrows indicate cracks potentially caused by diaphragm connection)

3.5.4 Shear Tests Compared to Shears Demands in Bridge

Another consideration from the full-scale girder tests is comparing the applied shear to the code DFs. In other words, what loads would have to be applied to a full-scale bridge to incur the same shear forces that caused the girders in question to fail? Considering Table 14, the applied shears for girder A were 159 kips and 180 kips. For girder C, the applied shears at failure were 204 kips and 179 kips. Table 16 compares the applied shears from the full-scale tests with the shears for beam line analysis and the "experimental rating factor" that would correspond to this level of shear. The "Exp. beam line shear" is the applied shear from the test divided by the DFs, resulting in the shear that would need to be applied to a bridge to reach this demand in the girder. The actual demand is the demand on the girder based on HL-93 loads and the given DF at the location of that test. The so-called experimental rating factor is the beam line shear (experimental capacity) divided by the HL-93 shear demand. This would be similar to

the rating factors discussed later but without any probabilistic factors included. Assuming the AASHTO or grillage DFs, the applied shear on a bridge system would have to increase greatly to achieve the same amount of shear witnessed in the girder tests. These factors provide an idea of the factor of safety of the bridges under the HL-93 load with respect to the applied shears in all the full-scale tests (with no impact or load factors included).

Table 16: Maximum applied shear in full-scale tests compared with applied shear in bridge

		A1		A2		C1		C2	
		Int.	**Ext.**	**Int.**	**Ext.**	**Int.**	**Ext.**	**Int.**	**Ext.**
	$V_{max,exp.}$ ***(kips)***	159		180		204		179	
DFs	*AASHTO*	0.791	0.649	0.791	0.649	0.791	0.649	0.791	0.649
	Grillage	0.688	0.497	0.688	0.497	0.657	0.513	0.657	0.513
Exp. beam line shear (kips)	*AASHTO*	201	245	228	277	258	314	226	276
	Grillage	231	320	262	362	310	398	272	349
Actual Demand (kips)	*AASHTO*	29.5	24.2	32.4	26.6	41.5	34.1	37.6	30.8
	Grillage	25.6	18.5	28.2	20.4	34.5	27.0	31.2	24.4
Experimental RF	*AASHTO*	5.39	6.57	5.55	6.76	4.91	5.98	4.76	5.80
	Grillage	6.20	8.57	6.38	8.82	5.91	7.57	5.73	7.34

Figure 59 and Figure 60 show the shear from the full-scale girder tests compared to beam line shears and demands for these cases. Beam line shear refers to the Exp. beam line shear in Table 16. The actual demands are the demands on the bridge using beam line analysis after the DFs are applied. In both figures, it is clear that the demands on the girders based on the AASHTO and grillage DFs are far less than the experimental capacities. Note that these figures do not include impact factors, load factors, or strength reduction factors.

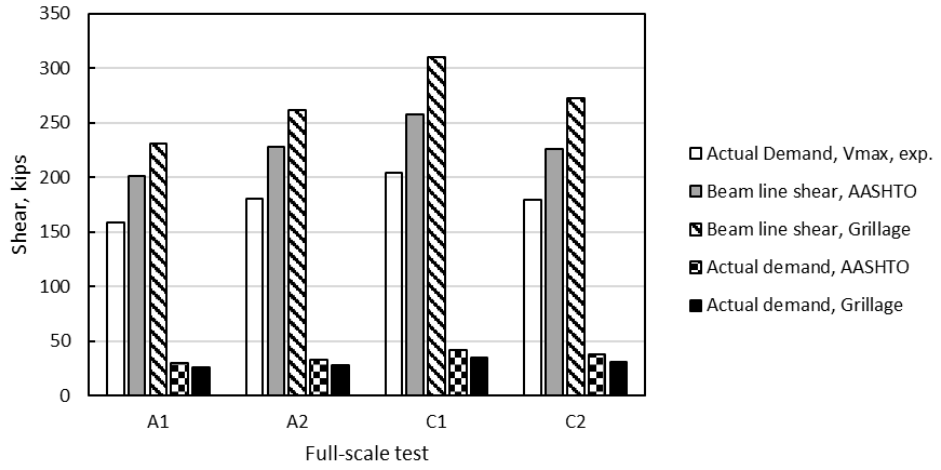

Figure 59: Girder demands for full-scale tests assuming interior girder

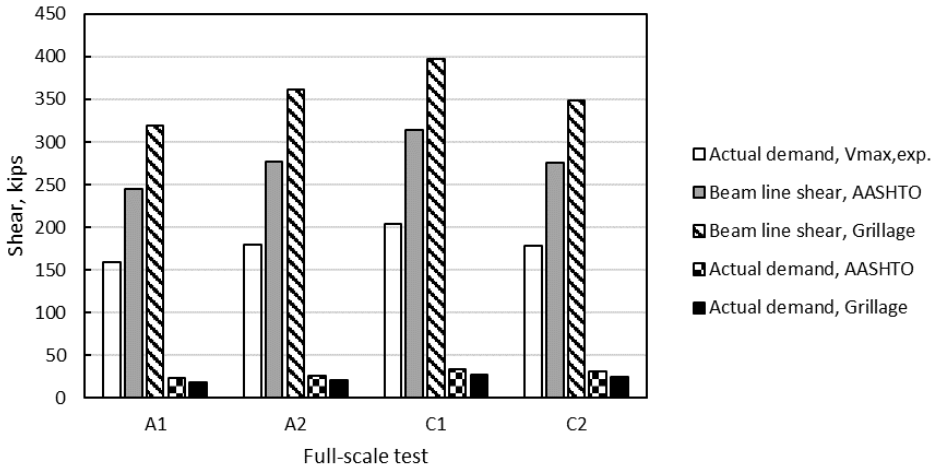

Figure 60: Girder demands for full-scale tests assuming exterior girder

Another question raised from the full-scale tests was the bearing issue reported in test C2. Using the methods above, what kind of loading would need to be applied to a bridge like the one from which girder C was taken to result in a similar support reaction (with potential to cause damage)? Bearing damage was observed between 90 and 110 kips of load, resulting in a roughly 54 to 66 kip reaction at the support. In the I-244 span from which girder C was taken, this level of support reaction could be achieved with a shear demand on the bridge as low as 82 kips for an interior girder. Between the girder

end and 4.2 ft into the span ($1/10^{th}$ span point), this level of shear is exceeded by the unfactored demands based on the HL-93 load (see Appendix D). It is therefore possible that at these potentially common levels of corrosion, traffic loads can cause concrete to spall at the ends, revealing more steel to harmful environmental conditions. This is a serviceability concern for these older bridges, especially for longer spans where reactions are larger. Despite this damage due to corrosion cracking at the ends, the girders are still capable of reaching capacities indicated by either strain compatibility or MCFT.

Chapter 4: Scale Girder Testing

4.1 Scale Section Test Methods

4.1.1 Overview

Eight approximately half-scale prestressed girders designed to mimic the configurations of girder A and girder C were cast to provide additional information on the behavior of the composite bridge section compared to the individual girders. Shear tests were conducted on individual girder specimens with a composite deck section matching the girder A and girder C configurations, and a scaled bridge section consisting of four girder lines with a composite deck cast atop all girders including end and middle diaphragms was constructed and tested. All girders were simply supported at the ends with a single point load applied directly over the girder web for destructive shear testing similar to the tests of girder A and girder C. The composite bridge section was tested using a specially built load frame on the Fears Lab strong floor as it was too wide for the typical load frames. Elastic tests were conducted first with the single point load applied at various locations to examine deflection and load transfer across the composite section. The elastic tests were followed by a test to failure with the single point load placed directly over the first interior girder. The individual small-scale girder tests were used to connect the behavior of individual girders to the behavior of a bridge system. The scale bridge was used to validate a modeling paradigm to be used for full-scale bridges. Scaling the girders and bridge properly is difficult for reasons explained in this chapter, limiting the comparison of these results to the full-scale girder tests.

4.1.2 Scale Girder Design and Construction

A comparative analysis of reinforcement configurations was conducted using an approximately half-scale (22.5 in. deep) AASHTO Type-II girder cross-section. Multiple reinforcement configurations were considered in order to identify a prestressing strand arrangement which would reasonably replicate the stress state in each of the two girder designs examined in the project (girder A and girder C). This process was detailed by Mayhorn (2016). Limitations on matching stresses exactly were the size of both the scale girder cross-section and the prestressing strands, which could not be scaled. A difference in in-service stresses between the actual girders and the test specimens of less than 20% was targeted in the comparative analysis. Two designs resulted, one corresponding to each original reinforcement configuration (girder A vs. girder C). While using small-diameter prestressing strands would have been ideal, the configuration of the prestressing bed hole pattern limited the prestressing reinforcement to only 0.5 in. or 0.6 in. diameter prestressing strands. The compressive stress in service was deemed to be the most important parameter for the design and priority was placed on matching this value to the original girders. The stress state of girder A could be best replicated using two 0.5 in. special prestressing strands tensioned to 186 ksi and the girder C section using two 0.6 in. prestressing strands tensioned to 202.5 ksi. In both cases the strands were located 4 in. from the bottom of the specimen. These configurations resulted in a difference in calculated compression stresses between the full-scale and small-scale designs of 0.8% and 3.1% for the girder A and girder C designs, respectively. The differences in calculated tensile stress were considerably higher, 53% and 77%. The goal was not to create a perfect scaled down version of the

original girders, but rather to emulate the design in a way that is true to the level of prestress in bridge girders from this time period.

The small-scale specimens were analyzed using the same spreadsheet devised for the full-scale girders described previously. The shear reinforcement configuration for the test specimens was scaled to represent that of the original girders based on the percentage contribution of concrete and steel to shear strength. For the original girder A and girder C configurations, concrete contributed approximately 30% of the shear strength and steel 70%. The shear reinforcement configuration of the scaled girders was then analyzed and adjusted to provide similar shear capacity and ratio of concrete contribution to steel contribution based on the chosen prestressing strand configurations. Shear reinforcement consisted of No. 3 Z-bars spaced as shown in Figure 61, which resulted in a concrete contribution to total shear strength of 26% and steel contribution of 74% for the girder A design and 19% concrete contribution and 81% steel contribution for the girder C design. While it was impossible to match the original reinforcement configuration exactly, the selected shear steel design provides reasonable agreement with the older girders. Both designs were examined at the quarter span point and d/2 from the support when calculating these shear strength ratios. Uncoated reinforcing steel was chosen to match what was used in the original girders.

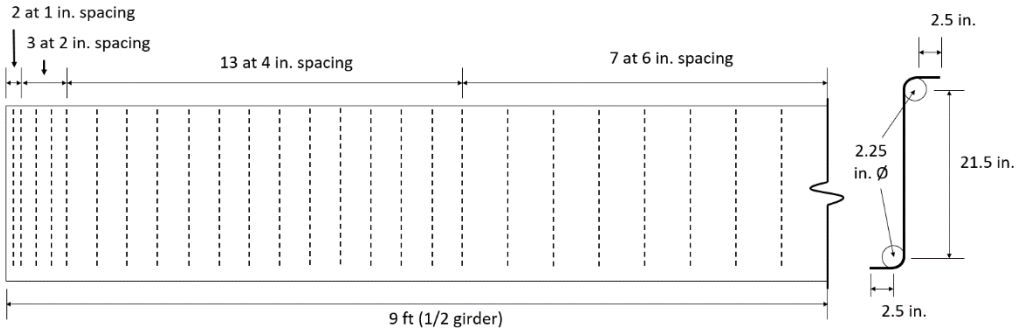

Figure 61: Shear reinforcement design for small-scale girder designs

A concrete mixture was selected based on previous work at OU, and it is shown in Table 17. It had a targeted compressive strength of 4,000 psi at one day of age and 6,000 psi at 28 days. The concrete was composed of type I cement, ¾ in. crushed limestone coarse aggregate, and river sand from Dover, Oklahoma. Wooden platforms and steel formwork sides were constructed for casting the girder specimens. The two steel prestressing abutments attached to the strong floor at Fears Lab were used for tensioning the prestressing steel and the length of the prestressing bed (40 ft) allowed for casting two girders at one time. In the days preceding each girder casting, one side of the formwork was put in place and all reinforcing steel was tied in place, as shown in Figure 62. The prestressing strands were then tensioned on the day of girder casting. Each set of two girders was cast using a single batch of concrete mixed using equipment and materials at Fears Lab. Slump, temperature, air content and unit weight were measured at the time of casting, and 4 in. by 8 in. cylinders were made for compressive strength testing at 1, 7, and 28 days of age (additional cylinders were kept and tested for modulus and compressive strength after the bridge was tested). An example of completed girder specimens is shown in Figure 63. The specimens were designated by an identifier matching the full-scale girder (A or C) that they represented, and a number,

as well as the letter *s* to indicate that these were scale. Six specimens corresponding to girder A were cast and two specimens corresponding to girder C.

Table 17: Scale girder mix design

Material	Quantity
Cement (lb/yd^3)	851
Sand (lb/yd^3)	1459
Rock (lb/yd^3)	1372
Water (lb/yd^3)	315
w/c	0.37

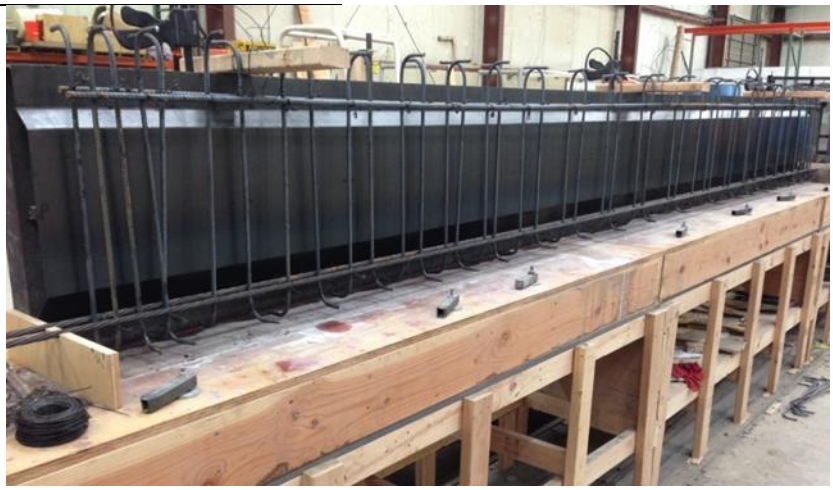

Figure 62: Reinforcing steel and formwork in place prior to casting scale girders

Figure 63: Completed scale girder before cutting prestressing strands

Tests for slump, temperature, air content (pressure method), and unit weight were performed on the fresh concrete conforming to ASTMs C1064, C143, C138, and C231 when the scale beams were cast (ASTM, 2012; ASTM, 2015; ASTM, 2017; ASTM, 2017; ASTM, 2015). Compressive strength specimens were also cast conforming to ASTM C31. Typically, concrete was mixed in the morning to prevent overheating, and ASTM standard tests were performed simultaneously with casting of girders. Companion cylinders were kept with the specimens for one day, then stored in the environmental chamber at 50 percent relative humidity and 73.4 degrees Fahrenheit. Compressive strength testing was performed based on ASTM C39 (ASTM, 2017). All cylinder ends were grinded to a plane surface perpendicular to the length of the cylinder prior to testing.

4.1.2 Additional Deck for Scale Versions of Girders A and C

After the scaled girders reached 28 days of age, a composite deck section matching the configuration of either girder A or girder C (as tested) was cast on top of two of the girders with the corresponding design. For simplicity, the small-scale replicas of girders A and C will be referred to as scale girders A and C from here on. The scale girder A design included a 4.25 in. thick deck section as wide as the top flange and the scale girder C design included a 4.25 in. thick by 23 in. wide deck section with both end and intermediate diaphragm sections as wide as the deck section. The interface shear reinforcement was provided by the top hooks of the Z-shaped shear reinforcement (as in the full-scale girders). The concrete mix design used for the deck sections and the subsequent scale bridge deck was a standard ODOT class AA mix design obtained from

Dolese Bros (Table 18 and Table 19). Overhanging formwork was constructed for the scale girder C sections and formwork the same width as the girder top flange was built for the scale girder A sections (Figure 64). All formwork was supported by the girders so that the non-composite girder cross-section would support the dead weight of the deck concrete. Concrete was placed using a bucket and the Fears Lab overhead crane. A completed scale girder C section is shown in Figure 65.

Table 18: ODOT class AA concrete requirements

Class of Concrete	Minimum Cement Content	Air Content	Maximum Water/Cement Ratio	Min. 28-day Compressive Strength
AA	611 lb/yd^3	6.5±1.5%	0.44	4,000 psi

Table 19: Class AA concrete delivered for scale bridge decks

Material	Amount
Cement	470 lb/yd^3
Fly Ash	118 lb/yd^3
Rock	1851 lb/yd^3
Sand	1330 lb/yd^3
Water	184 lb/yd^3
Air Entraining Agent	5.34 oz/yd^3
Water Reducing Admixture	17.6 oz/yd^3

Figure 64: Girder C replica formwork (a) and girder A replicas with fresh concrete (b)

Figure 65: Completed girder C replica showing deck overhang as well as end and intermediate diaphragms

4.1.3 Individual Scale Girder Shear Test Procedures

Each individual scale girder section was tested in shear with a single point load at locations intended to provide similar configurations to full-scale girders A and C and to limit the effects of bond loss on the shear tests due to the large diameter of the prestressing strands compared to the section size. The load testing arrangement used for

each specimen is shown in Figure 66. The load location was varied in these tests to match *a/d* ratios from the full-scale tests. Applied load was measured using a 100 kip capacity load cell placed beneath the load point, deflection was measured using two wire potentiometers placed beneath the load point, and LVDTs were placed on the strands at both ends to monitor any strand slip during the tests. A BDI strain gauge was placed on the bottom flange under the load point to measure the tensile strain during loading. Load was applied in 5 kip increments until cracking occurred, and at 2 kip increments after cracking. Cracks were marked on the west side of the girder after each load increment. The girders were simply supported on steel rollers and load was applied through a steel plate placed on a bed of sand to limit the effect of imperfections in the girder surface. In all tests, the supports were placed 4 in. from each end for a total span length of 17 ft 4 in.

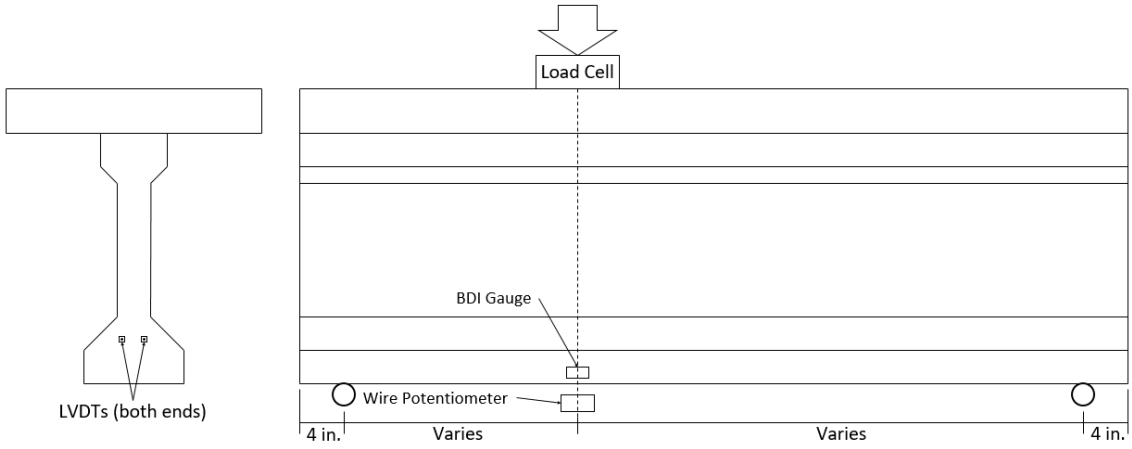

Figure 66: Scale section test setup

4.1.4 Scale Bridge Design and Construction

An approximately half-scale composite bridge section was designed to mimic the full bridge section based on the plans provided by ODOT. It consisted of four scale

girder A design girder lines and a 4.25 in. thick deck. The bridge had a total length of 18 ft and a girder spacing of 3 ft 10 in. resulting in a total width of 13.5 ft including a 1 ft overhang. The reinforcing steel in the deck was designed to mimic the original bridge configuration and transfer the expected loads between girders. End and midspan diaphragms were included and the girders were tied together through the diaphragms using threaded rods.

The depth of the deck was selected based on the original deck dimensions. Since the original deck was 8.5 in. (with wearing surface), the scale bridge deck was 4.25 in., or half the original deck thickness. To determine the amount of steel needed for the deck, the plans for the original deck were considered in order to provide a similar arrangement of reinforcement. The original bridge contained bent bars to provide additional bending resistance in negative moment regions over the girders. However, it was decided to simply provide straight bars on the top and bottom of the deck all the way across because of the small size of the scale bridge. This means the deck was not a true replica of the full-scale bridge deck, causing potentially reduced deck stiffness. In the original bridge, flexural reinforcement in the deck consisted of #5 bars on top and bottom spaced at 10 in. on center with bent bars alternating, also at 10 in. on center. Therefore, at sections of maximum negative or positive moment, #5 bars were provided at 5 in. on center. In the direction of traffic, the original bridge contained #4 bars at 18 in. on center near the top of the deck, and additional #4 bars arranged in 8 equal spaces near the bottom of the deck centered in the middle 50% of the span between girders (see Figure 67 for clarification). Clear cover of 1 in. on the bottom and 1.5 in. on top was indicated on the plans.

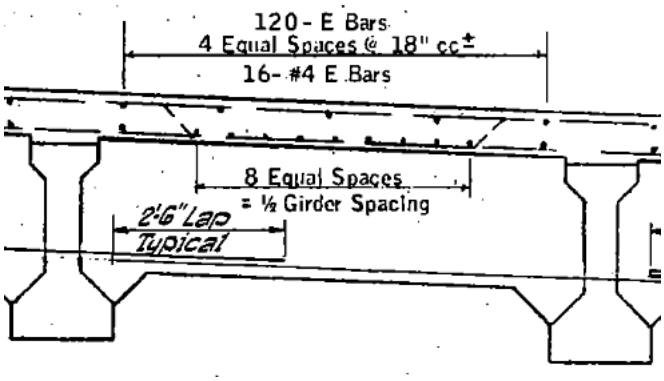

Figure 67: Longitudinal steel for original bridge deck (taken from plans provided by ODOT)

The reinforcement plan was simplified for the scale bridge in order to limit congestion of steel in the deck. In the direction of bending, #3 bars were placed at 10 in. on center at the top and the bottom of the deck. No bars were bent to simplify placement of the steel. In the direction of traffic, #3 bars were placed at 18 in. on center to resist potential temperature and shrinkage cracking (meeting ACI and AASHTO LRFD code requirements). The reinforcement ratio in the original deck with respect to flexure of the one-way slab transverse to the girder lines was 0.0073, for the scale bridge it was 0.0026 or about 35.5% of the reinforcement ratio of the original bridge. The scale bridge had proportionally less bending strength than the full-scale bridge; however, because of the way the scale bridge was loaded, this relative weakness did not come into play. The deck slab between girders was not intended to carry the primary loads applied to the bridge. Additionally, for the purposes of modeling the scale bridge section and all other bridges considered in this project, the gross section properties were used. As such, it was assumed that the level of reinforcement had a negligible influence on the elastic behavior of the bridge. The completed steel layout is shown in Figure 68. Clear cover of 0.5 in. on the bottom and 0.75 in. on top was provided, based on half the

clear cover given in the original plans. Although these dimensions are less than the requirements in Chapter 20 of the ACI Code and Section 5.12.3 in AASHTO LRFD, it was decided that having the steel proportionally in the correct location was more important to the behavior, since there was no need to be concerned about durability of the test section.

Figure 68: Scale bridge formwork showing steel in both directions

The diaphragms for the scale bridge were also designed based on the original bridge plans (Figure 69). The U bars shown in Figure 69 consisted of a U-shaped rebar with legs at the top to tie into the deck (similar to the interface steel in the girders). The L1 bar in Figure 69 is simply a straight #4 bar. At the bottom of the diaphragm there was a #8 rebar that passes through the web of each girder along the width of the girder. At the ends, this rebar was tied to an anchor rod that was attached to the exterior girders with a nut. These details were replicated in the scale bridge section. The details for the scale diaphragms are shown in Figure 70.

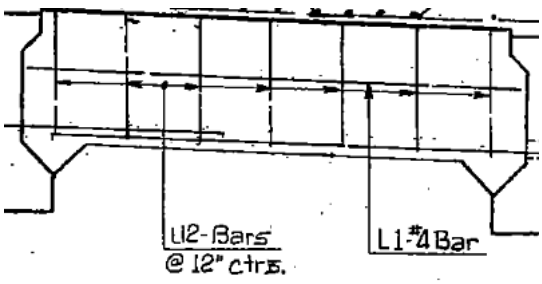

Figure 69: Diaphragm steel layout from original plans provided by ODOT

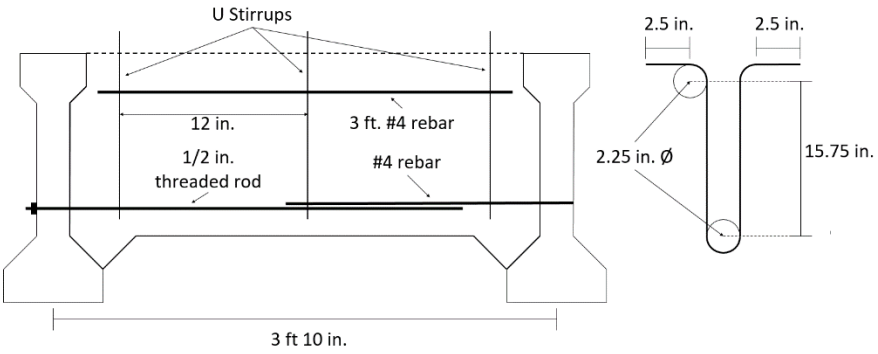

Figure 70: Scale bridge diaphragm details

The scale bridge diaphragms were connected through the girder webs to the outside girders with ½ in. threaded rods with nuts and washers attached to the exterior girders, and with a single #4 rebar passing through the interior girder webs and tied to the threaded rods at each end. Three #3 U-stirrups were spaced at 12 in. on the interior of the diaphragms, with the bent tops of the stirrups sticking out into the bridge deck. Additionally, there was a 3 ft #4 bar located near the top of the diaphragms to help hold the U stirrups in place. Holes were provided 11.5 in. from the bottom of the girders to allow the tie to pass through when the bridge was set in place (position chosen for ease of placement and to roughly match original plans from ODOT). These holes were placed 2 in. from the girder ends.

The scale bridge girders were supported on neoprene bearing pads placed on reinforced concrete block supports. Formwork was built between the girders using plywood and methods intended to mimic expected construction methods at the time the actual bridge was built (Figure 71 and Figure 72).

Figure 71: Framing for bridge deck formwork including middle diaphragm

Figure 72: Completed deck formwork showing end diaphragms and edges of deck

All formwork for the girders and diaphragms were supported by the girders alone; therefore, when concrete was poured the entire weight of the plastic concrete was carried by the girders (true to actual bridge construction). The reinforcing steel was held in place using steel rebar chairs (Figure 73 and Figure 74).

Figure 73: Bridge section with reinforcing steel

Figure 74: Close up of deck reinforcement including rebar chairs

The same class AA concrete provided by Dolese Bros. (as described in Section 4.1.3 on individual girder decks) was used for casting the deck on the bridge section. Concrete was discharged using a concrete bucket, vibrated, screeded and given a broom finish. Construction of the deck is shown in Figure 75 and the screeded and floated section is shown in Figure 76. A close up of the broom finish is shown in Figure 77. The bridge deck was cured under wet burlap and plastic for seven days, as shown in Figure 78.

Figure 75: Discharging concrete into deck forms, screeding operation visible on left of photo

Figure 76: Bridge after screeding and floating

Figure 77: Broom finish

Figure 78: Plastic covering wet burlap laid on the bridge deck while curing

Water was added to the wet burlap under the plastic on the bridge deck daily for the duration of curing. Companion cylinders were kept under the bridge for one day, then demolded and stored in an environmental chamber at 50% relative humidity and 73.4 degrees Fahrenheit.

A specially designed steel frame was built over the scale bridge section as the frames already available at Fears Lab were too narrow. The frame and completed bridge is shown in Figure 79. This frame was selected over the initial idea of using single anchors to the strong floor and a spreader beam as it allowed more flexibility in elastically loading the bridge specimen. The custom-built load frame consisted of W10x39 sections as tension columns attached to the strong floor with a W21x122 beam spanning the width of the bridge. The frame was designed to support a 200 kip point load at any location along the scale bridge section width.

Figure 79: Load frame as installed over bridge and completed bridge after curing

4.1.5 Scale Bridge Testing

A series of elastic tests were performed on the scale bridge to gather deflection and strain information at several locations on the bridge before destructive testing was performed. In order to avoid cracking, a maximum load of 20 kips was selected for load points over the girders (based on the individual scale girder tests). For the tests where load was placed in the center of the slab, loads were kept under 1 kip to be sure no

cracking was caused. Load was placed at the quarter span point for every elastic test. In the transverse direction load was applied above the exterior and interior girder, and over the exterior and interior slab (at the center of the slab span). Loading locations are shown in Figure 80.

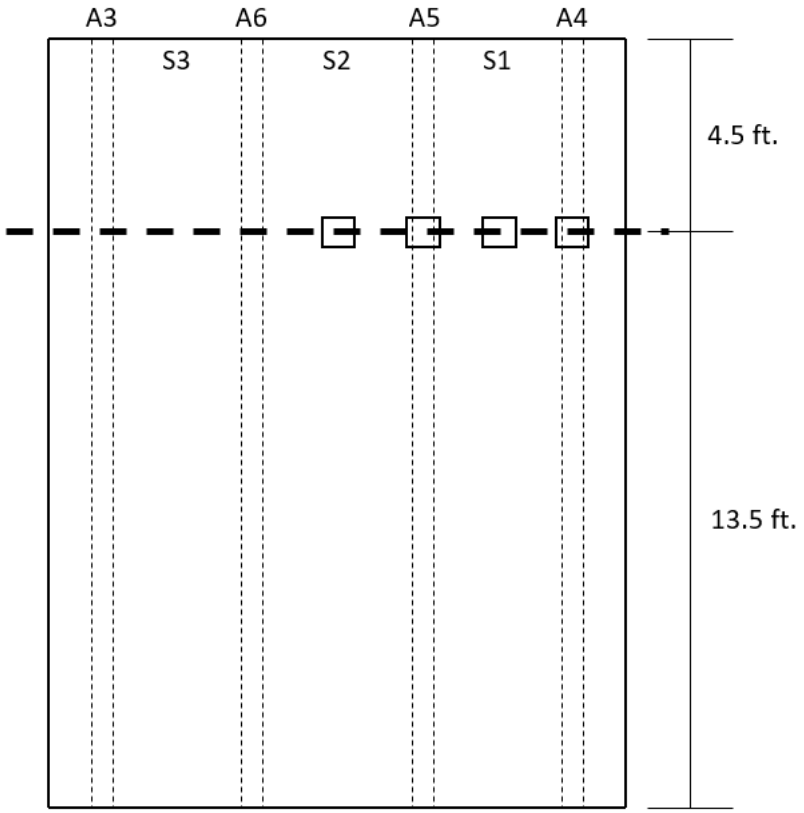

Figure 80: Bridge elastic test locations, squares indicate load points. The letter "S" indicates slab test locations, and the letters "A" indicate girder names.

For tests with load placed over girders A4 and A5, deflections and strains were collected. Because of the small magnitude of the loads and resulting deflections in the elastic tests, it was not possible to collect deflection information using wire pots (a linear response could not be achieved) due to signal noise from the sensors. For this reason, LVDTs were used for deflection at the load point and deflection of the bearing pads. For each load case, a series of tests was performed to collect deflection data under

every girder. Instrument limitations prevented gathering deflection data for all girders at once; therefore, the deflections of two girders could be monitored during one test. At least one set of sensors (associated with one girder) remained between tests at the same load location to ensure that the responses were adequately similar between tests. BDI gauges were used to collect strain data. The very small responses in the tests meant that only three BDI gauges could be used at once. The response of the BDI gauges proved too noisy unless connected to the NI 9219 module, which only had three available connections for the gauges. During the tests with the load over the slab spans, deflections were not measured because of their small magnitude and the small magnitude of the resulting deflections.

Deflections were measured by placing an LVDT under the load point such that the downward deflection of the bottom of the girders caused the LVDT to retract. Girder strains were measured by attaching BDI gauges on the underside of the girder flanges at the load point of each girder (quarter-point). Middle and end diaphragm strains were taken by attaching the gauges to the bottom of the center of the diaphragms (Figure 81). The diaphragms between each girder were instrumented in this manner. Slab strains were measured two ways, when the load point was above the girders, BDI gauges were glued to the center of the slab spans to measure strains transverse to the girder span direction. When the load point was in the middle of the slab span, strains were measured underneath the slab at the load point. More examples of the instrumentation are shown in Appendix A.

Figure 81: BDI gauge attached to center of end diaphragm

When load was placed over the girders (tests A4 and A5), deflections under the load point, deflections at the supports, diaphragm strains, slab strains, and girder strains were recorded. When load was placed over the slab spans (S1 and S2), strains at the diaphragms, slabs, and girders were measured. Deflections were not measured for the slab tests since the loads were too low to provide good response from the LVDTs.

Generally, multiple elastic tests were performed for each configuration of instruments in order to ensure that the responses were consistent. For example, when gathering deflection data under the girders, two cycles up to 20 kips of load would be performed, then the response would be checked by plotting load-deflection curves using Matlab to ensure that the data were reasonable, then the LVDTs would be moved to take deflections of the other two girders, and the process would repeat. The load setup for tests on girder A4 is shown in Figure 82 and consisted of a swivel head to account for any accidental eccentricity, a 100 kip load cell, a 200 kip hydraulic actuator, and a 8 in. by 8 in. steel plate placed on a bed of sand. The steel plate was chosen to remain consistent with the load setup between the full-scale tests, and individual scale girder

tests. This same load setup would be moved laterally along the bridge to load different locations and was used for the destructive test as well as the elastic tests. Because of the very small loads, there was some variability in the data. This data would later be used to help verify the grillage model used for the scale bridge.

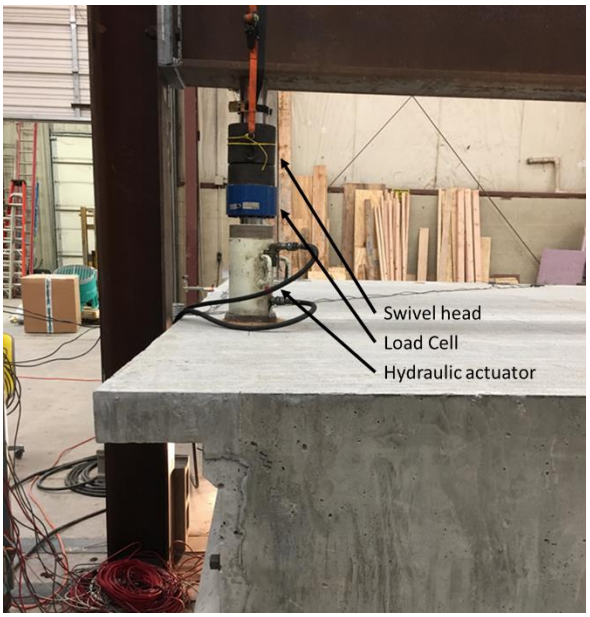

Figure 82: Load arrangement

The destructive test was performed after all elastic tests were completed, with the point load over an interior girder (A5). The use of a single point load allowed for more direct comparison between the scale bridge, individual scale girder tests, and full-scale testing. Because of issues with wire pots at lower loads, it was decided that a deflection under the girders would be monitored with both wire pots and LVDTs (Figure 83). This way LVDTs could capture small deflections accurately, then when the end of their stroke was reached, they could be removed and the wire pot data could be used. LVDTs were placed at each support to measure deflection of the bearing pads, which could be used to correct deflection measurements. Since all available LVDTs

were used to monitor deflection, dial gauges were used to monitor slip in all the strands at the end of the bridge being tested (Figure 84). These dial gauges had a limited range (0.050 in.) but were accurate to 0.0001 in., ensuring that initial stages of strand slip could be captured. Three BDI gauges were placed on the bridge, one on the diaphragm at the center of the bridge, and two on the end diaphragms on either side of the loaded girder (all on bottoms of diaphragms as in elastic tests). A summary of the instrumentation used and the locations of these instruments is given in Figure 85.

Figure 83: Underside of girders prior to destructive test showing LVDTs and wire pots used to measure deflection as well as LVDTs at the supports in the background

Figure 84: Dial gauges used to monitor strand slip

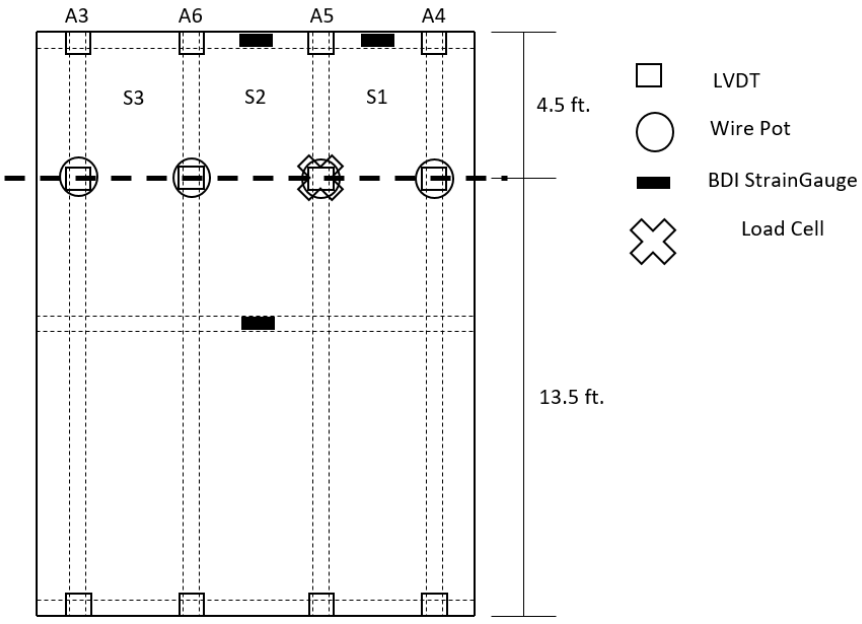

Figure 85: Instrumentation for the destructive scale bridge test

On the day of the destructive bridge test, load was applied in 5 kip increments with researchers watching for cracking after each load step. The dial gauges on the strands were also monitored after each increment so a load versus slip plot could be

created. Notes were taken about the progression of cracks at each step. Cracks were not marked until the test was completed for safety reasons since the deck prevented easy access to the girders.

4.2 Results from Scale Girder Tests

4.2.1 Scale Girder Properties

Typically, concrete was mixed in the morning to prevent overheating, and ASTM standard tests were performed simultaneously with casting of girders. The fresh concrete properties for the concrete used to cast each scale girder specimen are given in Table 20. For all girders, the fresh properties were reasonably consistent despite temperature variations between casting days.

Table 20: Fresh concrete properties for scale girders

Specimen ID	Slump (in.)	Temp. (°F)	Air (%)	Unit Weight (lb/ft^3)
A1s	9.5	65	2.6	148.6
A2s	9.5	69	2.7	147.7
A3s	9.75	72	2.3	148.4
A4s	9.0	76	2.7	147.1
A5s	9.5	80	2.3	147.3
A6s	9.0	82	2.4	147.5
C1s	9.25	79	2.8	148.0
C2s	9.75	80	2.4	148.8

Compressive strength testing was performed based on ASTM C39 (ASTM, 2017). All cylinder ends were grinded to a plane surface perpendicular to the length of the cylinder prior to testing. Compressive strength results are given in Table 21.

Table 21: Average compressive strengths at prestress release (1 day), 28 days, and after testing

Specimen ID	f'_{ci} (psi)	f'_c (psi)	$f'_{c,final}$ (psi)
A1s	4,190	6,700	7,087
A2s	4,360	6,720	6,895
A3s	4,200	6,250	6,745
A4s	4,440	6,520	6,862
A5s	4,250	5,930	6,443
A6s	4,300	6,100	6,365
C1s	4,390	5,820	6,515
C2s	4,170	5,700	6,275

Compressive strength results were generally consistent at 1 and 28 days with the exception of A1s and A2s which had higher compressive strengths than other specimens. These specimens had the lowest concrete temperature at the time of casting and potentially had more favorable curing conditions as a result. Figure 86 shows the strength gain for girders A3s and A4s (used in the scale bridge). This strength gain was typical for all scale girders. The final compressive strength tests for all specimens were performed after the girders had been tested. At this time modulus of elasticity was also measured. For most girders, these tests were performed between 265 and 287 days from casting. Figure 86 shows only marginal strength gain between 28 and 285 days, so it is likely that modulus at 28 days was similar to modulus at later age. All other compressive strengths for the scale girders can be found in Appendix B.

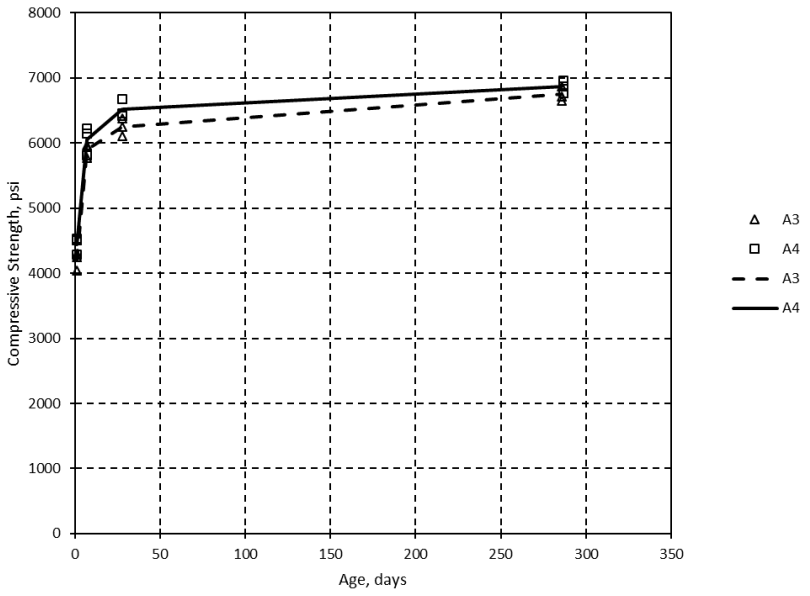

Figure 86: Typical compressive strength gain for scale girders (results from A3s and A4s shown)

Modulus of elasticity results from the scale girders are given in Table 22. Three cylinders were tested for modulus of elasticity from each scale girder, the cylinder moduli in the table are the average of the final two modulus tests on the cylinder, as given in ASTM C469 (ASTM, 2014). Again, these tests were performed after the girder specimens were tested, at between 265 and 287 days of age. The average modulus of elasticity for the girders was 4,290 ksi and the average compressive strength across all girders was 6,650 psi. The modulus of elasticity calculated using the ACI correlation of compressive strength to modulus was 4,650 ksi, 8.4% greater than the measured modulus. This is a reasonable agreement, especially considering how varied modulus measurements can be.

Table 22: Modulus of elasticity of girder concrete

	Cyl. 1 E (ksi)	Cyl. 2 E (ksi)	Cyl. 3 E (ksi)	AVG (ksi)	Std. Dev.	COV	f_c (psi)	ACI E (ksi)	% Difference
A1s	4,495	4,475	4,600	**4,525**	68	1.5%	7,090	4,800	6.1%
A2s	4,445	4,350	4,430	**4,410**	51	1.1%	6,900	4,735	7.5%
A3s	4,305	4,355	4,245	**4,300**	56	1.3%	6,750	4,685	8.9%
A4s	4,300	4,190	4,410	**4,300**	111	2.6%	6,870	4,725	9.9%
A5s	4,230	4,420	4,040	**4,230**	192	4.5%	6,450	4,580	8.2%
A6s	3,845	4,330	4,350	**4,175**	285	6.8%	6,370	4,550	9.0%
C1s	4,390	4,170	4,470	**4,345**	153	3.5%	6,520	4,600	5.0%
C2s	4,105	4,020	4,010	**4,045**	54	1.3%	6,280	4,520	11.7%

Finally, there were two deck pours for the scale girders, one for the scale individual sections and one for the scale bridge deck. One gallon of water per cubic yard was added to both mixes to improve workability on delivery. The individual specimen deck concrete fresh properties included a 4.75 in. slump after addition of water (3 in. on delivery), 4% air content, and 145.6 lb/ft^3 unit weight. The slightly low air content may be attributed to the additional water added to the mix when delivered. The scale bridge deck concrete was delivered with a 3 in. slump and had a 7 in. slump after adding water. The air content was 3% based on the second of two tests. There was an air leak of the pressure meter in the first test, so the second air content may also not be accurate. The unit weight of the scale bridge deck was 146.3 lb/ft^3. The average compressive strengths were 4,185 psi and 4,450 psi for the individual specimen decks and the scale bridge, respectively. The modulus of elasticity of the deck concrete was measured in the same way as explained for the girder concrete. The individual deck concrete had an average modulus of elasticity of 3,685 ksi and the scale bridge deck concrete had a modulus of 3,810 ksi. These moduli are reported in Appendix B, along with the compressive strength gain for the deck pours.

4.2.2 Test A1s

Test A1s was performed at an *a*/*d* ratio of 2.4, corresponding to the quarter-point of the girder similar to test C2s. This location was chosen since this was the location where the scale bridge would be tested, and because test C2s was performed at the same location. The load point was located at a distance of 54 in. from the end of the girder. Initial flexural cracking under the load point occurred at a load of 34.3 kips and 0.14 in. of deflection. This point is marked on the load-deflection plot given in Figure 87, and a drop in load occurred shortly after due to strand slip. Initial slip of roughly 0.025 in. was observed in both strands on the loaded end after cracking occurred. The strain in the bottom flange at the load point immediately prior to cracking was 251 microstrain. The measured strain reduced slightly after each new crack formed.

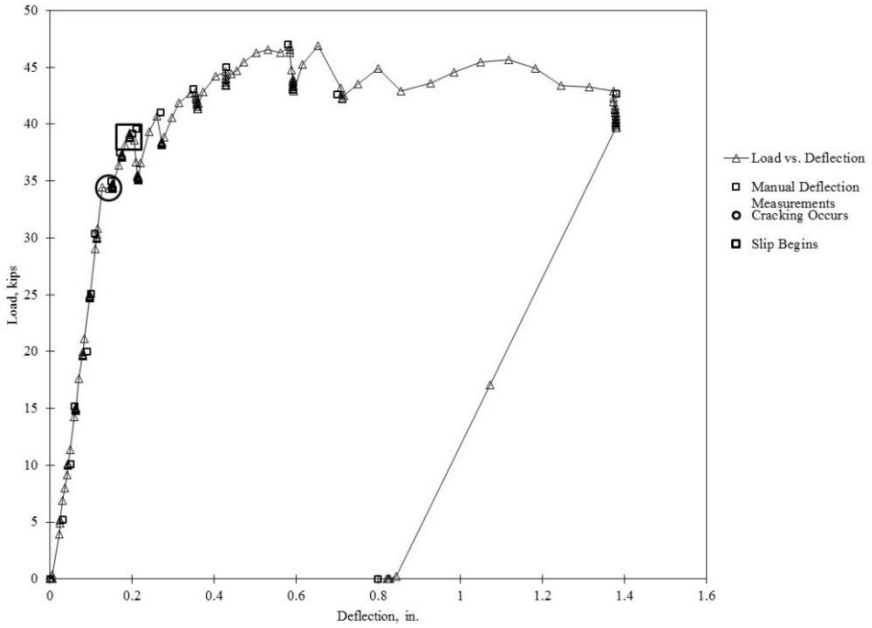

Figure 87: Load vs. deflection for test A1s

The final behavior of the girder is shown in Figure 88. Extensive shear and flexural cracking was observed, and there was some ductility observed after initial

cracking and strand slip. Crushing in the deck occurred at the final load increments. By the end of the test, a maximum slip of 0.64 and 0.66 in. was measured for the strands at the loaded end. The maximum point load for flexure at this location was 47 kips based on strain compatibility compared to a maximum load in the test of 47.8 kips. This is a difference of about 1.7 percent. This was very close to the actual load despite significant bond loss, potentially indicating that some yielding occurred. The estimated shear capacity corresponded to a point load of 80 kips by the ACI method. The MCFT methods would not converge for the small-scale sections because the resulting strains at the maximum load were outside the range of the method.

Figure 88: Test A1s cracking with initial cracks marked with red dashed lines

4.2.3 Test A2s

Test A2s was performed at an *a*/*d* ratio of 3.0, the same as for test C1s. The load point was located at a distance of 71.5 in. from the end of the girder. Initial flexural cracking under the load point occurred at a load of 26.7 kips and 0.15 in. of deflection.

This point is marked on the load-deflection plot given in Figure 89, and is located at the change in slope indicative of flexural cracking. Initial slip of only 0.004 in. was observed in both strands on the loaded end after cracking occurred. The strain before cracking was 241 microstrain at the load point. The measured strain reduced slightly after each new crack formed. Slip increased to 0.165 and 0.175 in. at the loaded end at a load of 44.8 kips; this location is noticeable on the graph when the load drops off sharply. At this load, large shear cracks formed near the end of the girder (Figure 90), and after the corresponding increase in slip, no more load could be applied.

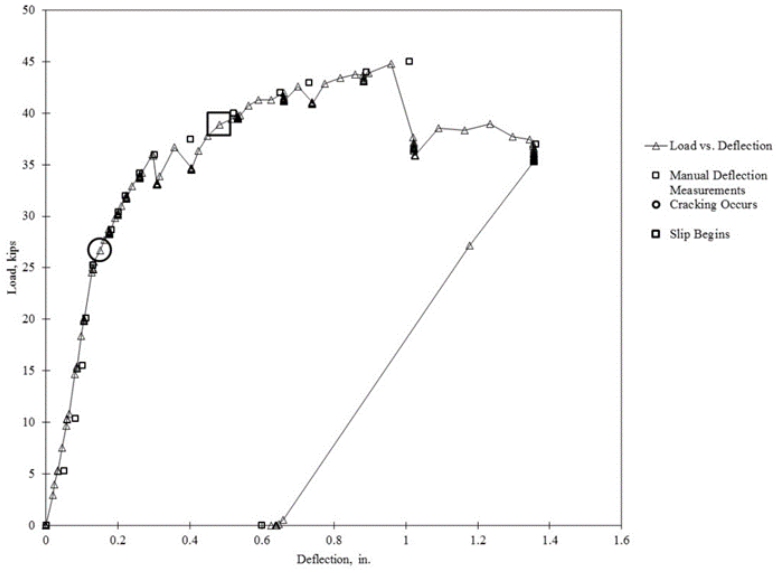

Figure 89: Load vs. deflection for test A2s

Figure 90: Cracking during test A2s, initial flexural crack (boxed) and shear cracks (circled) shown

The final cracking of the girder is shown in Figure 90. Extensive shear and flexural cracking was observed, and there was limited ductility after initial cracking. The strand slip and shear cracking at 44.8 kips reduced the load carrying ability of the girder. Crushing in the deck was not observed but some shear cracks oriented themselves horizontally near the top of the deck. By the end of the test, a maximum slip of 0.59 and 0.61 in. was measured for the strands at the loaded end. The maximum point load for flexure at this location was 42 kips based on strain compatibility compared to a maximum load in the test of 44.8 kips. This is a difference of 6.7 percent. Again, this was good agreement despite bond failure, indicating that slip potentially occurred after some strand yielding occurred. The estimated shear capacity corresponded to a point load of 71 kips by the ACI method.

4.2.4 Test C1s

Test C1s was performed at an *a/d* ratio of 3.0, corresponding to the *a/d* ratio of full-scale girder test C1. This *a/d* ratio resulted in a load point located at a distance of 71.5 in. from the end of the girder. Initially the girder was quite stiff, with only 0.13 in. of deflection when the first flexural cracking occurred at a load of 41.5 kips (Figure 91). This point is marked on the load-deflection plot given in Figure 92, and a change in slope can be noticed. This point is also corroborated by a rapid reduction in strain measured by the strain gauge north of the crack. When cracking occurred, the strain in the bottom flange was approximately 330 microstrain.

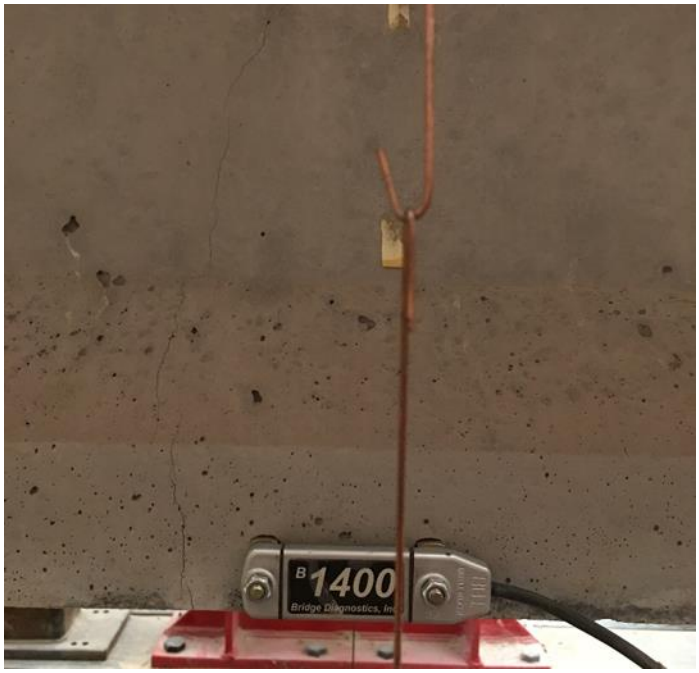

Figure 91: Initial flexural crack at 41.5 kips (load point at center of strain gauge)

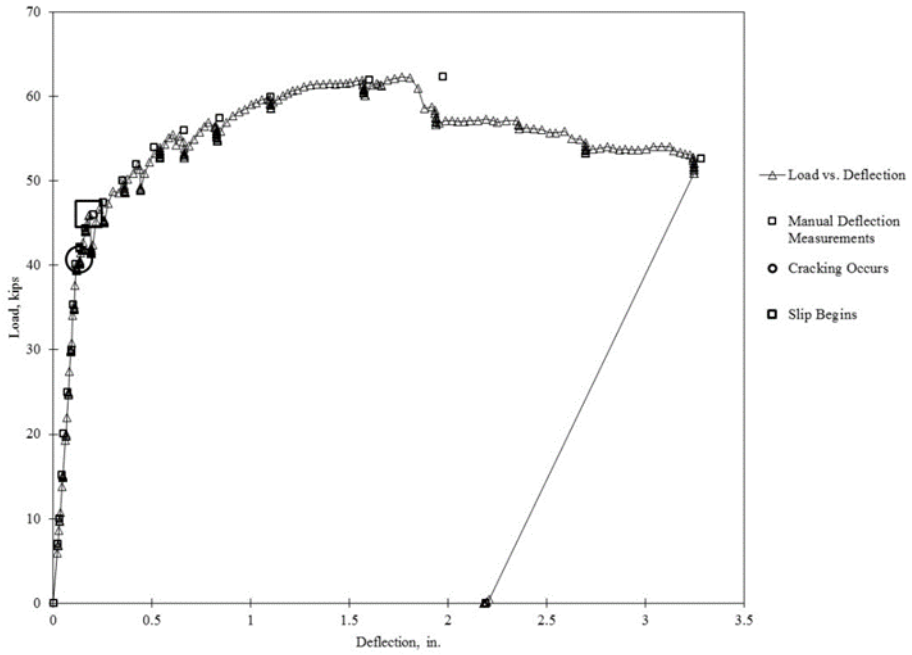

Figure 92: Load vs. deflection for test C1s

After this initial flexural crack, load was increased at 2 kip increments. At a load of 46 kips, shear cracks formed near the supports (highlighted in red dashed lines in Figure 93). The formation of these shear cracks led to strand slip of 0.02 in. for one strand on the south end of the girder. Slip increased from the point of shear cracking to the end of the test, resulting in a maximum slip of 0.52 and 0.72 in. for the strands on the loaded end. The test was continued to a maximum applied force of 62.3 kips, at which point the strand slip prevented any increase in load.

Figure 93: Test C1s cracking with initial cracks marked in red dashed lines

The flexural capacity based on strain compatibility at this section was 204.8 k-ft corresponding to a point load of 54 kips. The shear capacity using the ACI method at this section was 50.7 kips, which corresponds to a point load of 74 kips. The predicted capacity was exceeded for flexure despite the large amount of recorded slip. The partial center diaphragm appeared to arrest cracking near midspan, but it is difficult to make definite conclusions on the effect of the partial diaphragms since the tests of scaled girders without diaphragms were for a slightly different design (smaller prestress force). Differences in diaphragm construction over the years may reduce the applicability of any conclusions drawn from these tests as well.

4.2.5 Test C2s

Test C2s was performed at an *a/d* ratio of 2.4, corresponding to the quarter-point of the girder. This location was chosen since this is the location where the scale bridge would be tested and was the location of full-scale test C2. The load point was located at a distance of 54 in. from the end of the girder for this configuration. As with test C1s, little deflection was measured before cracking. A large shear crack formed at the support at a load of 40.5 kips and 0.09 in. of deflection. This point is marked on the

load-deflection plot given in Figure 94, and a reduction in load occurred due to strand slip. When this shear crack formed, slip of 0.031 and 0.037 in. was observed for the strands on the loaded end. The strain in the bottom flange at the load point before cracking was 239 microstrain. The measured strain reduced slightly after each new crack formed.

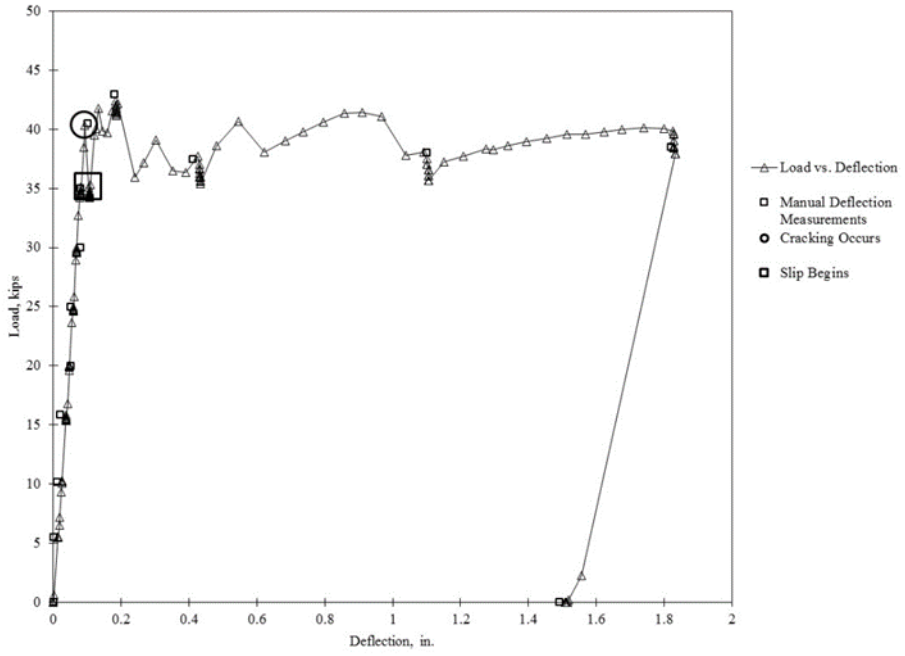

Figure 94: Load versus deflection for test C2s

Because of the proximity of the initial shear cracks to the support, slip increased with applied load after cracking, which prevented any increase in load. The maximum load reached in this test was 42.4 kips and the test was stopped when some crushing was observed in the deck. The maximum deflection was 1.83 in. The cracking pattern from this test is shown in Figure 95, with the initial cracks highlighted in red. Loss of bond between the prestressing strands and the concrete prevented the girder from reaching its estimated capacity. The girder's nominal moment capacity was 204.8 k-ft

based on strain compatibility (corresponding to a point load of 64.7 kips). The shear capacity by the ACI method was 63.2 kips corresponding to a point load of 82 kips. The capacity of the girder was reduced due to strand slip that began with initial shear cracking. Unfortunately, this slip is a limitation of the dimensions of the test specimens. Since the development length of the strands used for these specimens is roughly 92 in., the short embedment length required for this test influenced the bond behavior. Additionally, it is possible the stiffness of the end diaphragm may have influenced the test. The initial cracking occurred in shear at a very low deflection. It is possible the diaphragm contributed to the stiffness of the end region. Tests of girders A1s and A2s helped to evaluate the influence of the diaphragms on girder behavior, but again were for a slightly different girder design which reduces the applicability of the comparison. Another possibility is that the increased stiffness due to the available deck influenced the shear behavior.

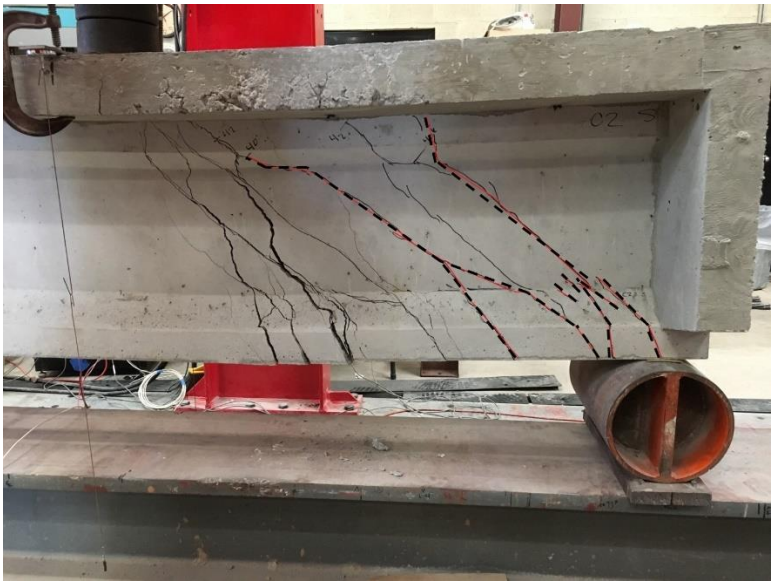

Figure 95: Test C2s cracking with initial cracks marked with red dashed lines

4.2.6 Individual Scale Girders Summary

Table 23 contains summarized information about the results of the scale girder testing. Moments and shears at cracking, slip, and failure are shown. Moments and shear include all forces acting on the specimens (self-weight, superimposed load, etc.). Failure mode in the table is based on the guidelines reported by Naji, Ross, and Floyd (2017). These tests were performed near discontinuities, potentially affecting shear behavior. Additionally, the slip in these tests affected their behavior.

Table 23: Summary of scale girder test results

Property/Result	**A1s**	**A2s**	**C1s**	**C2s**
a/*d*	2.4	3.0	3.0	2.4
Embed. L (in.)	54	71.5	71.5	54
$P_{cracking}$ (kips)	34.3	26.7	41.5	40.5
$V_{cracking}$ (kips)	26.7	18.7	28.7	31.8
$M_{cracking}$ (kip-ft)	112	101	164	134
P_{slip} (kips)	38.8	38.9	46.0	35.1
V_{slip} (kips)	30.1	27.0	31.8	27.7
M_{slip} (kip-ft)	126	154.5	182	117
P_{max} (kips)	46.8	44.8	62.3	42.4
V_{max} (kips)	36.2	31.0	42.8	33.2
M_{max} (kip-ft)	152	177	243	140
Failure Mode	Bond-Shear/Flexure	Bond-Shear	Bond-Shear	Bond-shear

4.2.7 Scale Bridge Test Results

An overview of the sensor layout for the scale bridge destructive test was shown in Figure 85. Similar to the individual scale sections, load was applied in 10 kip increments until initial cracking then load increments were reduced to 2 kips. The girder

naming convention is shown in Figure 80. Elastic test results are shown in Section 5.2.1.

Cracks were visible at the connection between the end diaphragms and girders was slightly cracked at the beginning of the test. The diaphragms were tied together with a #4 bar and lapped to threaded rods that attached with nuts to the outside girders. The concrete at these interfaces was not roughened, so there were small cracks along this interface before testing began likely due to differential shrinkage. At early load increments, these cracks expanded, indicating some bending in the diaphragms (Figure 96). Initial web shear cracking in the girder was observed at a load of 55 kips. Figure 97 shows the load versus deflection plot for the initial 60 kips of load. The initial observed crack is marked on this figure and the location where slope changed is also marked. It is likely the first crack occurred at a load closer to 43 kips, but the deck limited the visibility of cracks in the girders. The initial web shear crack is shown in Figure 98.

Figure 96: Diaphragm cracking at girder interface

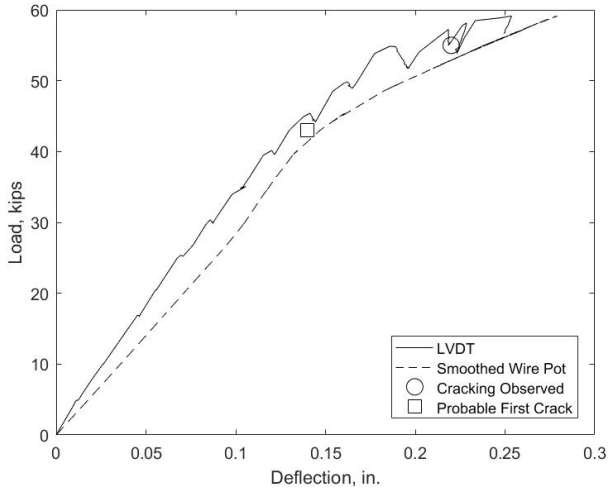

Figure 97: Initial load versus deflection for the scale bridge including locations of first visible crack and probably cracking

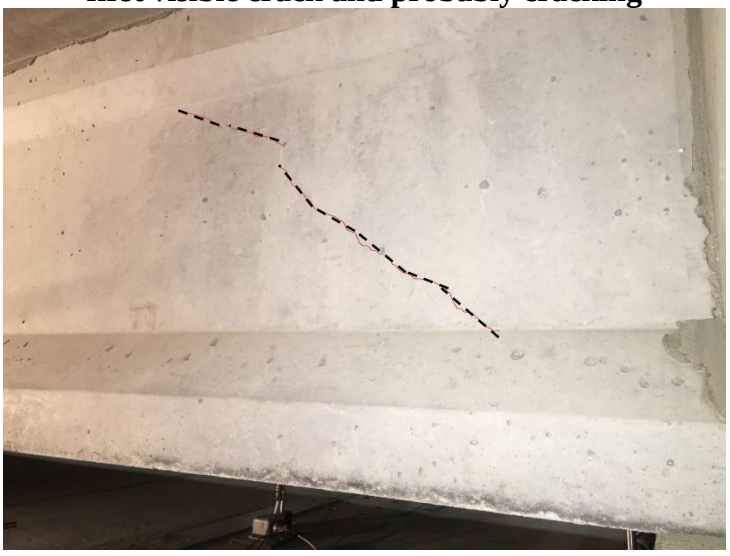

Figure 98: Initial shear crack in loaded girder (A5) outlined in red dashed lines

Shear cracks extended into the bottom flange at a load of 57 kips, and a flexural crack was observed beneath the load point at a load of 63 kips. It is very likely that this crack appeared before this load, but direct observation was difficult due to the crack's interior location. This flexural crack is shown in Figure 99. At this load, there was approximately 0.02 in. of slip in the strands of the loaded girder. Slip at the loaded girder is shown in Figure 100.

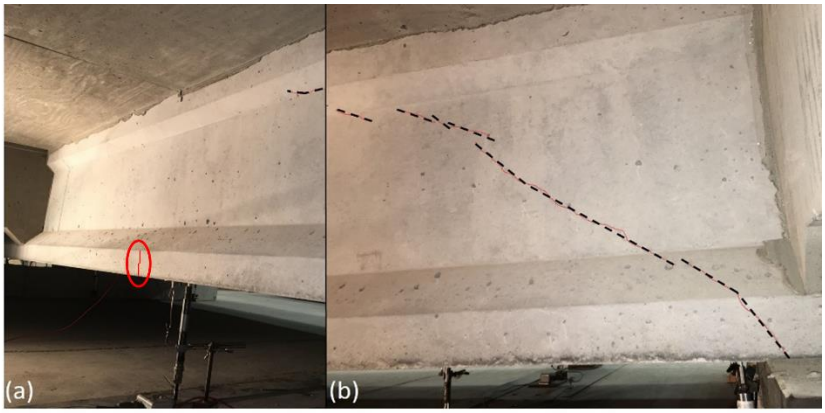

Figure 99: Cracking at 63 kips of load (a) flexural crack near midspan (circled), (b) shear crack near the support for the loaded girder

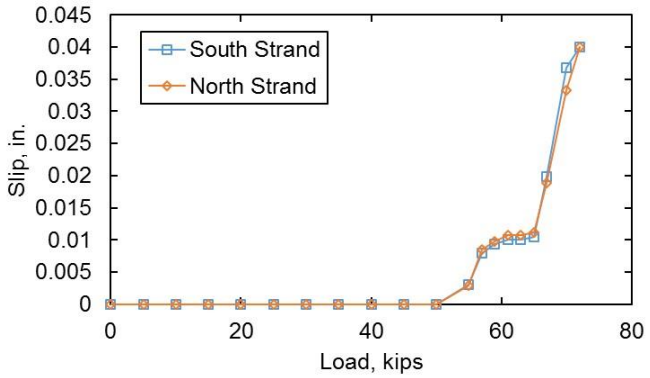

Figure 100: Slip in loaded girder (A5) during destructive test of scale bridge

It is possible that the apparent slip measurements were affected by shifting concrete at the end when the diaphragms cracked and separated from the girders. At a load of 67 kips, another shear crack appeared roughly 2 ft into the span from the previous crack (Figure 101). Between 67 and 75 kips of load, a bond-shear type crack appeared on the loaded girder and a diagonal crack indicative of two-way slab bending behavior appeared in the deck (Figure 102). The slab crack extended from the southeast corner of the bridge where the diaphragm and slab meet to the load point.

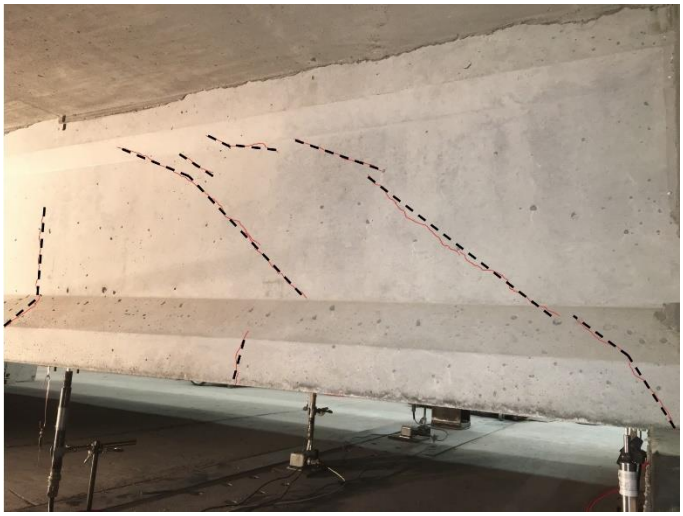

Figure 101: Cracking at 67 kips of load for the loaded girder

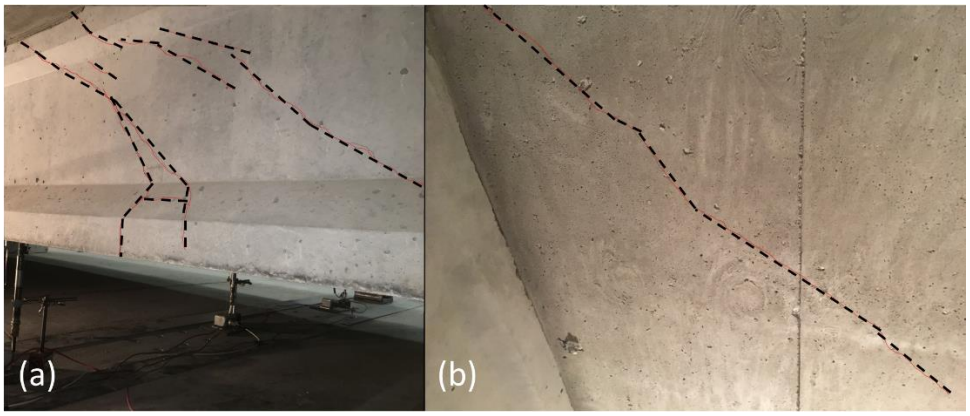

Figure 102: Bond-shear crack in the loaded girder (a) and diagonal crack in slab (b)

At a load of 78 kips, cracking in the outside girder (southernmost) occurred at the bolted connection to the diaphragm, likely due to limited cover between the bolt and the end of the beam. More adequate cover to the connection should have been provided, but the bolt hole spacer shifted during concrete placement (Figure 103). The horizontal crack at the web to flange interface on the girder, visible in Figure 103, indicates potential torsion in the end girder. Cracking there increased by the end of the test as

shown in Figure 104. Load was applied up to a maximum of 96.4 kips, at which point there was extensive cracking in the loaded girder, including a horizontal crack at the deck-girder interface. The load point also punched through the slab at the maximum load (see Figure 105).

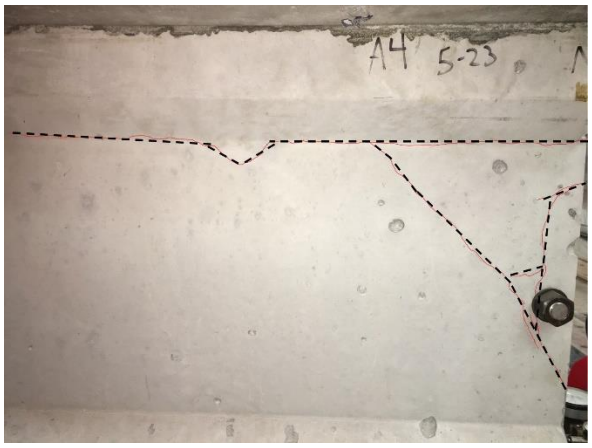

Figure 103: Cracking around diaphragm connection in the southernmost outside girder (A4)

Figure 104: Failure at diaphragm connection

Figure 105: Punching shear failure in slab at load point

Figure 106 shows the load versus deflection plot for the test. The northernmost girder (A3) raised off of its supports by the end of the test (Figure 107); this is the cause of the negative deflection in Figure 106. The change in slope of A5 at around 43 kips of load corresponds to initial cracking; as the cracks worsened, the deflection of the girder increased. Additionally, after the loaded girder cracked, the slopes of the other girders begin to change, particularly A6. This is due to the additional demand on the adjacent girders when the stiffness of A5 decreased. The response of girder A4 (exterior) remained roughly linear for the duration of the test. The slab likely transferred more of the demand to girder A6 than girder A4. This response is discussed further in Section 4.3.

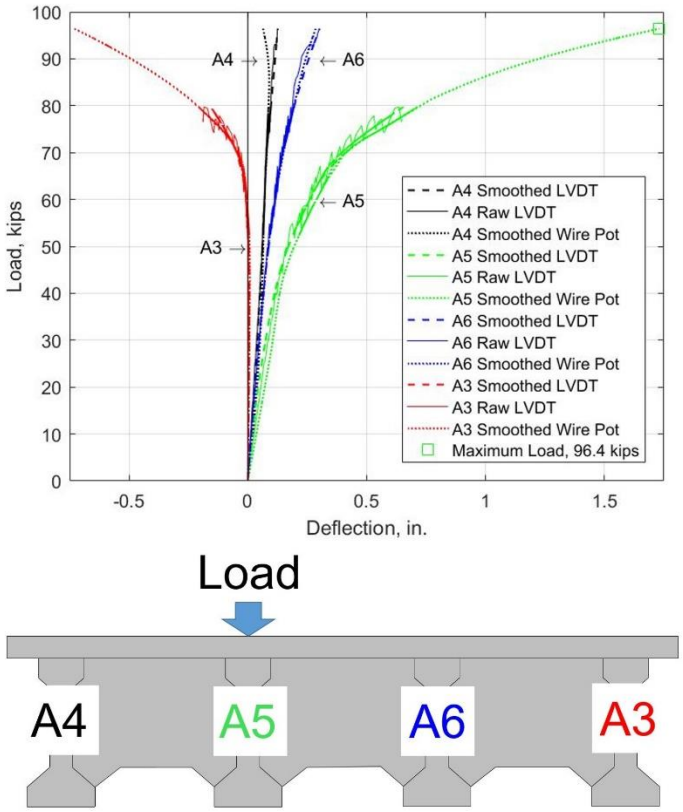

Figure 106: Load vs. deflection for all girders during the destructive test of the scale bridge

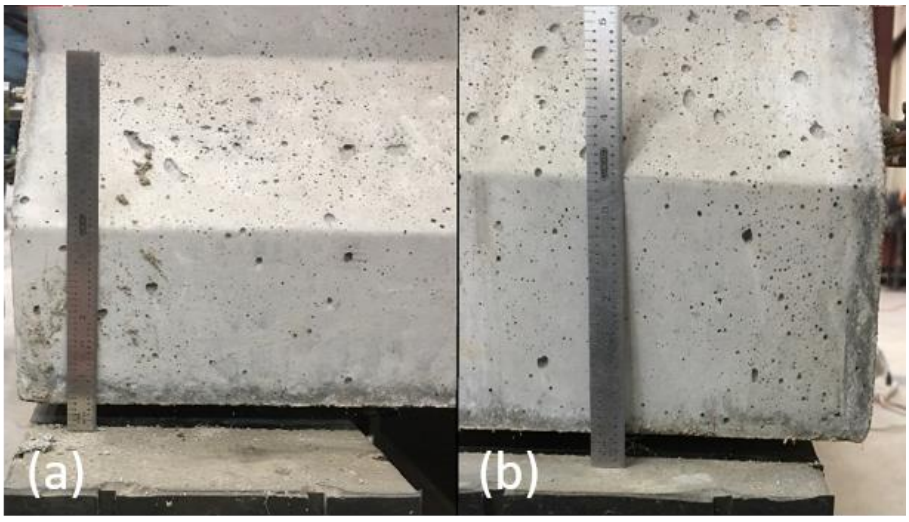

Figure 107: Girder A3 raised off of supports at (a) the east support and (b) the west support

Figure 108: Final shear cracking in loaded girder, note punching in slab

The loaded girder (A5) experienced a failure that was very similar to the individual scale section A1s (tested at the same *a/d* ratio). Cracking and slip was observed at a higher load for the bridge section than for the individual section. Cracking occurred at a load of 34 kips in A1s, but at 43 kips in the bridge test. Slip was observed at a load of 38 kips in A1s and 50 kips in the bridge test. The ultimate capacity was also increased 102%, from 47.8 kips in the individual section, to 96.4 kips in the bridge deck. This is a significant increase, particularly when the predicted ultimate loads for the two cases were 47 kips for A1s and 50 kips for the bridge (assuming a tributary width equal to the girder spacing). The girder had much larger post cracking and post slip stiffness due to the transfer of load through the diaphragm and the slab to the adjacent girders. Based on the results of the scale bridge test, the diaphragms and their connections to the girders are of concern after the loaded girder cracks. These locations, as well as the slab are the focus of much of the damage apart from the loaded girder. The outer girder (A4) has potential to be damaged by torsion when large forces are applied to the first interior girder based on this test.

More pictures are included of the final state of the bridge showing final cracking and deterioration in Figure 108 through Figure 110. Despite the limitations of the manner in which this bridge section was scaled down, this test provided useful information about the ultimate strength behavior of full bridge sections. It would be expected that if a single girder were tested and the strength was limited by its shear capacity or by strand slip, a full-scale section composed of these girders and a deck slab would distribute the force, increasing the post-cracking load carrying ability. It is unclear based on this scale bridge test how the behavior would be affected by multiple load points across a bridge, such as two trucks located side-by-side.

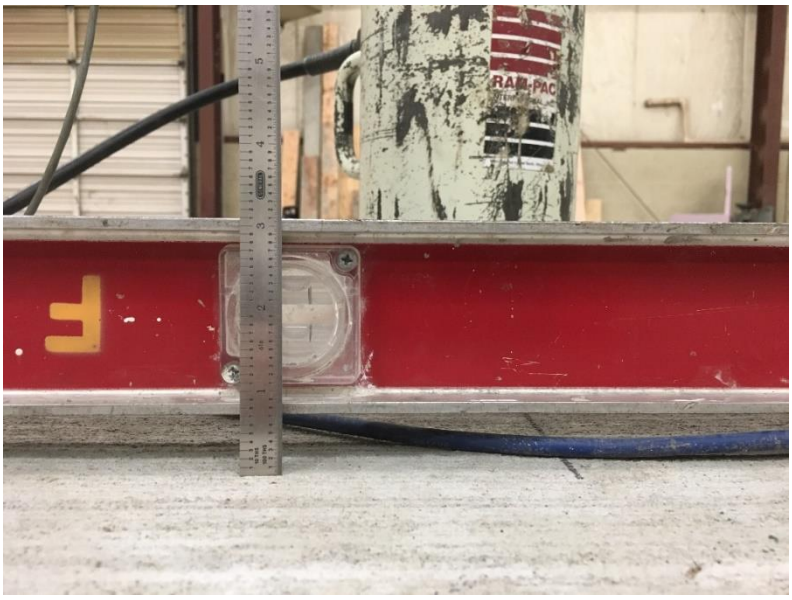

Figure 109: Deflection of scaled bridge section deck near the load point

Figure 110: Cracking in scaled bridge section slab at failure (highlighted in red and black for clarity)

4.3 Discussion of Scale Bridge Tests

There are a number of important takeaways from the destructive test of the scale bridge. The test consisted of a four-girder scale bridge with no skew and with diaphragms, so in some ways the implication of the results is limited. However, there are so few examples of destructive bridge tests in the literature that the qualitative ultimate response of the bridge, especially in light of the companion scale girder tests, provide insights into system level bridge behavior.

In the scale bridge test, a single point load was applied over an interior girder. As discussed later in the section on grillage modeling (5.2.1), the load distribution in a

case like this was predicted accurately using simple grillage models. These grillage models are only usable for the elastic range; for this reason they cannot be relied upon to evaluate bridge behavior post-cracking. Despite this shortcoming, these models are easy to create and provide a good way to find DFs for a wide range of bridges more accurately than the codified DF equations.

Another early takeaway from the scale bridge tests was the connectivity between the diaphragm and girders. Cracking was evident along the interface between the girders and the diaphragms. Any tension in the bottom of the diaphragms is carried solely by the connecting rod that passes through all of the girders. This connection can cause failures in the exterior girders if proper anchorage is not provided. In the scale bridge test, the outer bolted connection appeared to resist an appreciable tension force that resulted in local cracking due to shear near the bolt as well as some cracking near the top of the I-girder due to torsion. When creating detailed finite element models of bridges, this connection condition should be modeled carefully.

Based on grillage models of bridges at the elastic level with and without diaphragms examined in this study, the diaphragm appeared to have very little effect on load distribution. In the literature, there have been conflicting results regarding the influence of diaphragms on load distribution (Mertz, 2006; Dymond, French, & Shield, 2016). At the ultimate load levels, the effects of the diaphragms are more apparent. When the loaded girder failed in the scale bridge test, the diaphragms served as additional load transfer elements. From this point on, the slab behaved as a two-way slab supported on edges by the adjacent girders and the end and middle diaphragms. In this case, it appears that the diaphragms provide an important means of load transfer

when primary elements fail. In this study, very little damage was observed in the end and middle diaphragms, allowing them to continue carrying load after parts of the girders failed. If diaphragms were not present, the slab would likely behave more as a one-way slab with a span length equal to double the girder spacing. This slab arrangement would fail in flexure at lower loads than a two-way slab with the same span length.

The failure of the scale bridge was controlled by punching shear. This is similar to failures reported in past bridge tests (Miller et al., 1994; Dymond et al., 2016). This failure mechanism further confirms that the slab was behaving as a two-way slab when the ultimate load was reached. It is likely that if the load were spread out more (perhaps as separate wheel loads), the section could have reached an even higher ultimate load and higher shear at the loaded girder.

The scale bridge test offered an opportunity to investigate load distribution in bridges after the elastic range. DFs are assessed based on the behavior of the bridge under service level loads. Figure 111 shows a comparison of DFs determined in the elastic range (derived from support deflections of the scale bridge), DFs from the grillage model, and DFs during the load test up to a load of 70 kips (also derived from support deflections). Because the end girder lifted off of its supports during the test, this comparison could not be shown past 70 kips of load. As shown in the figure, load distribution remains very close to the linear factors derived from testing and from modeling up to a load of 40 kips (initial cracking). At this point, distribution in the girders begins to change. The loaded girder (A5) begins to take more of the load according to support deflections. This behavior could be accounted for in a couple of

ways. First, the end diaphragm may help carry the load directly into the support after the girder begins to lose the ability to carry as much shear. Secondly, the rotation at the end of this girder after shear cracking may increase the apparent support deflection since the deflections are measured on the inside of the span at the support. More load also appears to be carried by the other interior girder (A6). On the other hand, the load in girder A4 (exterior near load) appears to decrease. After the loaded girder fails, the load appears to be attracted to the stiffest elements. The end diaphragm distributes the shear into the supports from the slab, and the exterior and interior girders carry some of the load as well. If the deck behaves as an edge supported two-way slab, as hypothesized, it stands to reason that the end diaphragm would attract the most load, followed by the stiffest girder (A6), followed by the less stiff girder (A4), which is borne out by the test data.

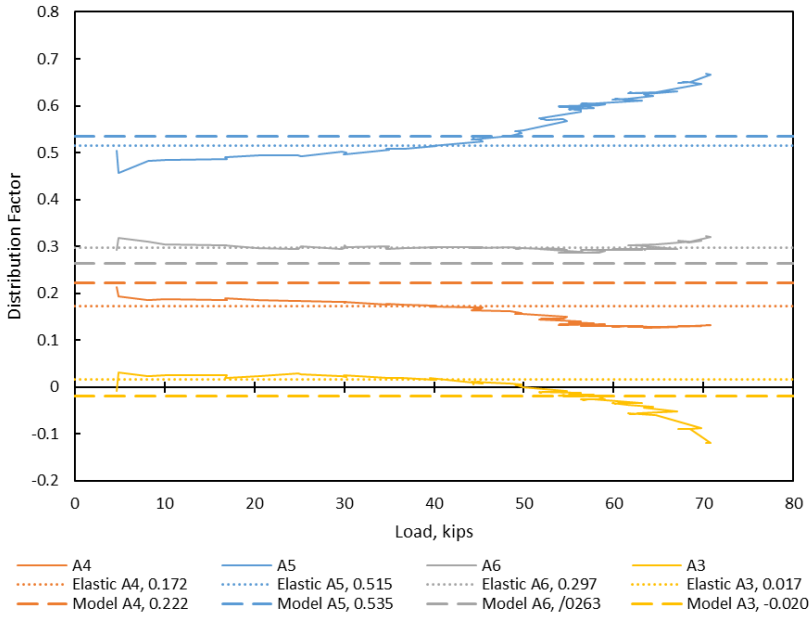

Figure 111: Distribution factors post-cracking compared to elastic range

Test A1s consisted of the same girder design as used in the bridge and was tested at the same location. The capacity was increased by more than 100% when included in the bridge system, and the capacity of the bridge was much higher than predicted by the code for a single girder. However, if the experimentally derived DF for this girder (0.515 given in section 5.2.1) is multiplied by the maximum applied load of 96.4 kips, the resulting load on the girder is 49.6 kips, which is very similar to the ultimate load carried by the individual section (47.8 kips), and very similar to the predicted flexural capacity (50 kips). This would suggest that DFs can help give a reasonable estimate of the ultimate capacity of a bridge given the corresponding capacity of an individual girder.

Chapter 5: Computer Modeling

This chapter contains information about the modeling techniques used, their derivation, and the decision making related to the parametric study and the real-world bridges modeled as part of the study. All grillage models were built in the finite element analysis program STAAD.Pro made by Bentley Systems. Any discussion of "conservativism" of the code methods here is only in relation to the grillage models, not a description of their overall level of conservativism compared to bridge behavior.

5.1 Modeling Procedures

Several options were considered for modeling the bridge sections from this study. Originally, a detailed finite element model containing solid elements to represent the concrete and rod elements to model the steel at discrete locations was planned. After performing preliminary analyses using ANSYS workbench it was decided that a simpler modeling paradigm would be more appropriate to understand bridge behavior. After consulting the work of other authors who have studied bridge behavior (Hambly, 1991; Lightfoot & Sawko, 1959; Mertz, 2006) it was decided that grillage models provide an efficient and accurate way to predict the response of a bridge system to external loads. The grillages are composed of nodes connected by beam elements.

The first step in modeling was to compare the response of the computer model to the scale bridge section. This was necessary to ensure the applicability of the modeling technique. Several iterations were performed, first checking the deflections of the model against the deflections predicted by the grillage. The grillage was assembled by discretizing the bridge into longitudinal grillage members (prestressed girders), and transverse members (slabs and diaphragms). The cross-sections of the members used for

the longitudinal grillage of the scale bridge are shown in Figure 112. The width of slab used to determine properties for the interior girders was selected based on the tributary width, specified by AASHTO LRFD Section 4.6.2.6 to determine the effective slab (AASHTO, 2015). Exterior girder tributary widths were chosen in a similar way, terminating at the edge of the slab, 12 in. away from the girder centerline.

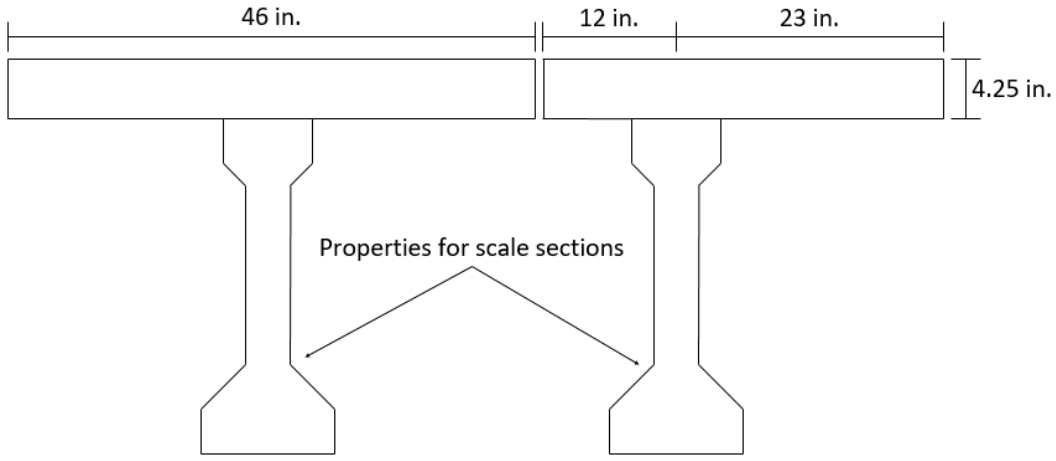

Figure 112: Longitudinal members used in grillage: interior girder (left), exterior girder (right)

The slab was divided into eighths along the girder span, so that each slab section was 2.25 ft wide (8 x 2.25 ft = 18 ft). Eighths were chosen based on general guidance from Hambly (1991). For most slab sections, the cross-section was simply a 4.25 in. by 27 in. (2.25 ft) rectangle. At the ends and middle, the slab member properties included the added stiffness from the diaphragms (Figure 113). Dummy beams were provided along the outside edge of the deck for geometric reasons. These beams were given negligible stiffness. Once the dimensions of the members were chosen, the bending and torsional stiffnesses and areas were calculated, and these could then be input into the model. The moment of inertia was calculated for bending in the direction of the

member's span, and the torsional stiffness was calculated based on recommendations listed the literature review (Section 2.7).

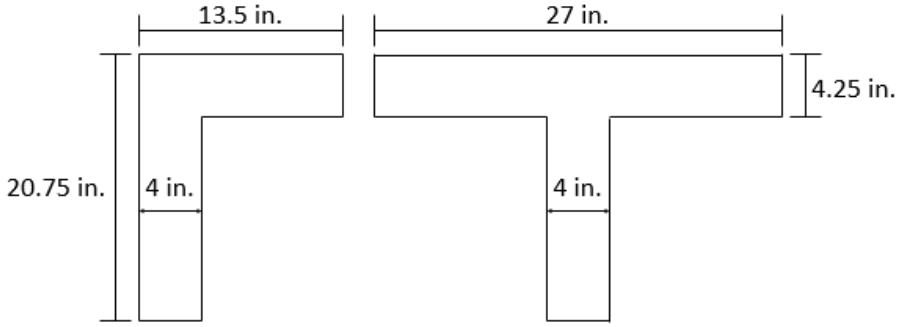

Figure 113: Transverse grillage members at diaphragm locations

Support conditions were selected to be consistent with the test setup for the scale bridge (Figure 114). One support was restrained in every direction (x, y, z) in order to ensure model stability. The support across the bridge from the fully constrained support only allowed displacement in one direction. All other supports only restrained vertical deflections. Because the bearing conditions of the actual test included elasticity of the support (elastomeric bearing pads), an elastic modulus was assigned to the supports. The vertical stiffness given to the supports was 500 MN/m (2,855 k/in.), representing "a rubber bearing on a stiff concrete structure" (Hambly, 1991). After comparing deflections at the supports from the physical testing to the model, the stiffness of the bearing was reduced to 300 k/in., which was more consistent with the response of the tested section. This large discrepancy was unusual, but given that the experimentally verified value agreed well it was determined to be best for use in future models.

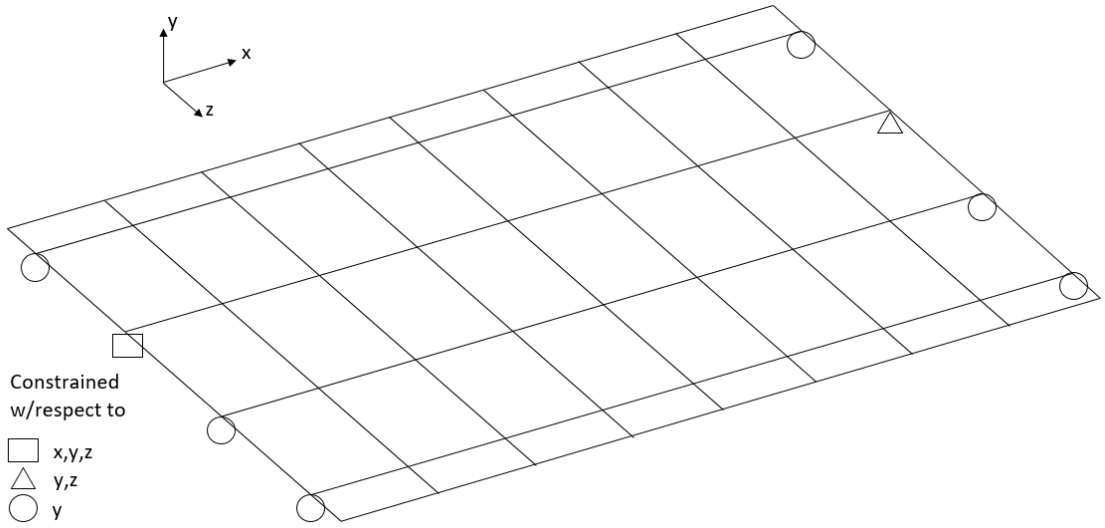

Figure 114: Grillage support conditions

In order to compare deflections of the scale bridge model with the test data, point loads of 20 kips and 40 kips were placed on girders A4 and A5 at the quarter-span point, respectively. These loads correspond to the 20 kips loaded on girder A4 during elastic testing and the linear portion of the destructive test when load was placed on girder A5. Initially, girder deflections were used to determine the accuracy of the model. After a model configuration was chosen, strains from the elastic tests were compared to strains in the grillage model. The model configurations were selected by trial and error originally; the modeling process was streamlined with guidance from the literature. When the behavior of the model compared to the measured response of the scale bridge was considered acceptable, the same modeling paradigm was applied to the bridge spans the full-scale girders were taken from. This allows the comparison of the physical testing of the full-scale girders to the behavior of the modeled bridge.

The compressive strengths for the girders and deck differed for all bridge configurations examined. For all grillage models, the difference in modulus of the deck

and the girders was accounted for using a modular ratio (E_{girder}/E_{deck}). This information was based on modulus tests performed on cores from the old girder and deck concrete and companion cylinders made when the scale sections were constructed. The modular ratio was used to adjust the areas and moments of inertias contributed by the decks.

As mentioned above, full-scale bridge models were created using the same procedures as were applied successfully to the scale bridge. In addition to the full bridge, individual models were created for girders A and C as tested in the lab. These models showed good agreement with the deflections from the elastic portion of the destructive test, further validating the modeling procedures.

5.1.1 Selected Oklahoma Bridges

Originally, three actual Oklahoma bridges were modeled: the I-244 spans from which girders A and C came (deconstructed in 2013), and the Little River Overflow bridge on Oklahoma Highway 70 (NBI # 19269, still in service). The two spans from I-244 (I-244A and I-244C) were modeled to compare with full-scale girder tests results. These bridges consisted of seven longitudinal Type-II girders spaced at 7 ft 8 in. with end and middle diaphragms and a 7 in. deck (when tested in the lab these girders included a 2 in. wearing surface as well). The girders in these bridges were spaced at 7 ft 8 in. The Little River Overflow (LRO) is also composed of Type-II girders and was an interesting case presented by ODOT engineers. This bridge has a relatively short span (35 ft) and a wide girder spacing (11 ft 9 in.). Another interesting aspect of the LRO was a relatively large deck overhang at the exterior girders (4 ft 3 in.). This increased load distribution to the exterior girders. The LRO also had a larger deck thickness as designed (9 in.). These cases were examples of specific bridges modeled

based on the original drawings. The other cases tested in the parametric study performed in this research were based on common dimensions found in the bridge inventory. Since the real-world bridges were cases found in Oklahoma, and since two girders from these bridges were tested in this study, the grillage models were compared to the load ratings for the bridges as well as to the results of the lab tests. Load ratings were carried out using LEAP Concrete Bridge, a commercial bridge design software by Bentley (Bentley Systems, Inc., 2016). Comparing actual tests of older girders to load ratings and finally comparing code DFs to grillage model derived load distribution provides a more complete view of the behavior of an in-service bridge that is not often found in the literature.

5.1.2 Selection of Full-Scale Bridges for Parametric Modeling

Full-scale bridge models were constructed to compare DFs given in the AASHTO LRFD with the distribution of load in the bridge models. The goal was to compare DFs for these model bridges with varying span length, girder spacing, and deck thickness, as well as with or without diaphragms.

The types of bridges selected for modeling in this study, were selected by considering actual bridge dimensions found in Oklahoma. The author obtained a spreadsheet containing the NBI data for Oklahoma bridges. This spreadsheet was filtered to include only the types of bridges of interest to the current study. First, bridges were limited to those built between 1960 and 1979. This year range was chosen to only study bridges composed of girders similar to those tested in the lab. The results were also limited to bridges open to traffic, with zero-degree skew (since there is a skew correction for DFs in the code), and beam-slab type bridges with prestressed concrete

superstructures. Of all of these bridges, the lengths were between 30 ft and 108 ft, as shown in Figure 115. Type-II girders are used today for typical span lengths between 30 ft and 55 ft according to the standard ODOT drawings for highway bridges (ODOT, 2016).

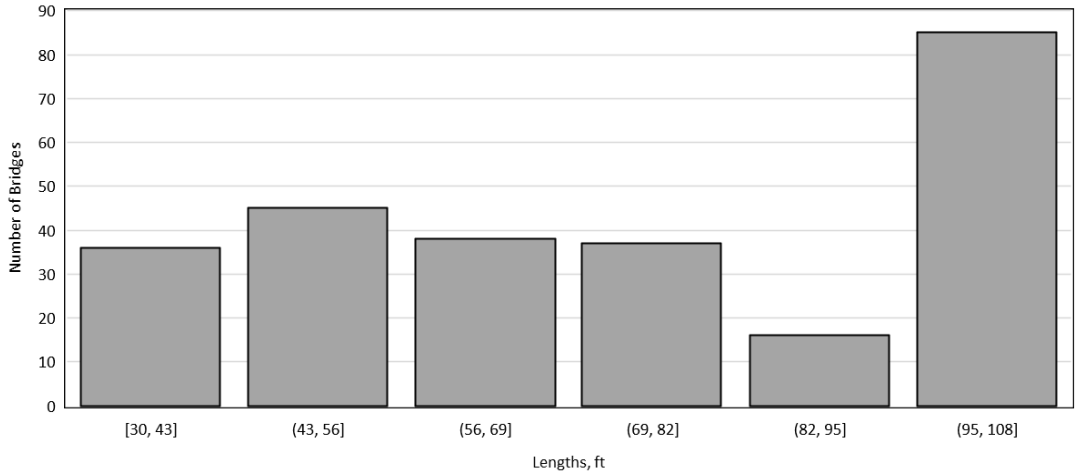

Figure 115: Oklahoma prestressed concrete bridges between 30 and 108 ft (1960-1979)

The filtered bridge data identified 257 bridges meeting the criteria listed in the previous paragraph. The lengths of these bridges are shown in the histogram in Figure 115. Based on this histogram, a range of potential Type-II girder lengths was selected (30 ft to 67.5 ft). 67.5 ft was selected to maintain even increments for bridge lengths. The bridge inventory does not list what type of cross-section each bridge consists of, however AASHTO Type-II girders tend to fit into this span length range. The Florida Department of Transportation has design aids that allow span lengths for Type-II girders up to 81 ft (FDOT, 2013); it seems that in Oklahoma shorter lengths are more common. Next, common bridge widths were sorted (Figure 116). The most common bridges of this type appear to be able to support 2, 3, or 4 lanes of traffic. Unfortunately,

the inventory data does not contain any indication of the girder spacing. Based on conversations with ODOT engineers, typical girder spacings at this time were between 7 ft and 9 ft (or less). The Little River Overflow bridge had a girder spacing of 11.75 ft, which was considered to be a relatively extreme case. The girder spacings selected for this study were 6 ft, 9 ft, and 12 ft, to provide a range including extremes of small and large spacings. A four-girder bridge was used for all parameter analyses for simplicity (lever rule only is used for distribution in three girder bridges).

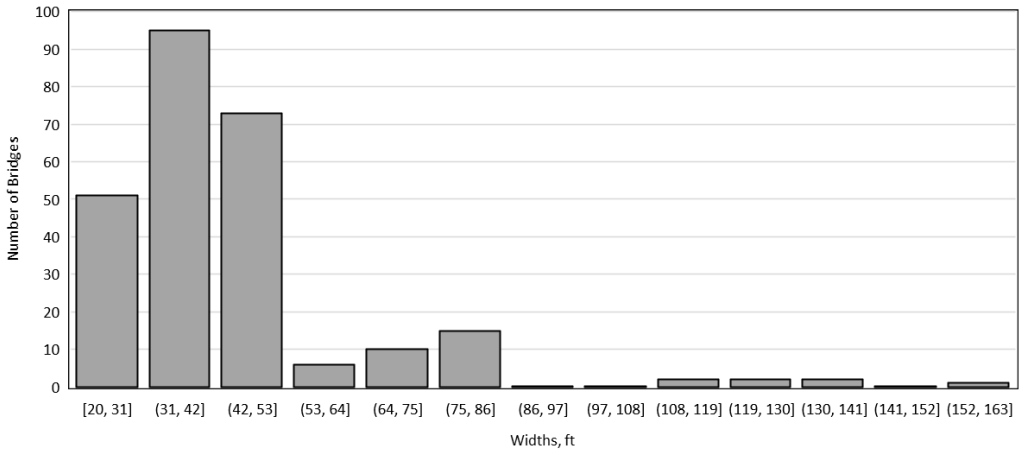

Figure 116: Roadway widths for bridges of interest

At the time these bridges were designed, deck thickness was determined based on girder spacing. Unfortunately, deck thicknesses are also not given in the bridge inventory data. Based on drawings obtained from the time period in question, it is inferred that most bridges tended to have slab thicknesses between 7 in. and 9 in. Because of this, these two thicknesses were used for the current study. Table 24 contains all the parameters examined in this study. These parameters resulted in examination of 48 bridge configurations with varying deck thickness, girder spacing, length, and presence or lack thereof of diaphragms.

Table 24: Bridge grillage models (deck thickness in in. on interior of table)

Spacing (ft)	Length (ft)								
	30		42.5		55		67.5		
6	7	9	7	9	7	9	7	9	Diaphragm
	7	9	7	9	7	9	7	9	No Diaphragm
9	7	9	7	9	7	9	7	9	Diaphragm
	7	9	7	9	7	9	7	9	No Diaphragm
12	7	9	7	9	7	9	7	9	Diaphragm
	7	9	7	9	7	9	7	9	No Diaphragm

Another important question for modeling purposes is the width of deck overhang on each side of the outside girder. The inventory data does not contain this information. Since the I-244 bridge had a 2 ft clearance from the center of the outside girder to the edge of the bridge, this distance was selected for the parametric models. Obviously, a larger slab overhang will increase distribution to the outside girder. However, since the I-244 bridge was taken to be a typical highway bridge, it was assumed that similar bridges will tend to have a shorter overhang due to the large live loads they support. For simplicity, no curb width was assumed. The distance a load is placed from the extreme edge of the deck will mostly affect the distribution to the exterior girder, which is generally designed using the lever rule.

Finally, loading the bridges is an important modeling question. Guidance for applying loads to the grillage models was taken from a similar study (Cross, et al., 2009). For the research in this dissertation, the HS-20 truck (Figure 117) was placed with the rear axle at the end of the span, to maximize the shear force, and the loading locations along the width of the bridge are given in Figure 118. The first tire load was placed 2 ft from the curb for maximum load on the exterior girder (as recommended by AASHTO). Next trucks were placed in each possible lane (12 ft away), then a design truck was placed with each tire load positioned over an interior girder. These

represented the cases for each design lane loaded individually, and the interior girders loaded for maximum effect. Finally, each design lane was loaded with a design truck (multiple lanes loaded). Since there are three girder spacings considered, the bridges have one, two, and three design lanes. Not shown in this figure is the case of a design truck centered over the interior girder. This load case governed in some cases. For bridges with 6 ft girders spacing, there was only one 12 ft design lane. In this case, a truck was placed 2 ft from the curb on both sides of the bridge for the two lanes loaded case.

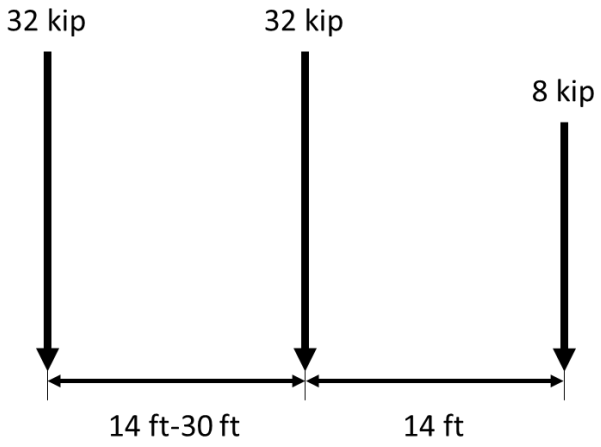

Figure 117: HS-20 truck loads

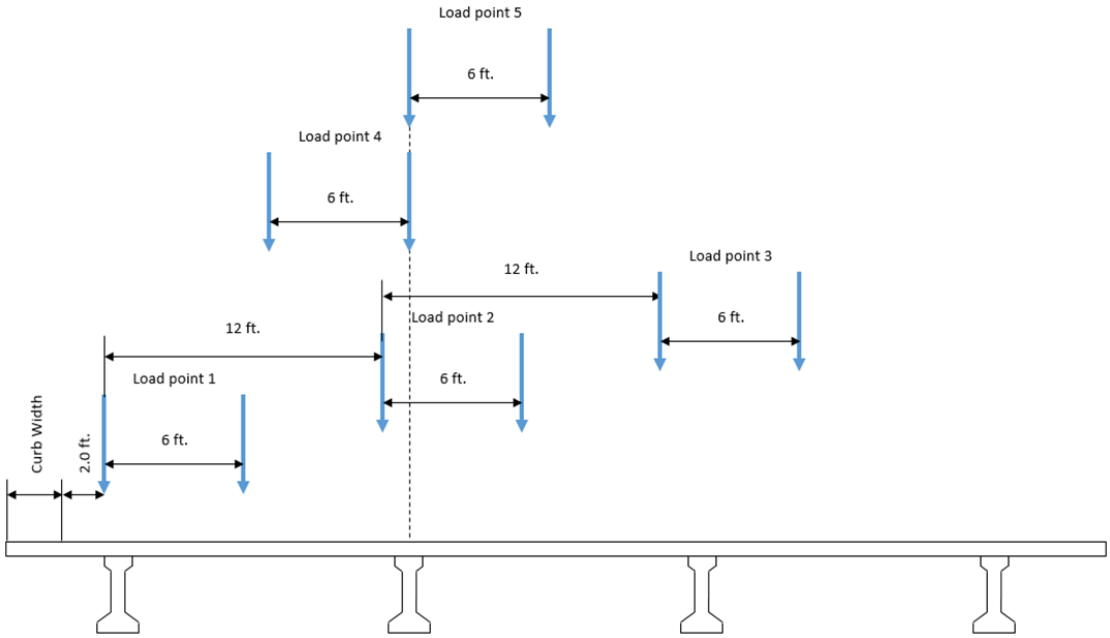

Figure 118: Locations of HS-20 truck for grillage model

The reactions from each load case were summed, and the fraction of the total reaction at each girder was compared to the AASHTO DFs. For the two or more lanes loaded case, the reaction at each support was divided by the static reaction of the design truck placed on a simple beam of the same length. Because exact materials properties were not known, the deck concrete was assumed to have a 4,500 psi compressive strength at 28 days, and the girder concrete was assumed to be 6,000 psi. These values were based on the properties of the girders tested in the lab and on the ODOT standard specifications. Using these values of compressive strength and ACI equation 19.2.2.1.b (ACI Committee 318, 2014), this resulted in a modulus for the deck of 3,824 ksi and a modulus for the girder of 4,415 ksi.

5.2 Results from Grillage Models

5.2.1 Scale Bridge Grillage

The first step in grillage modeling was to use the results of the scale bridge testing to calibrate a grillage model of the scale bridge (basic illustration shown in Figure 3). The properties used for the grillage members are given in Table 25. Initially, load versus deflection relationships from the scale bridge tests were compared to load versus deflection relationships from the model. The two load cases used were: 1) a single point load directly atop girder A4 (exterior) at the quarter span point (from elastic testing) and 2) a single point load directly atop girder A5 (interior) at the quarter span point. Because the loads and resulting deflections and strains were so small, elastic tests over the slab (S1 and S2) described in Section 4.1.5 could not be used for model validation. For the interior case, the deflections for all girders from the destructive test up to the cracking load (40 kips) were used for comparison. For the exterior case, the load was 20 kips and the deflections used for comparison were from the elastic testing. Figure 119 shows the agreement between the model and the scale bridge response when load was applied at girder A5 (exterior case). Figure 120 shows the agreement between the model and the scale bridge response when load was applied at girder A4. The numbers after the girder (e.g. A41, A51) refer to the elastic test, so some of the examples shown were the result of multiple elastic tests.

Table 25: Summary of properties used in scale bridge grillage

	Interior girder	**Exterior girder**	**Slab**	**Slab + middle diaphragm**	**Slab + end diaphragm**
Area (in^2)	280.8	238.9	102.7	161.8	110.4
Torsion Stiffness (in^4)	511.9	511.9	309.2	683.2	510.5
Bending Stiffness (in^4)	20,302.2	18,739.4	102.7	2,273.2	1,987.7

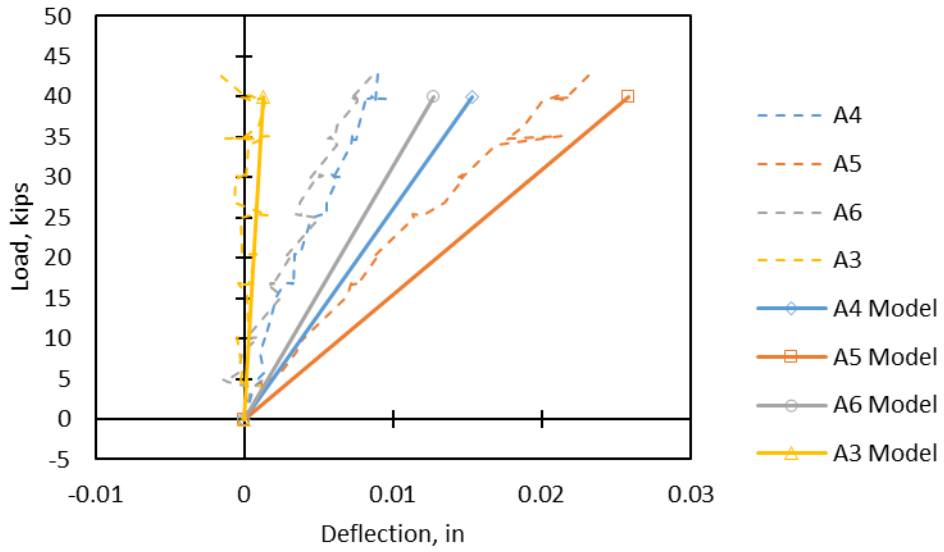

Figure 119: Comparison of load versus deflection relationships for grillage model and scale bridge loaded at girder A5

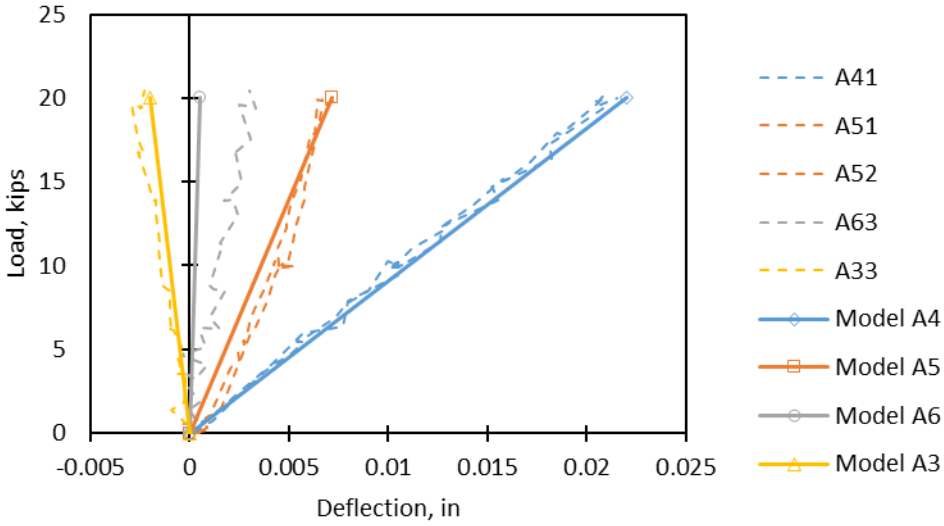

Figure 120: Comparison of load versus deflection relationships for grillage model and scale bridge loaded at girder A4

Referring to Figure 119, the deflection of girder A5 differs from the model by 18% at the maximum load. For load point A4 (Figure 120), the difference in deflections between the model and experimental results is 4% at the maximum load. Deflections for

some of the other girders do show larger differences. However, matching the behavior of the loaded girder was determined to be the most important parameter. Based on the two load locations, there seemed to be good agreement between the models and the experimental results. An important factor to consider in interpreting these deflections is their magnitude. The extremely small deflections for both load cases means some variation is expected. The magnitude of deflections for the loads examined is on the same order as the noise in the signal from the sensors used in the experimental tests, accounting for some of this error. Based on these results, it was decided that the behavior of the model was an acceptable representation of the recorded response, despite some percent difference. The differences were on the same magnitude of those observed in similar research (Petersen-Gauthier, 2013).

Another factor considered for acceptance of the modeling paradigm was strain in the bottom flange of the girders at the load point. Figure 121 and Figure 122 show strains measured at the load point on all girders compared to strains given by the model at the same locations. These figures show reasonable agreement with the behavior of the actual bridge. It is worth noting that grillage models are not excellent at representing local phenomena in the members as compared to more detailed finite element methods, but the objectives of this research were focused more on the overall structural behavior. The reasonable agreement of deflections and strains was seen as a validation of the modeling methods.

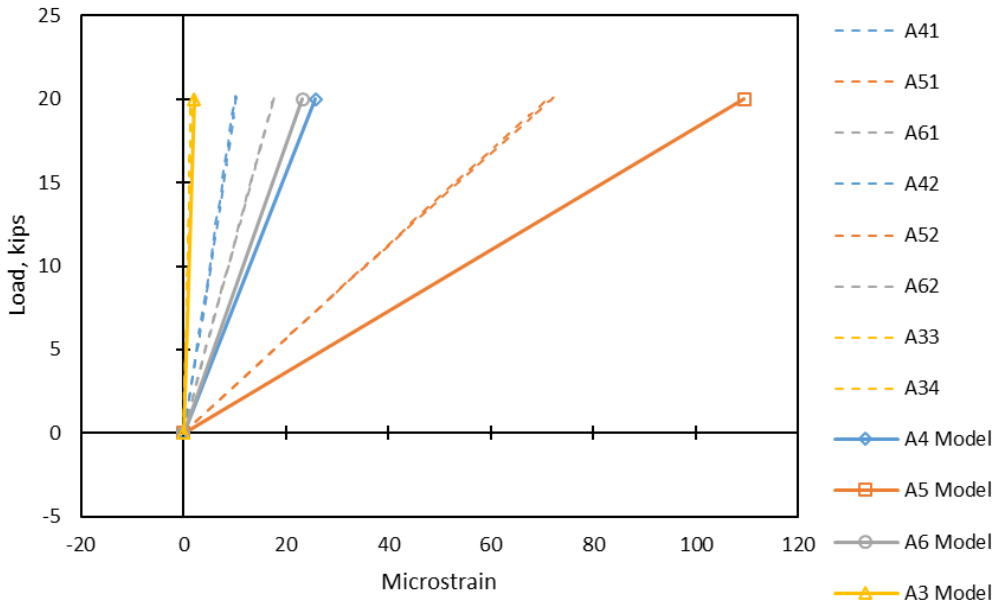

Figure 121: Comparison of load versus girder strain relationships for grillage model and scale bridge loaded at girder A5

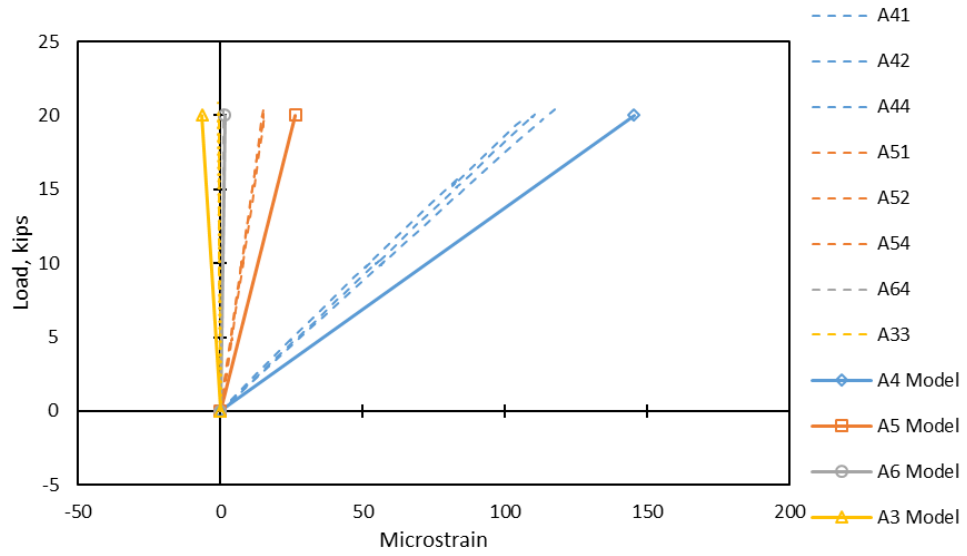

Figure 122: Comparison of load versus girder strain relationships for grillage model and scale bridge loaded at girder A4

Another method used to verify the modeling procedure was comparing the amount of shear force observed at each support. Since the models were intended to be used to evaluate shear DFs, this is likely the most important parameter. The way this

comparison was achieved was by summing the support deflections for each girder (at the loaded end of the bridge) and using the proportion of individual support deflections to total support deflection to represent the same proportion of the total load on the bridge. This method was used for the support deflections of the scale bridge in the elastic range (at 40 kips of load) and the same response of the model at 40 kips. This procedure is similar to that used in other research to determine DFs for tests and models (Cross et al., 2006). The results obtained from this method are summarized in Table 26. Table 26 also shows the DFs for the case where a 20 kip load was applied over girder A4. For both load cases, 75% of the total load is assumed to go to the support with the largest shear (from statics). This assumption is accurate based on the magnitude and proportion of deflections at every support.

Table 26: Method to find distribution factors from deflections shown for both load cases

		From Bridge Test			**From Grillage Model**		
Load Position		Support Deflection (in.)	Expressed as reaction force (kips)	Distribution Factor	Support Deflection (in.)	Expressed as reaction force (kips)	Distribution Factor
A5 (40 kips)	A4	0.019	5.15	**0.172**	0.022	6.67	**0.222**
	A5	0.058	15.44	**0.515**	0.053	16.06	**0.535**
	A6	0.033	8.91	**0.297**	0.026	7.88	**0.263**
	A3	0.002	0.51	**0.017**	-0.002	-0.61	**-0.020**
	Σ	0.113	30.00	1.000	0.099	30.00	1.000
A4 (20 kips)	A4	0.027	9.45	**0.630**	0.043	12.90	**0.860**
	A5	0.018	6.31	**0.421**	0.011	3.30	**0.220**
	A6	0.002	0.76	**0.051**	-0.001	-0.30	**-0.020**
	A3	-0.004	-1.52	**-0.101**	-0.003	-0.90	**-0.060**
	Σ	0.044	15.00	1.000	0.05	15.00	1.000

The comparison of DFs for the end with the highest shear (end nearest the load point) when load was placed directly above girder A5 is given in Figure 123, and shows very good agreement between the model and the actual response. When load was placed

on an exterior girder (Figure 124) the DF differences were larger, but still show reasonable agreement.

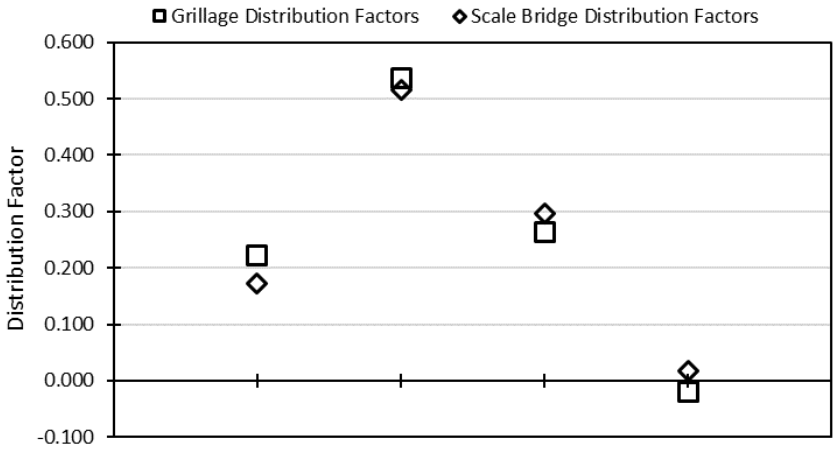

Figure 123: Distribution factor comparison for grillage model and scale bridge load test (load at A5)

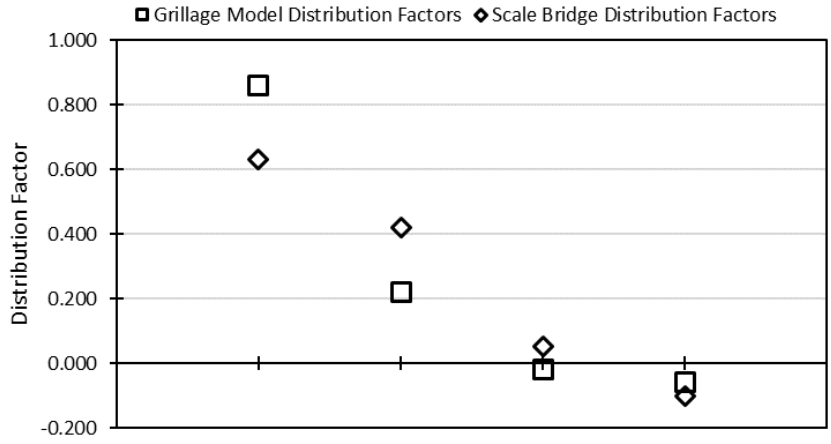

Figure 124: Distribution factor comparison for grillage model and scale bridge load test (load at A4)

5.2.2 Results of Parametric Study of Type-II Girder Bridges

This section will discuss the effects of various parameters (girder spacing, deck thickness, span length, diaphragm vs. no diaphragm) on AASHTO LRFD DFs and DFs derived from grillage models. The section properties used to build these models and the DFs collected from grillage models and from the AASHTO LRFD equations are given in Appendix E. The results presented in this section are separated by interior and exterior girders in the span and by loading (one lane loaded or two or more lanes loaded). These cases are considered separately in the code so they were separated for the discussion of grillage modeling results. This section merely shows the results and explains the trends that were seen. These results are discussed in more detail in Section 5.3. All models used in this parametric study were developed using the same procedures as for the scale bridge model described in Section 5.1.

In this section, differences in DFs between the code and the grillage models are discussed. A discussion of how these differences are expressed is warranted as a prelude to this section. Since a DF represents a fraction of the total shear at one end of a bridge, differences in the factors will be expressed as the absolute difference between the two. For example, where the AASHTO DF is 0.4 and the grillage model derived factor is 0.35, the difference is 0.05, or 5% of the total shear at that end of the bridge.

4.3.2.1 Effects of Girder Spacing

First, the effects of girder spacing were examined. DF equations in the code have always appreciated the effect of spacing on load distribution. Clearly a longer deck span will reduce the distribution of load to adjacent girders, and thus will increase the DF for the girder in question. Figure 125 shows the DFs for 6, 9, and 12 ft girder

spacings for each span length, deck thickness and diaphragm condition modeled for exterior girders with one lane loaded (note: the lines on figures in this section do not indicate a trend necessarily, but are in place to indicate the AASHTO DFs). As expected, the DFs increased with increasing spacing. The AASHTO DFs appear to show good agreement with the results of the parametric models examined, generally being conservative by a value of about 0.05 (or 5% greater shear at that end). For the case of 6 ft girder spacing, the AASHTO equations appear to be unconservative (by about 0.025 or 2.5% less shear) for the case of no diaphragms (lower DF means less conservative). For exterior girders, the code allows the end of the span to be modeled as a rigid body when diaphragms are present. This assumption is known as "special analysis." In this study, the special analysis was used when diaphragms were present (solid blue line in figures), and it was occasionally the controlling DF case in the AASHTO LRFD code. Based on the modeling presented here, diaphragms do not appear to have a significant effect on load distribution for exterior girders compared to the effect of spacing.

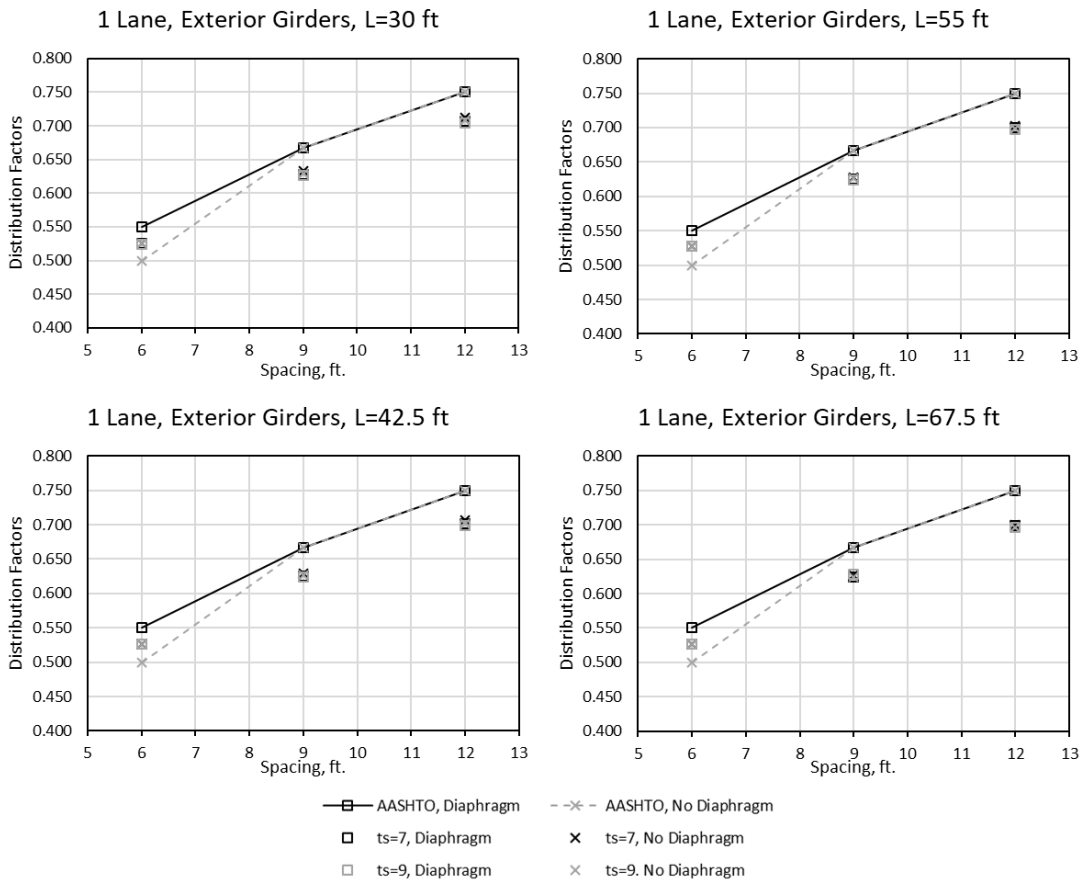

Figure 125: Distribution factors for exterior girders, one lane loaded versus girder spacing

Next, the same parameters were compared for exterior girders with two or more lanes loaded. For the 6 ft girder spacing case, two lanes loaded was achieved by placing a truck 2 ft from the deck's edge on each side of the bridge. This arrangement produces a situation that is smaller than the design lane width of 12 ft, but arranging loads more closely spaced than a typical design lane may be necessary for load rating of narrower bridges. Again, there is a trend of increasing DFs with increasing girder spacing (Figure 126). This finding is unsurprising. The DFs appear to vary more for exterior girders with two or more lanes loaded with respect to deck thickness and presence of diaphragms based on the grillage models. In other words, for two or more lanes loaded,

these variables have a more pronounced effect than for one lane loaded. The AASHTO LRFD DFs are conservative, especially when diaphragms are present and the "special analysis" is used. However, for the 6 ft girder spacing there appears to be very little influence from diaphragms or deck thickness. Based on the grillage models examined, it is a more conservative assumption to use the rigid section special analysis method. The controlling AASHTO LRFD code equations appear to become more conservative with larger girder spacings.

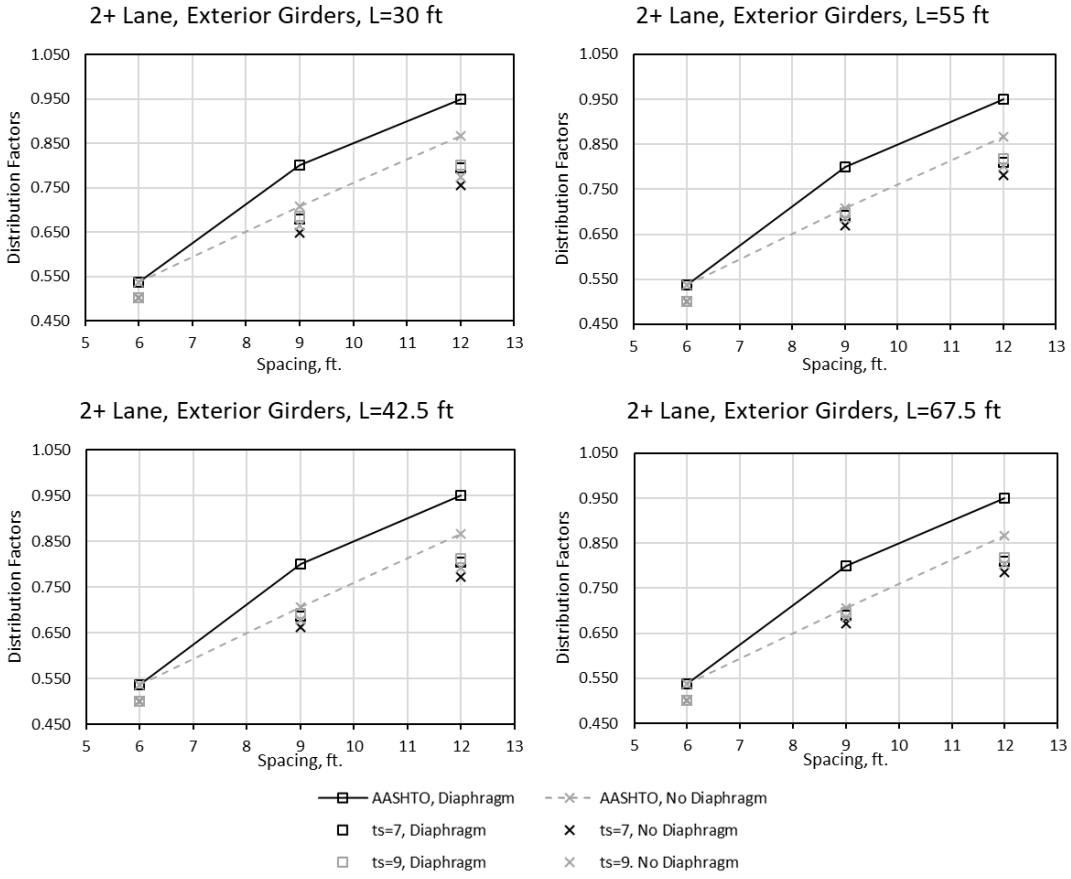

Figure 126: Distribution factors for exterior girders, 2+ lanes loaded versus girder spacing

Next, interior girder DFs were examined for the same variable combinations. Again, these were separated by number of lanes loaded. Results for the case of one lane

loaded are given in Figure 127. For this case, AASHTO DFs were generally conservative. However, the code DFs are slightly unconservative for thinner decks with shorter spans and wider girder spacings (top left in Figure 127). DFs from the grillage models tended to vary more as length increased, i.e. the effects of deck thickness and the presence of diaphragms are more pronounced as span length is increased.

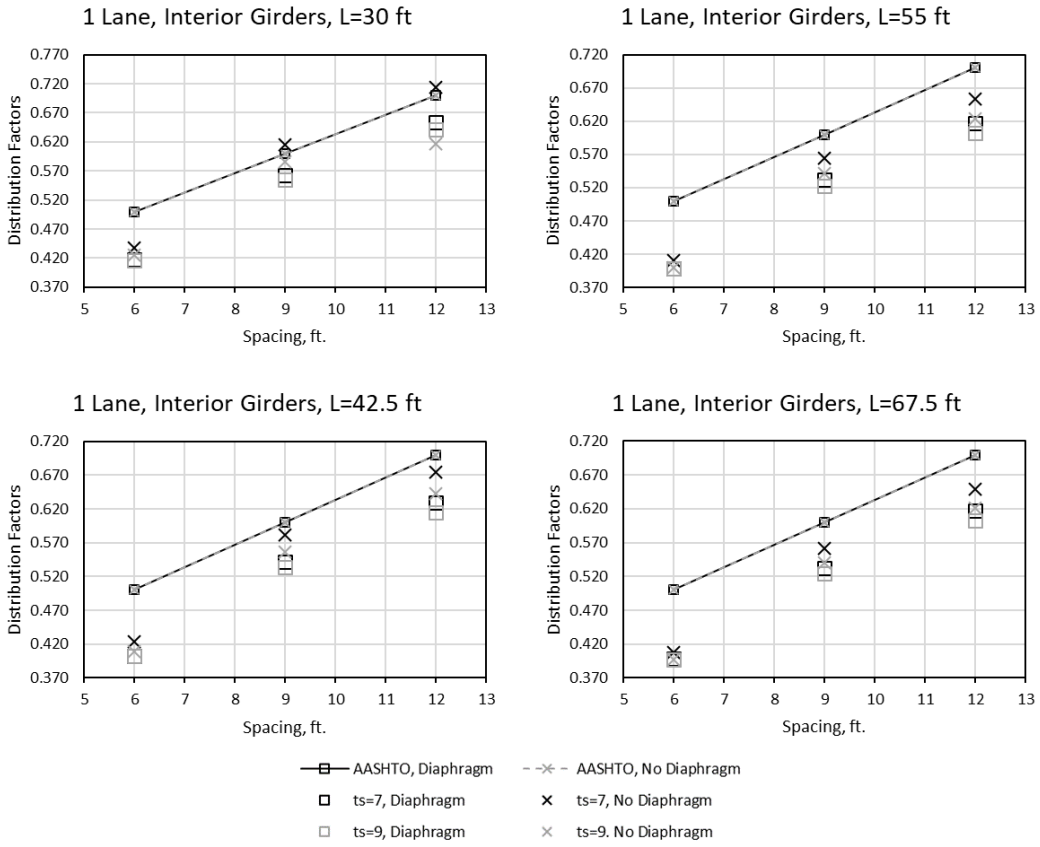

Figure 127: Distribution factors for interior girders, one lane loaded versus girder spacing

Figure 128 shows the DFs for interior girders with two or more lanes loaded. AASHTO DFs are conservative for all variable combinations considered for this case. It appears that the code DFs are less conservative for larger girder spacings and very conservative for shorter girder spacings.

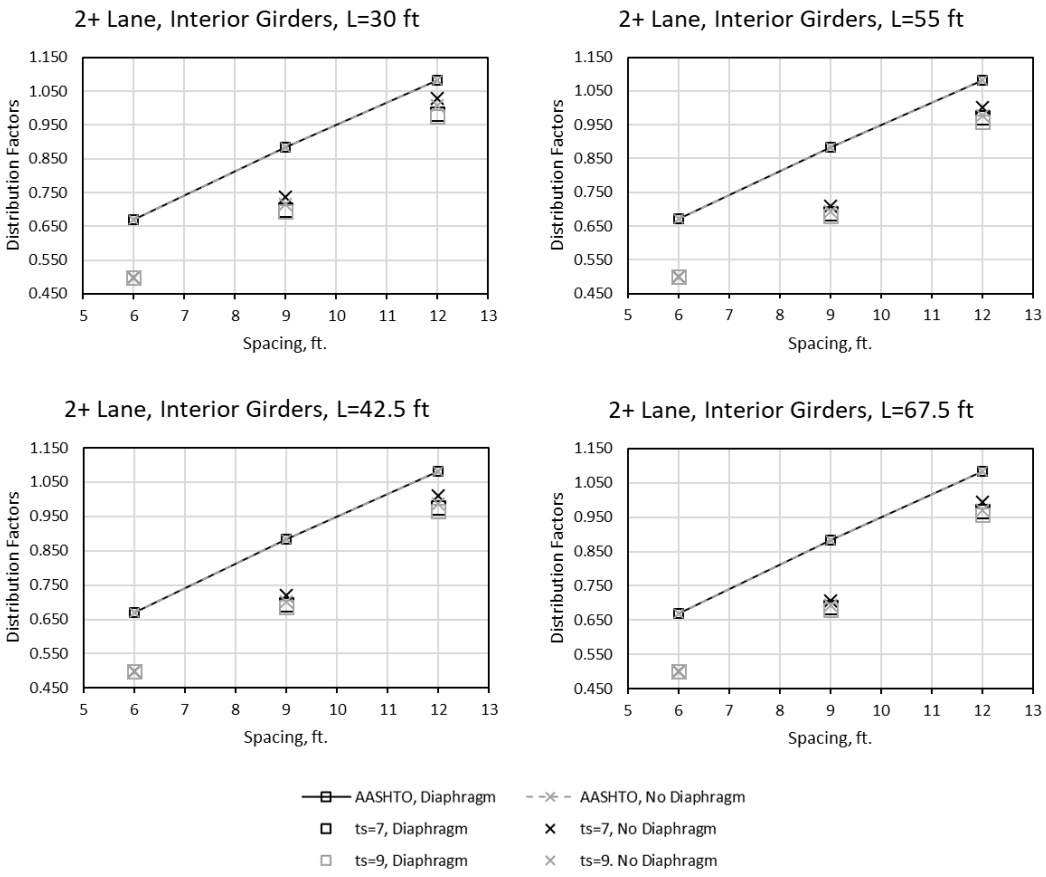

Figure 128: Distribution factors for interior girders, 2+ lanes loaded versus girder spacing

4.3.2.2 Effects of Span Length

The influence of span length on distribution was examined by plotting the DFs against length for each girder spacing. Note that the following figures have variable scales on the ordinate to better show the differences. Figure 129 shows the DFs for interior girders spaced at 6 ft for the case of one lane loaded. AASHTO DFs are conservative for this case, becoming more conservative for longer span lengths. For the 67.5 ft span length, DFs determined using the grillage models are approximately 0.1 less than the AASHTO predictions.

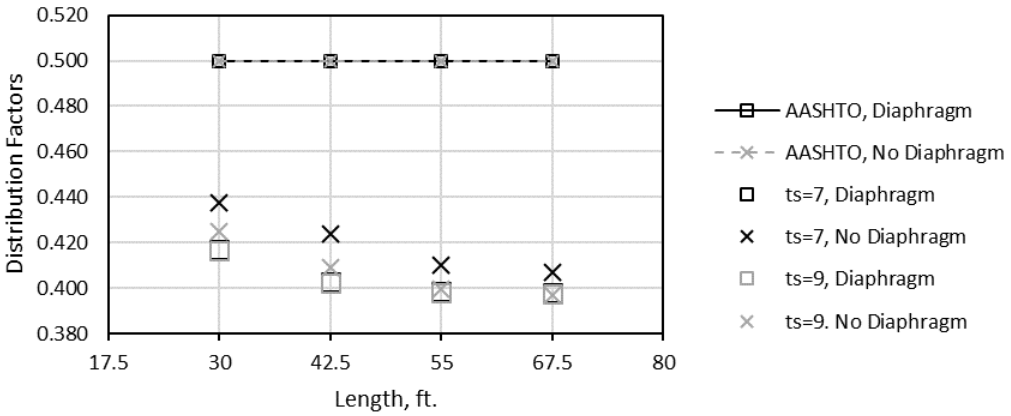

Figure 129: Distribution factors for interior girders with one lane loaded, 6 ft girder spacing

Figure 130 shows the same information for the 9 ft girder spacing case. There is a larger spread of DFs for this wider spacing, the difference between a given DF for lengths of 30 ft to 67.5 ft is 0.05 on average. The DFs from the AASHTO LRFD code are generally conservative, though less so for shorter spans. The grillage model derived DF for the case of a 30 ft span length with a 7 in. deck and no diaphragm exceeds the AASHTO factors by 0.015 (1.5% more shear).

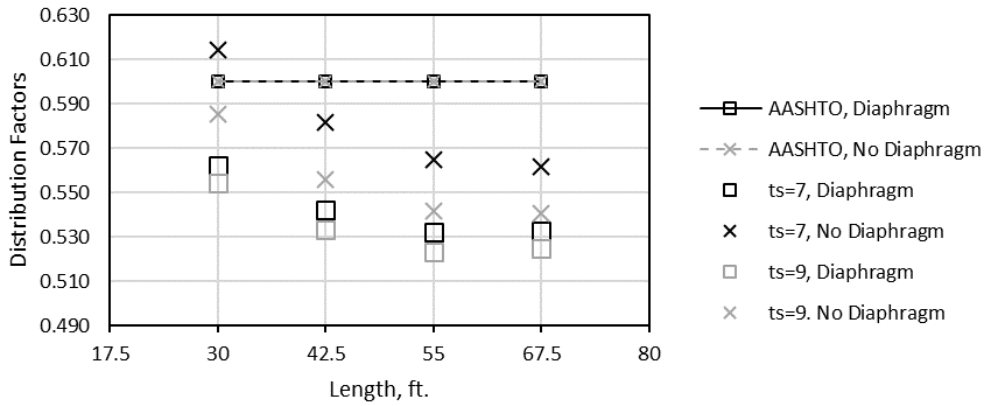

Figure 130: Distribution factors for interior girders with one lane loaded, 9 ft girder spacing

Finally, the case of 12 ft spacing is given in Figure 131. There is a general trend of decreasing DFs with length, as seen in the other figures. The code DFs are conservative except for 7 in. deck thickness with no diaphragms for shorter span lengths (<42.5 ft) and 6 ft girder spacing. For these unconservative cases, the code equations are at most unconservative by 0.01. For deck thickness of 9 in. with diaphragms, the code differs from the grillage by as much as 0.1 for the 67.5 ft span length. The effects of diaphragms and slab thickness appear to be more pronounced for larger spacings.

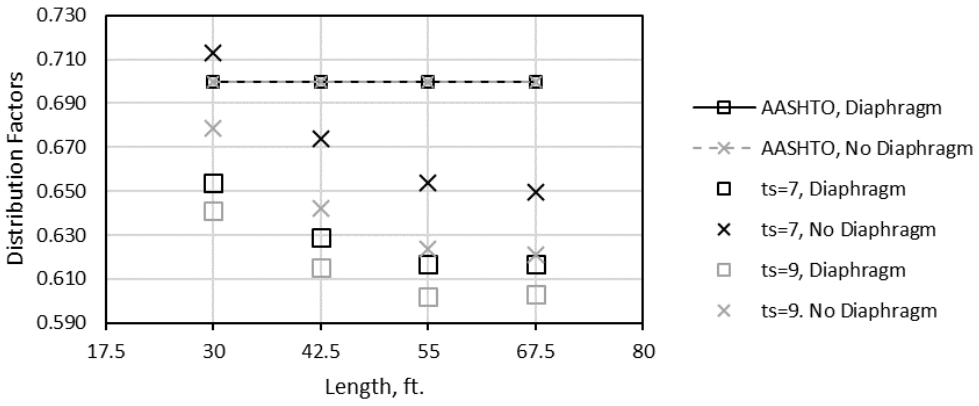

Figure 131: Distribution factors for interior girders with one lane loaded, 12 ft girder spacing

The same variables were considered for the case for 2+ lanes loaded for each girder spacing. Figure 132 shows the DFs for interior girders at a spacing of 6 ft. Regardless of deck thickness or diaphragms or length, the DFs are basically unchanged. The code is very conservative for this case, overpredicting distribution by 0.15. For this small spacing, the end of the bridge appears to be very stiff.

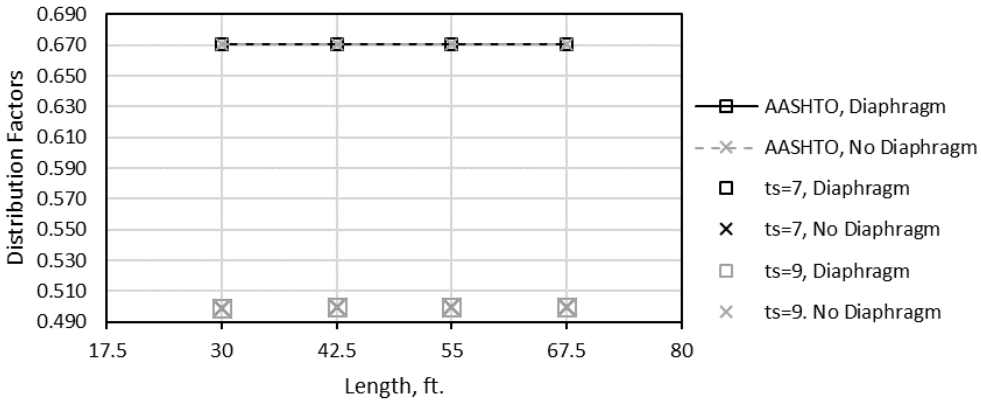

Figure 132: Distribution factors for interior girders with 2+ lanes loaded, 6 ft girder spacing

When the spacing is increased to 9 ft (Figure 133), DFs tend to decrease with increasing length. The AASHTO equations are generally very conservative for longer lengths at 9 ft spacing.

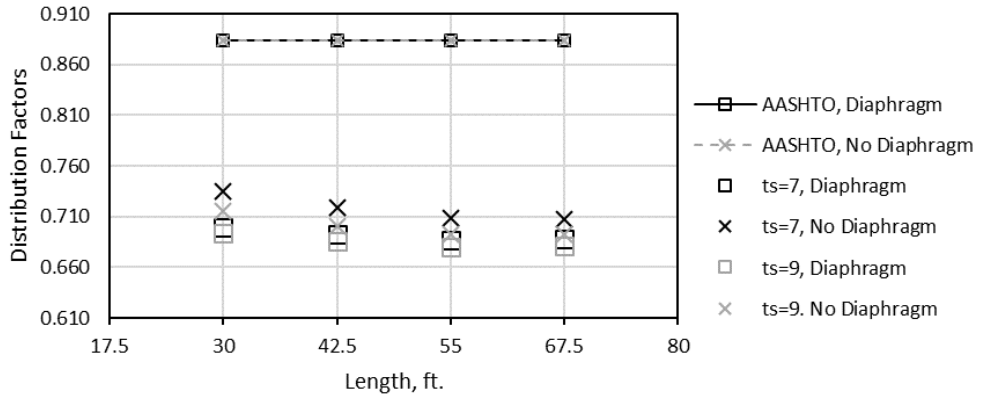

Figure 133: Distribution factors for interior girders with 2+ lanes loaded, 9 ft girder spacing

Finally, Figure 134 shows the DFs for interior girders at a spacing of 12 ft Again, the AASHTO DFs become more conservative for longer span lengths, and the conservativism is greater for 12 ft spacing compared to 9 ft spacing. The code equations

are generally conservative. At their most conservative they differ from the grillage model by 20.4% of the total shear (at 9 ft spacing, 55 ft length, 9 in. deck thickness, with no diaphragms).

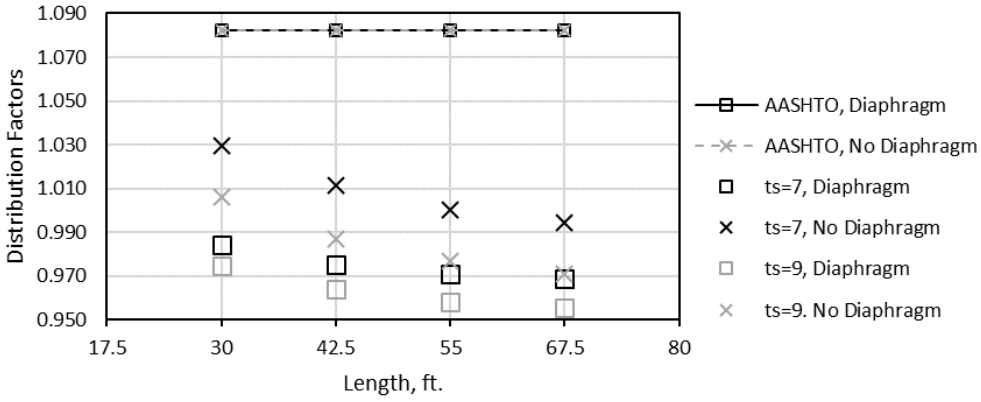

Figure 134: Distribution factors for interior girders with 2+ lanes loaded, 12 ft girder spacing

The previous six figures compared DFs for interior girders by length for one and two or more lanes loaded. The next six compare the same factors for exterior girders. For exterior girders, the DFs for 6, 9, and 12 ft spacings with one lane loaded are given in Figure 135, Figure 136, and Figure 137, respectively. For a spacing of 6 ft, the grillage models showed very little change with increasing slab thickness or with the presence of diaphragms. If the special analysis is not used (diaphragms not present), the code under predicts distribution by about 0.025. On the other hand, when the rigid section special analysis is used the code overpredicts DFs by the same margin.

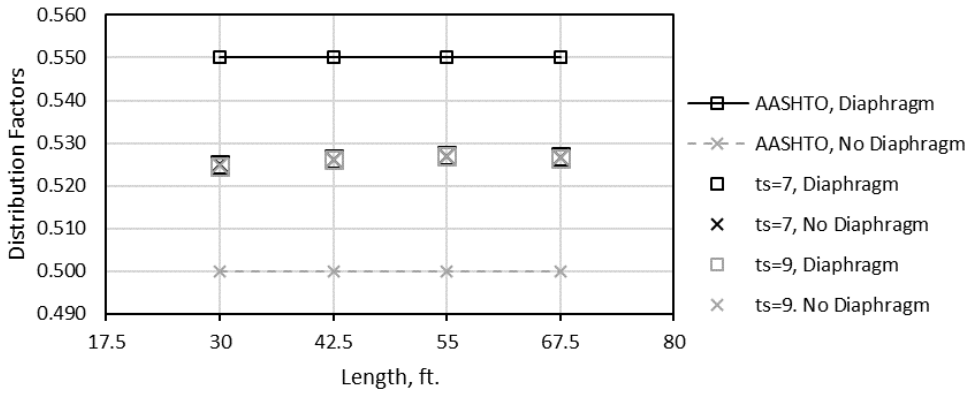

Figure 135: Distribution factors for exterior girders with one lane loaded, 6 ft girder spacing

For the 9 ft girder spacing (Figure 136), the code DFs are conservative at every span length. The code factors differ from the grillage factors by about 0.04 on average, so the difference is relatively small.

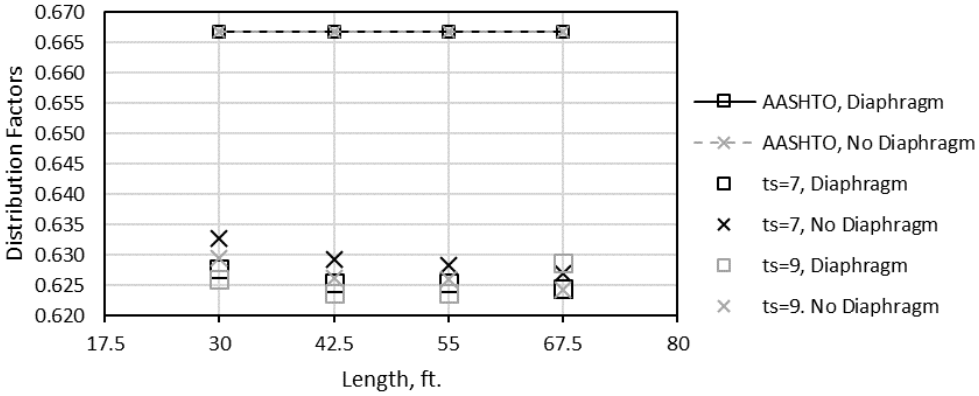

Figure 136: Distribution factors for exterior girders with one lane loaded, 9 ft girder spacing

The trend for the 12 ft girder spacing (Figure 137) is similar to that observed for the 9 ft girder spacing. On average, the code differs from the models by about 0.048. DFs tend to decrease for longer spans for both 9 ft and 12 ft girder spacings.

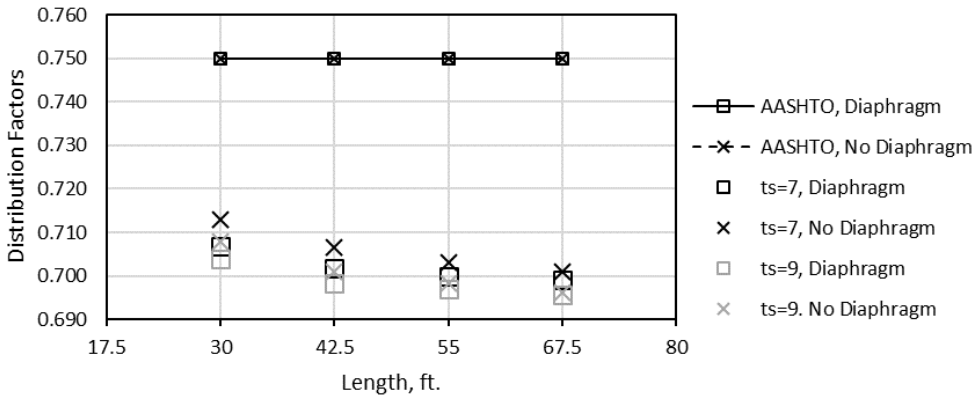

Figure 137: Distribution factors for exterior girders with one lane loaded, 12 ft girder spacing

Next, DFs were compared for exterior girders with two or more lanes loaded. Figure 138 shows the DFs for 6 ft girder spacing. There is a general trend of decreasing DF with length. The magnitude of the change with length is extremely small for this spacing, and the code factors predict distribution reasonably well (decrease of 0.035 for 67.5 ft as opposed to 30 ft).

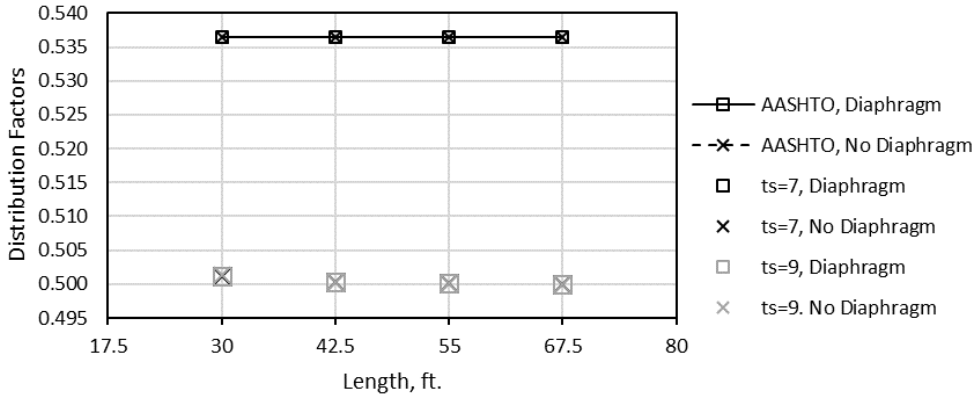

Figure 138: Distribution factors for exterior girders with 2+ lane loaded, 6 ft girder spacing

Figure 139 shows the DFs for 9 ft girder spacing and a trend of increasing DFs with length is present. This trend seems to diminish after a 55 ft span length. The

different code DFs (diaphragm versus no diaphragm) are a result of the "special analysis" used when diaphragms are present in exterior girders. Where diaphragms are accounted for (blue lines), the code is more conservative for all span lengths. Otherwise, the code is less conservative, particularly at longer spans.

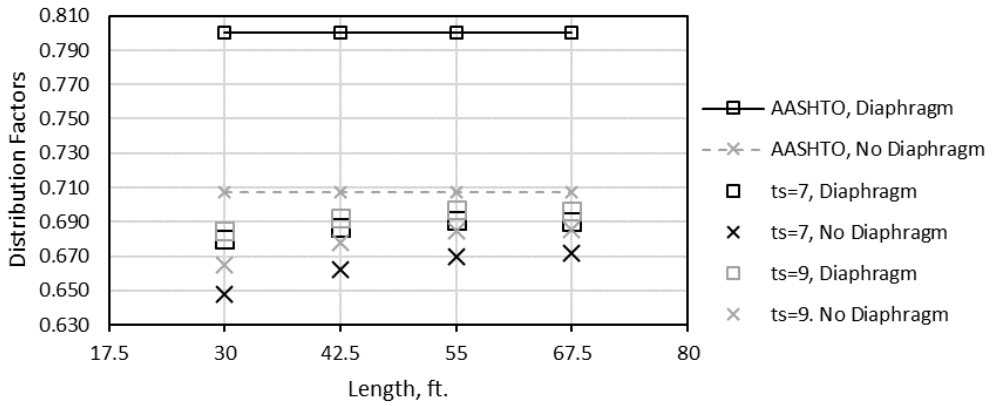

Figure 139: Distribution factors for exterior girders with 2+ lane loaded, 9 ft girder spacing

Finally, Figure 140 shows the DF comparison for 12 ft girder spacing. For the cases considered with this spacing, code is conservative, more so if the "special analysis" is used (diaphragms accounted for). For short span lengths where diaphragms are present, the code can be increasingly conservative (0.155 greater than the grillage model).

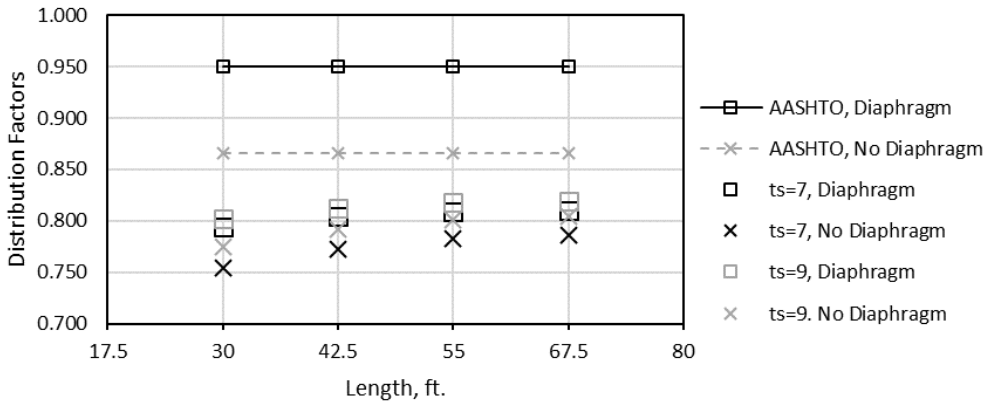

Figure 140: Distribution factors for exterior girders with 2+ lane loaded, 12 ft girder spacing

5.2.3 Results of Oklahoma Bridge Models

Several real-world bridges were modeled for this study based on plans provided by ODOT. The bridges considered were two spans of the I-244 bridge over the Arkansas river in Tulsa (demolished in 2013) corresponding to the spans from which girders A and C were taken and the Little River Overflow (LRO), a bridge with a wide girder spacing (11.75 ft) and of particular concern to ODOT. The purpose of looking at these bridges was to compare the results of the parametric study with real bridges and to compare the full-scale girder tests to models of the bridges themselves. The same processes were used for these models as for the models of the scale bridge and the parametric bridge models discussed in previous sections. Section properties used in the models are given in Appendix E.

The DFs for the three bridges modeled are given in Table 27. These factors include the DFs from grillage modeling and the AASHTO LRFD code for interior and exterior girders with one and two or more lanes loaded. This information is displayed

graphically in Figure 141 to show the differences between the factors amongst the bridges and compared to the AASHTO DFs.

Table 27: Shear distribution factors for selected Oklahoma bridges

	Ext. 1 Lane		Ext. 2+ Lanes		Int. 1 Lane		Int. 2+ Lanes	
	AASHTO LRFD	Grillage	AASHTO LRFD	Grillage	AASHTO LRFD	Grillage	AASHTO LRFD	Grillage
LRO	0.823	0.760	0.951	0.854	0.692	0.632	1.066	1.000
I244 A	0.478	0.467	0.649	0.497	0.556	0.402	0.791	0.688
I244 C	0.478	0.496	0.649	0.513	0.556	0.519	0.791	0.657

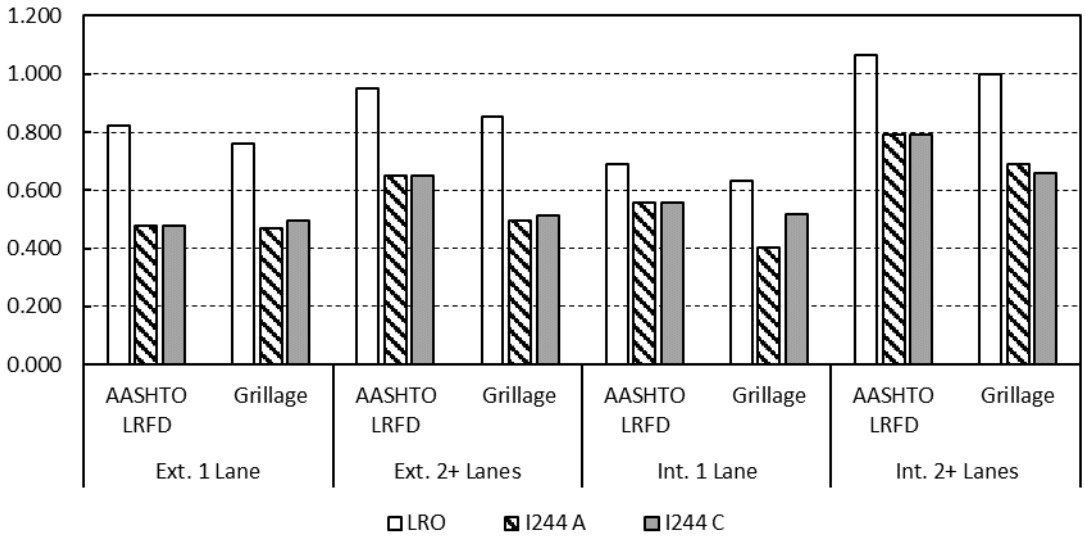

Figure 141: Comparison of distribution factors for selected Oklahoma bridges

Because the two spans of the I-244 bridge have the same girder spacing and the same edge distances, they have the same DFs according the AASHTO LRFD code. The grillage model shows that I-244C tends to have larger DFs than I-244A for most load cases except for interior girders loaded with 2+ lanes loaded. In some cases, the AASHTO DFs appear to be overly conservative for the I-244 spans (for two or more lanes loaded). On the other hand, there is agreement between the AASHTO LRFD code

and grillage DFs for the Little River Overflow. These results are examined further in the discussion (Section 5.4).

5.3 Discussion of Parametric Models

In Section 5.2.2, the results of the parametric models examined in this study were presented, comparing the DFs for the different variables studied. This section will expound on the results there and attempt to quantitatively assess combinations of these variables where the AASHTO LRFD code is more conservative or less conservative.

As stated in Section 5.2.2, spacing is the factor which influences load distribution the most. For bridges with middle and end diaphragms, the influence of girder spacing on ratio of AASHTO DF to grillage model DF is shown in Figure 142. This ratio is intended as a measure of the conservativism of the AASHTO factors as compared to those determined using grillage models. Obviously, the grillage factors should be compared to real bridges in the future, to verify their accuracy. For interior girders, the code tends to become less conservative at larger girder spacings. At a spacing of 6 ft the interior girder AASHTO DFs are 1.35 times the grillage model values for any span length. Conversely, at a 12 ft spacing this factor is between 1.1 and 1.15. On the other hand, exterior girders show the opposite trend of increasing conservativism with larger girder spacing. At a 6 ft spacing the code is only conservative by a factor of about 1.05 for exterior girders. This increases to between 1.13 and 1.16 for a 12 ft girder spacing. In general, it appears that the effects of deck thickness and span length have more of an effect on load distribution at larger girder spacings.

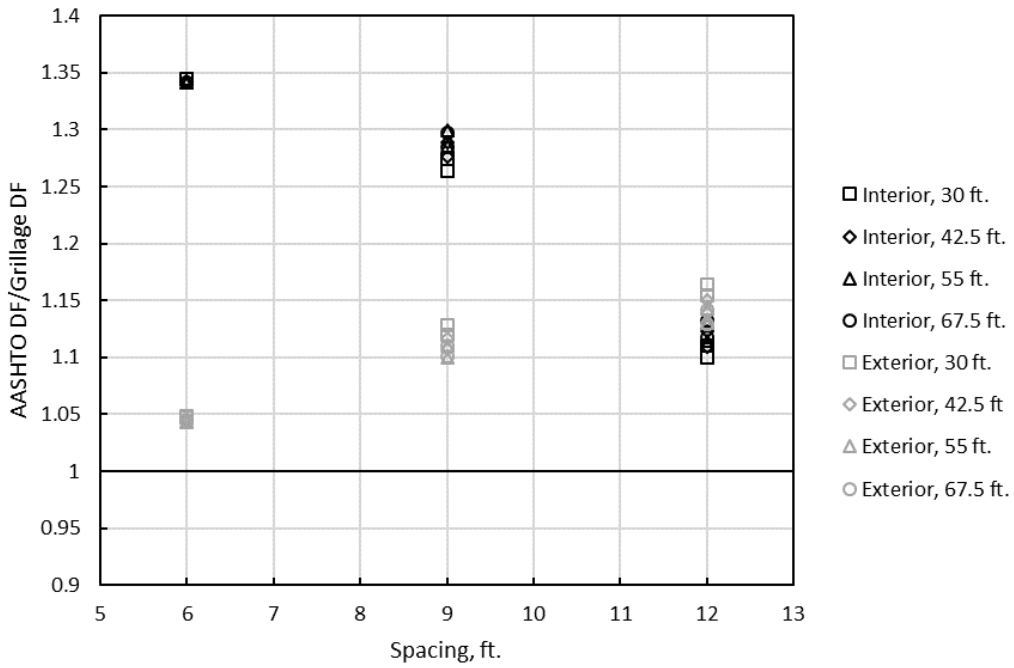

Figure 142: Conservativism of DFs for each girder spacing examined with diaphragms

Figure 143 shows the same comparison described above but for bridges with no diaphragms. The same trends are generally apparent as in Figure 142; decreasing conservativism for increasing length in interior girders, and the opposite for exterior girders. DFs tend to be slightly less conservative across the board for bridges with no diaphragms. In particular, exterior girders in bridges with no diaphragms and a 6 ft girder spacing are predicted very closely (~1.02). by the code.

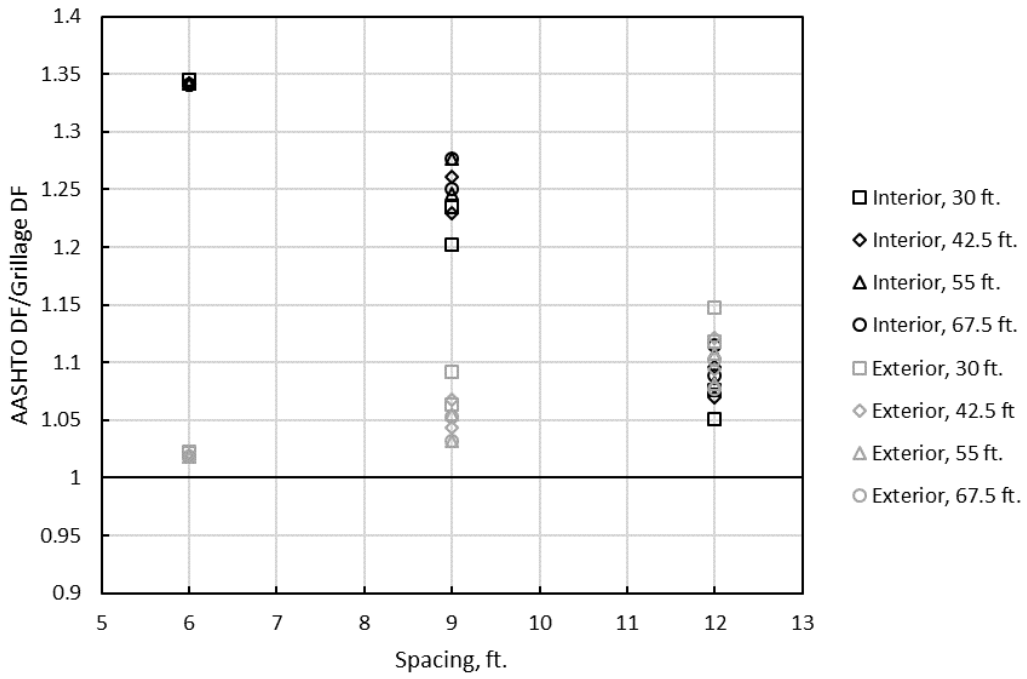

Figure 143: Conservativism of DFs for each girder spacing examined without diaphragms

For interior girders, longer spans tended to result in more conservative AASHTO DFs compared to those determined using grillage models. For exterior girders on the other hand, shorter spans resulted in more conservative DFs when other variables were equal. Slab thickness also affects the conservativism of the code factors compared to those derived using the grillage models, although to a lesser degree than spacing and span length. Interestingly, interior and exterior girders had alternate trends in the effects of slab thickness. For interior girders, increasing slab thickness increased conservativism; for exterior girders the opposite is true. The differences between AASHTO and grillage model DFs with varying slab thickness are very small however, so slab thickness does not affect load distribution as much as span length or spacing. Table 28 shows this comparison. The numbers in the table represent the average of the

AASHTO factors for varying lengths for the lengths divided by the grillage factors for the corresponding variables. Span length did not appear to alter the effects of slab thickness on load distribution.

Table 28: Conservativism of AASHTO LRFD code for varying slab thickness

s (ft)	t_s (in.)	Int. Diaphragm	Ext. Diaphragm	Int. No Diaphragm	Ext. No Diaphragm
6	7	1.342	1.045	1.342	1.020
	9	1.342	1.046	1.343	1.020
9	7	1.278	1.116	1.232	1.070
	9	1.290	1.107	1.262	1.043
12	7	1.110	1.150	1.073	1.120
	9	1.124	1.138	1.099	1.093

Figure 144 shows the percent difference for interior girder grillage model DFs for situations with or without diaphragms (factors decrease when diaphragms are included). In this figure, the two markers at each span length relate to the different slab thicknesses. Smaller slab thicknesses had larger percent differences when diaphragms were included in the model. At a girder spacing of 6 ft, diaphragms do not affect load distribution. A trend is similar for the 9 ft and 12 ft girder spacings, where the factors differ most for shorter span lengths. Factors are larger for the case where diaphragms are not present in all cases. At its largest, the difference is 4.9% (s=9 ft, t_s= 7 in., L=30 ft), which would correspond to a decrease in shear of about 2.4 kips for the design truck. The AASHTO DFs are the same in this case whether diaphragms are present or not.

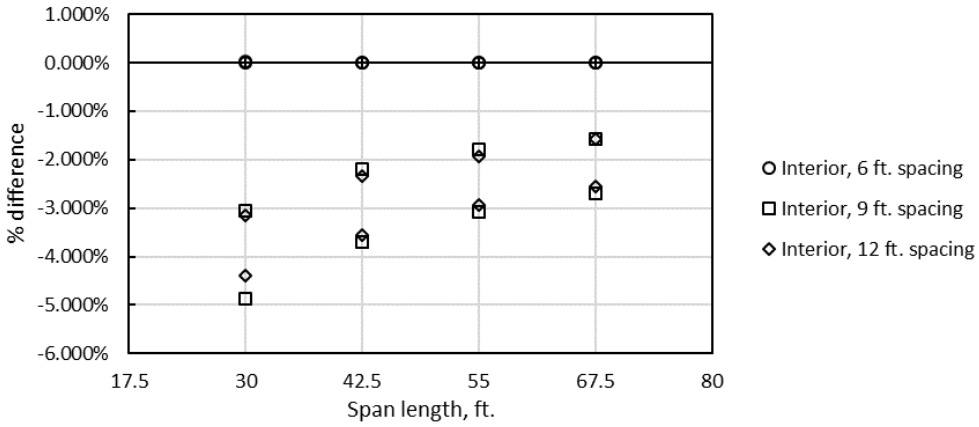

Figure 144: Difference in DFs for diaphragm versus no diaphragm for interior girders

Figure 145 shows the same information for exterior girders. The code accounts for diaphragms for exterior girders, unlike for interior girders (aforementioned "special analysis"). The opposite trend appears in this figure. Diaphragms increase DFs for exterior girders by almost the same degree as they decrease for interior girders. This effect is most apparent at shorter span lengths and larger girder spacings. Additionally, the difference is greater for 7 in. slabs than for 9 in. slabs at a given girder spacing and span length. Again, at shorter girder spacings (6 ft), diaphragms do not appear to affect load distribution.

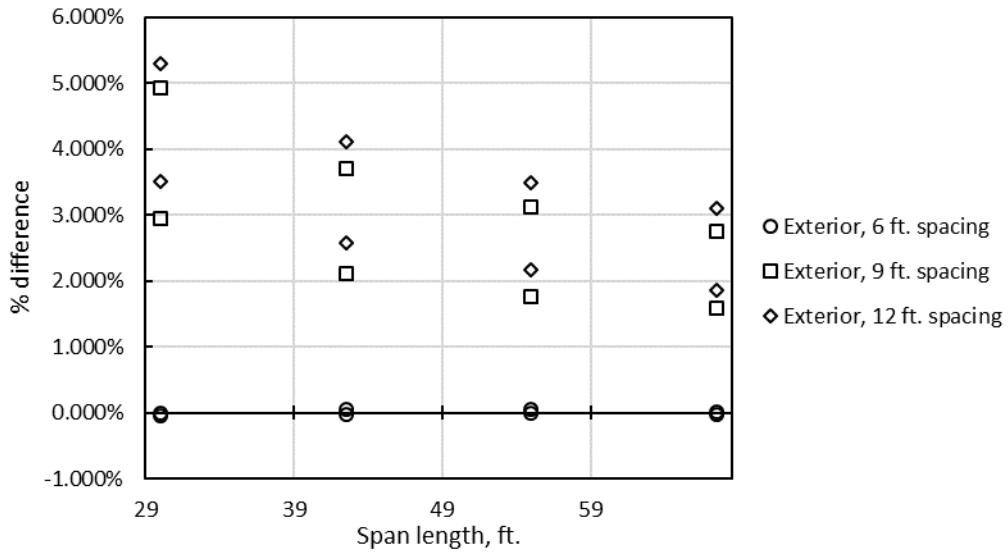

Figure 145: Difference in DFs for diaphragm versus no diaphragm for exterior girders

The implication of this information related to diaphragm effects on load distribution is that for exterior girders in bridges without diaphragms, the code DFs will tend to be less conservative at any length and spacing. Additionally, for interior girders, the opposite is true; the DFs are more conservative when diaphragms are present than when they are not.

In summary, the conservativism of the code DFs is primarily affected by girder spacing. For interior girders, smaller girder spacings (6 ft) result in very conservative DFs (1.35x), while the widest spacings (12 ft) are still conservative, although to a lesser degree (1.05x). The opposite trend was apparent for exterior girders, where a larger spacing resulted in a larger level of conservativism. In general, the code DFs are less conservative for exterior girders than interior girders except at larger girder spacings. The presence of diaphragms appears to cause the opposite effects for interior and exterior girders; diaphragms decrease DFs for interior girders and increase DFs for

exterior girders. The code accounts for this behavior for exterior girders, but not for interior girders. In general, the code factors are less conservative for interior and exterior girders without diaphragms than with diaphragms. Span length and slab thickness affect the conservativism of the code factors more when diaphragms are not present than when they are present. Span length has more of an effect on load distribution for larger girder spacings. Shorter span lengths lead to less conservative DFs for interior girders, and more conservative DFs for exterior girders. Finally, slab thickness has the smallest effect on distribution of all the factors examined for the two thicknesses modeled. The code is less conservative for thicker slabs for exterior girders, and more conservative for thicker slabs for interior girders.

5.4 Discussion of Oklahoma Bridge Models

First, the Oklahoma bridge grillage models are compared with the AASHTO DFs to determine how well the code matched these particular cases. The DFs for both cases were given in Section 5.2.3, but Figure 146 shows the ratio of AASHTO DF to grillage model DF (note: the multiple presence factor was removed from the one lane loaded AASHTO LRFD code DFs). Compared this way, a number greater than 1.0 indicates a conservative estimate of load distribution, and a number less than one indicates the DF is underpredicted by AASHTO compared to the grillage model. The DFs are typically quite accurate. For the I-244C bridge span, the DFs are governed by two or more lanes loaded for both exterior and interior girders. For these cases, the code is conservative relative to grillage model DFs by 0.265 and 0.204, respectively (26.5% and 20.4% more shear), based on the governing DFs. For the I-244A span, the distribution is governed by two or more lanes loaded for exterior girders and interior

girders. For these cases, the code is conservative by a factor of 0.305 and 0.150, respectively. This results in an increase in shear demand of 30.5% for exterior girders and 15.0% for interior girders. This difference represents an added degree of conservativism to an already conservative process of rating bridges for shear.

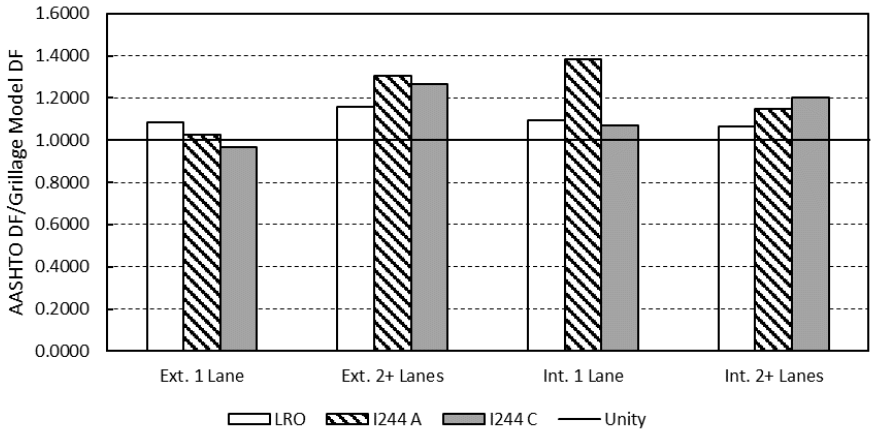

Figure 146: Distribution factor ratios for specific Oklahoma bridges

The AASHTO LRFD code predicts DFs for the LRO bridge relatively more accurately. The LRO bridge DFs are governed by two or more lanes loaded for exterior and interior girders. These factors differ from the code factors by 13.0% and 6.7% (corresponding to the same increase in shear), respectively. The DFs for the LRO are larger than those for the I-244 bridge, so as Figure 146 shows, these differences are proportionally less than for the spans of the I-244 bridge.

The conservativism of the governing AASHTO DFs for each case is shown in Figure 147. The trends in this figure conform to the observations made in the previous section. For the two spans of the I-244 bridge, longer spans tend to increase conservativism for interior girders and decrease it for exterior girders. On the other hand, the DFs for the LRO bridge are the least conservative of the three bridges. Since

this bridge had the largest girder spacing, less conservative DFs were expected based on the parametric modeling. For these real Oklahoma bridges, the results of the parametric model study are confirmed.

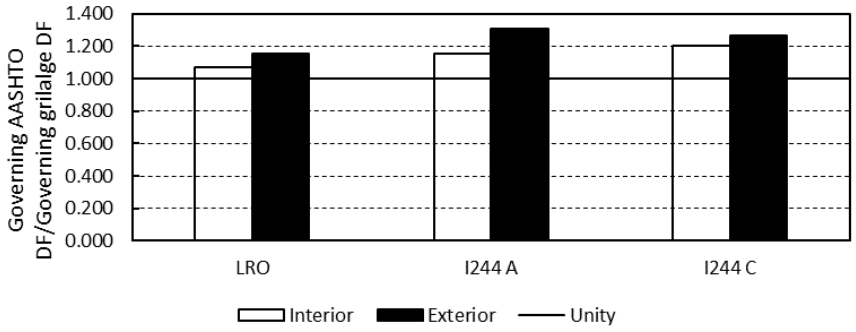

Figure 147: AASHTO DF/Grillage model DF for Oklahoma bridges

Grillage models can be used to provide better information on the load rating of bridges (Dymond, French, & Shield, 2016). In the hands of an experienced modeler grillages are simple to create and provide a more realistic prediction of load distribution. These three bridges were load rated in LEAP Concrete Bridge against the HL-93 load and the results of this rating are given in Table 29. These ratings are developed based on the code DF equations. Almost all girders rate well for shear. The only case where the rating is relatively low is for the LRO interior girders at the inventory rating. The rating factors determined using grillage DFs for these bridges are shown in Table 30. Across the board, the ratings increase when grillage models are used to evaluate DFs. For these bridges, some of the increases are significant.

Table 29: Shear load ratings for the three bridges of interest (using AASHTO DFs)

Ratings	**Inventory**		**Operating**	
(HL-93)	**Ext.**	**Int.**	**Ext.**	**Int.**
LRO	1.60	1.45	2.10	1.90
I244 A	3.97	2.26	5.15	4.08
I244 C	2.83	2.08	3.70	2.98

Table 30: Shear load ratings for the three bridges of interest (using grillage DFs)

Ratings	**Inventory**		**Operating**	
(HL93)	**Ext.**	**Int.**	**Ext.**	**Int.**
LRO	1.86	1.55	2.43	2.03
I244 A	5.20	3.64	6.74	4.85
I244 C	3.59	2.64	4.70	3.60

A comparison is given in Figure 148, this figure shows the ratio of grillage model rating factor to AASHTO rating factor. A rating factor greater than unity indicates the bridge is capable of carrying current design loads. Larger numbers would mean a greater factor of safety compared to current demands. The code DFs result in a particularly conservative rating for the I-244A bridge span. The smaller girder spacings of I-244A and C result in more conservative DFs as explained in Section 5.2.3.5. The LRO bridge rating is still greater than one, though by a slimmer margin. This conforms to the trend observed in the previous section of decreasing conservativism with increasing girder spacing for interior girders. The I-244A bridge rating was more conservative than the rating for I-244C span; this was a result of the differing lengths of the two spans. Because the spans were the same in terms of number of girders and spacing, the DFs were the same according to the code.

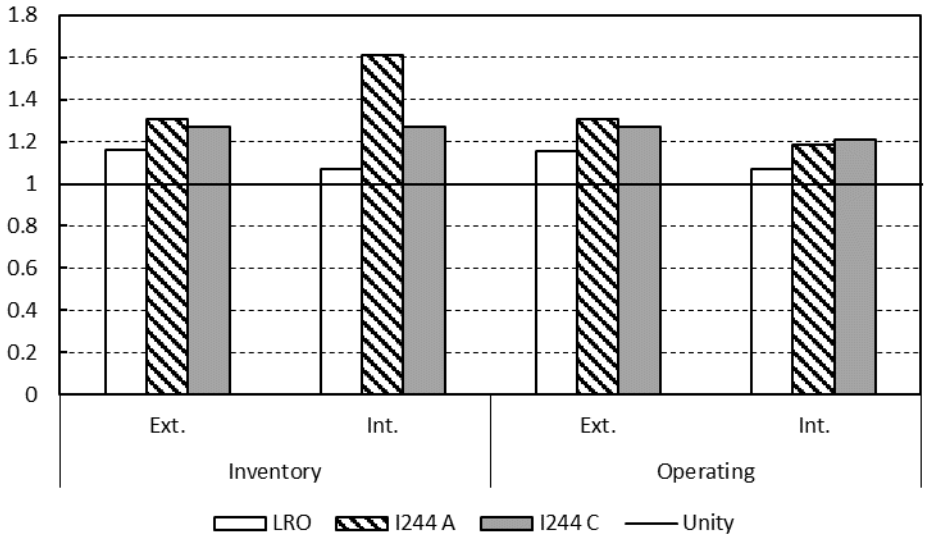

Figure 148: Grillage rating factors/AASHTO rating factors

In summary, for these selected bridges, the DFs provided by grillage models would increase the rating factors, allowing for larger permit loads and potentially increasing the life of the bridges. While these particular bridges rated well for shear, there may be examples of bridges that have rating factors closer to unity but whose DFs are overly conservative. In these cases, a grillage model could decrease DFs and increase the usable life of the bridge, saving time, money, and lost productivity upon replacing the bridge. For the bridges modeled in this study, the rating factors are increased with the use of grillage model DFs, allowing larger permit vehicles and giving a truer picture of the distribution behavior of the bridges.

Chapter 6: Conclusions and Recommendations

This dissertation reported a study that included three main components: full-scale shear tests of roughly 45-year-old prestressed AASHTO Type-II girders, testing of scale girders and a scale bridge section to its ultimate capacity, and a parametric study of factors influencing load distribution in Type-II girder bridges. Individually, these investigations each fill in areas in the literature that are lacking in depth of information. Few shear tests of older girders in shear have been performed, and few composite bridges have been tested to their ultimate capacity. Additionally, the use of grillage models has been somewhat limited compared to the potential of grillage modeling for better prediction of DFs. Taken as a whole, the three portions of this dissertation also provide a more holistic study of the behavior of a common bridge: the older Type-II girder bridge.

6.1 Conclusions from Full-Scale Testing

In the full-scale testing, the goal was to investigate the effects of age on the shear behavior. Tests were performed on two girders with different prestress forces and amounts of the original deck and diaphragms left intact. The test locations were chosen to encapsulate the shear performance from the quarter-point to two girder depths from the end. Of particular interest in these tests was the corrosion at both ends of each girder and whether this corrosion impacted the performance. Overall, the girders performed well despite their being in service for over 45 years. Regarding the ultimate capacities and qualitative performance, the girders generally exceeded predicted capacities and their failures were characterized by significant deflection and shear and flexural cracking. The main conclusions from the girder tests were as follows:

1. Experimental values were greater than the calculated capacities when the AASHTO MCFT shear methodologies (beta-theta equations or tables) or flexural capacity by strain compatibility were used. The beta-theta equations were the most conservative estimators of shear strength. The experimental capacities of the girders exceeded their current design demands. Tests were performed at *a/d* ratios of 2.0 or greater, so it was more likely that B-region behavior controlled.
2. The 1973 Standard Specifications resulted in unconservative predictions of shear strength compared to the experimental values. The current AASHTO simplified method was also unconservative in some cases. On the other hand, the ACI shear method was reasonably accurate and more conservative than the AASHTO simplified method.
3. Strand slip was observed in two tests and was considered to cause shear failures. The slip is potentially related to corrosion at the ends, but the loss in bond did not result in an underestimation of ultimate capacity. Despite slip, the MCFT method predicted shear capacity conservatively. Slip also did not lead to sudden shear failures.
4. Deck overlays on the girders were the initiating point of failure and limited the ultimate capacity in every test.
5. The partial remaining diaphragms were not observed to influence the failures, although the connections at the girder web were seen to cause some cracking during the tests potentially related to differential deformation of the girders and the diaphragms.

6. While shear capacities did not appear to be negatively influenced by corrosion, the presence of cracking due to corrosion caused bearing issues. This potential for cracking could be a serviceability issue for girders with similar levels of damage. This research revealed that unfactored shear demands for longer span bridges of this type were of a magnitude sufficient to cause additional damage to corroded girder ends, thereby exacerbating durability issues.

6.2 Conclusions from Scale Testing

Issues with bond reduced the applicability of the scale individual tests. These tests indicated that the partial diaphragms did not appear to significantly affect shear capacities. The diaphragms potentially limited flexure-shear cracking near midspan. Despite the limitation of the individual girders there were many new results from the corresponding scale bridge test. Since there are so few detailed tests of concrete bridges to failure, this information is of special importance. Specific conclusions are as follows:

1. Diaphragms can affect failure mechanisms in bridges, potentially causing torsion in exterior girders and pullout of the diaphragm connections.
2. Diaphragms appear to provide an important load transfer mechanism after damage in longitudinal girders.
3. When longitudinal members fail, the slab begins to carry the full load. As reported elsewhere (Dymond et al., 2016; Miller et al., 1994) the failure is often controlled by punching shear at this point. Notably, the slab appears to behave as a two-way edge supported slab that transfers load to the support primarily through the end diaphragm.

4. Grillage models were used to predict the load distribution in the scale bridge with reasonable accuracy.
5. While load distribution is altered slightly upon failure, applying the experimental DF (from elastic range tests) to the ultimate load placed on the bridge resulted in an ultimate load for the loaded girder that corresponded very closely to the expected flexural capacity and the capacity of same girder tested individually (A1s).

6.3 Conclusions from Grillage Modeling

A grillage model was found to provide realistic estimates of load distribution for the scale bridge constructed in this study. Furthermore, the method used to construct the grillage model presented in this dissertation was simple and rational. As a method to determine load distribution in bridges, grillage models are a very promising alternative to the DF equations in the AASHTO LRFD code. The parametric study that followed from this grillage model compared DFs for AASHTO Type-II girder bridges of varying dimensions that were found to be common in Oklahoma. Some results from the parametric models are as follows:

1. AASHTO DF were generally found to be conservative for the bridges modeled, by a varying degree depending on the parameters in question.
2. Spacing most influenced the level of conservativism. For interior girders, DFs tended to be very conservative at small girder spacings and less so for larger spacings. On the other hand, the DFs for exterior girders were much less conservative at small girder spacings. At larger spacings, interior girders had DFs roughly as conservative as for exterior girders. For girder spacings 9 ft or

greater in bridges with diaphragms the AASHTO factors were at least 1.1 times the grillage model DFs.

3. Span length was also found to affect DFs differently for interior and exterior girders. For interior girders, longer spans resulted in more conservative DFs but the opposite was true for exterior girders.
4. Diaphragms were found to be less important than girder spacing and span length in predicting DFs. Diaphragms changed DFs by as much as 4.9%. Their effects were greater for shorter spans and wider girder spacings. Diaphragms also distributed more load with thinner slabs for the two slab thicknesses examined.
5. Slab thickness was found to influence distribution less than the other factors investigated in this dissertation, although only two thicknesses were compared here since typical Oklahoma bridges have between 7 in. and 9 in. slabs. Thicker slabs will obviously distribute more load than thinner ones.

The most important result is that AASHTO factors are nearly always conservative when compared to the results of grillage models presented in this dissertation. A result of this finding is that if older bridges being load rated are modeled, their rating factors can be increased if grillage models are used to determine the DFs instead of the code equations. This procedure is allowed by the code. This does not result in a decrease in known safety level, but rather the elimination of an unnecessary level of conservativism. This finding was supported by the ratings of the selected Oklahoma bridges modeled and load rated in Sections 5.2.3 and 5.4. It was seen that the most conservative rating factors (in relation to the grillage derived rating factors) will be found in short bridges with smaller girder spacings (I-244A). These bridges will be

less of a concern at the load rating stage as they will tend to have conservative ratings (the demands will be artificially higher due to larger DFs from the code). On the other hand, less conservative ratings would be expected for long bridges (I-244C) or those with wide girder spacings (LRO).

6.4 Overall Conclusions

When rating older AASHTO Type-II girder bridges, it should be understood that the AASHTO DFs may add more conservativism to an already conservative process. Money and time can be saved for some bridges when the code DFs are replaced by grillage model derived DFs for load rating these types of bridges. Using a grillage model can increase load ratings, reducing the need to take some bridges out of service without sacrificing accuracy and safety. The girders tested in this study mostly reached expected capacities despite differences in the code at the time they were designed. The MCFT methods are the best for use in rating older girders due to their balance of accuracy and conservativism. End region corrosion visible in the tested girders was not seen to affect ultimate capacity, but potentially led to strand slip and influenced the failure mechanism. End region corrosion also led to bearing damage in one test at shear force levels which could reasonably be expected to occur in service for AASHTO Type-II girder spans. With the results of the shear testing and the findings of the grillage models, there may be conservativism built in when AASHTO DFs and the MCFT methods are used that leaves open the possibility of increased load ratings for some older bridges based on the girder tests in this dissertation. Shear behavior in beam tests is known to be highly variable, limiting the scope of the conclusions drawn from

individual tests. The results here should be considered in conjunction with other similar shear tests of older girders.

The scale bridge section uncovered interesting results in the behavior of bridges at ultimate loads. DFs from grillage models can accurately relate the expected capacity of a single bridge girder to the expected capacity of the entire bridge section. Diaphragms were not seen to significantly affect load distribution, but if they are connected to the deck they provide an important means of load transfer in the case when a girder fails.

This dissertation described three distinct studies that provide new information to the body of knowledge. Load distribution characteristics specific to Type-II girder spans were not found in the literature and will help ODOT and other departments of transportation evaluate the performance of their older bridges. The tests of the older girders add to a limited database of similar tests and provide information about the effects of corrosion in the end regions, which is not found in many studies. Finally, the scale bridge test represents an important addition to the understanding of ultimate bridge behavior. There have been surprisingly few tests of full bridge sections around the country, and clearly the ultimate behavior of a bridge can be best understood through experimental testing.

6.5 Suggestions for Future Research

This study achieved many of its stated goals, but there are some areas which future research could more elaborately investigate. The grillage models reported in the parametric study were verified based on the scale bridge. Ideally these should be checked against factors for real-world bridges. A study which compared this modeling

paradigm with results from field tests would be valuable in confirming the methods (although grillage models have been verified in some past research explained in the literature review). A study comparing the results of grillage models to bridges with skew, different girder types, and varying geometry would be useful in particular. In order to more fully understand the impact of corrosion on older girders it would be ideal to test several similar girders with varying levels of corrosion and compare results. Both girders tested in this study had similar levels of corrosion. The results of the scale bridge test provided insights into the behavior of bridges at ultimate load, more testing like this is recommended for varying spacings and lengths of bridges. The findings in this study related to end diaphragms and slab behavior post-cracking or post-girder failure should be verified by future testing. Finally, this study made recommendations related to load rating of bridges, including which shear methods are more conservative and how grillage model derived DFs can increase load ratings. These findings should be confirmed against some bridges that rate closer to unity for shear, or that rate poorly.

References

AASHTO. (1973). *Standard Specifications for Highway Bridges*. Washington, D.C.: AASHTO.

AASHTO. (2002). *Standard Specifications for Highway Bridges*. Washington, D.C.: AASHTO.

AASHTO. (2011). *Manual for Bridge Evaluation*. Washington, D.C.: AASHTO.

AASHTO. (2012). *AASHTO LRFD Bridge Design Specifications*. Washington, D.C.: American Association of State Highway and Transportation Officials.

AASHTO. (2015). *AASHTO LRFD Bridge Design Specifications* (7th ed.). Washington, D.C.: American Association of State Highway and Transportation Officials.

ACI Committee 318. (2014). *Building Code Requirements for Structural Concrete (ACI 318-14) and Commentary*. American Concrete Institute.

Altay, A. K., Arabbo, D. S., Corwin, E. B., Dexter, R. J., & French, C. E. (2003). *Effects of increasing truck weight on steel and prestressed bridges*. St. Paul, MN: Minnesota Department of Transportation.

ASTM. (2012). *C1064: Standard Test Method for Temperature of Freshly Mixed Concrete*. West Conshohocken, PA: ASTM International.

ASTM. (2014). *C469: Standard Test Method for Static Modulus of Elasticity and Poisson's Ratio of Concrete in Compression*. West Conshohocken, PA: ASTM International.

ASTM. (2015). *ASTM C31: Standard Practice for Making and Curing Concrete Test Specimens in the Field*. West Conshohocken, PA: ASTM International.

ASTM. (2015). *C143: Standard Test Method for Slump of Hydraulic-Cement Concrete*. West Conshohocken, PA: ASTM International.

ASTM. (2016). *ASTM 1061: Standard Test Methods for Testing Multi-Wire Steel Prestressing Strand*. West Conshohocken, PA: ASTM International.

ASTM. (2016). C42: *Standard Test Method for Obtaining and Testing Drilled Cores and Sawed Beams of Concrete*. West Conshohocken, PA: ASTM International.

ASTM. (2017). *ASTM C231: Standard Test Method for Air Content of Freshly Mixed Concrete by the Pressure Method*. West Conshohocken, PA: ASTM International.

ASTM. (2017). *ASTM C39: Standard Test Method for Compressive Strength of Cylindrical Concrete Specimens*. West Conshohocken, PA: ASTM International.

ASTM. (2017). *C138: Standard Test Method for Density (Unit Weight), Yield, and Air Content (Gravimetric) of Concrete*. West Conshohocken, PA: ASTM International.

Barr, P. J., Eberhard, M. O., & Stanton, J. F. (2001). Live-Load Distribution Factors in Prestressed Concrete Girder Bridges. *Journal of Bridge Engineering*, 298-306.

Bechtel, A., McConnell, J., & Chajes, M. (2011). Ultimate Capacity Destructive Testing and Finite-Element Analysis of Steel I-Girder Bridges. *Journal of Bridge Engineering*, 16(2), 197-206.

Bentley Systems, Inc. (2016). LEAP Bridge Concrete CONNECT Edition. (16.00.00.24).

Bentz, E. C., Vecchio, F. J., & Collins, M. P. (2006). Simplified Modified Compression Field Theory for Calculating Shear Strength of Reinforced Concrete Elements. *ACI Structural Journal*, 103(4), 614-624.

Burdette, E. G., & Goodpasture, D. W. (1973). Tests of four highway bridges to failure. *Journal of the Structural Division*, 99(3), 335-348.

Cranor, B. N. (2015). *Analysis and Experimental Testing for Shear Behavior of an AASHTO Type II Girder in Service for Several Decades*. Norman, OK: The University of Oklahoma.

Cross, B., Panahshahi, N., Vaughn, B., Petermeier, D., & Siow, Y. (2006). *Investigation of Select LRFD Design Factors Through Instrumentation of Bridge Bearings*. Springfield, IL: Illinois Department of Transportation.

Cross, B., Vaughn , B., Panahshahi, N., Petermeier, D., Shuenn Siow, Y., & Domagalski, T. (2009). Analytical and Experimental Investigation of Bridge Girder Shear Distribution Factors. *Journal of Bridge Engineering*, 154-163.

Dymond, B. Z., French, C. E., & Shield, C. K. (2016). *Investigation of Shear Distribution Factors in Prestressed Concrete Girder Bridges*. University of Minnesota. St. Paul: Minnesota Department of Transportation.

Elzanaty, A. H., Nilson, A. H., & Slate, F. O. (1986). Shear capacity of prestressed concrete beams using high-strength concrete. *ACI Journal*, 83(3).

FDOT. (2013, July). *Florida Department of Transportation*. Retrieved from FDOT.com: http://www.fdot.gov/roadway/ds/14/ids/ids-20120.pdf

Federal Highway Administration. (2016, February 19). *National Bridge Inventory*. Retrieved from https://www.fhwa.dot.gov/bridge/nbi.cfm

Floyd, R. W., Pei, J. S., Murray, C. D., Cranor, B., & Tang, P. F. (2016). *Understanding the Behavior of Prestressed Girders After Years of Service*. Oklahoma City, OK: Oklahoma Department of Transportation.

Fu, G. (2013). *Bridge Design and Evaluation: LRFD and LRFR*. Hoboken, NJ: John Wiley & Sons.

Ghali, A., & Neville, A. M. (1997). *Structural Analysis: A Unified Classical and Matrix Approach (4th ed.)*. London: Spon.

Guyon, Y. (1953). *Prestressed Concrete*. New York, NY: John Wiley.

Halsey, T. J., & Miller, R. (1996). Destructive Testing of Two Forty-Year-Old Prestressed Concrete Bridge Beams. *PCI Journal*.

Hambly, E. C. (1991). *Bridge deck Behaviour (2nd ed.)*. CRC Press.

Hamilton III, H. R., Llanos, G., & Ross, B. E. (2009). *Shear Performance of Existing Prestressed Concrete Bridge Girders*. Gainesville, FL: University of Florida Department of Civil & Coastal Engineering.

Hanson, J. M., & Hulsbos, C. L. (1964). Ultimate Shear Tests Of Prestressed Concrete I-Beams Under Concentrated And Uniform Loadings. *PCI Journal*, 9(3), 15-28.

Hanson, N. W., & Kaar, P. H. (1959). Flexural bond tests of pretensioned prestressed beams. *Journal of the American Concrete Institute, proceedings*, 55(7), 783-802.

Hawkins, N. M., Kuchma, D. A., Mast, R. F., & Reineck, K.-H. (2005). *NCHRP 549: Simplified Shear Design of Concrete Members*. Washington, D.C.: Transportation Reseach Board.

Jorgenson, J. L., & Lawson, W. (1972). Field testing of a reinforced concrete highway bridge to collapse. *Transportation Research Record*, 607, 66-71.

Kaufman, K. M., & Ramirez, J. A. (1988). Re-evaluation of the ultimate shear behavior of high-strength concrete prestressed I-beams. *ACI Structural Journal*.

Lightfoot, E., & Sawko, F. (1959). Structural frame analysis by electronic computer: grid frameworks resolved by generalized slope deflection. *Engineering*, 18-20.

MacGregor, J. G., & Hanson, J. M. (1969). Proposed Changes in Shear Provisions for Reinforced and Prestressed Concrete Beams. *ACI Journal*.

MacGregor, J. G., Sozen, M. A., & Siess, C. (1965, December). Strength of prestressed concrete beams with web reinforcement. *ACI Journal Proceedings*, 62(12).

Martin, R. D., Kang, T. H.-K., & Pei, J.-S. (2011). Experimental and code analyses for shear design of AASHTO prestressed concrete girders. *PCI Journal*.

Mayhorn, D. T. (2016). *Investigation of the effects of end region deterioration in precast, prestressed concrete bridge girders*. Norman, OK: The University of Oklahoma.

Mehta, P. K., & Monteiro, P. J. (2006). *Concrete Microstructure, Properties, and Materials*. New York, NY: McGraw-Hill.

Mertz, D. (2006). *NCHRP Report 592: Simplified Live Load Distribution Factor Equations*. Washington, D.C.: NCHRP.

Miller, R. A., Aktan, A. E., & Shahrooz, B. M. (1994). Destructive Testing of Decommissioned Concrete Slab Bridge. *Journal of Structural Engineering*, 120(7), 2176-2198.

Morcous, G., Hanna, K., & Tadros, M. K. (2011). Use of 0.7-in.-diameter strans in pretensioned bridge girders. *PCI Journal*, 65-82.

Naji, B., Ross, B. E., & Floyd, R. W. (2017). Characterization of bond-loss failures in pretensioned concrete girders. *Journal of Bridge Engineering*.

Nasser, G. D., Tadros, M., Sevenker, A., & Nasser, D. (2015). The legacy and future of an American icon: The precast, prestressed concrete double tee. *PCI Journal*.

National Instruments. (2016). LabVIEW System Design Software. Austin, TX.

Newmark, N. M., Siess, C. P., & Peckham, R. R. (1946). *Studies of Slab and Beam Highway Bridges. Part I: Tests of Simple Span Highway Bridges*. Urbana, IL: University of Illinois.

Nordby, G. M., & Venuti, W. J. (1957). Fatigue and Static Tests of Steel Strand Prestressed Beams of Expanded Shale Concrete and Conventional Concrete. *Journal of the American Concrete Institute*.

Nutt, R. V., Schamber, R. A., & Zokaie, T. (1988). *NCHRP 12-26: Distribution of Wheel Loads on Highway Bridges*. Washington, D.C.: Transportation Research Board.

O'Brien, E. J., & Keogh, D. L. (1999). *Bridge deck analysis (1st ed.)*. E & FN Spon.

ODOT. (2016, December). *Bridge Design Standards & Specifications*. Retrieved from Oklahoma Department of Transportation: http://www.okladot.state.ok.us/bridge/2009-sb/brd_std_2009-lrfd-sb-index.php

Osborn, G. P., Barr, P. J., Petty, D. A., Halling, M. W., & Brackus, T. R. (2010). Residual prestress forces and shear capacity of salvaged prestressed concrete bridge girders. *Journal of Bridge Engineering*, 17(2), 302-309.

Patrick, M. D., Huo, X. S., Puckett, J. A., Jablin, M., & Mertz, D. (2006). Sensitivity of Live Load Distribution Factors to Vehicle Spacing (technical note). *Journal of Bridge Engineering*, 131-134.

Pessiki, S., Kaczinski, M., & Wescott, R. H. (1996). Evaluation of Effective Prestress Force in 28-Year-Old Prestressed Concrete Bridge Beams . *PCI Journal*.

Peterman, R. J., Ramirez, J. A., & Olek, J. (2000). Influence of flexure-shear cracking on strand development length in prestressed concrete members. *PCI Journal*, 45(5), 76-94.

Petersen-Gauthier, J. A. (2013). *Application of the grillage methodology to determine load distribution factors for spread slab beam bridges*. College Station, TX: Texas A&M University.

Ross, B. E., Ansley, M. H., & Hamilton III, H. R. (2011). Load Testing of 30-Year-Old AASHTO Type-III Highway Bridge Girders. *PCI Journal*.

Runzell, B., Shield, C., & French, C. (2007). *Shear Capacity of Prestressed Concrete Beams*. St. Paul, MN: Minnesota Department of Transportation.

Russell, B. W., & Burns, N. H. (1996). Measured Transfer Lengths of 0.5 and 0.6 in. Strands in Pretensioned Concrete. *PCI Journal, 41*(5), 44-65.

Sanayei, M., Reiff, A. .., Brenner, B. R., & Imbaro, G. R. (2015). Load rating of a fully instrumented bridge: comparison of LRFR approaches. *Journal of Performance of Constructed Facilities*.

Shahawy, M. A., & Batchelor, B. (1996). Shear Behavior of Full-Scale Prestressed Concrete Girders: Comparison Between AASHTO Specifications and LRFD Code. *PCI Journal*, 48-62.

Shenoy, C. V., & Frantz, G. C. (1991). Structural Tests of 27-Year-Old Prestressed Concrete Bridge Beams. *PCI Journal*.

Sotelino, E. D., Liu, J., Chung, W., & Phuvoravan, K. (2004). *Simplified Load Distribution Factor for Use in LRFD Design.* Indianapolis, IN: Indiana Department of Transporation.

Taly, N. (2014). *Highway bridge superstructure engineering: LRFD approaches to design and analysis.* CRC Press.

Vecchio, F. J., & Collins, M. P. (1986). The Modified Compression-Field Theory for Reinforced Concrete Elements Subjected to Shear. *ACI Journal*.

Westergaard, H. M. (1930). Computations of Stresses in Bridge Slabs Due to Wheel Loads. *Public Roads, 11*(1), 1-23.

Wight, J. K., & MacGregor, J. G. (2012). *Reinforced Concrete: Mechanics and Design.* Upper Saddle River, NJ: Pearson Education, Inc.

Zia, P., & Mostafa, T. (1977). Development Length of Prestressing Strands. *PCI Journal*.

Zokaie, T. (2000). AASHTO-LRFD Live Load Distribution Specifications. *Journal of Bridge Engineering, 5*(2), 131-138.

Zokaie, T., Imbsen, R. A., & Okstercamp, T. A. (1991b). Distribution of wheel loads on highway bridges. *Transportation Research Record Report 1290* (pp. 119-126). Washington, D.C.: Transportation Research Board.

Zokaie, T., Osterkamp, T. A., & Imbsen, R. A. (1991a). *NCHRP report 12-2611: Distribution of wheel loads on highway bridges.* Washington, D.C.: Transportation Research Board.

Zwoyer, E. M., & Siess, C. P. (1954). Ultimate strength in shear of simply-supported prestressed concrete beams without web reinforcement. *ACI Journal, 51*(10).

Appendix A: Instrumentation Pictures, Matlab Code, and Analysis Examples

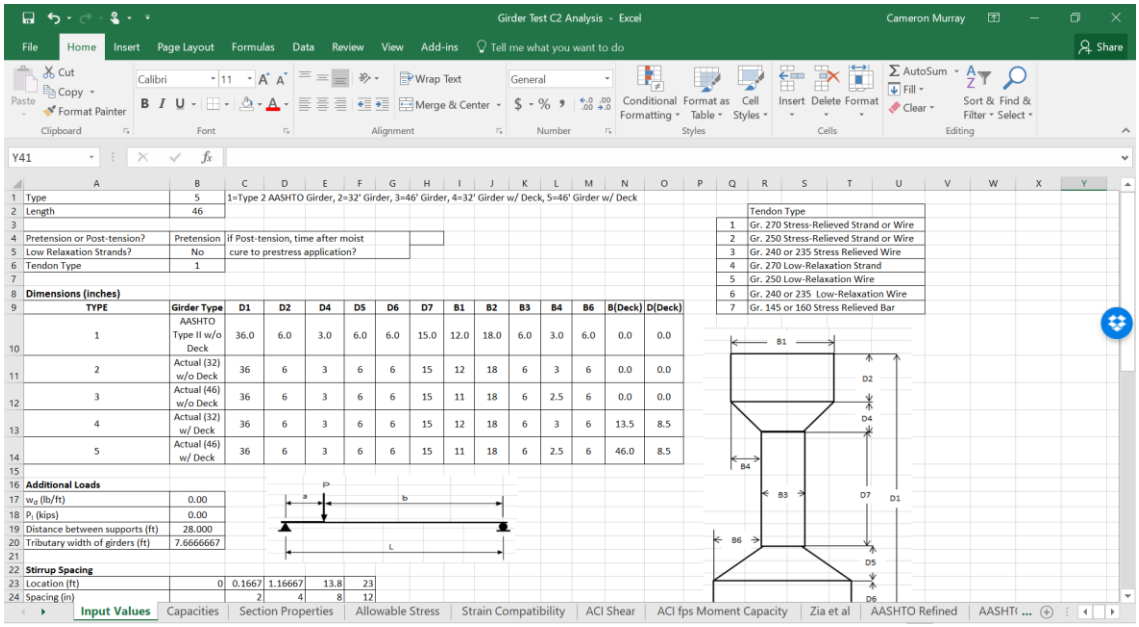

1	Type	5	1=Type 2 AASHTO Girder, 2=32' Girder, 3=46' Girder, 4=32' Girder w/ Deck, 5=46' Girder w/ Deck
2	Length	46	
3			
4	Pretension or Post-tension?	Pretension	if Post-tension, time after moist
5	Low Relaxation Strands?	No	cure to prestress application?
6	Tendon Type	1	

	Tendon Type
1	Gr. 270 Stress-Relieved Strand or Wire
2	Gr. 250 Stress-Relieved Strand or Wire
3	Gr. 240 or 235 Stress Relieved Wire
4	Gr. 270 Low-Relaxation Strand
5	Gr. 250 Low-Relaxation Wire
6	Gr. 240 or 235 Low-Relaxation Wire
7	Gr. 145 or 160 Stress Relieved Bar

Dimensions (inches)

TYPE	Girder Type	D1	D2	D4	D5	D6	D7	B1	B2	B3	B4	B6	B(Deck)	D(Deck)
1	AASHTO Type II w/o Deck	36.0	6.0	3.0	6.0	6.0	15.0	12.0	18.0	6.0	3.0	6.0	0.0	0.0
2	Actual (32) w/o Deck	36	6	3	6	6	15	12	18	6	3	6	0.0	0.0
3	Actual (46) w/o Deck	36	6	3	6	6	15	11	18	6	2.5	6	0.0	0.0
4	Actual (32) w/ Deck	36	6	3	6	6	15	12	18	6	3	6	13.5	8.5
5	Actual (46) w/ Deck	36	6	3	6	6	15	11	18	6	2.5	6	46.0	8.5

Additional Loads

17	w_d (lb/ft)	0.00
18	P, (kips)	0.00
19	Distance between supports (ft)	28.000
20	Tributary width of girders (ft)	7.6666667

Stirrup Spacing

23	Location (ft)	0	0.1667	1.16667	13.8	23
24	Spacing (in)		2	4	8	12

Figure 149: Screen capture of inputs for girder analysis spreadsheet

Figure 150: Scale bridge with load set up shown

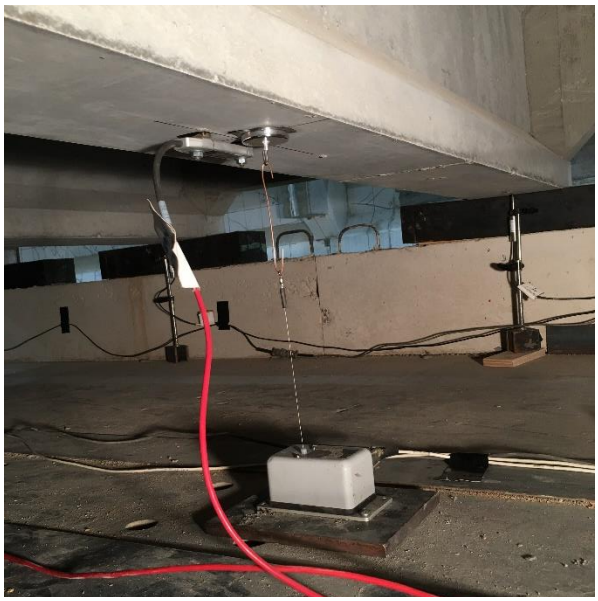

Figure 151: Scale bridge wire pot, girder strain gauge, and bearing deflection locations

Figure 152: Scale bridge instrument locations, including strain gauge at center of slab span (top of picture)

Figure 153: LVDT positioned to measure deflection at bearing

Figure 154: Deflection measurement under load point showing LVDT and wire pot (note tabs remaining for attachment of BDI strain gauge on girder)

Matlab code to create graphs of C2 load versus deflection and load versus strain in deck

```
clc
clear all
load C2a.dat
[M I]= max(C2a(:,18))
J=find(C2a(:,18),1)
C2a=C2a((J-1):I,:);
LC=C2a(:,18);
Time=C2a(:,1);
```

```
%support deflection
init=C2a(1,1:36);
Suppz=C2a(:,2:5)-repmat(init(:,2:5),length(C2a),1);
SuppDefl=((Suppz(:,1)+Suppz(:,2))./2+(Suppz(:,3)+Suppz(:,4))./2)./2;
Defl=-(C2a(:,14)+C2a(:,15))./2;
Deflmsupp=Defl-SuppDefl;
load troy2a.dat
LoadT=troy2a(:,1);
DeflT=troy2a(1,2).*ones(size(troy2a,1),1)-troy2a(:,2);
%to increase number of values
vq=interp1(LoadT,DeflT,LC./1000);
DeflTmsupp=vq-SuppDefl;
load C2c.dat
[M I]= max(C2c(:,18))
J=find(C2c(:,18),1)
C2c=C2c((J-1):I,:);
LCc=C2c(:,18);
Timec=C2c(:,1);
initc=C2c(1,1:36);
Suppzc=C2c(:,2:5)-repmat(initc(:,2:5),length(C2c),1);
SuppDeflc=((Suppzc(:,1)+Suppzc(:,2))./2+(Suppzc(:,3)+Suppzc(:,4))./2).
/2;
Deflc=-(C2c(:,14)+C2c(:,15))./2-SuppDeflc;
MomentP=[297.472 297.472];
ACIP=[313 313];
AASHTOIT=[299 299];
AASHTOsimp=[455 455];

interval=150;
figure('name','Load vs. Deflection');
plot(Deflmsupp(1:interval:21966),LC(1:interval:21966)./1000,'-
k','linewidth',0.5);
hold on;
plot(Deflc,LCc./1000,'-b','linewidth',1)
plot([DeflTmsupp(1:interval:end); 3.9484],[LC(1:interval:end)./1000;
LC(end)/1000],'--k','linewidth',.5);
plot(Deflmsupp(5020),LC(5020)/1000,'sk','markersize',10,'linewidth',2)
plot(Deflmsupp(5563),LC(5563)/1000,'ok','markersize',10,'linewidth',2)
plot(3.9484, LC(end)./1000,'xk','markersize',10,'linewidth',2)
plot(Deflc(end),LCc(end)./1000,'xb','markersize',10,'linewidth',2)
xlim([0,4.25]);
ylim([0,325]);
legend('Test A','Test B','Manual Measurements','Shear Cracking
Observed, 150 kips','Flexural Cracking Observed, 160 kips','Test C2a
Max. Load: 301 kips','Test C2b Max. Load: 292
kips','location','southeast');
grid on
ax = gca;
ax.XTick = [0:0.25:4.25];
ax.YTick = [0:25:325];
ax.XTickLabelRotation = 90;
hold off;
xlabel('Deflection (in)')
ylabel('Load (kips)')
print('-djpeg','loadvsdeflC2.jpg')

init=C2a(1,1:36);
```

```
SGzero=C2a(:,22:25)-repmat(init(:,22:25),length(C2a),1);
LCzero=C2a(:,18)-repmat(init(:,18),length(C2a),1);

figure('name','Deck strain gauges');
plot(-SGzero(:,2),LCzero(:)./1000,'-b')
hold on
plot(-SGzero(:,3),LCzero./1000,'-k')
plot(-SGzero(:,4),LCzero./1000,'-r')
plot([0 2500],[max(LCzero)./1000 max(LCzero)./1000],'--k')
legend('Strain Gauge 2','Strain Gauge 3', 'Strain Gauge 4','Maximum
Load: 301 kips','location','best')
xlabel('Microstrain')
ylabel('Load, kips')
xlim([0 2500])
ylim([0 325])
hold off
print('-dpng','deckstrainC2.png')
```

Appendix B: Material Properties

Table 31: Compressive strength results from girder C

Web Cores								
Web core 1			**Web core 2**			**Web core 3**		
Length 1:	6.008	in.	Length 1:	5.874	in.	Length 1:	5.99	in.
Length 2:	6.016	in.	Length 2:	5.884	in.	Length 2:	5.99	in.
Diameter 1:	3.73	in.	Diameter 1:	3.731	in.	Diameter 1:	3.743	in.
Diameter 2:	3.732	in.	Diameter 2:	3.756	in.	Diameter 2:	3.745	in.
Diameter 3:	3.743	in.	Diameter 3:	3.597	in.	Diameter 3:	3.739	in.
Diameter 4:	3.743	in.	Diameter 4:	3.599	in.	Diameter 4:	3.712	in.
Avg. Diameter:	3.737	in.	Avg. Diameter:	3.670	in.	Avg. Diameter:	3.735	in.
Applied Load:	85850	lb	Applied Load:	73195	lb	Applied Load:	72780	lb
Area:	10.968	in^2	Area:	10.583	in^2	Area:	10.955	in^2
Compressive strength:	7827.2	psi	Compressive strength:	6916.4	psi	Compressive strength:	6643.5	psi
L/D Ratio:	1.609		L/D Ratio:	1.602		L/D Ratio:	1.604	
Corr.:	1.007		Corr:	1.008		Corr:	1.006	
Reported Strength:	**7879.7**	**psi**	**Reported Strength:**	**6968.6**	**psi**	**Reported Strength:**	**6681.6**	**psi**
Deck Cores								
Deck core 1			**Deck core 2**			**Deck core 4**		
Length 1:	6.002	in.	Length 1:	5.687	in.	Length 1:	6.052	in.
Length 2:	6.002	in.	Length 2:	5.691	in.	Length 2:	6.038	in.
Diameter 1:	3.738	in.	Diameter 1:	3.74	in.	Diameter 1:	3.748	in.
Diameter 2:	3.737	in.	Diameter 2:	3.738	in.	Diameter 2:	3.748	in.
Diameter 3:	3.74	in.	Diameter 3:	3.739	in.	Diameter 3:	3.748	in.
Diameter 4:	3.74	in.	Diameter 4:	3.74	in.	Diameter 4:	3.755	in.
Avg. Diameter:	3.739	in.	Avg. Diameter:	3.739	in.	Avg. Diameter:	3.750	in.
Applied Load:	71925	lb	Applied Load:	74760	lb	Applied Load:	52850	lb
Area:	10.978	in^2	Area:	10.981	in^2	Area:	11.043	in^2
Compressive strength:	6551.4	psi	Compressive strength:	6807.9	psi	Compressive strength:	4785.8	psi
L/D Ratio:	1.605		L/D Ratio:	1.521		L/D Ratio:	1.612	
Corr.:	1.006		Corr:	0.997		Corr:	1.005	
Reported Strength:	**6588.9**	**psi**	**Reported Strength:**	**6784.3**	**psi**	**Reported Strength:**	**4810.8**	**psi**

Table 32: Summary of scale girder compressive strengths

Girder	1 Day (psi)				7 Day (psi)				
	1	**2**	**3**	**Avg.**	**1**	**2**	**3**	**Avg.**	
A1s	4230	4135	4185	*4183*	6290	6230	5830	*6117*	
A2s	4440	4225	4400	*4355*	6210	6010	6075	*6098*	
A3s	4300	4250	4040	*4197*	5965	5940	5775	*5893*	
A4s	4505	4285	4530	*4440*	6220	6150	5810	*6060*	
A5s	4190	4330	4205	*4242*	5930	5835	5815	*5860*	
A6s	4350	4315	4210	*4292*	5535	5590	5505	*5543*	
C1s	4510	4295	4350	*4385*	5980	6045	6335	*6120*	
C2s	4125	4145	4215	*4162*	6055	5830	5785	*5890*	
	28 Day (psi)				**Long Term (psi)**				**# Days**
A1s	**1**	**2**	**3**	**Avg.**	**1**	**2**	**3**	**Avg.**	
A2s	6625	6760	6710	*6698*	7310	6740	7210	*7087*	292
A3s	6775	6590	6770	*6712*	6815	6910	6960	*6895*	292
A4s	6375	6110	6250	*6245*	6645	6720	6870	*6745*	286
A5s	6415	6450	6680	*6515*	6955	6765	6865	*6862*	287
A6s	6235	5990	5555	*5927*	6150	6680	6500	*6443*	285
C1s	6155	5920	6205	*6093*	6625	6305	6165	*6365*	285
C2s	5755	5780	5925	*5820*	6560	6425	6560	*6515*	265
	5715	5835	5545	*5698*	6215	6200	6410	*6275*	265

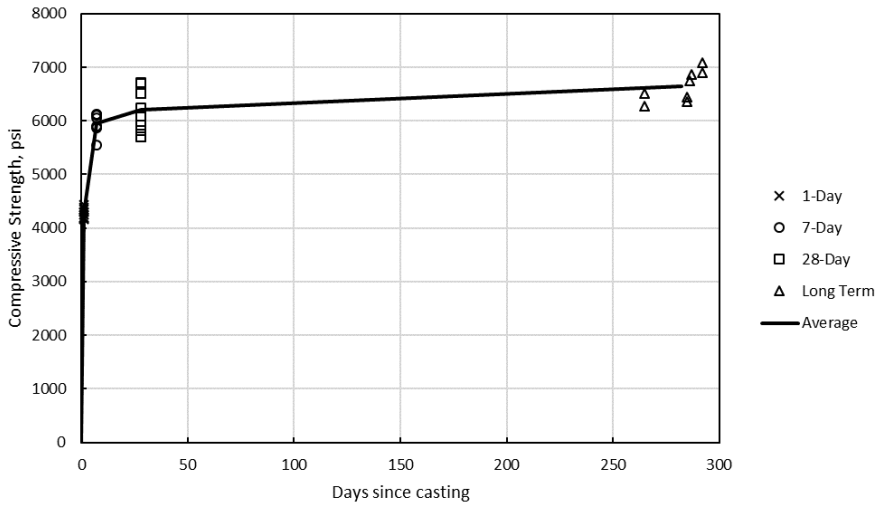

Figure 155: Compressive strengths of scale girders over time

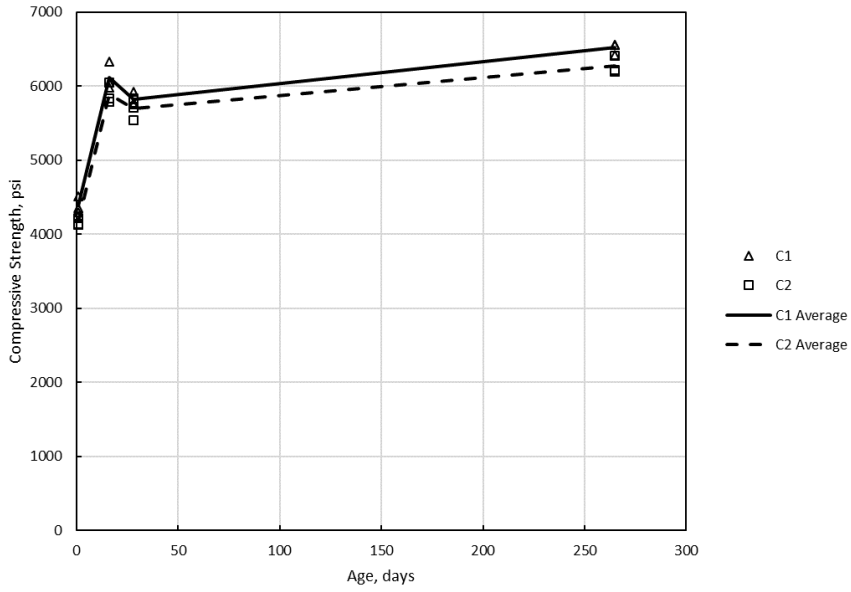

Figure 156: Compressive strengths of C1s and C2s over time

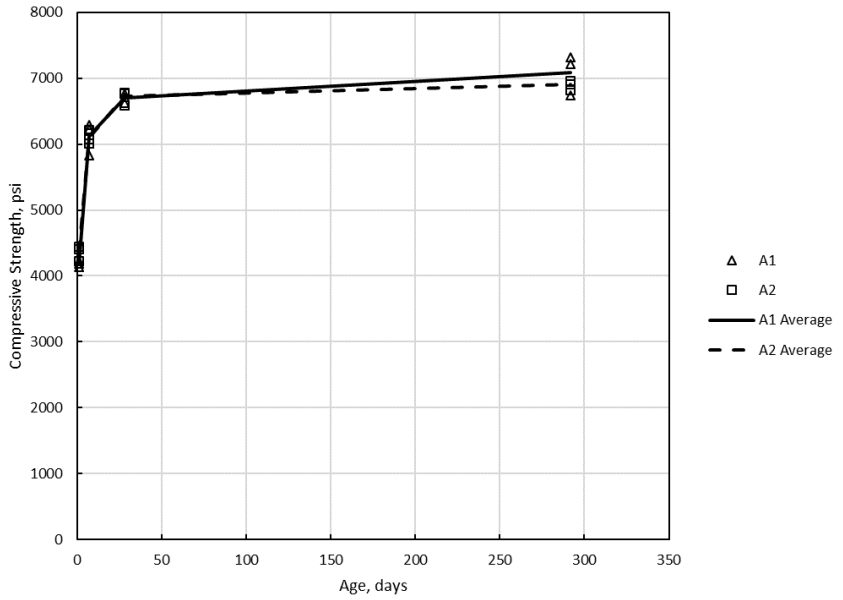

Figure 157: Compressive strengths of A1s and A2s over time

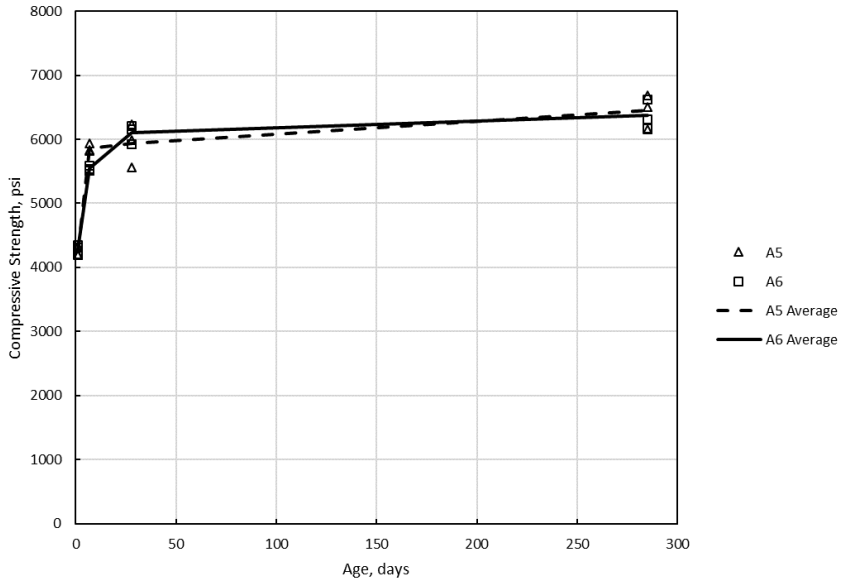

Figure 158: Compressive strength of A5s and A6s over time

Table 33: Summary of compressive strengths from deck pours

Concrete	1 Day				
	1	**2**	**3**	**Avg.**	
Ind. Girder Deck	1920	1960	2200	*2027*	
Bridge Deck	2655	2695	2540	*2630*	
	7 Day				
	1	**2**	**3**	**Avg.**	
Ind. Girder Deck	4150	4160	3650	*3987*	
Bridge Deck	3895	4060	4320	*4092*	
	14 Day				
	1	**2**	**3**	**Avg.**	
Ind. Girder Deck	4305	3760	4025	*4030*	
Bridge Deck	4310	4315	4435	*4353*	
	28 Day				
	1	**2**	**3**	**Avg.**	
Ind. Girder Deck	4220	3930	4405	*4185*	
Bridge Deck	4740	4125	4485	*4450*	
	Long Term				
	1	**2**	**3**	**Avg.**	**# Days**
Ind. Girder Deck	4320	4410	4265	*4332*	132
Bridge Deck	4065	3830	4035	*3977*	188

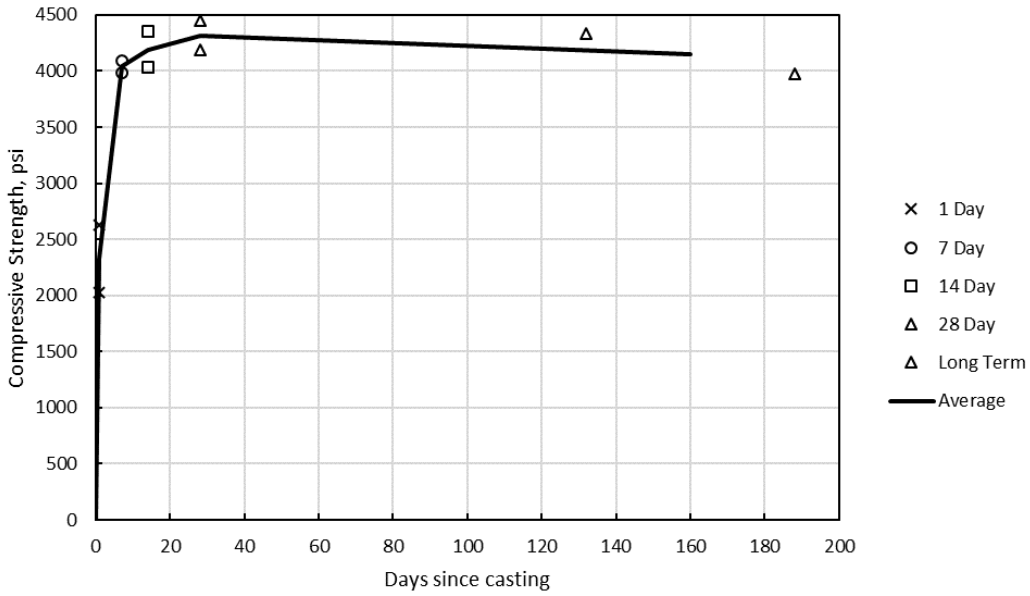

Figure 159: Compressive strengths of deck pours over time

Table 34: Scale deck modulus of elasticity

	Cyl. 1 Modulus (ksi)	Cyl. 2 Modulus (ksi)	Cyl. 3 Modulus (ksi)	Average (ksi)	Std. Dev.	Coefficient of Variation	Compr. Strength (psi)	ACI Eqn. (ksi)	% Difference
Ind. Deck	3745	3632	3674	3684	56.97	1.55%	3980	3596	-2.38%
Brd. Deck	36230	3934	3854	3806	157.86	4.15%	4340	3755	-1.33%

Appendix C: Additional data from girder and bridge tests

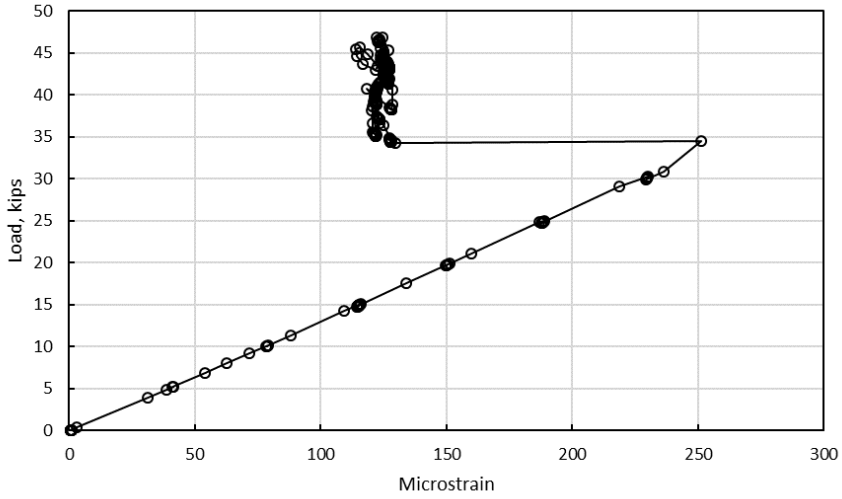

Figure 160: Strains under load point during test A1s

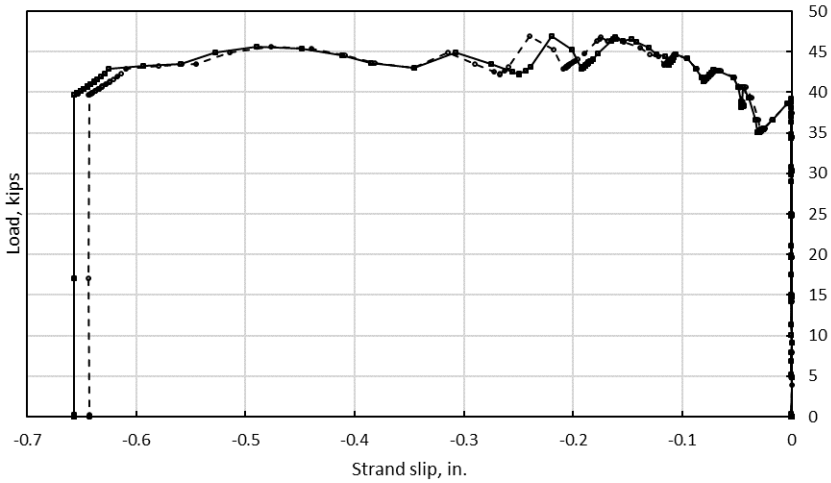

Figure 161: Strand slip during test A1s

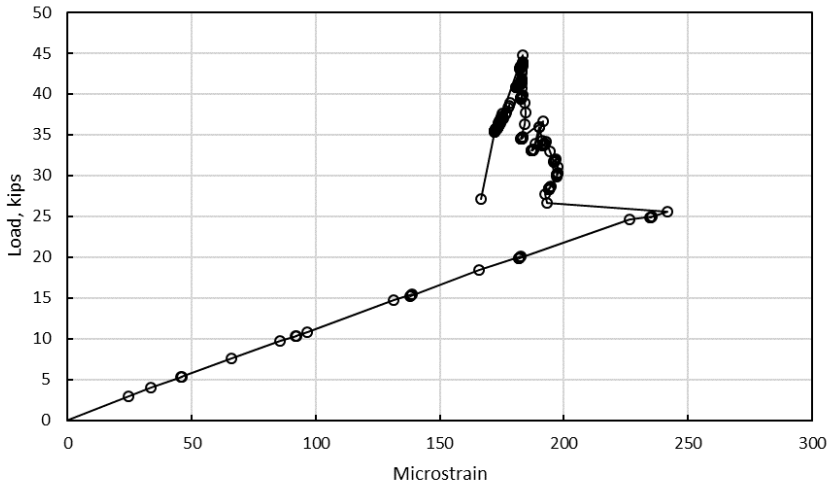

Figure 162: Strains under load point during test A2s

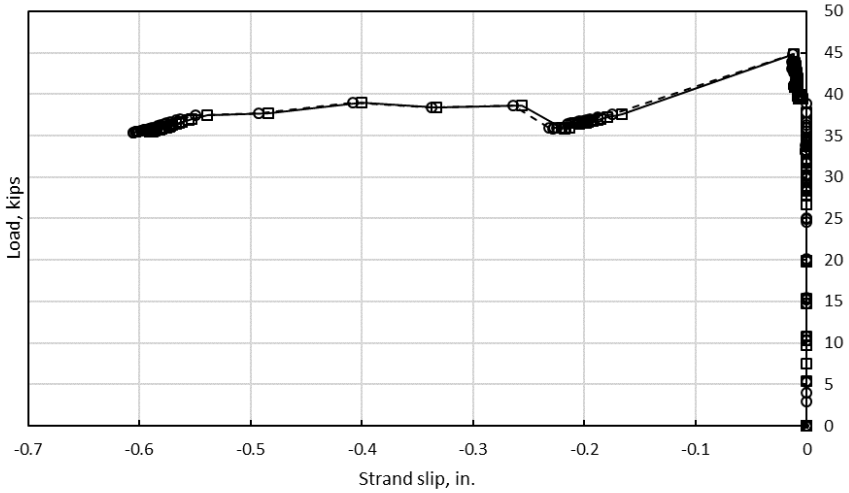

Figure 163: Strand slip during test A2s

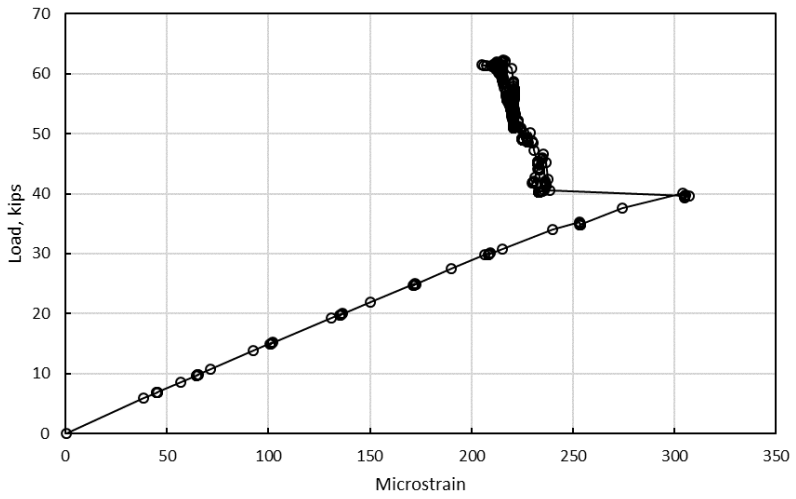

Figure 164: Strains under load point during test C1s

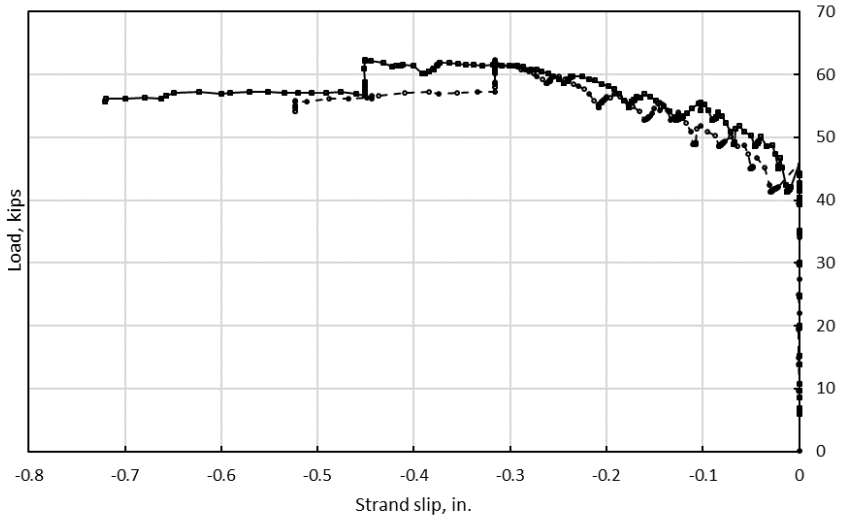

Figure 165: Strand slip during test C1s

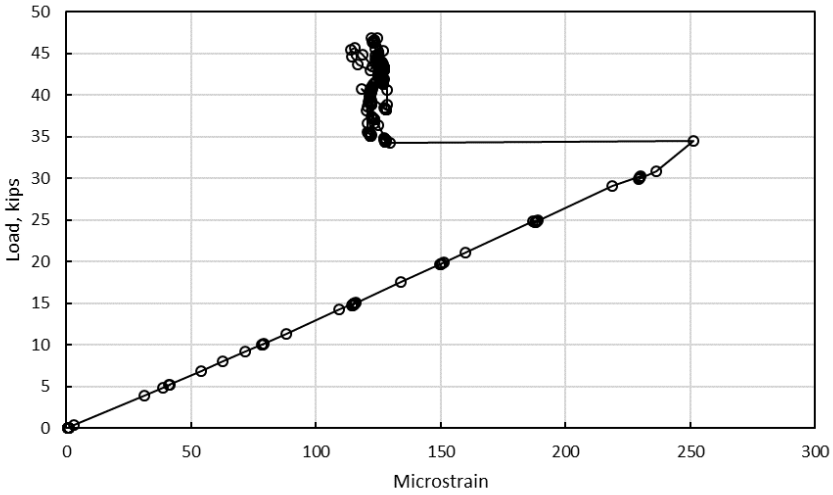

Figure 166: Strains under load point during test C2s

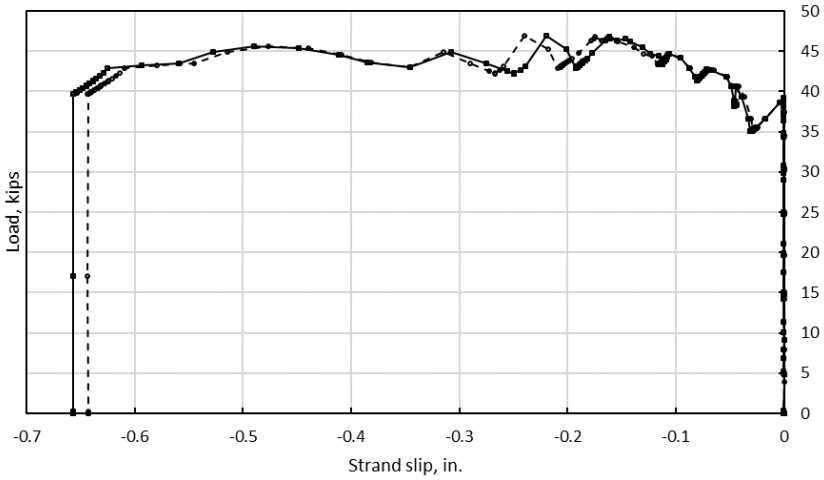

Figure 167: Strand slip during test C2s

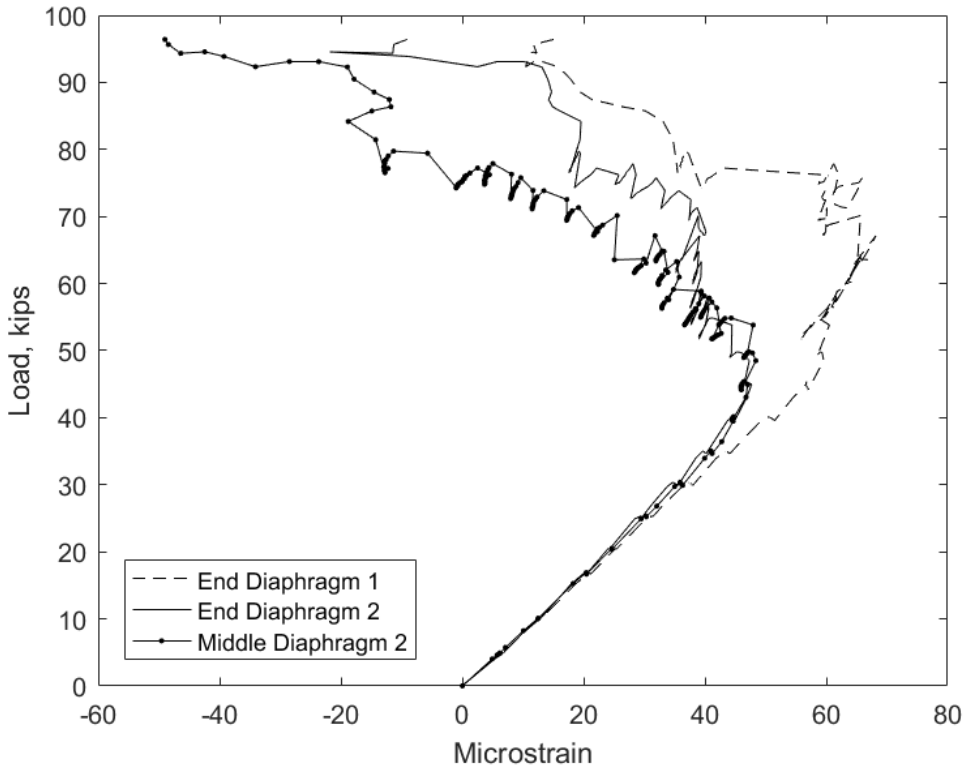

Figure 168: Diaphragm strains measured during scale bridge test

Appendix D: Live Load Shear Demands for I244 Spans

Table 35: Live load shear demands for I244 spans A and C

1244 A demands								
Location	**Truck Shear**	**Lane**	**Sum**	**LL+IM (Truck)**	**Total LL**	**Factored LL**	**Ext. Demand**	**Int. Demand**
(ft)	**(kips)**	**(kips)**	**(kips)**	**(kips)**	**(kips)**	**(kips)**	**(kips)**	**(kips)**
0.0	49.6	9.6	59.2	66.0	75.6	132.2	85.8	104.6
2.2	42.7	8.2	50.9	56.8	64.9	113.6	73.8	89.9
5.4	36.3	6.2	42.5	48.2	54.5	95.3	61.9	75.4
8.6	29.9	4.7	34.6	39.7	44.4	77.7	50.5	61.5
11.8	23.5	3.5	26.9	31.2	34.7	60.7	39.4	48.0
15.0	17.1	2.4	19.5	22.7	25.1	43.9	28.5	34.7
18.2	23.5	3.5	26.9	31.2	34.7	60.7	39.4	48.0
21.4	29.9	4.7	34.6	39.7	44.4	77.7	50.5	61.5
24.6	36.3	6.2	42.5	48.2	54.5	95.3	61.9	75.4
27.8	42.7	8.2	50.9	56.8	64.9	113.6	73.8	89.9
30.0	49.6	9.6	59.2	66.0	75.6	132.2	85.8	104.6

1244 C demands								
Location	**Truck Shear**	**Lane**	**Sum**	**LL+IM (Truck)**	**Total LL**	**Factored LL**	**Ext. Demand**	**Int. Demand**
(ft)	**(kips)**	**(kips)**	**(kips)**	**(kips)**	**(kips)**	**(kips)**	**(kips)**	**(kips)**
0.0	57.4	14.7	72.1	76.3	91.0	159.3	103.4	126.0
4.2	50.8	12.0	62.9	67.6	79.6	139.3	90.4	110.2
8.9	43.3	9.4	52.7	57.6	67.0	117.3	76.1	92.7
13.6	36.1	7.2	43.3	48.0	55.2	96.6	62.7	76.4
18.3	28.7	5.3	34.0	38.1	43.4	76.0	49.3	60.1
23.0	22.3	3.7	25.9	29.6	33.3	58.3	37.8	46.1
27.7	28.7	5.3	34.0	38.1	43.4	76.0	49.3	60.1
32.4	36.1	7.2	43.3	48.0	55.2	96.6	62.7	76.4
37.1	43.3	9.4	52.7	57.6	67.0	117.3	76.1	92.7
41.8	50.8	12.0	62.9	67.6	79.6	139.3	90.4	110.2
46.0	57.4	14.7	72.1	76.3	91.0	159.3	103.4	126.0

Appendix E: Distribution factor data

Table 36: Distribution factors from STAAD and model parameters

	Model Parameters				Max DFs from STAAD			
	Spacing (ft)	L (ft)	Thickness (in.)	Diaphragm?	Ext. 1 Lane	Int. 1 Lane	Ext. 2+ Lane	Int. 2+ Lane
Grill1YD	6	30	7	y	0.525	0.417	0.501	0.499
Grill1ND	6	30	7	n	0.525	0.437	0.501	0.499
Grill2YD	6	30	9	y	0.525	0.416	0.501	0.499
Grill2ND	6	30	9	n	0.525	0.425	0.501	0.499
Gill13YD	6	42.5	7	y	0.526	0.403	0.500	0.500
Grill13ND	6	42.5	7	n	0.526	0.424	0.500	0.500
Grill14YD	6	42.5	9	y	0.526	0.402	0.500	0.500
Grill14ND	6	42.5	9	n	0.526	0.409	0.500	0.500
Grill3YD	6	55	7	y	0.527	0.399	0.500	0.500
Grill3ND	6	55	7	n	0.527	0.410	0.500	0.500
Grill4YD	6	55	9	y	0.527	0.398	0.500	0.500
Grill4ND	6	55	9	n	0.527	0.399	0.500	0.500
Grill19YD	6	67.5	7	y	0.527	0.398	0.500	0.500
Grill19ND	6	67.5	7	n	0.527	0.407	0.500	0.500
Grill20YD	6	67.5	9	y	0.526	0.397	0.500	0.500
Grill20ND	6	67.5	9	n	0.527	0.397	0.500	0.500
Grill5YD	9	30	7	y	0.628	0.562	0.680	0.700
Grill5ND	9	30	7	n	0.633	0.615	0.648	0.735
Grill6YD	9	30	9	y	0.626	0.555	0.685	0.694
Grill6ND	9	30	9	n	0.629	0.586	0.665	0.716
Grill15YD	9	42.5	7	y	0.625	0.542	0.686	0.692
Grill15ND	9	42.5	7	n	0.629	0.582	0.662	0.719
Grill16YD	9	42.5	9	y	0.624	0.533	0.692	0.686
Grill16ND	9	42.5	9	n	0.626	0.556	0.678	0.701
Grill7YD	9	55	7	y	0.625	0.532	0.691	0.687
Grill7ND	9	55	7	n	0.628	0.565	0.670	0.709
Grill8YD	9	55	9	y	0.624	0.523	0.697	0.680
Grill8ND	9	55	9	n	0.626	0.541	0.685	0.693
Grill21YD	9	67.5	7	y	0.624	0.533	0.690	0.688
Grill21ND	9	67.5	7	n	0.627	0.562	0.672	0.707
Grill22YD	9	67.5	9	y	0.629	0.525	0.696	0.681
Grill22ND	9	67.5	9	n	0.624	0.540	0.685	0.692
Grill9YD	12	30	7	y	0.707	0.654	0.795	0.984
Grill9ND	12	30	7	n	0.713	0.713	0.755	1.030
Grill10YD	12	30	9	y	0.704	0.641	0.802	0.975
Grill10ND	12	30	9	n	0.708	0.679	0.774	1.006
Grill17YD	12	42.5	7	y	0.702	0.629	0.804	0.975
Grill17ND	12	42.5	7	n	0.706	0.674	0.772	1.011

Grill18YD	12	42.5	9	y	0.698	0.615	0.812	0.964
Grill18ND	12	42.5	9	n	0.701	0.642	0.792	0.987
Grill11YD	12	55	7	y	0.700	0.617	0.809	0.971
Grill11ND	12	55	7	n	0.703	0.654	0.782	1.000
Grill12YD	12	55	9	y	0.697	0.602	0.818	0.958
Grill12ND	12	55	9	n	0.698	0.624	0.801	0.977
Grill23YD	12	67.5	7	y	0.699	0.617	0.810	0.969
Grill23ND	12	67.5	7	n	0.701	0.649	0.786	0.994
Grill24YD	12	67.5	9	y	0.696	0.603	0.819	0.956
Grill24ND	12	67.5	9	n	0.696	0.621	0.804	0.971

Table 37: AASHTO distribution factors for parametric models

	Model Parameters				AASHTO Shear DFs (m included)			
	Spacing (ft)	**L (ft)**	**Thickness (in.)**	**Diaphragm?**	**Ext. 1 Lane**	**Ext. 2 Lane**	**Int. 1 Lane**	**Int. 2 Lane**
Grill1YD	6	30	7	y	0.660	0.536	0.600	0.671
Grill1ND	6	30	7	n	0.600	0.536	0.600	0.671
Grill2YD	6	30	9	y	0.660	0.536	0.600	0.671
Grill2ND	6	30	9	n	0.600	0.536	0.600	0.671
Gill13YD	6	42.5	7	y	0.660	0.536	0.600	0.671
Grill13ND	6	42.5	7	n	0.600	0.536	0.600	0.671
Grill14YD	6	42.5	9	y	0.660	0.536	0.600	0.671
Grill14ND	6	42.5	9	n	0.600	0.536	0.600	0.671
Grill3YD	6	55	7	y	0.660	0.536	0.600	0.671
Grill3ND	6	55	7	n	0.600	0.536	0.600	0.671
Grill4YD	6	55	9	y	0.660	0.536	0.600	0.671
Grill4ND	6	55	9	n	0.600	0.536	0.600	0.671
Grill19YD	6	67.5	7	y	0.660	0.536	0.600	0.671
Grill19ND	6	67.5	7	n	0.600	0.536	0.600	0.671
Grill20YD	6	67.5	9	y	0.660	0.536	0.600	0.671
Grill20ND	6	67.5	9	n	0.600	0.536	0.600	0.671
Grill5YD	9	30	7	y	0.800	0.800	0.720	0.884
Grill5ND	9	30	7	n	0.800	0.707	0.720	0.884
Grill6YD	9	30	9	y	0.800	0.800	0.720	0.884
Grill6ND	9	30	9	n	0.800	0.707	0.720	0.884
Grill15YD	9	42.5	7	y	0.800	0.800	0.720	0.884
Grill15ND	9	42.5	7	n	0.800	0.707	0.720	0.884
Grill16YD	9	42.5	9	y	0.800	0.800	0.720	0.884
Grill16ND	9	42.5	9	n	0.800	0.707	0.720	0.884
Grill7YD	9	55	7	y	0.800	0.800	0.720	0.884
Grill7ND	9	55	7	n	0.800	0.707	0.720	0.884

Grill8YD	9	55	9	y	0.800	0.800	0.720	0.884
Grill8ND	9	55	9	n	0.800	0.707	0.720	0.884
Grill21YD	9	67.5	7	y	0.800	0.800	0.720	0.884
Grill21ND	9	67.5	7	n	0.800	0.707	0.720	0.884
Grill22YD	9	67.5	9	y	0.800	0.800	0.720	0.884
Grill22ND	9	67.5	9	n	0.800	0.707	0.720	0.884
Grill9YD	12	30	7	y	0.900	0.950	0.840	1.082
Grill9ND	12	30	7	n	0.900	0.866	0.840	1.082
Grill10YD	12	30	9	y	0.900	0.950	0.840	1.082
Grill10ND	12	30	9	n	0.900	0.866	0.840	1.082
Grill17YD	12	42.5	7	y	0.900	0.950	0.840	1.082
Grill17ND	12	42.5	7	n	0.900	0.866	0.840	1.082
Grill18YD	12	42.5	9	y	0.900	0.950	0.840	1.082
Grill18ND	12	42.5	9	n	0.900	0.866	0.840	1.082
Grill11YD	12	55	7	y	0.900	0.950	0.840	1.082
Grill11ND	12	55	7	n	0.900	0.866	0.840	1.082
Grill12YD	12	55	9	y	0.900	0.950	0.840	1.082
Grill12ND	12	55	9	n	0.900	0.866	0.840	1.082
Grill23YD	12	67.5	7	y	0.900	0.950	0.840	1.082
Grill23ND	12	67.5	7	n	0.900	0.866	0.840	1.082
Grill24YD	12	67.5	9	y	0.900	0.950	0.840	1.082
Grill24ND	12	67.5	9	n	0.900	0.866	0.840	1.082

Table 38: Girder properties for parametric bridge models

Model Number	(Diaphragm Y or N)	Length (ft)	Spacing (ft)	Slab thickness (in.)	Interior Girders			Exterior Girders		
					A (in^2)	J (in^4)	I (in^4)	A (in^2)	J (in^4)	I (in^4)
1	*Y*	30	6	7	805.5	7387.4	68335.1	732.8	7387.4	66731.0
1	*N*	30	6	7	805.5	7387.4	68335.1	732.8	7387.4	66731.0
2	*Y*	30	6	9	930.3	7451.7	72106.1	836.7	7451.7	70200.3
2	*N*	30	6	9	930.3	7451.7	72106.1	836.7	7451.7	70200.3
3	*Y*	55	6	7	805.5	7387.4	68335.1	732.8	7387.4	66731.0
3	*N*	55	6	7	805.5	7387.4	68335.1	732.8	7387.4	66731.0
4	*Y*	55	6	9	930.3	7451.7	72106.1	836.7	7451.7	70200.3
4	*N*	55	6	9	930.3	7451.7	72106.1	836.7	7451.7	70200.3
5	*Y*	30	9	7	1023.8	7387.4	72032.9	841.9	7387.4	69052.5
5	*N*	30	9	7	1023.8	7387.4	72032.9	841.9	7387.4	69052.5
6	*Y*	30	9	9	1210.9	7451.7	76642.2	977.0	7451.7	72967.5
6	*N*	30	9	9	1210.9	7451.7	76642.2	977.0	7451.7	72967.5
7	*Y*	55	9	7	1023.8	7387.4	72032.9	841.9	7387.4	69052.5
7	*N*	55	9	7	1023.8	7387.4	72032.9	841.9	7387.4	69052.5
8	*Y*	55	9	9	1210.9	7451.7	76642.2	977.0	7451.7	72967.5
8	*N*	55	9	9	1210.9	7451.7	76642.2	977.0	7451.7	72967.5
9	*Y*	30	12	7	1242.1	7387.4	74744.4	951.0	7387.4	70943.5
9	*N*	30	12	7	1242.1	7387.4	74744.4	951.0	7387.4	70943.5
10	*Y*	30	12	9	1491.5	7451.7	80184.2	1117.3	7451.7	75277.6
10	*N*	30	12	9	1491.5	7451.7	80184.2	1117.3	7451.7	75277.6
11	*Y*	55	12	7	1242.1	7387.4	74744.4	951.0	7387.4	70943.5
11	*N*	55	12	7	1242.1	7387.4	74744.4	951.0	7387.4	70943.5
12	*Y*	55	12	9	1491.5	7451.7	80184.2	1117.3	7451.7	75277.6
12	*N*	55	12	9	1491.5	7451.7	80184.2	1117.3	7451.7	75277.6
13	*Y*	42.5	6	7	805.5	7387.4	68335.1	732.8	7387.4	66731.0
13	*N*	42.5	6	7	805.5	7387.4	68335.1	732.8	7387.4	66731.0
14	*Y*	42.5	6	9	930.3	7451.7	72106.1	836.7	7451.7	70200.3
14	*N*	42.5	6	9	930.3	7451.7	72106.1	836.7	7451.7	70200.3
15	*Y*	42.5	9	7	1023.8	7387.4	72032.9	841.9	7387.4	69052.5
15	*N*	42.5	9	7	1023.8	7387.4	72032.9	841.9	7387.4	69052.5
16	*Y*	42.5	9	9	1210.9	7451.7	76642.2	977.0	7451.7	72967.5
16	*N*	42.5	9	9	1210.9	7451.7	76642.2	977.0	7451.7	72967.5
17	*Y*	42.5	12	7	1242.1	7387.4	74744.4	951.0	7387.4	70943.5
17	*N*	42.5	12	7	1242.1	7387.4	74744.4	951.0	7387.4	70943.5
18	*Y*	42.5	12	9	1491.5	7451.7	80184.2	1117.3	7451.7	75277.6
18	*N*	42.5	12	9	1491.5	7451.7	80184.2	1117.3	7451.7	75277.6
19	*Y*	67.5	6	7	805.5	7387.4	68335.1	732.8	7387.4	66731.0

19	*N*	67.5	6	7	805.5	7387.4	68335.1	732.8	7387.4	66731.0
20	*Y*	67.5	6	9	930.3	7451.7	72106.1	836.7	7451.7	70200.3
20	*N*	67.5	6	9	930.3	7451.7	72106.1	836.7	7451.7	70200.3
21	*Y*	67.5	9	7	1023.8	7387.4	72032.9	841.9	7387.4	69052.5
21	*N*	67.5	9	7	1023.8	7387.4	72032.9	841.9	7387.4	69052.5
22	*Y*	67.5	9	9	1210.9	7451.7	76642.2	977.0	7451.7	72967.5
22	*N*	67.5	9	9	1210.9	7451.7	76642.2	977.0	7451.7	72967.5
23	*Y*	67.5	12	7	1242.1	7387.4	74744.4	951.0	7387.4	70943.5
23	*N*	67.5	12	7	1242.1	7387.4	74744.4	951.0	7387.4	70943.5
24	*Y*	67.5	12	9	1491.5	7451.7	80184.2	1117.3	7451.7	75277.6
24	*N*	67.5	12	9	1491.5	7451.7	80184.2	1117.3	7451.7	75277.6

Table 39: Continued properties for parametric bridge models

Model Number (Diaphragm Y or N)		Slab			Slab + Middle Diaphragm			End Slab		
		A (in^2)	I (in^4)	J (in^4)	A (in^2)	J (in^4)	I (in^4)	A (in^2)	J (in^4)	I (in^4)
1	*Y*	272.8	2228.1	1286.3	439.1	6546.0	12299.4	302.7	5259.7	10862.5
1	*N*	272.8	2228.1	1286.3	X	X	X	136.4	1114.1	557.0
2	*Y*	350.8	4735.6	2367.8	517.1	9267.6	14073.0	341.7	6533.8	11983.2
2	*N*	350.8	4735.6	2367.8	X	X	X	175.4	2367.8	1183.9
3	*Y*	500.2	4084.9	2042.5	666.5	8689.7	13893.7	416.4	6331.6	12099.9
3	*N*	500.2	4084.9	2042.5	X	X	X	250.1	2042.5	1021.2
4	*Y*	643.1	8682.0	4341.0	809.4	13823.8	16683.6	487.9	8812.0	13770.0
4	*N*	643.1	8682.0	4341.0	X	X	X	321.6	4341.0	2170.5
5	*Y*	272.8	2228.1	1114.1	439.1	6546.0	12299.4	302.7	5259.7	10862.5
5	*N*	272.8	2228.1	1114.1	X	X	X	136.4	1114.1	557.0
6	*Y*	350.8	4735.6	2367.8	517.1	9267.6	14073.0	341.7	6533.8	11983.2
6	*N*	350.8	4735.6	2367.8	X	X	X	175.4	2367.8	1183.9
7	*Y*	500.2	4084.9	2042.5	666.5	8689.7	13893.7	416.4	6331.6	12099.9
7	*N*	500.2	4084.9	2042.5	X	X	X	250.1	2042.5	1021.2
8	*Y*	643.1	8682.0	4341.0	809.4	13823.8	16683.6	487.9	8812.0	13770.0
8	*N*	643.1	8682.0	4341.0	X	X	X	321.6	4341.0	2170.5
9	*Y*	272.8	2228.1	1114.1	439.1	6546.0	12299.4	302.7	5259.7	10862.5
9	*N*	272.8	2228.1	1114.1	X	X	X	136.4	1114.1	557.0
10	*Y*	350.8	4735.6	2367.8	517.1	9267.6	14073.0	341.7	6533.8	11983.2
10	*N*	350.8	4735.6	2367.8	X	X	X	175.4	2367.8	1183.9
11	*Y*	500.2	4084.9	2042.5	666.5	8689.7	13893.7	416.4	6331.6	12099.9
11	*N*	500.2	4084.9	2042.5	X	X	X	250.1	2042.5	1021.2
12	*Y*	643.1	8682.0	4341.0	809.4	13823.8	16683.6	487.9	8812.0	13770.0
12	*N*	643.1	8682.0	4341.0	X	X	X	321.6	4341.0	2170.5

13	*Y*	386.5	3156.5	1578.3	552.8	7617.9	13165.0	359.6	5795.7	11542.4
13	*N*	386.5	3156.5	1578.3	X	X	X	193.3	1578.3	789.1
14	*Y*	496.9	6708.8	3354.4	663.2	11545.7	15448.6	414.8	7672.9	12947.1
14	*N*	496.9	6708.8	3354.4	X	X	X	248.5	3354.4	1677.2
15	*Y*	386.5	3156.5	1578.3	552.8	7617.9	13165.0	359.6	5795.7	11542.4
15	*N*	386.5	3156.5	1578.3	X	X	X	193.3	1578.3	789.1
16	*Y*	496.9	6708.8	3354.4	663.2	11545.7	15448.6	414.8	7672.9	12947.1
16	*N*	496.9	6708.8	3354.4	X	X	X	248.5	3354.4	1677.2
17	*Y*	386.5	3156.5	1578.3	552.8	7617.9	13165.0	359.6	5795.7	11542.4
17	*N*	386.5	3156.5	1578.3	X	X	X	193.3	1578.3	789.1
18	*Y*	496.9	6708.8	3354.4	663.2	11545.7	15448.6	414.8	7672.9	12947.1
18	*N*	496.9	6708.8	3354.4	X	X	X	248.5	3354.4	1677.2
19	*Y*	613.9	5013.3	2506.7	780.2	9761.6	14545.4	473.2	6867.6	12579.3
19	*N*	613.9	5013.3	2506.7	X	X	X	306.9	2506.7	1253.3
20	*Y*	789.3	10655.1	5327.6	955.6	16102.0	17842.7	560.9	9951.0	14507.0
20	*N*	789.3	10655.1	5327.6	X	X	X	394.6	5327.6	2663.8
21	*Y*	613.9	5013.3	2506.7	780.2	9761.6	14545.4	473.2	6867.6	12579.3
21	*N*	613.9	5013.3	2506.7	X	X	X	306.9	2506.7	1253.3
22	*Y*	789.3	10655.1	5327.6	955.6	16102.0	17842.7	560.9	9951.0	14507.0
22	*N*	789.3	10655.1	5327.6	X	X	X	394.6	5327.6	2663.8
23	*Y*	613.9	5013.3	2506.7	780.2	9761.6	14545.4	473.2	6867.6	12579.3
23	*N*	613.9	5013.3	2506.7	X	X	X	306.9	2506.7	1253.3
24	*Y*	789.3	10655.1	5327.6	955.6	16102.0	17842.7	560.9	9951.0	14507.0
24	*N*	789.3	10655.1	5327.6	X	X	X	394.6	5327.6	2663.8

Table 40: Properties for grillage models of selected Oklahoma bridges

	Length	Spacing	Slab thickness	Interior girder			Exterior Girder		
Bridge	**(ft)**	**(ft)**	**(in.)**	**A (in^2)**	**J (in^4)**	**I (in^4)**	**A (in^2)**	**J (in^4)**	**I (in^4)**
Little River Overflow	34.83	11.75	9	1468.1	7451.7	79913.1	1105.7	7451.7	75098.3
I244 A	30.5	7.67	7	1053.7	7387.4	72448.6	889.9	7387.4	69928.5
I244 C	46	7.67	7	960.1	7387.4	71085.7	818.8	7387.4	68601.7

	Slab			Slab + middle diaphragm			Slab + end diaphragm		
	A (in^2)	**J (in^4)**	**I (in^4)**	**A (in^2)**	**J (in^4)**	**I (in^4)**	**A (in^2)**	**J (in^4)**	**I (in^4)**
Little River Overflow	407.3	5498.6	2749.3	573.6	10148.5	14628.4	369.9	6974.3	12377.9
I244 A	340.5	2780.6	1390.3	544.6	6588.9	15144.4	374.4	5281.2	13370.8
I244 C	443.3	3620.5	1810.3	619.6	7918.0	14178.4	397.9	5945.7	12407.6